

Effect of Flow on the Formation of Iron Carbonate and Influence of Exposed Iron
Carbide Layer

A thesis presented to
the faculty of
the Russ College of Engineering and Technology of Ohio University

In partial fulfillment
of the requirements for the degree
Master of Science

Maria C. Di Bonaventura

August 2017

© 2017 Maria C. Di Bonaventura. All Rights Reserved.

This thesis titled

Effect of Flow on the Formation of Iron Carbonate and Influence of Exposed Iron
Carbide Layer

by

MARIA C. DI BONAVENTURA

has been approved for

the Department of Chemical and Biomolecular Engineering
and the Russ College of Engineering and Technology by

Marc Singer

Assistant Professor of Chemical and Biomolecular Engineering

Dennis Irwin

Dean, Russ College of Engineering and Technology

ABSTRACT

DI BONAVENTURA, MARIA C., M.S., August 2017, Chemical & Biomolecular Engineering

Effect of Flow on the Formation of Iron Carbonate and Influence of Exposed Iron Carbide Layer

Director of Thesis: Marc Singer

Iron carbonate (FeCO_3) is the commonest corrosion product that forms on the surface of mild steel as a by-product of the CO_2 corrosion process. This FeCO_3 layer slows down further corrosion by acting as a diffusion barrier, blocking corrosive species from reaching the steel surface. However, high flow velocities, which can be common in various industrial operations, have been postulated either to lead to partial mechanical removal of FeCO_3 layers or to impede the nucleation of FeCO_3 crystals on the steel surface altogether.

In the experimental study described herein, corrosion product formation in highly turbulent conditions was investigated with surface analysis techniques. Experiments were divided in relation to three different sets of tasks focusing on high initial saturation values, low and constant saturation values, and high velocity experiments. The first set of experiments was performed in a three electrode glass cell and rotating cylinder setup and investigated the presence/attachment/adherence of FeCO_3 on the steel surface in short term experiments with high initial saturation values ($S_{\text{FeCO}_3} \sim 150$). The aim was to study the precipitation of FeCO_3 in conditions where the bulk solution has a high concentration of ferrous ions at continuous rotational speeds, from the start to the end of each experiment. It was found that as the fluid velocity increased, there was less attachment of FeCO_3 , with

the highest velocity of 2.0 m/s (wall shear stress of 7 Pa) showing no FeCO₃ formation/attachment on the metal surface.

The second task focused on controlling the pH and ferrous ion concentration in solution, in order to better mimic actual field conditions. Additionally, a controlled mass transfer setup was utilized that eliminated any non-uniformity of flow and centrifugal forces often associated with rotating cylinder working electrodes. In this set of experiments, four different materials and/or microstructures were tested, namely pure Fe (99.8%), UNS G10180⁽¹⁾ with two different microstructures (tempered martensite and ferritic-pearlitic), and API 5L X65⁽²⁾. It was observed that the carbon content and microstructure (distribution of iron carbide [Fe₃C]) have a strong effect on the results with the ferritic-pearlitic steel clearly favoring FeCO₃ precipitation.

The third task consisted of exposing the material tested to highly turbulent conditions in a Thin Channel Flow Cell (TCFC) to identify a critical velocity for removal of Fe₃C. The material chosen displayed formation of FeCO₃ in task 2, which was UNS G10180 with a ferritic-pearlitic microstructure. A critical velocity for Fe₃C removal was clearly identified, which further inhibited formation of FeCO₃, although it is fully expected that its value should depend on the operating conditions.

⁽¹⁾ Unified Numbering System for Metals and Alloys (UNS). UNS numbers are listed in Metals & Alloys in the Unified Numbering System, 10th ed. (Warrendale, PAE: SAE International and West Conshohocken, PA: ASTM International, 2004).

⁽²⁾ American Petroleum Institute (API), 1220 L St. NW, Washington, DC 20005.

DEDICATION

To

My parents, Carolina Furno and Claudio Di Bonaventura,

my beloved companion, Roberto Ruiz

and other family members

who give me constant love and support

ACKNOWLEDGMENTS

I would like to give thanks to my advisor Prof. Marc Singer for his guidance during my Master's degree studies. I appreciate the chance to work with him and for exposing me to challenging environments as well as the financial support provided for my Masters.

I would like to recognize my parents, for inspiring me and yearning in me a love for science. Thank you for all that you did and have done to make me into the woman I am today. My only hope is to have made and continue to make you proud. Although afar, you both always knew how to make things better and care for me. To my grandparents, your determination, hard work, ability to get out of your comfort zone by migrating to a new continent, inspired me to learn the best of both worlds – who I am and where I came from – two different persons in one. To my younger sisters, thank you for letting me learn from you, being the good girls that you are, listening and being inspired by my love for science and engineering. Without you, I would not be me. To my sweetheart, Roberto, thank you for being by my side on this new experience, for challenging me, for your tenacity, unconditional love and encouragement. I could simply not have been able to do this without you. To baby Bruno, thanks for teaching me patience, keeping me sane and for showing me the meaning of love.

I would like to acknowledge my project leader, Dr. Bruce Brown, for his suggestions and help throughout my Master's research. I would also like to thank Dr. David Young for assisting me when I needed support and guidance.

I would like to express my most sincere gratitude to Alexis Barxias and Cody Shafer for being my helping hands in the laboratory. Your company in the lab has made

this experience all the better. Thank you both for your friendship and for welcoming Roberto and I into Athens.

I would like to acknowledge Prof. M. Toufiq Reza, Prof. Craig Grimes, and Prof. Srdjan Nesic for agreeing to be my committee members. Additionally, some of the surface analysis done would not have been possible without the help of the Center for Electrochemical Engineering Research (CEER) and Ali Raifei along with Prof. Hugh Richardson at the Department of Chemistry & Biochemistry. Last but not least, Ezechukwu Anyanwu is thanked for his support in running flow simulations.

Lastly, I would like to thank the sponsors of the Corrosion Center Joint Industry Project for their financial support and all students at the Institute for Corrosion and Multiphase Technology (ICMT) for their ongoing support and laughs during stressful times.

TABLE OF CONTENTS

	Page
Abstract.....	3
Dedication.....	5
Acknowledgments.....	6
List of Tables	11
List of Figures.....	12
Chapter 1: Introduction.....	21
Chapter 2: Literature Review.....	24
2.1 CO ₂ Corrosion.....	24
2.1.1 CO ₂ Corrosion Mechanism	24
2.2 Factors Affecting CO ₂ Corrosion.....	26
2.2.1 Temperature	26
2.2.2 CO ₂ Partial Pressure.....	26
2.2.3 pH.....	27
2.2.4 Turbulence	27
2.3 CO ₂ Corrosion Modeling.....	28
2.4 FeCO ₃ Layer Formation.....	29
2.4.1 Layer Formation Mechanism	29
2.5 Factors Affecting Formation of FeCO ₃	31
2.5.1 Temperature	32
2.5.2 CO ₂ Partial Pressure.....	32
2.5.3 pH.....	33
2.5.4 Turbulence	34
2.6 Summary of Effects	34
2.7 FeCO ₃ Layer Removal	35

2.7.1	Layer Removal Mechanism	35
2.8	Material Microstructure	40
Chapter 3: Motivation, Hypotheses and Research Objectives.....		44
3.1	Motivation.....	44
3.2	Objectives	46
3.3	Hypotheses.....	46
Chapter 4: Methodology, Results and Discussion		48
4.1	Task #1: Effect of Flow on the Formation of FeCO ₃ at High Initial S(FeCO ₃).....	48
4.1.1	Methodology	48
4.1.2	Results and Discussion	57
4.1.3	Summary	84
4.2	Task #2: Study of the Effect of Microstructure on FeCO ₃ Nucleation and Retention	88
4.2.1	Methodology	88
4.2.2	Results and Discussion	109
4.2.3	Summary	151
4.3	Task # 3: Removal of Fe ₃ C	152
4.3.1	Methodology	152
4.3.2	Results and Discussion	159
4.3.3	Summary	173
Chapter 5: Summary and Discussion.....		174
Chapter 6: Conclusions and Future Work.....		182
6.1	Conclusions.....	182
6.2	Future Work	183
References.....		185

Appendix 1: Preliminary Experimentation for FeCO ₃ Reproducibility	197
Appendix 2: High Initial S(FeCO ₃), Short-Term Experiments with API 5L X65.....	201
Appendix 3: Water Chemistry with No Ferrous Iron Control	204
Appendix 4: Flow Simulations of Impeller Setup	205

LIST OF TABLES

	Page
Table 1. Literature summary of environmental effects of non-layer forming conditions <i>versus</i> layer forming conditions.....	35
Table 2. Summary of results on FeCO ₃ removal	39
Table 3. Test matrix for task # 1: effect of flow on the formation of FeCO ₃ at high initial S(FeCO ₃).....	50
Table 4. Summary of RCE rotational speeds and corresponding pipe fluid velocities and wall shear stresses.....	56
Table 5. Test matrix for task # 2: study of the effect of microstructure on FeCO ₃ nucleation and retention.....	90
Table 6. Summary of impeller rotational speeds and corresponding pipe fluid velocities and wall shear stresses	99
Table 7. Chemical composition of API 5L X65 (wt.%).....	100
Table 8. Chemical composition of UNS G10180 steel (wt.%).....	100
Table 9. Test matrix for task # 3: removal of Fe ₃ C	153
Table 10. Summary of TCFC flow velocities, wall shear stresses and corresponding pipe fluid velocities.....	158
Table 11. Comparison of equivalent pipe velocities, wall shear stresses, final corrosion rates and surface morphologies showing no FeCO ₃ precipitation on pure Fe for RCE and impeller setups	176
Table 12. Comparison of equivalent pipe velocities, wall shear stresses, final corrosion rate and precipitation of FeCO ₃	178
Table 13. Comparison of equivalent pipe velocities, wall shear stresses, final corrosion rates and surface morphologies showing FeCO ₃ precipitation for impeller and TCFC setups under the conditions: T=80 ⁰ C, pCO ₂ = 0.53 bar, pH 6.6, SFeCO ₃ ≈ 10	179
Table 14. Test matrix for replicated work	198

LIST OF FIGURES

	Page
Figure 1. Typical steel microstructures (a) ferritic-pearlitic ⁷ (b) tempered martensite ⁴⁸ ..	41
Figure 2. Schematic showing source of ferrous ion (a) from metal (corrosion) (b) supersaturated electrolytes	45
Figure 3. Experimental setup of 2 L glass cell using rotating shaft (image courtesy of Cody Shafer, ICMT).....	49
Figure 4. Saturation value with respect to FeCO ₃ over the course of 48 hours in a 2 L glass cell under the conditions: T=80 ⁰ C, pCO ₂ = 0.53 bar, initial pH 6.6, initial SFeCO ₃ ≈ 150	59
Figure 5. Comparison of LPR corrosion rates, predicted initial FREECORP 2.0 and saturation of FeCO ₃ over time for stagnant experiment with pure Fe under the conditions: T=80 ⁰ C, pCO ₂ = 0.53 bar, initial pH 6.6, initial SFeCO ₃ ≈ 150.....	60
Figure 6. x800 and x1000 SEM images showing surface morphology for stagnant experiment with pure Fe under the conditions: T=80 ⁰ C, pCO ₂ = 0.53 bar, initial pH 6.6, initial SFeCO ₃ ≈ 150	61
Figure 7. x800 SEM image showing areas used for EDS analysis showing surface morphology for stagnant experiment with pure Fe surface under the conditions: T=80 ⁰ C, pCO ₂ = 0.53 bar, initial pH 6.6, initial SFeCO ₃ ≈ 150.....	62
Figure 8. EDS spectra taken on stagnant pure Fe surface (a) point 1 (b) area 2 shown in Figure 7	63
Figure 9. x800 SEM image showing EDS elemental mapping for stagnant experiment with pure Fe under the conditions: T=80 ⁰ C, pCO ₂ = 0.53 bar, initial pH 6.6, initial SFeCO ₃ ≈ 150	64
Figure 10. Raman spectra of stagnant pure Fe surface confirming presence of Fe ₂ (OH) ₂ CO ₃ and FeCO ₃ under the conditions: T=80 ⁰ C, pCO ₂ = 0.53 bar, initial pH 6.6, initial SFeCO ₃ ≈ 150	65
Figure 11. Comparison of LPR corrosion rates, predicted initial FREECORP 2.0 and saturation of FeCO ₃ over time for 500 rpm (<i>V</i> _{eq} = 0.6 m/s, 0.8 Pa) experiment with pure Fe under the conditions: T=80 ⁰ C, pCO ₂ = 0.53 bar, initial pH 6.6, initial SFeCO ₃ ≈ 150	66

Figure 12. x800 and x1000 SEM images showing surface morphology for 500 rpm ($V_{eq} = 0.6$ m/s, 0.8 Pa) experiment with pure Fe under the conditions: T=80 ⁰ C, pCO ₂ = 0.53 bar, initial pH 6.6, initial SFeCO ₃ ≈ 150	67
Figure 13. x800 SEM image showing areas used for EDS analysis showing surface morphology for 500 rpm ($V_{eq} = 0.6$ m/s, 0.8 Pa) experiment with pure Fe surface under the conditions: T=80 ⁰ C, pCO ₂ = 0.53 bar, initial pH 6.6, initial SFeCO ₃ ≈ 150	68
Figure 14. EDS spectra taken on 500 rpm ($V_{eq} = 0.6$ m/s, 0.8 Pa) pure Fe surface at (a) area 1 (b) area 2 shown in Figure 13.....	69
Figure 15. x800 SEM image showing EDS elemental mapping for 500 rpm ($V_{eq} = 0.6$ m/s, 0.8 Pa) experiment with pure Fe under the conditions: T=80 ⁰ C, pCO ₂ = 0.53 bar, initial pH 6.6, initial SFeCO ₃ ≈ 150	70
Figure 16. Raman spectra of 500 rpm ($V_{eq} = 0.6$ m/s, 0.8 Pa) pure Fe surface confirming presence of FeCO ₃ under the conditions: T=80 ⁰ C, pCO ₂ = 0.53 bar, initial pH 6.6, initial SFeCO ₃ ≈ 150	71
Figure 17. Comparison of LPR corrosion rates, predicted initial FREECORP 2.0 and saturation of FeCO ₃ over time for 1000 rpm ($V_{eq} = 1.2$ m/s, 2 Pa) experiment with pure Fe under the conditions: T=80 ⁰ C, pCO ₂ = 0.53 bar, initial pH 6.6, initial SFeCO ₃ ≈ 150	72
Figure 18. x800 and x1000 SEM images showing surface morphology for 1000 rpm ($V_{eq} = 1.2$ m/s, 2 Pa) experiment with pure Fe under the conditions: T=80 ⁰ C, pCO ₂ = 0.53 bar, initial pH 6.6, initial SFeCO ₃ ≈ 150	73
Figure 19. SEM showing areas used for EDS analysis showing surface morphology (a) x800 image of area 1 and point 2 (b) x3500 image of point 2 for 1000 rpm ($V_{eq} = 1.2$ m/s, 2 Pa) experiment with pure Fe surface under the conditions: T=80 ⁰ C, pCO ₂ = 0.53 bar, initial pH 6.6, initial SFeCO ₃ ≈ 150	75
Figure 20. EDS spectra taken on 1000 rpm ($V_{eq} = 1.2$ m/s, 2 Pa) pure Fe surface (a) area 1 (b) point 2 shown in Figure 19 (a) and Figure 19 (b), respectively	76
Figure 21. x3500 SEM image showing EDS elemental mapping for 1000 rpm ($V_{eq} = 1.2$ m/s, 2 Pa) experiment with pure Fe under the conditions: T=80 ⁰ C, pCO ₂ = 0.53 bar, initial pH 6.6, initial SFeCO ₃ ≈ 150	77
Figure 22. Raman spectra of 1000 rpm ($V_{eq} = 1.2$ m/s, 2 Pa) pure Fe surface confirming presence of FeCO ₃ under the conditions: T=80 ⁰ C, pCO ₂ = 0.53 bar, initial pH 6.6, initial SFeCO ₃ ≈ 150	78

Figure 23. Comparison of LPR corrosion rates, predicted initial FREECORP 2.0 and saturation of FeCO ₃ over time for 2000 rpm ($V_{eq} = 2.0$ m/s, 7 Pa) experiment with pure Fe under the conditions: T=80 ⁰ C, pCO ₂ = 0.53 bar, initial pH 6.6, initial SFeCO ₃ ≈ 150	79
Figure 24. x800 and x1000 SEM images showing surface morphology for 2000 rpm ($V_{eq} = 2.0$ m/s, 7 Pa) experiment with pure Fe under the conditions: T=80 ⁰ C, pCO ₂ = 0.53 bar, initial pH 6.6, initial SFeCO ₃ ≈ 150.....	80
Figure 25. x800 SEM image showing areas used for EDS analysis showing surface morphology for 2000 rpm ($V_{eq} = 2.0$ m/s, 7 Pa) experiment with pure Fe surface under the conditions: T=80 ⁰ C, pCO ₂ = 0.53 bar, initial pH 6.6, initial SFeCO ₃ ≈ 150	81
Figure 26. EDS spectrum taken on 2000 rpm ($V_{eq} = 2.0$ m/s, 0.8 Pa) pure Fe surface at area 1 shown in Figure 25	82
Figure 27. x800 SEM image showing EDS elemental mapping for 2000 rpm ($V_{eq} = 2.0$ m/s, 7 Pa) experiment with pure Fe under the conditions: T=80 ⁰ C, pCO ₂ = 0.53 bar, initial pH 6.6, initial SFeCO ₃ ≈ 150	83
Figure 28. Raman spectra of 2000 rpm ($V_{eq} = 2.0$ m/s, 7 Pa) pure Fe surface under the conditions: T=80 ⁰ C, pCO ₂ = 0.53 bar, initial pH 6.6, initial SFeCO ₃ ≈ 150	84
Figure 29. Comparison of LPR corrosion rates over time for stagnant, 500 rpm ($V_{eq} = 0.6$ m/s, 0.8 Pa), 1000 rpm ($V_{eq} = 1.2$ m/s, 2 Pa), and 2000 rpm ($V_{eq} = 2.0$ m/s, 7 Pa) experiments with pure Fe under the conditions: T=80 ⁰ C, pCO ₂ = 0.53 bar, initial pH 6.6, initial SFeCO ₃ ≈ 150	85
Figure 30. Comparison of average saturation of FeCO ₃ values over time for stagnant, 500 rpm ($V_{eq} = 0.6$ m/s, 0.8 Pa), 1000 rpm ($V_{eq} = 1.2$ m/s, 2 Pa), and 2000 rpm ($V_{eq} = 2.0$ m/s, 7 Pa) experiments with pure Fe under the conditions: T=80 ⁰ C, pCO ₂ = 0.53 bar, initial pH 6.6, initial SFeCO ₃ ≈ 150	86
Figure 31. Comparison of scaling tendency, final LPR corrosion rate, and FREECORP 2.0 after 8 hours for stagnant, 500 rpm ($V_{eq} = 0.6$ m/s, 0.8 Pa), 1000 rpm ($V_{eq} = 1.2$ m/s, 2 Pa), and 2000 rpm ($V_{eq} = 2.0$ m/s, 7 Pa) experiments with pure Fe under the conditions: T=80 ⁰ C, pCO ₂ = 0.53 bar, initial pH 6.6, initial SFeCO ₃ ≈ 150.....	87
Figure 32. Experimental setup of 2 L glass cell using impeller (image courtesy of Cody Shafer, ICMT).....	89
Figure 33. Experimental setup of 2 L glass cell with controlled mass-transfer system (a) side view and (b) top view (images courtesy of Cody Shafer, ICMT).....	92
Figure 34. Stable solution chemistry setup (image courtesy of Cody Shafer, ICMT).....	93

Figure 35. Specimen holders (a) electrochemical sample (b) removable weight loss sample (images courtesy of Cody Shafer, ICMT).....	95
Figure 36. Pitched blade turbine impeller geometry (image courtesy of Cody Shafer, ICMT)	97
Figure 37. Cathodic potentiodynamic sweeps showing limiting currents for various impeller rotational velocities ⁷⁴	98
Figure 38. Current density comparison between rotating cylinder shaft and impeller ⁷⁴ ..	99
Figure 39. Optical micrograph of as-received UNS G10180 with a ferritic-pearlitic microstructure	101
Figure 40. x2000 SEM image of as-received UNS G10180 with a ferritic-pearlitic microstructure	102
Figure 41. Optical micrograph showing tempered martensite microstructure of heat treated UNS G10180.....	103
Figure 42. x2000 SEM image of UNS G10180 with a tempered martensitic microstructure	104
Figure 43. Optical micrograph showing microstructure of heat treated API 5L X65	105
Figure 44. x2000 SEM image of heat treated API 5L X65 with a ferritic with Fe ₃ C precipitates microstructure.....	105
Figure 45. x8000 SEM image of heat treated API 5L X65 showing Fe ₃ C precipitate ...	106
Figure 46. EDS spectra taken on API 5L X65 sample on (a) point 1 and (b) point 2	107
Figure 47. Comparison of pH change over time for 150 rpm ($V_{eq} = 0.4$ m/s, 0.3 Pa) and 250 rpm ($V_{eq} = 0.6$ m/s, 0.5 Pa) experiments with pure Fe under the conditions: T=80 ⁰ C, pCO ₂ = 0.53 bar, pH 6.6, SFeCO ₃ ≈ 10	110
Figure 48. Comparison of [Fe ²⁺] change over time for 150 rpm ($V_{eq} = 0.4$ m/s, 0.3 Pa) and 250 rpm ($V_{eq} = 0.6$ m/s, 0.5 Pa) experiments with pure Fe under the conditions: T=80 ⁰ C, pCO ₂ = 0.53 bar, pH 6.6, SFeCO ₃ ≈ 10.....	111
Figure 49. Comparison of LPR corrosion rate over time for 150 rpm ($V_{eq} = 0.4$ m/s, 0.3 Pa) and 250 rpm ($V_{eq} = 0.6$ m/s, 0.5 Pa) experiments with pure Fe under the conditions: T=80 ⁰ C, pCO ₂ = 0.53 bar, pH 6.6, SFeCO ₃ ≈ 10.....	112

Figure 50. Comparison of OCP over time for 150 rpm ($V_{eq} = 0.4$ m/s, 0.3 Pa) and 250 rpm ($V_{eq} = 0.6$ m/s, 0.5 Pa) experiments with pure Fe under the conditions: T=80 ⁰ C, pCO ₂ = 0.53 bar, pH 6.6, SFeCO ₃ ≈ 10.....	113
Figure 51. x400 SEM images showing comparison of surface morphologies over time for 150 rpm ($V_{eq} = 0.4$ m/s, 0.3 Pa) and 250 rpm ($V_{eq} = 0.6$ m/s, 0.5 Pa) experiments with pure Fe under the conditions: T=80 ⁰ C, pCO ₂ = 0.53 bar, pH 6.6, SFeCO ₃ ≈ 10.....	115
Figure 52. x800 SEM image showing the surface morphology of pure Fe for 150 rpm ($V_{eq} = 0.4$ m/s, 0.3 Pa) experiment on day 5 showing FeCO ₃ crystals under the conditions: T=80 ⁰ C, pCO ₂ = 0.53 bar, pH 6.6, SFeCO ₃ ≈ 10.....	116
Figure 53. EDS spectrum of FeCO ₃ crystals shown in Figure 52	116
Figure 54. XRD analysis on pure Fe day 5 specimen for 250 rpm ($V_{eq} = 0.6$ m/s, 0.5 Pa) experiment under the conditions: T=80 ⁰ C, pCO ₂ = 0.53 bar, pH 6.6, SFeCO ₃ ≈ 10....	117
Figure 55. x500 SEM images showing cross-sectional morphologies over time for 150 rpm ($V_{eq} = 0.4$ m/s, 0.3 Pa) and 250 rpm ($V_{eq} = 0.6$ m/s, 0.5 Pa) experiments with pure Fe under the conditions: T=80 ⁰ C, pCO ₂ = 0.53 bar, pH 6.6, SFeCO ₃ ≈ 10	119
Figure 56. x500 SEM image showing cross-sectional elemental mapping of pure Fe on day 5 at 150 rpm ($V_{eq} = 0.4$ m/s, 0.3 Pa) confirming evidence of FeCO ₃ due to oxygen peak under the conditions: T=80 ⁰ C, pCO ₂ = 0.53 bar, pH 6.6, SFeCO ₃ ≈ 10	120
Figure 57. Comparison of pH change over time for 150 rpm ($V_{eq} = 0.4$ m/s, 0.3 Pa) and 250 rpm ($V_{eq} = 0.6$ m/s, 0.5 Pa) experiments with UNS G10180 ferritic-pearlitic under the conditions: T=80 ⁰ C, pCO ₂ = 0.53 bar, pH 6.6, SFeCO ₃ ≈ 10	121
Figure 58. Comparison of [Fe ²⁺] change over time for 150 rpm ($V_{eq} = 0.4$ m/s, 0.3 Pa) and 250 rpm ($V_{eq} = 0.6$ m/s, 0.5 Pa) experiments with UNS G10180 ferritic-pearlitic under the conditions: T=80 ⁰ C, pCO ₂ = 0.53 bar, pH 6.6, SFeCO ₃ ≈ 10	122
Figure 59. Comparison of LPR corrosion rate over time for 150 rpm ($V_{eq} = 0.4$ m/s, 0.3 Pa) and 250 rpm ($V_{eq} = 0.6$ m/s, 0.5 Pa) experiments with UNS G10180 ferritic-pearlitic under the conditions: T=80 ⁰ C, pCO ₂ = 0.53 bar, pH 6.6, SFeCO ₃ ≈ 10	124
Figure 60. Comparison of OCP over time for 150 rpm ($V_{eq} = 0.4$ m/s, 0.3 Pa) and 250 rpm ($V_{eq} = 0.6$ m/s, 0.5 Pa) experiments with UNS G10180 ferritic-pearlitic under the conditions: T=80 ⁰ C, pCO ₂ = 0.53 bar, pH 6.6, SFeCO ₃ ≈ 10	124
Figure 61. x400 SEM images showing comparison of surface morphologies over time for 150 rpm ($V_{eq} = 0.4$ m/s, 0.3 Pa) and 250 rpm ($V_{eq} = 0.6$ m/s, 0.5 Pa) experiments with UNS G10180 ferritic-pearlitic under the conditions: T=80 ⁰ C, pCO ₂ = 0.53 bar, pH 6.6, SFeCO ₃ ≈ 10	126

Figure 62. XRD analysis on UNS G10180 ferritic-pearlitic day 5 specimens for 150 rpm ($V_{eq} = 0.4$ m/s, 0.3 Pa) and 250 rpm ($V_{eq} = 0.6$ m/s, 0.5 Pa) experiments under the conditions: T=80 ⁰ C, pCO ₂ = 0.53 bar, pH 6.6, SFeCO ₃ ≈ 10	127
Figure 63. x500 SEM images showing cross-sectional morphologies over time for 150 rpm ($V_{eq} = 0.4$ m/s, 0.3 Pa) and 250 rpm ($V_{eq} = 0.6$ m/s, 0.5 Pa) experiments with UNS G10180 ferritic-pearlitic and metal loss from LPR corrosion rate under the conditions: T=80 ⁰ C, pCO ₂ = 0.53 bar, pH 6.6, SFeCO ₃ ≈ 10	130
Figure 64. x1000 SEM image showing cross-sectional elemental mapping of UNS G10180 ferritic-pearlitic on day 5 at 250 rpm ($V_{eq} = 0.6$ m/s, 0.5 Pa) confirming evidence of FeCO ₃ due to oxygen peak under the conditions: T=80 ⁰ C, pCO ₂ = 0.53 bar, pH 6.6, SFeCO ₃ ≈ 10	131
Figure 65. Comparison of pH change over time for 150 rpm ($V_{eq} = 0.4$ m/s, 0.3 Pa) and 250 rpm ($V_{eq} = 0.6$ m/s, 0.5 Pa) experiments with UNS G10180 tempered martensitic under the conditions: T=80 ⁰ C, pCO ₂ = 0.53 bar, pH 6.6, SFeCO ₃ ≈ 10	132
Figure 66. Comparison of [Fe ²⁺] change over time for 150 rpm ($V_{eq} = 0.4$ m/s, 0.3 Pa) and 250 rpm ($V_{eq} = 0.6$ m/s, 0.5 Pa) experiments with UNS G10180 tempered martensitic under the conditions: T=80 ⁰ C, pCO ₂ = 0.53 bar, pH 6.6, SFeCO ₃ ≈ 10	133
Figure 67. Comparison of LPR corrosion rate over time for 150 rpm ($V_{eq} = 0.4$ m/s, 0.3 Pa) and 250 rpm ($V_{eq} = 0.6$ m/s, 0.5 Pa) experiments with UNS G10180 tempered martensitic under the conditions: T=80 ⁰ C, pCO ₂ = 0.53 bar, pH 6.6, SFeCO ₃ ≈ 10	134
Figure 68. Comparison of OCP corrosion rate over time for 150 rpm ($V_{eq} = 0.4$ m/s, 0.3 Pa) and 250 rpm ($V_{eq} = 0.6$ m/s, 0.5 Pa) experiments with UNS G10180 tempered martensitic under the conditions: T=80 ⁰ C, pCO ₂ = 0.53 bar, pH 6.6, SFeCO ₃ ≈ 10	135
Figure 69. x400 SEM images showing comparison of surface morphologies over time for 150 rpm ($V_{eq} = 0.4$ m/s, 0.3 Pa) and 250 rpm ($V_{eq} = 0.6$ m/s, 0.5 Pa) experiments with UNS G10180 tempered martensitic under the conditions: T=80 ⁰ C, pCO ₂ = 0.53 bar, pH 6.6, SFeCO ₃ ≈ 10	137
Figure 70. XRD analysis on UNS G10180 tempered martensitic day 5 specimens for 150 rpm ($V_{eq} = 0.4$ m/s, 0.3 Pa) and 250 rpm ($V_{eq} = 0.6$ m/s, 0.5 Pa) experiments under the conditions: T=80 ⁰ C, pCO ₂ = 0.53 bar, pH 6.6, SFeCO ₃ ≈ 10	138
Figure 71. x500 SEM images showing cross-sectional morphologies over time for 150 rpm ($V_{eq} = 0.4$ m/s, 0.3 Pa) and 250 rpm ($V_{eq} = 0.6$ m/s, 0.5 Pa) experiments with UNS G10180 tempered martensitic and metal loss from LPR corrosion rate under the conditions: T=80 ⁰ C, pCO ₂ = 0.53 bar, pH 6.6, SFeCO ₃ ≈ 10	140

Figure 72. x1000 SEM image showing cross-sectional elemental mapping of UNS G10180 tempered martensitic on day 5 at 150 rpm ($V_{eq} = 0.4$ m/s, 0.3 Pa) under the conditions: T=80 ⁰ C, pCO ₂ = 0.53 bar, pH 6.6, SFeCO ₃ ≈ 10.....	141
Figure 73. Comparison of pH change over time for 150 rpm ($V_{eq} = 0.4$ m/s, 0.3 Pa) and 250 rpm ($V_{eq} = 0.6$ m/s, 0.5 Pa) experiments with API 5L X65 under the conditions: T=80 ⁰ C, pCO ₂ = 0.53 bar, pH 6.6, SFeCO ₃ ≈ 10.....	142
Figure 74. Comparison of [Fe ²⁺] change over time for 150 rpm ($V_{eq} = 0.4$ m/s, 0.3 Pa) and 250 rpm ($V_{eq} = 0.6$ m/s, 0.5 Pa) experiments with API 5L X65 under the conditions: T=80 ⁰ C, pCO ₂ = 0.53 bar, pH 6.6, SFeCO ₃ ≈ 10.....	143
Figure 75. Comparison of LPR corrosion rate over time for 150 rpm ($V_{eq} = 0.4$ m/s, 0.3 Pa) and 250 rpm ($V_{eq} = 0.6$ m/s, 0.5 Pa) experiments with API 5L X65 under the conditions: T=80 ⁰ C, pCO ₂ = 0.53 bar, pH 6.6, SFeCO ₃ ≈ 10.....	144
Figure 76. Comparison of OCP over time for 150 rpm ($V_{eq} = 0.4$ m/s, 0.3 Pa) and 250 rpm ($V_{eq} = 0.6$ m/s, 0.5 Pa) with API 5L X65 under conditions: T=80 ⁰ C, pCO ₂ = 0.53 bar, pH 6.6, SFeCO ₃ ≈ 10 ..	145
Figure 77. x400 SEM images showing comparison of surface morphologies over time for 150 rpm ($V_{eq} = 0.4$ m/s, 0.3 Pa) and 250 rpm ($V_{eq} = 0.6$ m/s, 0.5 Pa) experiments with API 5L X65 under the conditions: T=80 ⁰ C, pCO ₂ = 0.53 bar, pH 6.6, SFeCO ₃ ≈ 10 ..	147
Figure 78. XRD analysis on API 5L X65 day 5 surface specimens for 150 rpm ($V_{eq} = 0.4$ m/s, 0.3 Pa) and 250 rpm ($V_{eq} = 0.6$ m/s, 0.5 Pa) experiments under the conditions: T=80 ⁰ C, pCO ₂ = 0.53 bar, pH 6.6, SFeCO ₃ ≈ 10.....	148
Figure 79. x500 SEM images showing cross-sectional morphologies over time for 150 rpm ($V_{eq} = 0.4$ m/s, 0.3 Pa) and 250 rpm ($V_{eq} = 0.6$ m/s, 0.5 Pa) experiments with API 5L X65 and metal loss from LPR corrosion rate under the conditions: T=80 ⁰ C, pCO ₂ = 0.53 bar, pH 6.6, SFeCO ₃ ≈ 10 ..	150
Figure 80. x1000 SEM image showing cross-sectional elemental mapping of API 5L X65 on day 5 at 150 rpm ($V_{eq} = 0.4$ m/s, 0.3 Pa) under the conditions: T=80 ⁰ C, pCO ₂ = 0.53 bar, pH 6.6, SFeCO ₃ ≈ 10 ..	151
Figure 81. Thin channel flow cell (TCFC) (image courtesy of Cody Shafer, ICMT)....	152
Figure 82. Piping & instrumentation diagram of the TCFC ⁸⁶⁻⁸⁸	155
Figure 83. Specimen mount and flow test section of TCFC ⁸⁷	155
Figure 84. Specimens used for TCFC experiments (a) electrochemical specimen (b) characterization specimens ⁷	156

Figure 85. Comparison of Patel's correlations ⁸⁹ with Li's experimental results using a floating element sensor ⁸⁶⁻⁸⁸	157
Figure 86. Comparison of pH change over time for 0.4 m/s ($V_{eq} = 0.75$ m/s, 0.8 Pa), 2 m/s ($V_{eq} = 4.7$ m/s, 20 Pa) and 6 m/s ($V_{eq} = 12$ m/s, 100 Pa) experiments with UNS G10180 ferritic-pearlitic under the conditions: T=80 ⁰ C, pCO ₂ = 0.53 bar, initial pH 6.6, initial SFeCO ₃ ≈ 10	160
Figure 87. Comparison of [Fe ²⁺] change over time for 0.4 m/s ($V_{eq} = 0.75$ m/s, 0.8 Pa), 2 m/s ($V_{eq} = 4.7$ m/s, 20 Pa) and 6 m/s ($V_{eq} = 12$ m/s, 100 Pa) experiments with UNS G10180 ferritic-pearlitic under the conditions: T=80 ⁰ C, pCO ₂ = 0.53 bar, initial pH 6.6, initial SFeCO ₃ ≈ 10	161
Figure 88. Comparison of LPR corrosion rate over time for 0.4 m/s ($V_{eq} = 0.75$ m/s, 0.8 Pa), 2 m/s ($V_{eq} = 4.7$ m/s, 20 Pa) and 6 m/s ($V_{eq} = 12$ m/s, 100 Pa) experiments with UNS G10180 ferritic-pearlitic under the conditions: T=80 ⁰ C, pCO ₂ = 0.53 bar, initial pH 6.6, initial SFeCO ₃ ≈ 10	162
Figure 89. x800 SEM images showing comparison of surface morphologies over time for 0.4 m/s ($V_{eq} = 0.75$ m/s, 0.8 Pa), 2 m/s ($V_{eq} = 4.7$ m/s, 20 Pa) and 6 m/s ($V_{eq} = 12$ m/s, 100 Pa) experiments with UNS G10180 ferritic-pearlitic under the conditions: T=80 ⁰ C, pCO ₂ = 0.53 bar, initial pH 6.6, initial SFeCO ₃ ≈ 10	165
Figure 90. Raman spectra of surface confirming FeCO ₃ as a corrosion product for 0.4 m/s ($V_{eq} = 0.75$ m/s, 0.8 Pa) experiment with UNS G10180 ferritic-pearlitic under the conditions: T=80 ⁰ C, pCO ₂ = 0.53 bar, initial pH 6.6, initial SFeCO ₃ ≈ 10	166
Figure 91. Raman spectra of surface confirming FeCO ₃ as a corrosion product for 2 m/s ($V_{eq} = 4.7$ m/s, 20 Pa) experiment with UNS G10180 ferritic-pearlitic under the conditions: T=80 ⁰ C, pCO ₂ = 0.53 bar, initial pH 6.6, initial SFeCO ₃ ≈ 10	166
Figure 92. x5000 SEM image used for EDS analysis showing surface morphology after day 5 for 6 m/s ($V_{eq} = 12$ m/s, 100 Pa) experiment with UNS G10180 ferritic-pearlitic under the conditions: T=80 ⁰ C, pCO ₂ = 0.53 bar, initial pH 6.6, initial SFeCO ₃ ≈ 10 ..	168
Figure 93. EDS spectrum taken at point labelled 1 shown in Figure 92 confirming presence of alloying elements	168
Figure 94. EDS spectrum taken at point labelled 2 shown in Figure 92	169
Figure 95. Raman spectra of surface for 6 m/s ($V_{eq} = 12$ m/s, 100 Pa) experiment with UNS G10180 ferritic-pearlitic under the conditions: T=80 ⁰ C, pCO ₂ = 0.53 bar, initial pH 6.6, initial SFeCO ₃ ≈ 10	170

Figure 96. x500 SEM images showing cross-sectional morphologies over time for 0.4 m/s ($V_{eq} = 0.75$ m/s, 0.8 Pa), 2 m/s ($V_{eq} = 4.7$ m/s, 20 Pa) and 6 m/s ($V_{eq} = 12$ m/s, 100 Pa) experiments with UNS G10180 ferritic-pearlitic under the conditions: T=80°C, pCO ₂ = 0.53 bar, initial pH 6.6, initial SFeCO ₃ ≈ 10	172
Figure 97. x500 SEM images showing pattern of FeCO ₃ formation and Fe ₃ C exposure for 0.4 m/s ($V_{eq} = 0.75$ m/s, 0.8 Pa), 2 m/s ($V_{eq} = 4.7$ m/s, 20 Pa) and 6 m/s ($V_{eq} = 12$ m/s, 100 Pa) experiments with UNS G10180 ferritic-pearlitic under the conditions: day 5, T=80°C, pCO ₂ = 0.53 bar, initial pH 6.6, initial SFeCO ₃ ≈ 10	181
Figure 98. Comparison of LPR corrosion rates and saturation of FeCO ₃ over time from Yang's study ⁶ for stagnant experiment with API 5L X65 (0.14 wt.% C) under the conditions: T=80°C, pCO ₂ = 0.53 bar, initial pH 6.6, initial SFeCO ₃ ≈ 300	198
Figure 99. Comparison of LPR corrosion rates and saturation of FeCO ₃ over time for stagnant experiment with API 5L X65 (0.14 wt.% C) under the conditions: T=80°C, pCO ₂ = 0.53 bar, initial pH 6.6, initial SFeCO ₃ ≈ 300	199
Figure 100. x800 SEM images showing comparison of surface morphologies for stagnant experiment with API 5L X65 (0.14 wt.% C) under the conditions: T=80°C, pCO ₂ = 0.53 bar, initial pH 6.6, initial SFeCO ₃ ≈ 300	199
Figure 101. Comparison of LPR corrosion rates over time for stagnant, 0.6 m/s (0.8 Pa), 1.2 m/s (2 Pa), and 2.0 m/s (7 Pa) experiments with API 5L X65 under the conditions: T=80°C, pCO ₂ = 0.53 bar, initial pH 6.6, initial SFeCO ₃ ≈ 150	201
Figure 102. x400 and x800 SEM images showing comparison of surface morphologies after 8 hours for stagnant, 0.6 m/s (0.8 Pa), 1.2 m/s (2 Pa), and 2.0 m/s (7 Pa) experiments with API 5L X65 under the conditions: T=80°C, pCO ₂ = 0.53 bar, initial pH 6.6, initial SFeCO ₃ ≈ 150	203
Figure 103. [Fe ²⁺] change over time with no [Fe ²⁺] control for 150 rpm experiment with API 5L X65 under the conditions: T=80°C, pCO ₂ = 0.53 bar, initial pH 6.6, initial SFeCO ₃ ≈ 10	204
Figure 104. Glass cell geometry and domains setup	205
Figure 105. Velocity contour for 150 rpm and 250 rpm impeller rotational speeds in stationary frame for pitched blade impeller in 2 L glass cell in water at 80°C	206
Figure 106. Wall shear contour profile in stationary frame for pitched blade impeller in 2 L glass cell in water at 80°C	207

CHAPTER 1: INTRODUCTION

According to a two-year study published in 2002 conducted by NACE International and backed by the U.S. Federal Highway Administration, the total annual estimated cost of corrosion in the U.S. is approximately \$276 billion; equivalent to 3.1% of the nation's Gross Domestic Product (GDP)¹. This study is frequently cited and serves as means of precaution, as well as to stimulate interest in corrosion research. A key outcome of this research is the study of corrosion mechanisms in order to arrive at accurate predictions of the rate of corrosion – a tool that is particularly useful in the oil and gas industries when designing and operating steel pipelines exposed to CO₂/H₂S containing environments. If an appropriate corrosion rate prediction tool is unavailable or an inappropriate tool is used, inadequacies relating to material selection, costly equipment failures, and even fatalities can result. Thus, it is of uttermost necessity to formulate and validate models that can accurately, easily, and efficiently predict corrosion rates based on specific conditions.

Concurrent with CO₂ corrosion, at certain conditions, a protective iron carbonate (FeCO₃) layer forms on the surface of the steel as a by-product. This layer acts as a diffusion barrier for corrosive species, thus slowing down and even ultimately prohibiting further corrosion. However, previous studies have shown that removal of FeCO₃ is possible under high velocity conditions and can lead to increase in metal loss and pitting – a very aggressive type of corrosion better known as localized corrosion². Thus, it is imperative to understand how this layer behaves and forms under a variety of environmental conditions which can allow appropriate prediction of not only the corrosion rate, but also FeCO₃ formation.

Ruzic, *et al.*³⁻⁵, have studied the mechanical removal, chemical dissolution, and simultaneous chemo-mechanical removal of the FeCO₃ layer on steel. Their results confirmed that purely mechanical removal in single-phase flow occurs. Velocity was said to have a significant impact as the specimens exposed to high velocity flow showed more damage to the FeCO₃ layer than the specimens exposed to low velocity flow. Yang⁶ studied the synergistic effect of chemo-mechanical removal of the FeCO₃ layer, and her conclusions differed from those of Ruzic, *et al.* Yang's experimental results showed that the hydrodynamic forces typically encountered in oil and gas systems cannot solely remove the FeCO₃ layer from a mild steel surface. Farelas⁷ took these studies a step further and investigated the influence of iron carbide (Fe₃C) on the formation of FeCO₃. Farelas found that, with time, the presence of a residual Fe₃C layer, derived from the steel microstructure, acted as a diffusion barrier for generated ferrous (Fe²⁺) and carbonate (CO₃²⁻) ions; this promoted a higher saturation level with respect to FeCO₃ adjacent to the actively corroding steel surface. Consequently, FeCO₃ could form within the exposed porous layer of Fe₃C, without having to achieve optimal conditions for layer formation relating to bulk water chemistry.

Although Yang and Ruzic made somewhat contradictory conclusions, they share a similar gap in their experimental procedures – they both formed FeCO₃ layers in stagnant to “mild” hydrodynamic conditions before exposing them to higher fluid velocity. This does not reflect field conditions where high shear stresses can be encountered, and how this can affect the initial nucleation step for FeCO₃ formation. Farelas also did not consider

the effect of flow, which can have an impact on his findings since residual Fe₃C is reported to be fragile⁸.

Within this context, a key objective of the proposed research is to determine the effect of flow on formation of FeCO₃ on steel over time. The focus is on constant velocity experiments from approximately 0.1 m/s to 2 m/s in electrochemical setups and up to 6 m/s in a flow loop to investigate the characteristics of FeCO₃ formation, and the effect of environmental conditions, and material selection. Additionally, various techniques such as scanning electron microscopy (SEM), energy dispersive X-ray spectroscopy (EDS), Raman spectroscopy, X-ray diffraction (XRD), and cross-sections are implemented to complement electrochemical measurements over time including open circuit potential (OCP) and linear polarization techniques (LPR). The influence of the exposed Fe₃C is examined by comparison of two steels with different carbon contents and microstructures.

CHAPTER 2: LITERATURE REVIEW

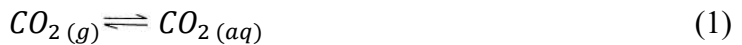
Corrosion is a major problem that impacts various industries and society as a whole.

In addition to economic losses, environmental damage and loss of life can result. A direct corrosion cost of \$1.4 billion per year, according to a NACE International Study¹, has been attributed to the oil and gas industry. Although it is widely known how vast corrosion costs are, many aspects of the corrosion mechanisms remain elusive. As a background to the proposed research, this section discusses pertinent literature relating to CO₂ corrosion mechanisms of mild steel, FeCO₃ formation and removal, and the role of Fe₃C pertaining to each.

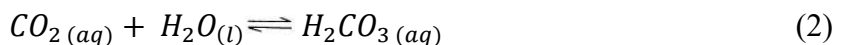
2.1 CO₂ Corrosion

2.1.1 CO₂ Corrosion Mechanism

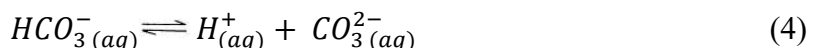
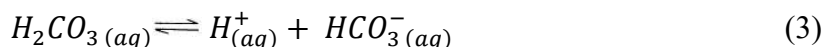
Many electrochemical, chemical and transport processes occur simultaneously in CO₂ corrosion⁹. When CO₂ is dissolved in water, as shown by reaction (1):



A hydration process occurs that generates carbonic acid:



The carbonic acid then partially dissociates as described by the following steps:



Thus, it can be seen that carbonic acid provides an extra source of hydrogen ions in the electrolyte that can favor further corrosion by simple dissociation as a weak acid. These

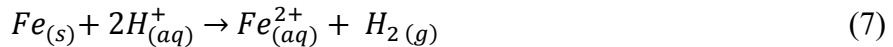
hydrogen ions will travel by diffusion and convection to the surface of the substrate material and be reduced to hydrogen gas:



In tandem, iron atoms from the steel lose electrons (oxidation) which are consumed by reaction (5) (reduction) as shown in the following chemical reaction (6):



The net process is metal corrosion (7), which is a combination of equations (5) and (6):

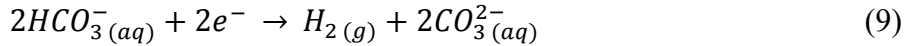


Additionally, the direct reduction of H_2CO_3 on the surface of the metal has been reported to occur, in an effort to explain the higher corrosion rate of steel in the presence of CO_2 when compared to a strong acid at the same conditions; which was proposed by De Waard in an earlier model¹⁰:



This reaction adds an additional cathodic reaction. The overall cathodic reactions, equations (5) and (8), are said to be independent of each other and the net cathodic current is the sum of the currents for the two reactions¹¹. However, recent research alludes to the fact that the direct reduction of H_2CO_3 does not occur as the charge transfer line may not be affected as shown on an Evans Diagram¹². H_2CO_3 does contribute, nonetheless, by being an extra source of H^+ ions in the electrolyte through its dissociation, as shown in equation (3). This is more popularly known as the buffering effect¹².

Gray, *et al.*, reported that the direct reduction of bicarbonate ion becomes significant at a higher pH since there are higher concentrations of bicarbonate¹³:



However, it is difficult to distinguish through experiments from the two main cathodic reactions discussed, equations (5) and (8)¹¹. Whether or not the direct reduction of H₂CO₃ or HCO₃⁻ actually occurs, it is of prime for the understanding of corrosion mechanisms but has no practical effect on the scope of the present study.

2.2 Factors Affecting CO₂ Corrosion

2.2.1 Temperature

Higher temperatures exacerbate all electrochemical processes which cause metal corrosion¹¹. It is often expected that there is a direct relationship with temperature and corrosion rate, but this is only true at electrolytes with low pH (pH < 5)¹¹. At higher pH, precipitation of FeCO₃ is expected since FeCO₃ precipitation is favorable. Thus, this changes the effect of temperature^{11,14,15}. In conditions favoring corrosion product layer formation, an increase in temperature will decrease corrosion rate. This will be discussed in more detail in the next section, section 22.5, which discusses factors affecting FeCO₃ formation.

2.2.2 CO₂ Partial Pressure

The effect of CO₂ partial pressure is very similar to the effect of temperature, as it presents a strong and direct relationship with corrosion rate. When there is no possible precipitation of FeCO₃, an increase in CO₂ partial pressure accelerates the cathodic reaction, equation (5). The presence of carbonic acid in solution leads to an extra source of H⁺ ions, as described in equations (3) and (4), which accelerates the net corrosion reaction, equation (7), and in turn increases the corrosion rate^{11,16,17}. However, when formation of

FeCO_3 is possible, the effect of CO_2 partial pressure differs from what is described here (this will be discussed in more details in a later section, section 22.5, which will describe conditions that favor FeCO_3 formation).

2.2.3 *pH*

The reduction of H^+ ions, as described in reaction (5), is relevant when discussing pH effects. As more H^+ ions are readily available, the net corrosion process described in equation (7) favors the dissolution of iron since the H^+ reduction is the limiting step. The availability of H^+ ions in solution presents a strong relationship with corrosion rate^{11,18,19} – as the pH decreases, the corrosion rate increases. There may be a different effect, however, when both pH and temperature increase in situations where precipitation of FeCO_3 is favorable. This will be discussed in more detail in a below section discussing factors affecting precipitation of FeCO_3 .

2.2.4 *Turbulence*

Turbulence is of extreme importance when considering flow effects in CO_2 corrosion. Flow effects aid the transport of species towards and away from the surface, which often increases the corrosion rate^{11,18}. High flow rates can induce severe corrosion attack by different modes, such as by erosion-corrosion, cavitation and flow-induced corrosion¹⁷. However, low flow rates or low turbulence are also detrimental, as solids can deposit (A phenomenon known as underdeposit attack) due to the tendency to create galvanic cells or even create a friendly site for bacteria accumulation¹⁸.

2.3 CO₂ Corrosion Modeling

De Waard²⁰⁻²² was the first to publish a paper on corrosion prediction in environments containing CO₂. De Waard's findings constituted a major development since an electrochemical approach was introduced in order to explain the higher corrosion rate found with carbonic acid than with completely dissociated acids for the same temperature and pH ranges. After a thorough analysis of his findings, he constructed an easy to use monogram which related the corrosion rate with CO₂ partial pressure. This monogram gained much popularity throughout the oil and gas industry. De Waard's model predicts corrosion rate based on the partial pressure of CO₂ and temperature as shown in formula²¹ popularly denoted as the De Waard-Milliams Equation:

$$\log(V_{cor}) = 5.8 - \frac{1710}{273+t} + 0.67 \log(pCO_2) \quad (10)$$

Where V_{cor} is the corrosion rate in mm/yr, t is temperature in °C and pCO_2 is the partial pressure of CO₂ in bar. Additionally, the effect of corrosion product layer formation effect is incorporated by adding a scaling factor, which also depends on the partial pressure of CO₂ and temperature²¹. This scaling factor ranges from 0.1 to 1. The effect of flow is taken into account by adding mass transfer contributions into the corrosion rate formula, which depend on fluid properties as well as flow geometry²². Lastly, the effect of material/microstructure is acknowledged by adding correction factors which are calculated based on the material carbon content, and chromium content, where applicable²². The correction factors differ on whether it is a normalized or quenched and tempered carbon steel. Although this model accounts for many influential factors in the calculation of corrosion rate in CO₂ environments, it lacked key components on the prediction of

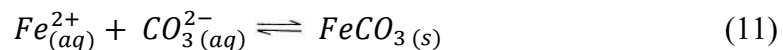
corrosion since it is a semi-empirical model and does not allow for simple extrapolation²⁰⁻²².

Currently, a model exists at the Institute for Corrosion and Multiphase Technology (ICMT)²³ that improves upon De Waard's. This model, called FREECOPR⁽³⁾, is underpinned by a theoretical approach that includes modelling individual electrochemical reactions in a water-CO₂ system. Different from De Waard's model, the effect of FeCO₃ in corrosion rate calculations is acknowledged by an empirical formula derived from the FeCO₃ saturation value, as will be discussed in the section on FeCO₃ layer formation mechanism, equation (15). Similar to De-Waard's model, FREECOPR uses mass transfer coefficients to account for the effect of flow. However, FREECOPR is still missing key information that can ultimately lead to more accurate prediction of corrosion rates in relation to the influence of FeCO₃ precipitation, such as the effect of microstructure.

2.4 FeCO₃ Layer Formation

2.4.1 Layer Formation Mechanism

As equation (4) states, the bicarbonate ion can further dissociate into a hydrogen ion and carbonate ion in the electrolyte. When there is an increase in the concentration of ferrous ions in the solution as the steel corrodes, as described in equation (6), the ferrous ions and carbonate ions combine to form FeCO₃ as follows:



⁽³⁾ FREECOPR is a product of the Institute for Corrosion and Multiphase Technology, Ohio University

This precipitation process occurs when the solubility limit with respect to both ions is exceeded, termed saturation, and is scientifically defined as follows in terms of the solubility product constant (K_{sp}):

$$K_{sp} = [Fe^{2+}]_{eq}[CO_3^{2-}]_{eq} \quad (12)$$

Essentially, when the product of the concentrations of ferrous and carbonate ions in the electrolyte (mol/L) exceeds K_{sp} , precipitation can occur. Both temperature and ionic strength affect K_{sp} , and in turn corrosion, as reported by Sun, *et al.*²⁴. In their study, a FeCO_3 solubility equation was written as follows:

$$\log(K_{sp}) = -59.3498 - 0.041377T_k - \frac{2.1963}{T_k} + 24.5724 \log(T_k) + 2.518I^{0.5} - 0.675I \quad (13)$$

Where T_k is the temperature in Kelvin and I is the ionic strength defined as:

$$I = \frac{1}{2} \sum_i c_i z_i^2 = \frac{1}{2}(c_1 z_1^2 + c_2 z_2^2 + \dots) \quad (14)$$

Where c_i (mol/L) are the concentrations of the various species in the electrolyte, and z_i are the species charges.

Additionally, a parameter often used to determine whether FeCO_3 precipitation is likely is the saturation value, which is defined as:

$$S_{\text{FeCO}_3} = \frac{[Fe^{2+}][CO_3^{2-}]}{K_{sp}} \quad (15)$$

When $S > 1$, precipitation of FeCO_3 is likely to occur. However, when $S < 1$ dissolution of the FeCO_3 layer or no formation at all are possible^{4,5,11}.

Sun and Nesic also developed an equation which describes the kinetics of FeCO_3 formation²⁵. The experimental procedure required that the specimen weight be measured before the experiment, and after the experiment twice - once with corrosion product and once again after corrosion product was removed; they thereby developed a precipitation

rate equation based on the corrosion layer accumulation rate²⁶. Previous precipitation rate equations used the concentration of ferrous ions in the bulk to determine an equation and assumed that all of the iron carbonate precipitated on the steel surface. However, bulk conditions may not accurately represent steel surface conditions. The equation (16) developed by Sun and Nesic for corrosion layer accumulation rate (CLAR) is²⁵:

$$CLAR \left(\frac{mol}{m^3 s} \right) = k_r e^{-\frac{\Delta G}{RT}} K_{sp} \frac{S}{V} (S_{FeCO_3} - 1) \quad (16)$$

Where k_r is a kinetics constant ($1.8 \times 10^{-6} \text{ m}^4/(\text{mol} \cdot \text{s})$), ΔG is the activation energy of $FeCO_3$ precipitation (64,851.4 J/mol) and $\frac{S}{V}$ is the ratio of the surface area of the specimen to the volume of the solution.

Furthermore, a popular expression frequently used to predict the likelihood to form a protective $FeCO_3$ layer in a specific environmental condition is referred to as the scaling tendency (ST)²⁶, as determined by the following equation:

$$ST = \frac{R_{FeCO_3}}{CR} \quad (17)$$

where R_{FeCO_3} the precipitation rate of $FeCO_3$ and CR is the corrosion rate. Both of these parameters are expressed in the same units ($\text{kmol}/(\text{m}^2 \cdot \text{s})$). Typically, a ST value greater than or equal to one indicates formation of a protective and dense layer; whereas, a ST value less than one is indicative of a porous, non-protective, and undermined layer.

2.5 Factors Affecting Formation of $FeCO_3$

Many factors can impact, in different ways, the formation and characteristics of $FeCO_3$ corrosion product layers, these are discussed individually below.

2.5.1 Temperature

As reported in the literature, peaks in corrosion rate occur between 60°C and 80°C^{11,14,15}. However, at temperatures higher than 80°C, formation of FeCO₃ is very likely^{11,14,15}, typically at pH > five¹⁸ and when saturation, as described in equation (15), is above 1. Temperature can undoubtedly affect the morphology and formation kinetics of FeCO₃²⁷⁻²⁹. Between 60°C and 130°C²⁹ the corrosion product mostly consists of FeCO₃, typically forming as a dense and protective layer above 60°C²⁷⁻²⁹. Tanupabrungsun, however, found that the corrosion product consisted of a mixture of plate-like crystals and prismatic-shaped crystals, referred to as prisms, between the temperatures of 80°C and 120°C²⁹. Specimen characterization by X-ray diffraction revealed that the plate-like crystals were Fe₂(OH)₂CO₃ (chukanovite) and, in a time study, were shown to act as a metastable precursor for FeCO₃^{29,30,31}. A temperature of 80°C was chosen as an optimum condition for corrosion product layer formation.

2.5.2 CO₂ Partial Pressure

At very high partial pressures of CO₂, a higher concentration of carbonate ions is expected in solution. This tends to favor FeCO₃ precipitation^{11,16,17} as a saturation higher than 1 is likely achieved, even with low Fe²⁺ concentration, as shown in equation (15). Formation of FeCO₃ is then facilitated when the partial pressure of CO₂ is relatively high. This relationship can be seen in the section on CO₂ corrosion mechanism, where all the reactions in a saturated CO₂ system are explained, equations (1) to (9), and (11). Furthermore, a recent study showed that as the partial pressure of CO₂ increased, the corrosion product layer appeared thicker and denser³². However, it was found that the

interfacial (between substrate and corrosion product layer) fracture toughness values obtained by tensile tests decreased and higher corrosion rates were observed (both uniform and localized) as the partial pressure of CO₂ increased. These findings showed that although a higher concentration of carbonate ions is available at higher partial pressures of CO₂, the protectiveness of the layer can be compromised.

2.5.3 pH

For FeCO₃, higher pH values lead to decreased solubility¹¹. This decrease in solubility (typically at pH >6), results in faster precipitation of FeCO₃; this in turn, is associated with a steady decrease of corrosion rate throughout the course of the experiments^{11,19}. Additionally, higher level of compactness of the FeCO₃ is favored with an increase in pH²⁷. In a study conducted by Nazari, Allahkaram & Kermani, it was found that anchoring of the FeCO₃ layer to the substrate material surface, in this case a carbon steel containing 0.17 wt.% C, was poor at pH below 6 since the layer was characterized as being very porous and did not yield a lower corrosion rate over time²⁷. Additionally, Ieamsupapong conducted experiments in a pH range of 5.4 – 6.0 and found that a higher pH showed a more protective FeCO₃ corrosion product layer based on the final corrosion rate³². Pessu, Barker & Neville found similar results since the morphology of FeCO₃ crystals differed at pH 6.6 and pH 7.5, as the crystals precipitated in pH 7.5 experiments were sharper prisms in nature (more crystalline). Also, due to the higher pH (lower solubility of FeCO₃) FeCO₃ precipitated on the steel surface faster in the pH 7.5 experiment than at the pH 6.6 experiment³⁴.

2.5.4 *Turbulence*

The main role of turbulence is postulated to interfere with the nucleation and growth of the FeCO₃ layer or/and to shear it away from the surface in saturated solutions, which consequently increases the corrosion rate^{2,11,14,15}. Turbulence usually plays a role in two different ways *via* a mass transfer effect or mechanical effect. For the mass transfer effect, flow typically aids in supplying ionic species to the steel surface, or by moving them away from the surface. This effect typically promotes corrosion¹¹. For the mechanical effect, high turbulence can permanently damage an already-precipitated FeCO₃ and lead to severe localized corrosion¹⁸. The effect of flow on FeCO₃ formation and protectiveness was also tested by Gao, *et al.*, and it was found that although higher flow rates formed thicker and denser layers, they were in fact less protective at higher velocities due to corrosion rate values and interfacial fracture toughness³²

2.6 Summary of Effects

As discussed above, the environmental effects on corrosion rate can vary whether the solution favors precipitation of FeCO₃ or not. **Table 1** summarizes effects for CO₂ corrosion in non-layer forming conditions, and conditions favoring FeCO₃ precipitation.

Table 1. Literature summary of environmental effects of non-layer forming conditions *versus* layer forming conditions

Effects	Non-Layer Forming Conditions	Conditions Favoring FeCO ₃ Precipitation
Temperature	Higher temperature leads to higher corrosion rate	Higher temperature favors FeCO ₃ precipitation which leads to lower corrosion rate
CO ₂ Partial Pressure	Higher CO ₂ partial pressure leads to higher corrosion rates	Higher CO ₂ partial pressure favors FeCO ₃ precipitation which leads to lower corrosion rates
pH	Higher pH leads to lower corrosion rates	Higher pH leads to lower corrosion rates
Turbulence	More turbulence leads to higher corrosion rates by increasing mass transfer	More turbulence leads to higher corrosion rates by damaging an already formed layer or by preventing effective nucleation

2.7 FeCO₃ Layer Removal

Previous studies have shown that removal of FeCO₃ is possible under certain conditions and can lead to increase in metal loss rate and pitting². Studies for the removal of FeCO₃ fall have been performed in many apparatus with a wide range of shear stresses and mass transfer coefficients. Studies focusing on the removal of FeCO₃ can be categorized in two different areas: *in-situ* removal (wall shear stress) and removal of FeCO₃ crystals by determining the mechanical properties of the protective FeCO₃ layer.

2.7.1 Layer Removal Mechanism

Removal mechanisms of the protective FeCO₃ layer are often studied by researchers, since this can lead to highly detrimental damage to the steel surface by exposing it to corrosive environments; this can subsequently promote very aggressive localized corrosion². The idea that the exposed surface and the FeCO₃ covered surface

could form a galvanic couple and thus cause this aggressive type of corrosion was explored by Han, Brown & Nesic, and Xia, Chou, & Szklarska-Smialowska^{35,36}.

In studies where the removal of FeCO₃ by mechanical forces (determination of mechanical properties) was investigated, Xiong³⁷ ran 20 hour experiments in a glass cell with high initial supersaturation for fast precipitation of FeCO₃ crystals on the steel surface. After 20 hours, he removed the sample from the electrolyte and used Atomic Force Microscopy (AFM) to determine the force required to remove FeCO₃. He found that MPa-level lateral stress values are required to remove FeCO₃ crystals, indicating that the shear stress from pipe flow alone (typically in the order of kPa) cannot remove such a constituent phase in a corrosion product layer. Furthermore, Yang³⁸ ran similar glass cell experiments in order to generate steel samples covered with FeCO₃ crystals and used a tensile test machine to determine the mechanical strength of FeCO₃ and the adhesion strength of the FeCO₃ layer to the steel substrate. Both were found to be above 10 MPa. Gao, *et al.*, found similar results to Yang in that the adhesion strength (measured through micro indentation tests) of the corrosion product layer to the steel was in the range of 2-10 MPa³². Xiong and Yang concluded that the mechanical force required to remove FeCO₃ is in the order of MPa^{37,38}. However, both Yang and Xiong formed FeCO₃ in supersaturated environments, where the ferrous ions are coming from the bulk solution, whilst, in a more realistic scenario, the steel itself should be the source of ferrous ions. This aspect could affect the mechanical properties of the formed layer as layer growth interactions with a residual Fe₃C network can be expected.

Additional studies considering various aspects of FeCO₃ removal by flow (shear stress) have been performed by several researchers. Ruzic, *et al.*³, studied mechanical removal of FeCO₃ from steel specimens in a chemically controlled environment. Ruzic found that samples exposed to high velocity had more damage to the FeCO₃ layer than those exposed to low velocity, shown by areas of the steel surface with partial layer removal, pits, and higher corrosion rates over time. Contrary to Yang and Xiong's conclusions, Ruzic determined that purely mechanical removal of FeCO₃ in single-phase flow, with shear stress values not exceeding 85 Pa, did occur. However, the centripetal/centrifugal forces and vibration due to the rotation of the cylinder electrode may have significantly affected the results. More recently, Yang⁶ expanded on her initial work by performing a study of the effect of removal of the FeCO₃ layer by flow in glass cell. Yang first formed FeCO₃ in stagnant conditions in a glass cell then exposed the resultant specimen to turbulent flow (45 Pa) using a rotating cylinder shaft, and observed that there was no removal of FeCO₃. Yang's conclusions were different from Ruzic's in that her experimental results showed that the FeCO₃ layer would require more than just hydrodynamic forces, in the range tested in experiments, to facilitate its removal from a mild steel surface. Yang attempted to reproduce Ruzic's results and was not successful, further emphasizing the detrimental influence that vibrational effects from the RCE setup may have had on the findings. When comparing results that report removal of FeCO₃ *in-situ* obtained in a glass cell as compared to those studies

Lastly, Akeer^{39,40} investigated the formation of FeCO₃ at high wall shear stress in a Thin Channel Flow Cell (TCFC), a thin rectangular channel (3 mm thick and 10 mm wide)

used for high velocity single phase flow experiments. After forming FeCO_3 in stagnant conditions, Akeer observed partial failure of the FeCO_3 when the wall shear stress was increased above a critical value of 535 Pa. However, Akeer further performed experiments for a variety of steel types at highly turbulent conditions (535 Pa) from the beginning of the experiment, and found that no protective FeCO_3 layer formed on the surface even at high bulk supersaturation. Additionally, the high wall shear stress led to the removal of iron carbide (Fe_3C), which would normally form on carbon steel and provide a matrix where FeCO_3 would precipitate⁴⁰. Based on Akeer's findings, Paolinelli³⁰ proposed an estimation of static micro-drag loads, or local shear stresses, as a result of the highly turbulent flow on the steel surface which lead to detachment of precipitated nuclei of FeCO_3 . This study postulated that FeCO_3 or $\text{Fe}_2(\text{OH})_2\text{CO}_3$ plates are formed as precursors to FeCO_3 prisms. However, these plates are easily detached as the turbulent flow exceeds their adhesion resistance, which further causes their removal from the steel surface³⁰.

Although Yang and Ruzic^{3,6} seem to contradict each other's conclusions, they share a similar gap in their experimental procedure – they first form the iron carbonate layer in stagnant to low flow conditions and then investigate its behavior when exposed to flow. This does not reflect field conditions where high shear stresses can be encountered even at the initial nucleation step of FeCO_3 formation. Furthermore, although Akeer had interesting findings that contradict findings from both Ruzic and Yang, there was no systematic approach employed that could be used to determine a critical velocity for FeCO_3 formation and Fe_3C removal. **Table 2** summarizes all findings on the removal of FeCO_3 and the wall shear stress (Pa) required to partially or fully remove the corrosion product layer. A

discrepancy is evident when comparing findings from Ruzic to results obtained from Yang, Xiong, and Gao. Yang, Xiong, and Gao evaluated the mechanical properties of FeCO₃ by assessing the adhesion strength of FeCO₃ to the steel surface. On the other hand, Ruzic studied the removal of FeCO₃ by exposing steel to higher flow rate and shear stress. The discrepancy between these findings can be attributed to experimental artifacts (centripetal/centrifugal forces and vibration) and possibly to fatigue caused by turbulence when looking at *in-situ* removal of FeCO₃ which can result in lower wall shear stress required to remove FeCO₃.

Table 2. Summary of results on FeCO₃ removal

Author	Test Conditions	Wall Shear Stress (Pa) required for FeCO ₃ removal
Ruzic	Removal of FeCO ₃ after forming FeCO ₃ in stagnant conditions ³	45-82
Yang	Removal of FeCO ₃ after forming FeCO ₃ in stagnant conditions	10^6 (mechanical strength) ³⁸
Xiong	Removal of FeCO ₃ after forming FeCO ₃ in stagnant conditions ³⁷	10^6 - 10^7
Gao	Removal of FeCO ₃ after forming FeCO ₃ in stagnant conditions ³²	$2 \cdot 10^6$ - 10^6
Akeer	Removal of FeCO ₃ after forming FeCO ₃ in stagnant conditions ³⁹ & formation of FeCO ₃ at high velocities ⁴⁰	535

In studies considering the effect of flow velocity in multiphase conditions⁴¹⁻⁴⁴, an apparatus referred to as a dynamic field tester, an apparatus installed in various fields that allowed to test multiple velocities (by changing diameters of flow loop) and coupons, was used to determine critical flow velocity in CO₂ environments using various steels. It was found that both carbon content of the material and flow velocity affected the corrosion rate and morphology of corrosion products^{41,45,46}. It was also found that at higher velocities (greater than 4 m/s; wall shear stress greater than 24 Pa), corrosion product consisted mostly of Fe₃C and almost no FeCO₃; XRD analysis showed a decrease in intensity in the FeCO₃ peaks⁴⁴. Consequently, it was demonstrated that wall shear stress⁴² and high flow velocities⁴³ affected formation and morphology of corrosion products.

2.8 Material Microstructure

Cementite (Fe₃C) is a metastable compound⁴⁷ often classified as a “corrosion-product” but it is originally found in the material’s microstructure and, unlike FeCO₃, it is not precipitated on the steel surface. Rather, it represents the leftover steel structure once the ferrite phase has been corroded away.

When considering steels with less than 0.76 wt.% C with a ferritic pearlitic microstructure, as shown on **Figure 1 (a)**⁷, the microconstituents are proeutectoid ferrite and pearlite colonies, which are alternating lamellar-like layers of ferrite and Fe₃C. In a tempered martensitic microstructure (quenched and tempered), shown in **Figure 1 (b)**⁴⁸, there is evidence of an acicular ferrite phase with Fe₃C precipitates. Clover, *et al.*⁴⁹, have demonstrated that corrosion rate behavior depended on the material microstructure. It was

found that a ferritic-pearlitic microstructure experienced localized corrosion, whereas a tempered martensite or ferritic microstructure underwent uniform corrosion⁴⁹.

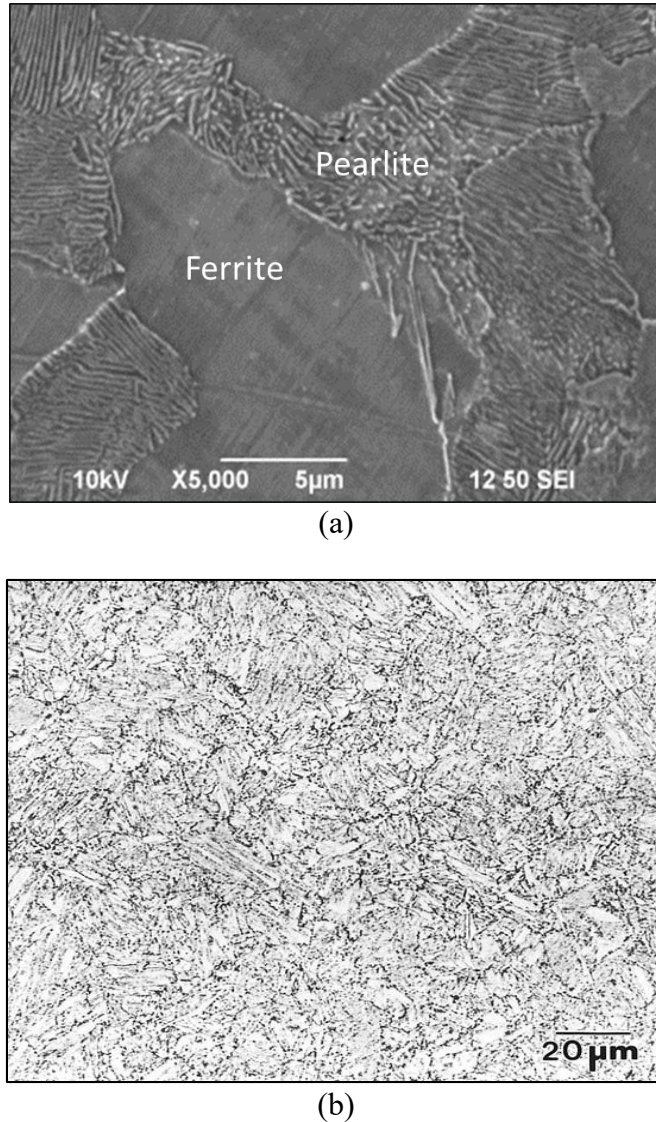


Figure 1. Typical steel microstructures (a) ferritic-pearlitic⁷ (b) tempered martensite⁴⁸

Throughout the literature, it is found that the ferrite phases behave as the anode relative to the Fe₃C, which acts as a cathode^{8,46,47,49-54}. Consequently, ferrite corrodes, leaving exposed Fe₃C residues on the surface of the steel^{7,51,53}. The reason for this is

because the electric potential of iron is -0.4 to -0.5 V and the electric potential of Fe₃C is +0.37 V⁸, with respect to a standard hydrogen electrode. Additionally, the ferrite phase corrodes at faster rates when the ratio of the cathode to anode surface area is large⁸, which occurs when the ferrite phase preferentially corrodes over Fe₃C, leaving a large cathode area with respect to the anode surface area.

Farelas⁷ studied the influence of having an exposed Fe₃C layer on the formation of FeCO₃ on two different materials and microstructures, API 5L X65 tempered martensite and UNS G10180 ferritic-pearlitic; the results were revealing. Farelas concluded that formation of FeCO₃ is possible within the exposed ‘skeletal’ carbide layer (or within pores), even when bulk water chemistry conditions are unfavorable. The exposed Fe₃C is said to act as a diffusion barrier for ferrous and carbonate ions favoring localized conditions for formation of a FeCO₃ layer at the surface of the steel. Although Farelas’s findings are a breakthrough in studying the role of Fe₃C, the author did not incorporate flow effects into his studies. Flow effects are said to play a major role in the formation of FeCO₃ within the pores of Fe₃C since it is weak and fragile⁸, and thus very susceptible to removal by flowing conditions.

In a more recent study, Iteamsupapong³² also found that the presence and nature of Fe₃C played a governing role with regard to the formation of FeCO₃ on steel. His findings were similar to those of Farelas that Fe₃C acts as a diffusion barrier for generated ferrous ions which allows formation of FeCO₃ when tests were ran in controlled conditions using UNS G10180 ferritic-pearlitic at various pH values.

Ambiguous results have been found in the literature as no consensus has been reached in regards to what microstructure favors FeCO_3 precipitation. Dugstad, *et al.*, found that a ferritic-pearlitic microstructure did not yield to FeCO_3 formation as corrosion rates remained high⁵⁵. Ochoa, *et al.*, found that both ferritic-pearlitic or quenched and tempered microstructures exhibited formation of a protective FeCO_3 layer⁵⁶. Eliyan and Alfantazi, which found similar results to Farelas and Ieamsupapong, claimed that a ferritic-pearlitic microstructure was superior to other microstructures in regards to FeCO_3 formation due to the distribution of Fe_3C ⁵¹.

It has also been postulated that an exposed Fe_3C , obtained through pre-corrosion of the metal, did not have an effect in the formation of FeCO_3 ⁴⁶; in other words, it does not have any beneficial impact to FeCO_3 formation, contrary to what has been previously proposed^{7,32}. This is due to the fact that most of the Fe_3C had spalled off during the experiment as witnessed by SEM images, while FeCO_3 still formed. Although this study presents results contrary to the findings described above, these experiments, however, had superstation values in the range of 300-500, which likely facilitated FeCO_3 formation due to the high concentration of ferrous ions in solution.

CHAPTER 3: MOTIVATION, HYPOTHESES AND RESEARCH OBJECTIVES

3.1 Motivation

The main motivation of this study is to better assess the effect of flow in the formation of FeCO_3 and whether it forms at all at highly turbulent conditions. In addition, microstructure may play a role in the formation of FeCO_3 at highly turbulent conditions allowing for precipitation of FeCO_3 within a remaining Fe_3C layer that acts as a diffusion barrier for ferrous ions, preventing their release into solution. Some of the gaps found in the literature review include the fact that even though Xiong³⁷ and Yang³⁸ agreed on MPa stress level findings to remove FeCO_3 layer or crystals; both formed FeCO_3 in supersaturated environments and did not investigate whether the source of the Fe^{2+} ions (bulk or steel surface) had any impact on their findings. The source of ferrous ions is crucial in the precipitation of FeCO_3 . **Figure 2** shows two different scenarios for the source of ferrous ions. **Figure 2 (a)** shows when the ferrous ion comes from the metal (corrosion process), a diffusion barrier (Fe_3C) can trap ferrous ions and allow for FeCO_3 formation. Whereas in the case of ferrous ions coming from bulk solution (in the case of a supersaturated solution), as shown in **Figure 2 (b)**, precipitation of FeCO_3 may not occur by removing ferrous ions from the steel surface.

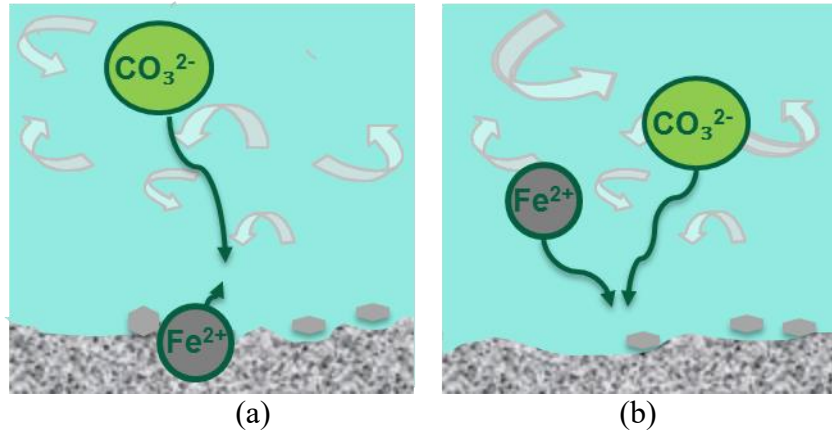


Figure 2. Schematic showing source of ferrous ion (a) from metal (corrosion) (b) supersaturated electrolytes

Additionally, Ruzic's previous findings showed that removal of FeCO_3 can occur at high flow velocities (wall shear stress up to 85 Pa)³. Yang later contradicted Ruzic's findings and saw that when carbon steel was covered with a protective FeCO_3 layer and was subsequently exposed to intense turbulent flow (wall shear stress up to 45 Pa), the layer remained on the steel surface⁶. However, both Ruzic and Yang allowed layer formation first before introducing intense turbulent flow, which may not accord to actual field conditions. Within this context, the precipitation of FeCO_3 will be investigated when specimen is exposed to highly turbulent conditions from beginning of experiment to better correlate with industrial operations.

Last but not least, it is unclear at what shear stress or fluid flow velocity the precipitation/nucleation of FeCO_3 is impeded because either ferrous ions are removed away from the surface or because the exposed Fe_3C that allows for anchoring of FeCO_3 is removed from the steel surface. Although, Akeer found that at a shear stress of 535 Pa, there is no evidence of carbide on the surface⁴⁰, a range of velocities was not tested and it is unclear at what fluid velocity/shear stress removal of Fe_3C starts to occur.

3.2 Objectives

The overall objective of the current study is to identify if FeCO_3 formation is impeded by high flow velocities; commonly encountered in oil and gas related industrial operations. The scope of work also includes the effect of microstructure and environmental conditions (source of ferrous ions and saturation level). In order to accomplish the overall objective, the following tasks were proposed and accomplished:

- Task # 1: Investigate how flow impedes formation of FeCO_3 in highly saturated solutions (replete with ferrous ions) in the absence of Fe_3C .
- Task #2: Determine the effects of environmental conditions (ferrous ion concentration and source) and material properties that influence the nucleation and/or precipitation of FeCO_3 .
- Task #3: Identify a velocity where the formation of FeCO_3 is not possible due to the removal of Fe_3C in highly turbulent flow.

3.3 Hypotheses

Based on the literature review described above, three hypotheses are proposed and explored in this study:

1. A critical flow velocity exists above which nucleation of FeCO_3 is prevented, in the absence of Fe_3C , even in solutions replete with ferrous ions (high bulk FeCO_3 saturation).
2. Material microstructure and Fe_3C aid in the precipitation of FeCO_3 at high flow velocities when the source of ferrous ions is the metal.

3. Fe₃C layer attachment to the metal surface is susceptible to flow. It can be sheared away from the steel surface at high enough flow velocities, which will in turn impede nucleation of FeCO₃.

CHAPTER 4: METHODOLOGY, RESULTS AND DISCUSSION

4.1 Task #1: Effect of Flow on the Formation of FeCO₃ at High Initial S(FeCO₃)

The aim of this set of experiments is to identify the range of velocities above which FeCO₃ does not form on the metal substrate (in the absence of Fe₃C) even though the bulk solution is replete with ferrous ions.

4.1.1 *Methodology*

This set of experiments were performed in the glass cell setup shown in **Figure 3**. Three velocities, as rotations per minute (rpm), and a stagnant condition were tested with a high initial saturation value of 150 with respect to FeCO₃. In each condition, the flow velocity was set from the start of the test and kept constant until the end. In this set of experiments, the source of the ferrous ions was overwhelmingly from the bulk solution. This assures that any limitation due to mass transfer is avoided and allows to determine whether or not high flow velocity can impede the nucleation of FeCO₃.

Table 3 summarizes all of the described experimentation parameters above in the form of a test matrix. The environmental conditions selected ensure optimum corrosion product layer forming conditions based on the literature review and analysis performed. All experiments were performed in three trials to ensure reproducibility of the results.

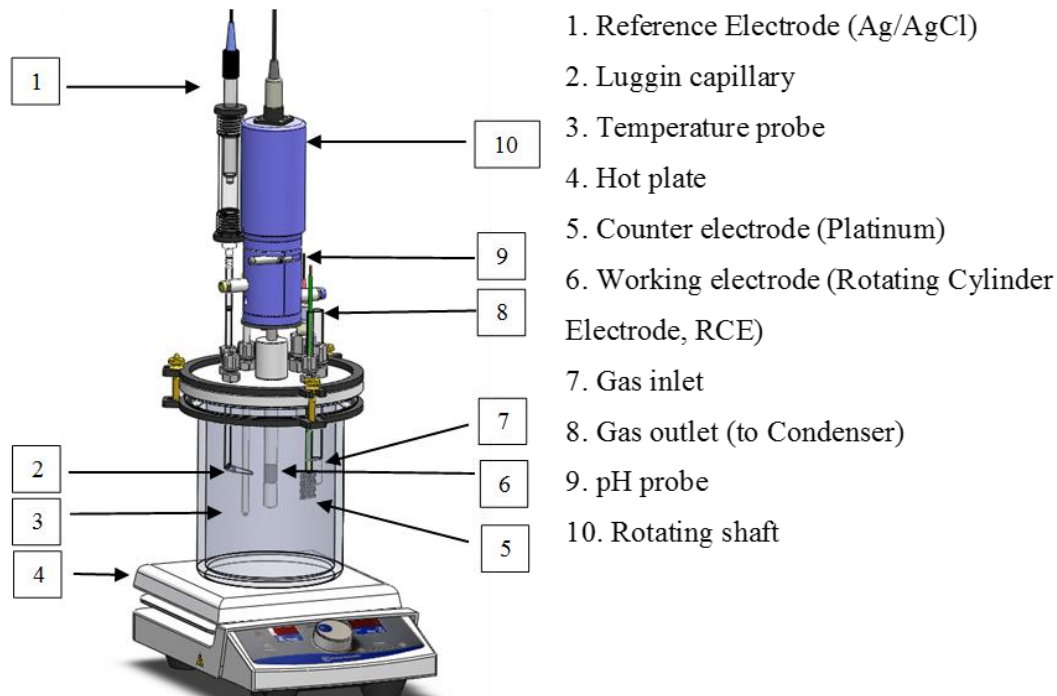


Figure 3. Experimental setup of 2 L glass cell using rotating shaft (image courtesy of Cody Shafer, ICMT)

Table 3. Test matrix for task # 1: effect of flow on the formation of FeCO₃ at high initial S(FeCO₃)

Material	Pure Fe (99.8%)	
	RCE (rpm)	Equivalent Pipe Velocity (m/s)
Flow Velocities	0	0
	500	0.6
	1,000	1.2
	2,000	2.0
Shear Stress (Pa)	Stagnant, 0.8, 2 and 7	
Experimental Setup	2 L Glass cell	
Electrolyte	1 wt.% NaCl	
Initial pH	6.6 ± 0.01	
Temperature (°C)	80	
Total Pressure (Bar)	1.0	
CO ₂ Partial Pressure (Bar)	0.53	
Initial [Fe ²⁺] (ppm)	25	
Initial Saturation w.r.t. FeCO ₃	150	
Electrochemical Measurements	LPR ± 5 mV vs. EOC, 0.125 mV/s $B = 26$ mV/decade EIS 0 mV vs. EOC, Frequency range: 5000- 0.1 Hz.	
Surface Analysis	SEM EDS Raman	

4.1.1.1 Experimental Setup

Typically, corrosion experiments are carried out in a three-electrode electrochemical setup such as the one shown in **Figure 3**. The setup consisted of a 2 L glass cell with a working electrode, reference electrode, and counter electrode. In this case, the

working electrode was a cylindrical pure iron sample with an outer diameter of *ca.* 12 mm and a height of *ca.* 14 mm. The exposed surface of the working electrode was in the range of 5.0 – 5.6 cm². The reference electrode was a saturated silver/silver chloride (Ag/AgCl) reference electrode that was externally connected to the cell *via* a glass-body Luggin capillary through a Vycor® porous glass frit placed adjacent to the RCE in order to reduce the solution resistance. A platinum mesh acted as the counter electrode for this cell. The glass cell was mounted on a ceramic-topped hotplate, which heated up the glass cell utilizing a thermocouple immersed in the solution and connected to the hotplate.

A 1 wt% NaCl electrolyte was prepared by combining 2 L of deionized water and 20.2 g of NaCl. Once this solution was prepared, it was poured in the 2 L glass cell. The glass cell was then sealed with an O-ring and a Teflon® lid, the system was then sparged with CO₂ gas for two hours in order to keep the oxygen gas content below 10 ppb. After all of this was done, the temperature was raised slowly to 80°C using the hotplate. The temperature was raised slowly in order to avoid overheating the hotplate and loss of desired temperature control (overshoot). The total pressure of the system was 1 bar since it was an open system. However, since it was sparged with CO₂, the partial pressure of CO₂ is 0.53 bar (at 80°C) with the rest being vapor pressure. Additionally, a temperature compensated pH meter was used to monitor the bulk pH of the solution at all times. The pH was initially set to pH and adjusted accordingly by injecting deoxygenated hydrochloric acid (HCl) or sodium bicarbonate (NaHCO₃) to decrease or increase the solution pH, respectively. The temperature and pH were continuously monitored during the course of the experiments.

A pure iron (Fe) specimen (Surepure Chemetals, 99.8%) was used for electrochemical and surface analysis. Prior to immersion of the working electrode in the glass cell, specimen dimensions were taken in order to calculate the exposed surface area. Specimen weights were taken in order to determine the corrosion rate through weight loss at the end of experiments. Specimens were previously wet-polished with silicon carbide abrasive paper up to 600 grit; they were rinsed with isopropyl alcohol and placed in an ultrasonic bath to remove any remaining iron particles from their surfaces. After this, the RCEs were dried with cold air and mounted onto the Pine rotating shaft, which was then subsequently assembled and contacted with the electrolyte.

4.1.1.2 Electrochemical Measurements

A potentiostat connected to a computer was used for electrochemical and potential measurements. The working electrode was polarized ± 5 mV *versus* the open circuit potential using a scan rate of 0.125 mV/s for Linear Polarization Resistance (LPR) measurements. The B value that was used was 26 mV/decade^{6,7,33,40} and can be obtained from equation (18) below by using 120 mV/decade as both anodic and cathodic Tafel slopes obtained from the literature for CO₂ corrosion of steel^{11,13,18}. The polarization resistance from these measurements, R_p , was used to calculate the current density (i_{corr} , A/cm²) and in turn the corrosion rate (CR) in millimeters per year (mm/yr) using the Stern-Geary Equation (18)^{7,18,55,58} as follows:

$$B = \frac{\beta_a * \beta_c}{2.3 * (\beta_a + \beta_c)} \quad (18)$$

$$i_{corr} = \frac{B}{A * R_p} \quad (19)$$

$$CR = a * \frac{i_{corr} * MW}{\rho n F} \quad (20)$$

Where β_a and β_c are the anodic and cathodic Tafel slope, respectively, MW is the molecular weight of iron in grams (g/mol), ρ is the density of iron (g/cm³), n is the number of electrons involved in the electrochemical reaction (2 for iron, as shown in equation (6)), F is Faraday's constant, 96,485 C/mol, and a is a conversion factor to obtain corrosion rate in mm/yr units. Based on the experimental conditions tested and according to the corrosion prediction software FREECORP, the first LPR corrosion rate measurement should give an initial corrosion rate (before adjustment of the FeCO₃ saturation level) between 1.0 and 3.0 mm/yr (sensitive to velocity). If the corrosion rate was significantly lower than this value, the experiment was stopped then restarted as unwanted experimental artefacts were assumed to have altered the tests. Additionally, electrochemical impedance spectroscopy (EIS) was used to measure the solution resistance and ensure that the polarization resistance values from LPR measurements were accurate. The frequency range was 5,000 – 0.1 Hz and the sample was polarized 0 mV *versus* the open circuit potential.

4.1.1.3 Water Chemistry

Aqueous FeCl₂ was injected into the solution after the first LPR measurement, provided its value was within the expected range, in order to reach the desired starting ferrous ion concentration of 25 ppm. The deoxygenated aqueous FeCl₂ was prepared by dissolving 2.0 grams of ferrous chloride tetrahydrate (FeCl₂·4H₂O) in 50 mL solution of deionized water sparged with nitrogen gas (N₂) for 30 minutes (oxygen free solution). After this solution was prepared, 10 mL was added into the glass cell using a syringe. By following this procedure, the saturation of the solution was set at 150, according to equation

(15). Ferrous ion concentration in solution was measured three times during the course of the experiment using a spectrophotometer. This was done by drawing 20 mL out of the glass cell solution and filtered with 0.45 μm filter; 10 mL were used as a blank solution and the remaining 10 mL were mixed with an iron reagent. These two solutions were measured against other in order to determine ferrous ion concentration.

The saturation value of the bulk solution dropped significantly from 150 to *ca.* 30 after 8 hours of exposure, at which point the test was ended. The high saturation value allowed to isolate mass transfer limitations and focused on identifying a shear stress value where the precipitation of FeCO_3 on the metal surface does not occur.

4.1.1.4 Flow Velocities

The numerical value of rotational speed of the RCE, rotations per minute (rpm), is only meaningful if translated in equivalent pipe velocities, since its effects are strongly setup dependent. In order to appropriately characterize the flow velocity for the Pine rotating shaft once the RCE has been mounted, key findings from the literature were employed. Silverman⁵⁹⁻⁶³ has developed equation (22) which relates rpm ranges for these experiments to equivalent mass transfer conditions in a pipeline:

$$U_{cyl} = \frac{\pi d_{cyl} F}{60} \quad (21)$$

$$V_{eq} = \sqrt[5]{\left(\frac{1}{0.1185} Sc^{0.0857} \nu^{\frac{1}{4}} \left(\frac{d_p^{\frac{5}{28}}}{d_{cyl}^{\frac{3}{7}}} \right) U_{cyl} \right)^4} \quad (22)$$

Where:

U_{cyl} = surface velocity of RCE (cm/s)

d_{cyl} = diameter of RCE (cm)

F = rotational speed of RCE (rpm)

V_{eq} = fluid velocity through the pipe (cm/s)

Sc = Schmidt Number

ν = kinematic viscosity (cm²/s)

d_p = diameter of typical pipe (cm)

These equations help simulate a nearly equivalent mass transport as in turbulent flow through a smooth, straight pipe in the glass cell set-up. The internal diameter (ID) of a typical pipe was selected to be 25.5 cm, as per consultation with field experts. The RCE diameter is *ca.* 1.22 cm. All parameters used to calculate the Schmidt number, such as density, dynamic viscosity and diffusivity were calculated for a temperature of 80 °C^{9,64}. Based on these numbers, a different range of rpm velocities were analyzed going from standard to highly turbulent conditions (0-2,000 rpm).

The wall shear stress on the surface of the RCE (g/cm·s²) is also found using the following equation (23)^{59-63,65,66}:

$$\tau_{cyl} = 0.0791 \rho Re^{-0.3} U_{cyl}^2 \quad (23)$$

The same logic behind equation (22) applies to Equation (23). The parameters needed to calculate the Reynolds number were obtained at a temperature of 80°C^{9,64}. **Table 4** summarizes the RCE rotational speeds chosen, surface velocity of RCE obtained from equation (21), fluid velocity through a pipe calculated from equation (22), and the wall shear stress on the RCE surface calculated from equation (23).

Table 4. Summary of RCE rotational speeds and corresponding pipe fluid velocities and wall shear stresses

RCE Rotational Speed (rpm)	RCE Surface Velocity (m/s)	Wall Shear Stress on RCE Surface (Pa)	V_{eq} , Equivalent Velocity in 25.5 cm ID pipe (m/s)
Stagnant	0	0	0
500	0.4	0.8	0.6
1,000	0.6	2	1.2
2,000	1.3	7	2.0

Within this context, three different experimental setups are used with dissimilar wall shear stresses and mass transfer coefficients. Thus, fluid velocities and rotational speeds cannot be used to directly compare the results obtained using the different setups, but rather wall shear stress values and velocities calculated based on mass transfer coefficient for a 10" pipe.

The same experimental procedures shown in **Table 3** were followed using API 5L X65 as a material, instead of pure Fe, in order to compare results with the literature and ensure reproducibility of results. These results are shown in Appendix 1: Preliminary Experimentation for FeCO₃ Reproducibility.

4.1.1.5 Sample Characterization

After a test duration of eight hours, RCEs were removed the glass cell and cleaned with N₂ sparged deionized water followed by isopropyl alcohol, drying, and storage in a dessicator cabinet. Corrosion rates obtained by the potentiostat were plotted over time and analysis of results performed. These plots permitted determination of the protectiveness of

the FeCO₃ layer formed, if any, if the corrosion rate decreased to a low and steady value. SEM was used to characterize layer morphology, thickness, and surface topography. Compositional analysis and element mapping was performed through quantitative EDS; the EDS system is coupled to the SEM. Typically, large prismatic crystals are seen on the surface as evidence that the FeCO₃ layer has formed^{6,26,29,32,34,37-39}. Preliminary experiments were performed in order to ensure reproducibility of the FeCO₃ corrosion product layer and compared with the literature, the results are shown in Appendix 1: . An SEM image will help identify adherence, presence or attachment of FeCO₃ onto the steel surface. EDS can help differentiate between FeCO₃ and Fe₂(OH)₂CO₃ since there is a larger iron to carbon ratio in Fe₂(OH)₂CO₃ than FeCO₃. Raman analysis was performed using Witec Alpha 300 Confocal Raman through x20 objective lenses to properly characterize corrosion products. The laser detector was used at a 532 nm wavelength at a laser intensity of ~ 1000 kW/cm².

4.1.2 Results and Discussion

The purpose of this set of experiments was to identify if attachment of FeCO₃ occurs at high flow velocities when the ferrous ions are abundant (high S_{FeCO_3}) and came from the bulk solution. This velocity was identified using a pure Fe sample in order to exclude the effect of microstructure, in this case related to the presence of Fe₃C. The effect of microstructure is further explained in section 4.2. The sample bare surface, in contrast with previous studies, was immediately subjected to high shear stresses; meaning that there was no preformed FeCO₃ layer on the steel surface. This is an improvement in studying formation of FeCO₃; Xiong³⁷ and Yang³⁸ found that shear stress levels of the order of MPa

were required to remove FeCO_3 from the surface once it had been formed. However, this is not typical of oil and gas operations and does not offer a fair comparison between laboratory setups and field conditions.

It is noteworthy that the precipitation rate of FeCO_3 , as represented by its saturation value dropped quickly over the first 12 hours, from 150 to *ca.* 10, when there was no metal sample in the solution, as shown in **Figure 4**. This was done to determine an appropriate experiment duration required for significant FeCO_3 precipitation when ferrous ions come from the bulk solution and not from corrosion process (corroded metal). Ideally, the tests should have been performed at constant saturation levels but maintaining a high S_{FeCO_3} is difficult. Consequently, the tests duration was set at 8 hours as a compromise between maintaining ‘high enough’ saturation and ensuring meaningful exposure time. At the end of 8 hours, the final saturation value of *ca.* 40 ensured that substantial amount of ferrous ions remained in the bulk solution. This still allowed focusing on mechanical effects while minimizing mass transfer effects.

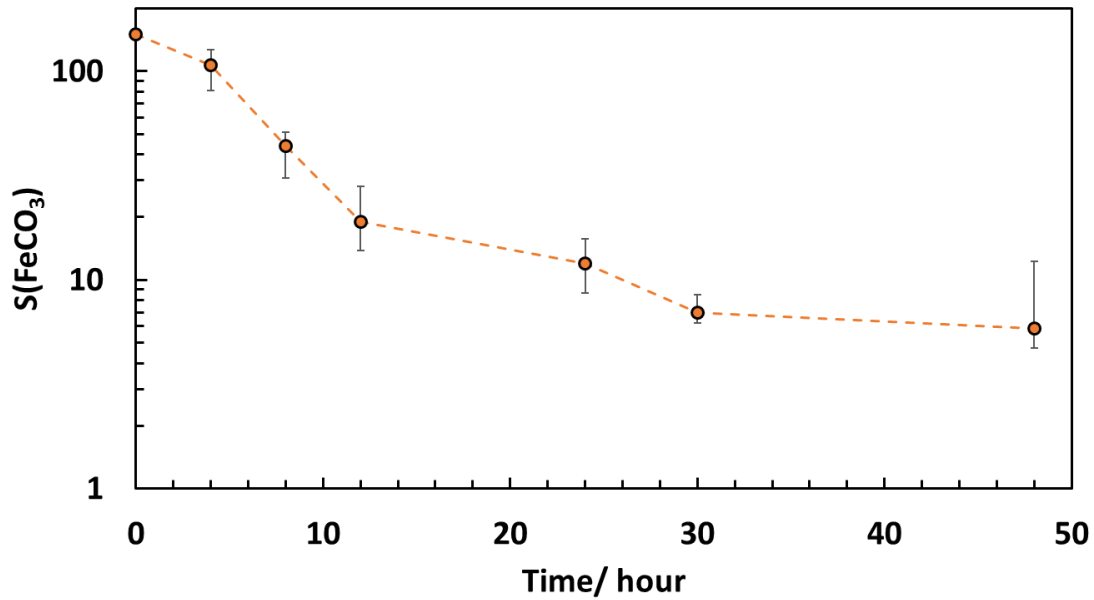


Figure 4. Saturation value with respect to FeCO_3 over the course of 48 hours in a 2 L glass cell under the conditions: $T=80^{\circ}\text{C}$, $p\text{CO}_2 = 0.53$ bar, initial pH 6.6, initial $S_{\text{FeCO}_3} \approx 150$

Subsequent flow experiments were conducted at four different velocities: stagnant, 500 rpm (0.6 m/s or 0.6 Pa), 1000 rpm (1.2 m/s or 2 Pa), 2000 rpm (2.0 m/s or 7 Pa) [equivalent 25.5 cm ID pipe velocities have been calculated based on equation (22) and wall shear stress values based on Equation (23)]. In order to improve accuracy in results, as well as isolate the effect of centrifugal forces associated with the working electrode, each experiment was repeated a total of three times, which gives a total of 12 experiments at four different velocities.

4.1.2.1 Stagnant

Figure 5 shows the LPR corrosion rate measurements, taken hourly during the 8 hour experiment at stagnant conditions, on the left axis, and the saturation value on the right axis. Also, the initial corrosion rate is compared to predictions from FREECORP 2.0

under the same environmental conditions. It is noteworthy that there is a good agreement between what FREECORP predicts *versus* the initial corrosion rated measured by LPR. **Figure 5** shows a relatively high initial corrosion rate, which then decreases to a value lower than 1.0 mm/yr for the rest of the experiment. This was true for all three experiments, as shown by the error bars associated with the hourly LPR corrosion rate measurements. It is also noteworthy that the saturation values remain reasonably constant during the 8 hour experiment; the final saturation value is only slightly lower than 100. In that case, ferrous ions consumed due to the precipitation of FeCO_3 were replenished by the ferrous ions coming from the metal (corrosion process).

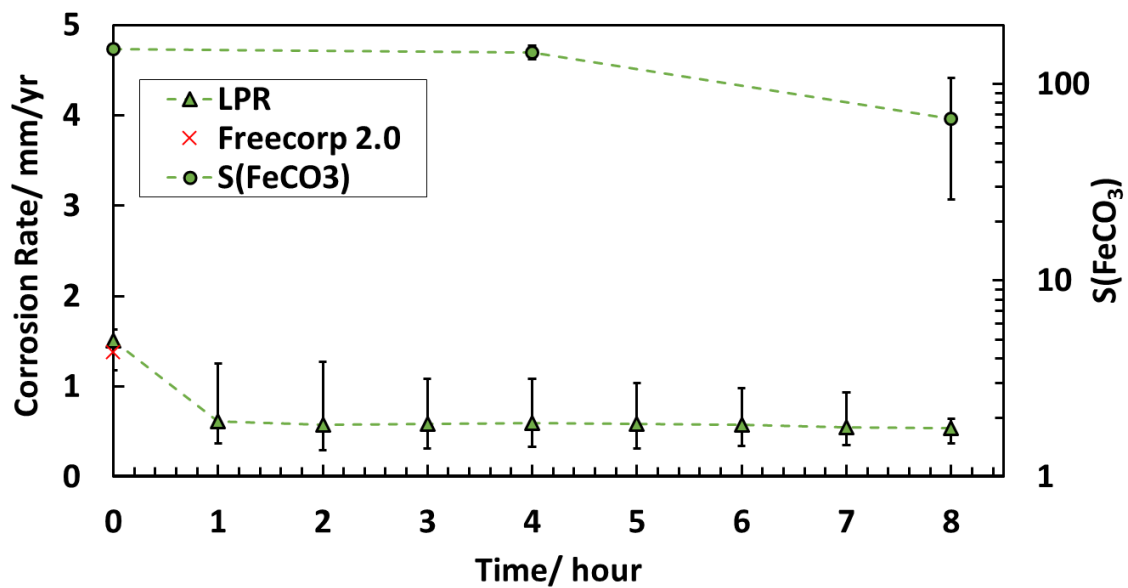


Figure 5. Comparison of LPR corrosion rates, predicted initial FREECORP 2.0 and saturation of FeCO_3 over time for stagnant experiment with pure Fe under the conditions: $T=80^\circ\text{C}$, $p\text{CO}_2 = 0.53$ bar, initial pH 6.6, initial $S_{\text{FeCO}_3} \approx 150$

Figure 6 shows the SEM images of the sample surface at different magnifications. The specimen surface is completely covered by plates and prisms. As discussed in the literature review section, these plates have been characterized as $\text{Fe}_2(\text{OH})_2\text{CO}_3$ ^{29,31}, and are known to be precursors to FeCO_3 ^{29,30,31}. EDS was used to characterize and differentiate the elements present in both of these morphologies.

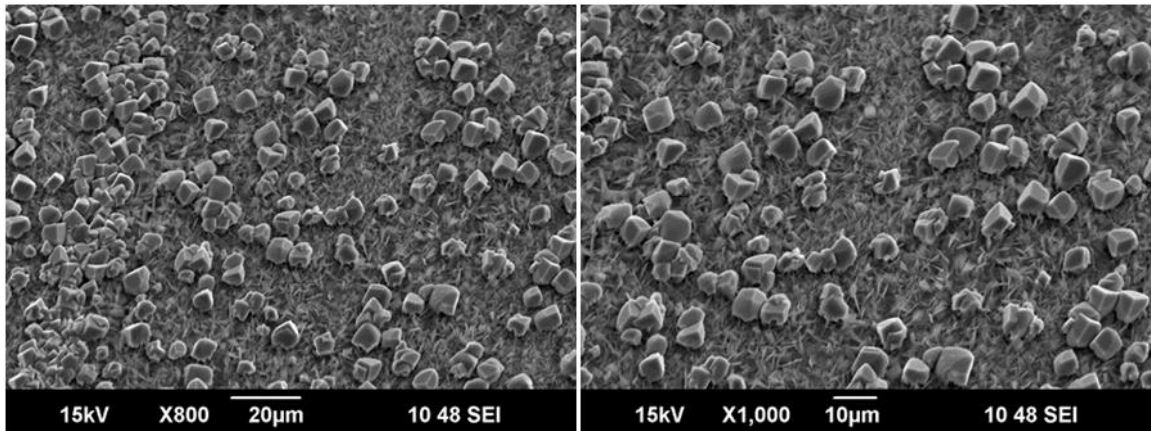


Figure 6. x800 and x1000 SEM images showing surface morphology for stagnant experiment with pure Fe under the conditions: $T=80^{\circ}\text{C}$, $p\text{CO}_2 = 0.53$ bar, initial pH 6.6, initial $S_{\text{FeCO}_3} \approx 150$

Figure 7 shows the image of the sample surface that was used for EDS analysis. The red cross labelled 1 and the red area labelled 2 show the areas of the specimen surface that were analyzed. According to the findings of Tanupabrungsun²⁹ and Pandarinathan³¹ as well as Paolinelli's hypothesis³⁰, it is alluded that point 1 is an FeCO_3 prism and area 2 covers $\text{Fe}_2(\text{OH})_2\text{CO}_3$ plates.

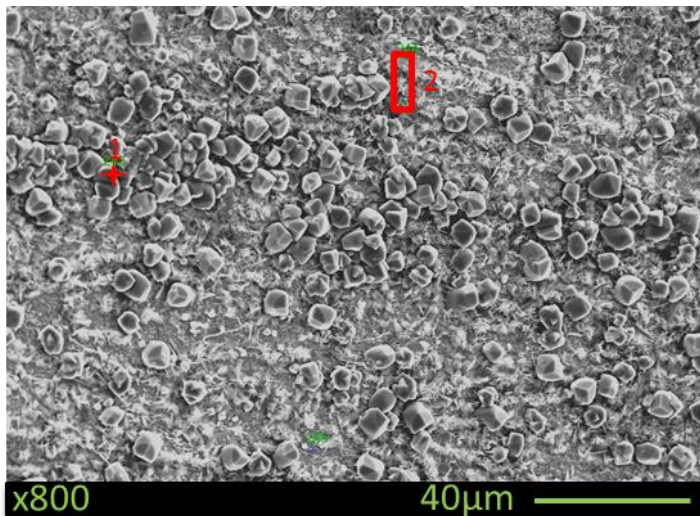


Figure 7. x800 SEM image showing areas used for EDS analysis showing surface morphology for stagnant experiment with pure Fe surface under the conditions: $T=80^0\text{C}$, $\text{pCO}_2 = 0.53 \text{ bar}$, initial pH 6.6, initial $S_{\text{FeCO}_3} \approx 150$

EDS analysis on the red cross labelled 1 and the red area labelled 2 are shown in **Figure 8 (a)** and **Figure 8 (b)**, respectively. FeCO_3 is enriched with oxygen over $\text{Fe}_2(\text{OH})_2\text{CO}_3$, corresponding to $\text{O/Fe} = 3$ versus $\text{O/Fe} = 2.5$; and **Figure 8 (a)** shows a higher oxygen content (mass %) and energy peak of oxygen than **Figure 8 (b)**. This can give an indication that the prisms are FeCO_3 . **Figure 8 (b)** shows the lower intensity peaks for all elements, except iron. The intensity of the iron peak at area 2 may indicate that FeCO_3 is not the phase present in this area and may be $\text{Fe}_2(\text{OH})_2\text{CO}_3$ plates, which is consistent with what has been reported in the literature^{29,31}. This is also supported by the fact that trends of oxygen to iron ratio (evidenced in mass %) are consistent with prisms being FeCO_3 and plates being $\text{Fe}_2(\text{OH})_2\text{CO}_3$.

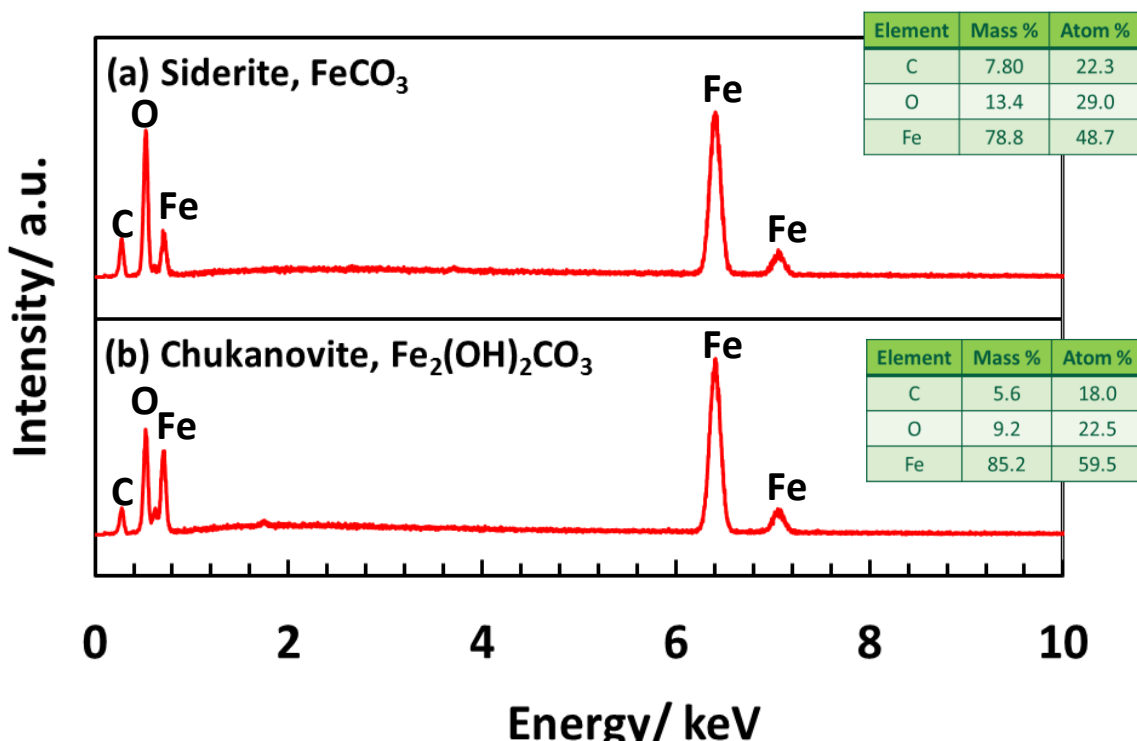


Figure 8. EDS spectra taken on stagnant pure Fe surface (a) point 1 (b) area 2 shown in **Figure 7**

Furthermore, elemental mapping was performed by EDS to determine distribution of elements on the sample surface shown in **Figure 7**. **Figure 9** shows how elements are distributed on the sample surface as shown by color intensity identification of each element (O – yellow; Fe – green; C – fuchsia). It can be observed that the surface is uniformly covered by FeCO_3 and $\text{Fe}_2(\text{OH})_2\text{CO}_3$. In areas where there are more plates present, enrichment with respect to iron is observed. In contrast, in areas where prisms are present, oxygen shows the greatest dominance (given enrichment of oxygen in FeCO_3 over $\text{Fe}_2(\text{OH})_2\text{CO}_3$). This agrees with the EDS point spectra shown in **Figure 8**.

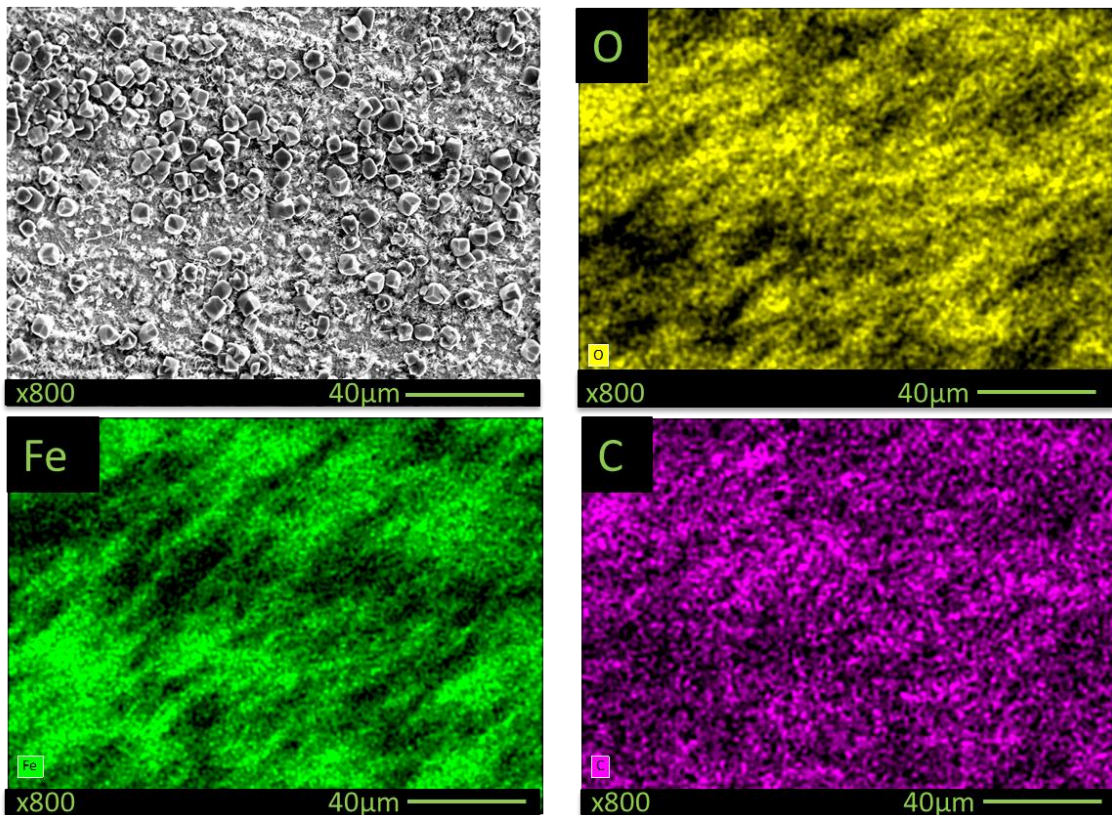


Figure 9. x800 SEM image showing EDS elemental mapping for stagnant experiment with pure Fe under the conditions: $T=80^{\circ}\text{C}$, $\text{pCO}_2 = 0.53 \text{ bar}$, initial pH 6.6, initial $S_{\text{FeCO}_3} \approx 150$

Raman analysis was done to confirm that the corrosion products formed were siderite, FeCO_3 (prisms), and chukanovite, $\text{Fe}_2(\text{OH})_2\text{CO}_3$ (plates). **Figure 10**, which shows Raman analysis performed on the different areas of the specimen surface, confirms that the corrosion product consists of a mixture of FeCO_3 and $\text{Fe}_2(\text{OH})_2\text{CO}_3$, based on results obtained from the literature on siderite and chukanovite⁶⁷⁻⁶⁹. It is evident that there is shift of *ca.* 17 cm^{-1} between the siderite and chukanovite's most intense vibrational modes (associated with bonding within the CO_3^{2-} polyatomic ion within their lattices), which help differentiate between the two phases^{67,69}. Also, $\text{Fe}_2(\text{OH})_2\text{CO}_3$ has no peak at 284 cm^{-1} .

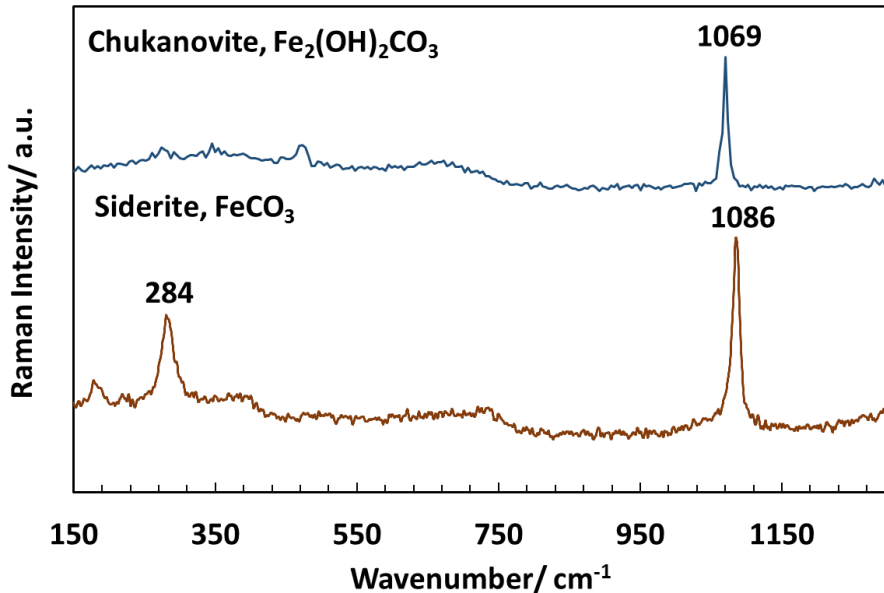


Figure 10. Raman spectra of stagnant pure Fe surface confirming presence of $\text{Fe}_2(\text{OH})_2\text{CO}_3$ and FeCO_3 under the conditions: $T=80^{\circ}\text{C}$, $p\text{CO}_2 = 0.53$ bar, initial pH 6.6, initial $S_{\text{FeCO}_3} \approx 150$

4.1.2.2 500 rpm, $V_{eq} = 0.6 \text{ m/s (0.8 Pa)}$

Figure 11 shows the LPR corrosion rate measurements, taken hourly during the 8 hour experiment at 500 rpm ($V_{eq} = 0.6 \text{ m/s, 0.8 Pa}$), on the left axis, and the saturation value on the right axis. Also, the initial corrosion rate is compared to what FREECORP 2.0 predicts under the same environmental conditions. In this case, there is about a 0.8 mm/year difference between what FREECORP 2.0 predicts *versus* the obtained LPR corrosion rate measurement at the beginning of the experiment. It was found in the literature that the purity of iron greatly affects the corrosion rate. An iron with 99.997% purity had corrosion rates an order of magnitude higher than a 99.75% pure iron⁷⁰. The cause for discrepancy is alluded to the fact that FREECORP 2.0 predicts the corrosion rate for a low carbon steel and not for a high purity iron. Additionally, it was found that the corrosion rate of high

purity iron is affected by high flow velocities, as coupons in a dynamic system had slightly higher corrosion rates than those in a static system⁷¹.

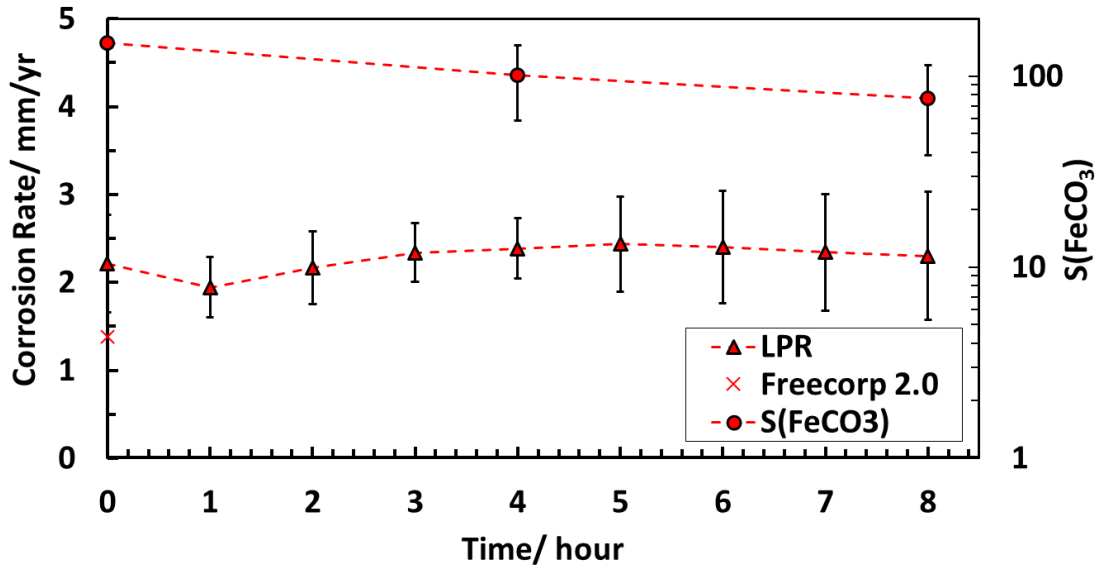


Figure 11. Comparison of LPR corrosion rates, predicted initial FREECORP 2.0 and saturation of FeCO₃ over time for 500 rpm ($V_{eq} = 0.6$ m/s, 0.8 Pa) experiment with pure Fe under the conditions: T=80°C, pCO₂ = 0.53 bar, initial pH 6.6, initial S_{FeCO₃} ≈ 150

Figure 11 shows a higher initial corrosion rate than the stagnant case, as shown in **Figure 5**, by 0.7 mm/yr. Additionally, it is noteworthy that the LPR corrosion rate stays constant and does not deviate from the initial corrosion rate throughout the rest of the experiment for all three trials, in contrast to the stagnant case shown in **Figure 5** which shows lower corrosion rates than the initial corrosion rate. However, similarities are shown in the saturation values when comparing the 500 rpm ($V_{eq} = 0.6$ m/s, 0.8 Pa) condition with the stagnant one, as shown in **Figure 11** and **Figure 5**, respectively. The saturation values

remain supersaturated and do not deviate significantly from the initial saturation value of 150.

Figure 12 shows SEM images of the 500 rpm ($V_{eq} = 0.6$ m/s, 0.8 Pa) specimen surface at different magnifications. The sample surface shows sporadic FeCO_3 prisms with areas showing a bare/exposed surface. This can be related to the corrosion rate measurements shown in **Figure 11**. The fact that the corrosion rate never reached a low and stable corrosion rate value may be attributed to the fact that a non-protective FeCO_3 formed in the 500 rpm ($V_{eq} = 0.6$ m/s, 0.8 Pa) sample in contrast to what was seen in the stagnant samples. No evidence of plates could be identified on the entirety of the sample surface.

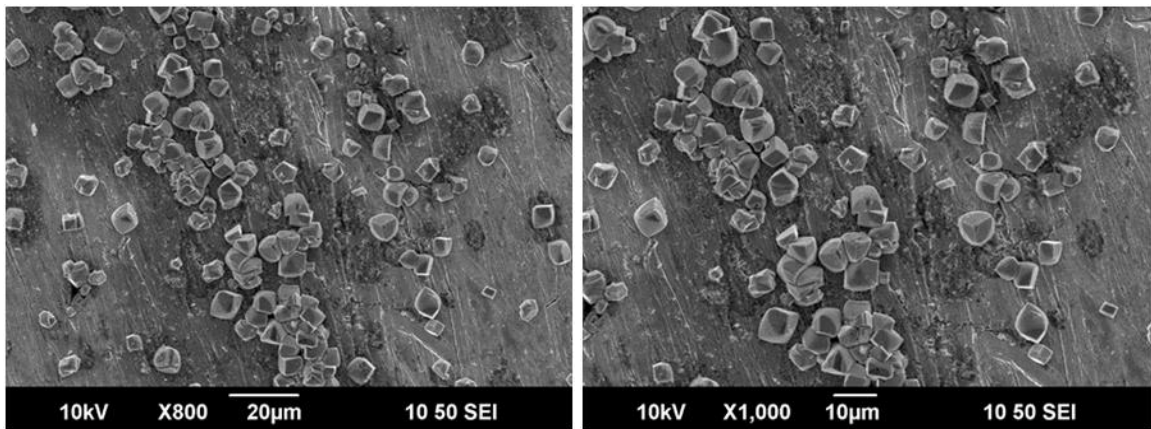


Figure 12. x800 and x1000 SEM images showing surface morphology for 500 rpm ($V_{eq} = 0.6$ m/s, 0.8 Pa) experiment with pure Fe under the conditions: $T=80^{\circ}\text{C}$, $p\text{CO}_2 = 0.53$ bar, initial pH 6.6, initial $S_{\text{FeCO}_3} \approx 150$

Figure 13 shows the image of the specimen surface that was used for EDS analysis, the red area labeled 1 and the red area labeled 2 show the areas that were analyzed.

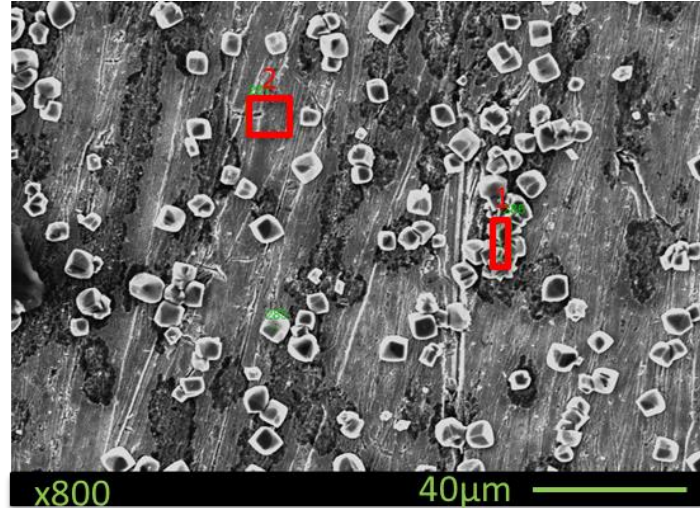


Figure 13. x800 SEM image showing areas used for EDS analysis showing surface morphology for 500 rpm ($V_{eq} = 0.6$ m/s, 0.8 Pa) experiment with pure Fe surface under the conditions: T=80°C, pCO₂ = 0.53 bar, initial pH 6.6, initial S_{FeCO₃} ≈ 150

Figure 14 (a) alludes to the presence of FeCO₃ prisms in area 1, selected and shown in **Figure 13**, given the intensity of the peak for oxygen. **Figure 14 (b)** shows no presence of oxygen. This is indicative of the absence of FeCO₃ in the selected area.

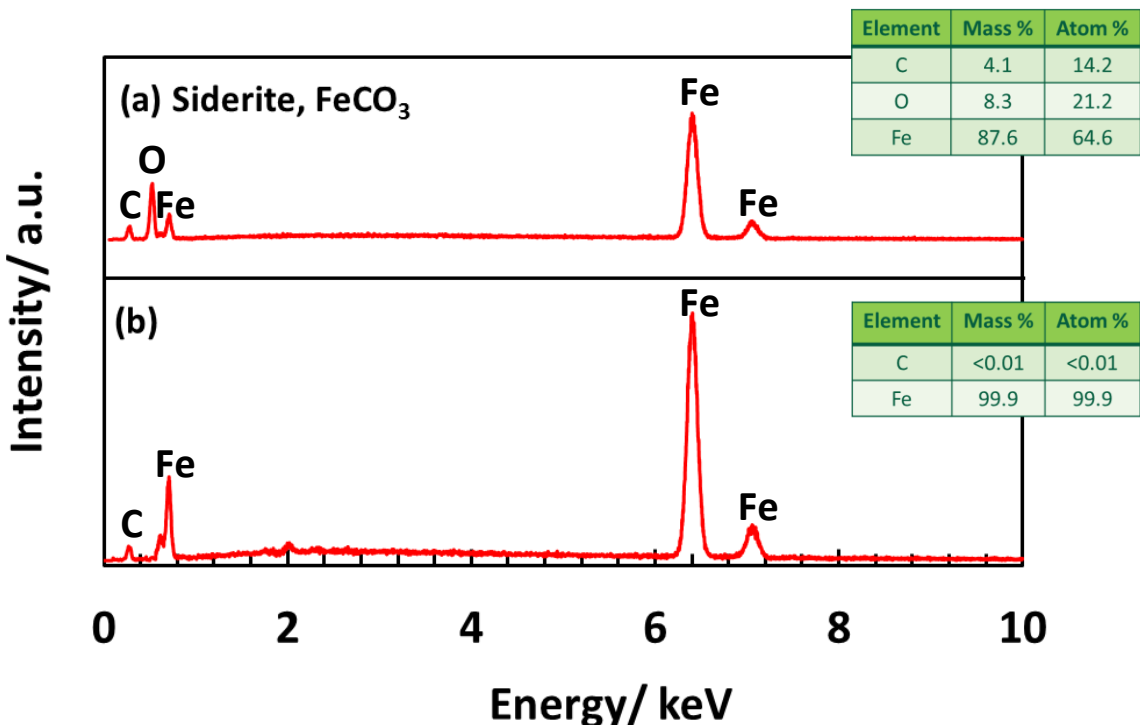


Figure 14. EDS spectra taken on 500 rpm ($V_{eq} = 0.6 \text{ m/s}$, 0.8 Pa) pure Fe surface at (a) area 1 (b) area 2 shown in **Figure 13**

Elemental mapping was again performed by EDS as discussed above. **Figure 15** shows how Fe, C and O are distributed on the specimen surface, represented by the color intensity. Oxygen is exclusively present in areas where there are crystals (presumed to be FeCO_3 given their morphology), iron is most dominant on the bare steel surface, and carbon is present at a higher concentration in the FeCO_3 than in the metal. Because oxygen exclusively represents FeCO_3 prisms, it acts as a proxy that represents surface coverage by corrosion product. Based on this concept and EDS analysis, pending Raman characterization, approximately 38% of the sample surface is covered by FeCO_3 .

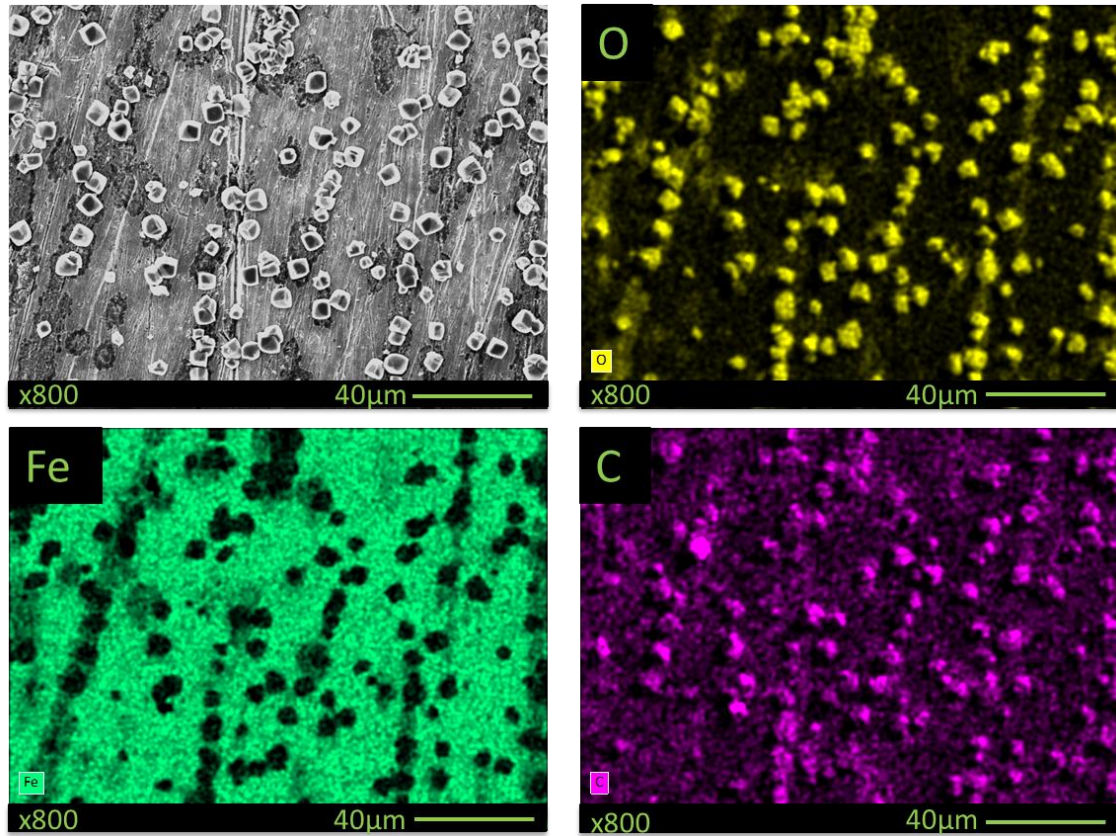


Figure 15. x800 SEM image showing EDS elemental mapping for 500 rpm ($V_{eq} = 0.6$ m/s, 0.8 Pa) experiment with pure Fe under the conditions: T=80⁰C, pCO₂ = 0.53 bar, initial pH 6.6, initial S_{FeCO₃} ≈ 150

Figure 16 shows the Raman spectra obtained after performing surface analysis of the 500 rpm ($V_{eq} = 0.6$ m/s, 0.8 Pa) specimen. Raman analysis confirmed that the corrosion product consisted of FeCO₃, based on the prismatic crystals shown in **Figure 12** and the peak positions obtained from Raman analysis upon comparison with the literature⁶⁷⁻⁶⁹.

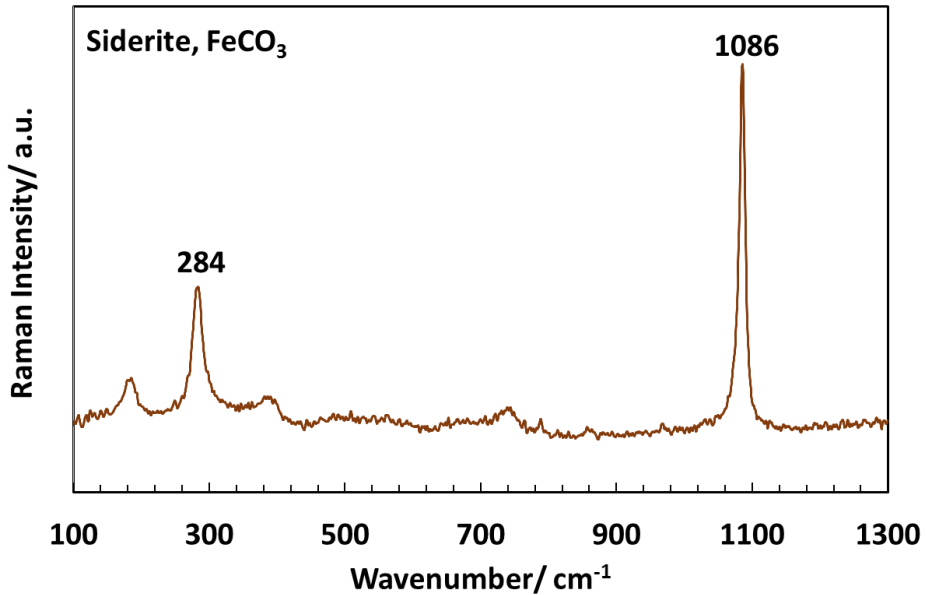


Figure 16. Raman spectra of 500 rpm ($V_{eq} = 0.6 \text{ m/s}$, 0.8 Pa) pure Fe surface confirming presence of FeCO_3 under the conditions: $T=80^\circ\text{C}$, $p\text{CO}_2 = 0.53 \text{ bar}$, initial pH 6.6, initial $S_{\text{FeCO}_3} \approx 150$

4.1.2.3 1000 rpm, $V_{eq} = 1.2 \text{ m/s}$ (2 Pa)

Figure 17 shows the LPR corrosion rate measurements, taken hourly during the 8 hour experiment at 1000 rpm ($V_{eq} = 1.2 \text{ m/s}$, 2 Pa), on the left axis and the saturation value on the right axis. Also, the initial corrosion rate is compared to what FREECORP 2.0 predicts under the same environmental conditions. The disagreement of 1.4 mm/yr between the predicted FREECORP 2.0 value and the obtained LPR corrosion rate measurement at the beginning of the experiment is larger than those obtained in lower velocity conditions, as shown in **Figure 5** and **Figure 11**. As previously discussed, the discrepancy between FREECORP 2.0 and LPR corrosion rate measurement can be cause by a combination of the high purity iron⁷⁰ and higher flow velocities⁷¹.

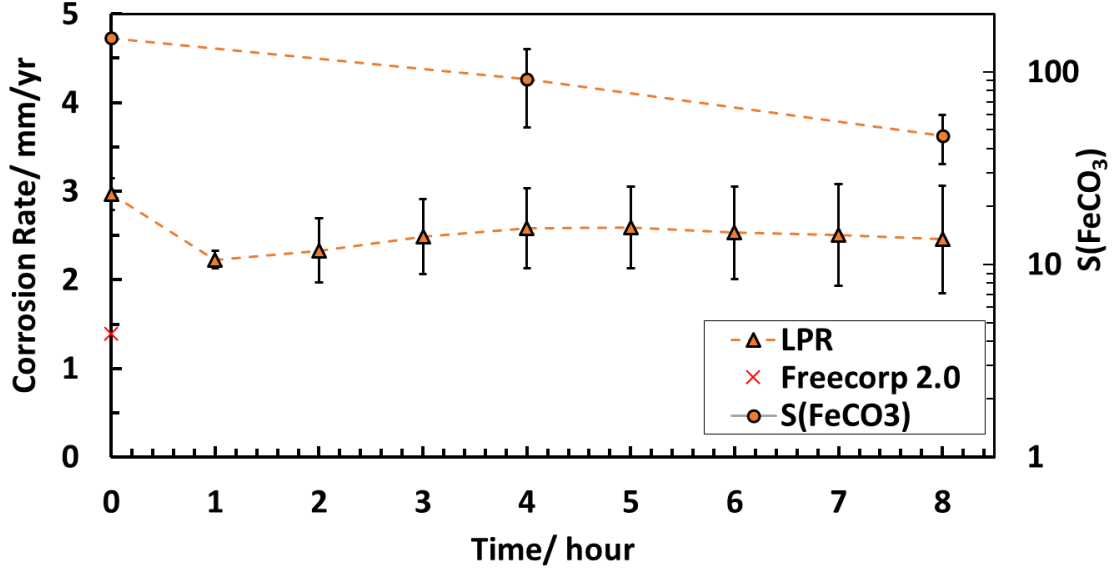


Figure 17. Comparison of LPR corrosion rates, predicted initial FREECORP 2.0 and saturation of FeCO_3 over time for 1000 rpm ($V_{eq} = 1.2 \text{ m/s}$, 2 Pa) experiment with pure Fe under the conditions: $T=80^\circ\text{C}$, $p\text{CO}_2 = 0.53 \text{ bar}$, initial pH 6.6, initial $S_{\text{FeCO}_3} \approx 150$

Figure 17 shows a higher initial corrosion rate than both stagnant and 500 rpm ($V_{eq} = 0.6 \text{ m/s}$, 0.8 Pa) cases, as expected, due to added turbulence at increasing velocities. The difference between the stagnant and 1000 rpm ($V_{eq} = 1.2 \text{ m/s}$, 2 Pa) cases is about 2 mm per year. Also, it can be observed that the LPR corrosion rates throughout the course of the experiment does not vary significantly from the initial corrosion rate; this is true for all three experiments. Also, this is similar to the 500 rpm ($V_{eq} = 0.6 \text{ m/s}$, 0.8 Pa) case, as shown in **Figure 11**. The data presented in **Figure 17** shows that saturation drops considerably from its initial value of 150. This differs from the stagnant and 500 rpm ($V_{eq} = 0.6 \text{ m/s}$, 0.8 Pa) conditions, where saturation did not significantly change from the initial values, as shown in **Figure 5** and **Figure 11**, respectively. This may be due to the fact that at higher fluid velocities, mass transfer is facilitated and thus promoting precipitation of

FeCO_3 ; however shear stresses on the specimen surface are high enough as to impede nucleation of FeCO_3 . Hence, promoting precipitation of FeCO_3 elsewhere besides the specimen surface.

Figure 18 shows the SEM images of the 1000 rpm ($V_{eq} = 1.2 \text{ m/s}, 2 \text{ Pa}$) sample surface at two different magnifications. Similar to the 500 rpm ($V_{eq} = 0.6 \text{ m/s}, 0.8 \text{ Pa}$) sample surface, it can be observed that the relatively scarce FeCO_3 crystals are adhered to the sample surface. Most of what can be seen on the SEM image is an uncovered sample surface. **Figure 17**, as discussed previously, shows stable corrosion rate measurements which correlate to the sample surface shown on **Figure 18**, which shows poor coverage and/or protection from FeCO_3 crystals. This is a similar finding to that of the 500 rpm ($V_{eq} = 0.6 \text{ m/s}, 0.8 \text{ Pa}$) sample surface, but different from the stagnant sample. There was no evidence of plates on the sample surface.

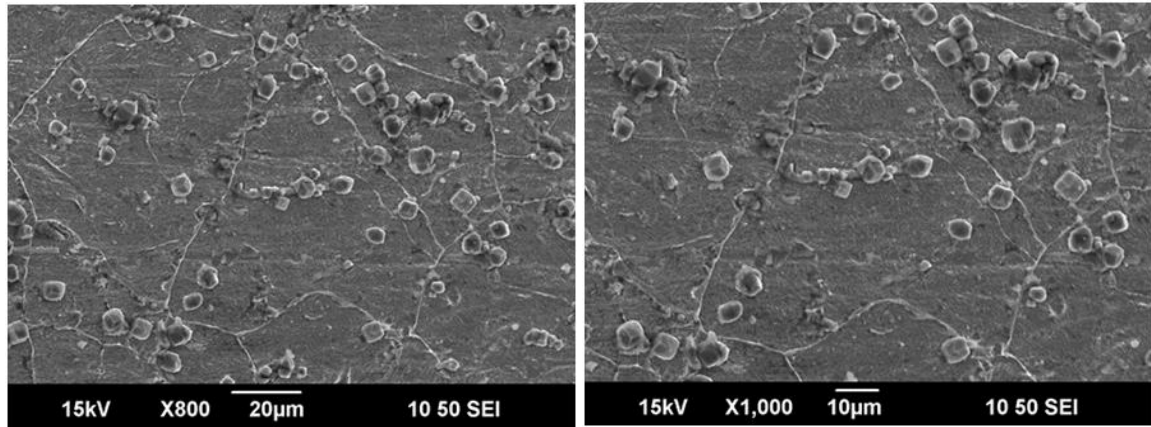


Figure 18. x800 and x1000 SEM images showing surface morphology for 1000 rpm ($V_{eq} = 1.2 \text{ m/s}, 2 \text{ Pa}$) experiment with pure Fe under the conditions: $T=80^{\circ}\text{C}$, $p\text{CO}_2 = 0.53 \text{ bar}$, initial pH 6.6, initial $S_{\text{FeCO}_3} \approx 150$

Figure 19 (a) shows the SEM image of the specimen surface that was used for EDS analysis; the area marker with a red border and labeled 1 is representative of the bare steel surface, the area labeled 2 in the area bounded by a red dashed border is representative of locations with FeCO_3 prisms. Area 2 cannot give an accurate EDS elemental analysis of the FeCO_3 prism. Instead, **Figure 19** (b) zooms into the red dashed area labeled 2 in **Figure 19** (a) to obtain better results of a single crystal from the EDS in order to determine if the characterization data is consistent with FeCO_3 .

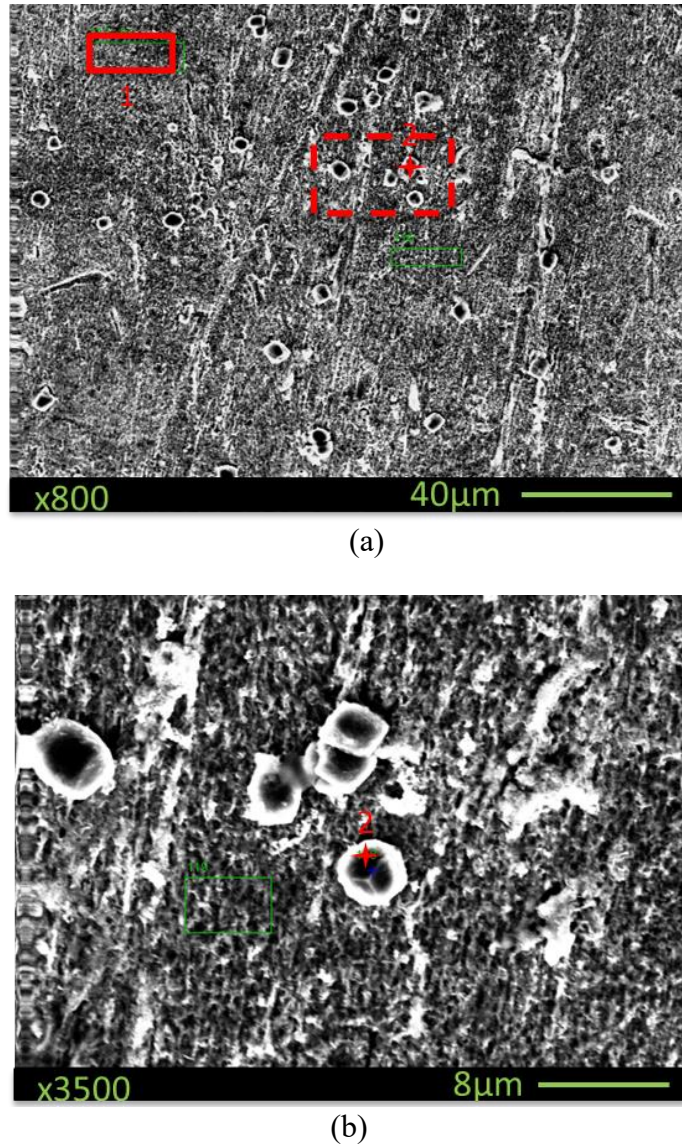


Figure 19. SEM showing areas used for EDS analysis showing surface morphology (a) x800 image of area 1 and point 2 (b) x3500 image of point 2 for 1000 rpm ($V_{eq} = 1.2$ m/s, 2 Pa) experiment with pure Fe surface under the conditions: $T=80^{\circ}\text{C}$, $p\text{CO}_2 = 0.53$ bar, initial pH 6.6, initial $S_{\text{FeCO}_3} \approx 150$

Figure 20 (a) confirms that there is no FeCO_3 in area 1, since there is no spectral peak for oxygen. **Figure 20** (b) does show an oxygen peak, which is higher in intensity than the adjacent carbon and iron peaks. This finding indicates that point 2 as shown in

Figure 19 (b) covers a FeCO₃ crystal, as has been shown in **Figure 8** and **Figure 14** for stagnant and 500 rpm ($V_{eq} = 0.6$ m/s, 0.8 Pa) experiments, respectively.

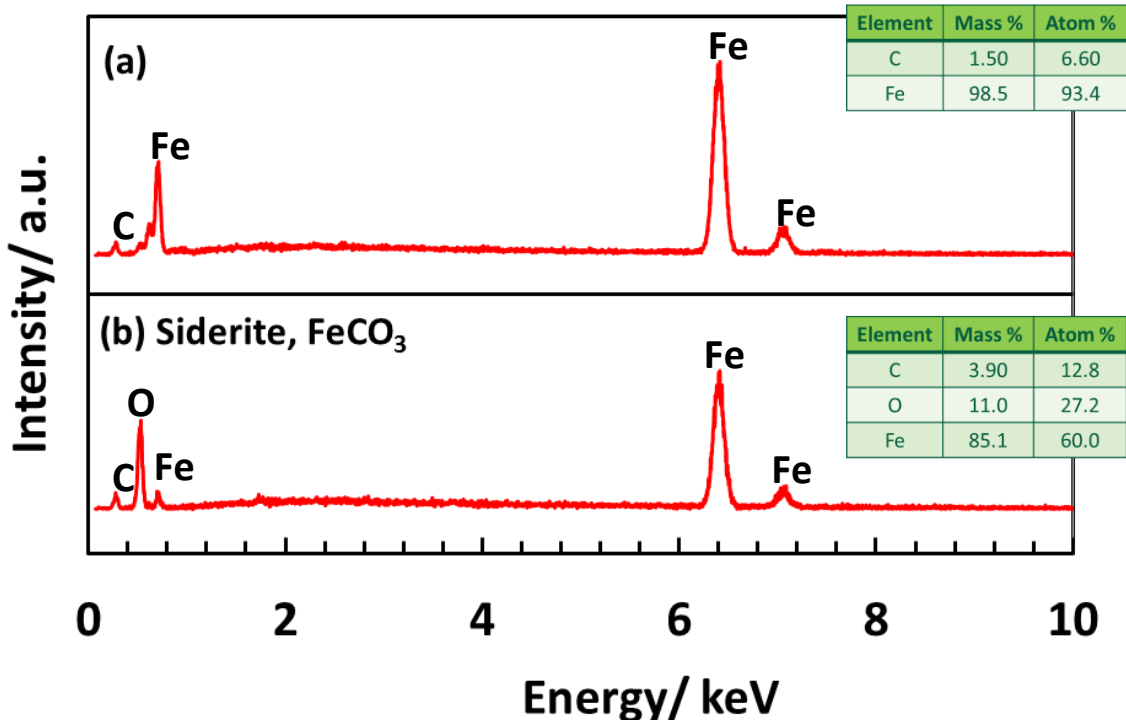


Figure 20. EDS spectra taken on 1000 rpm ($V_{eq} = 1.2$ m/s, 2 Pa) pure Fe surface (a) area 1 (b) point 2 shown in **Figure 19 (a)** and **Figure 19 (b)**, respectively

Elemental mapping on the specimen retrieved from the 1000 rpm ($V_{eq} = 1.2$ m/s, 2 Pa) test was performed by EDS, **Figure 21** showing the distribution of elements on the surface. It is noted that oxygen is only present in the FeCO₃ crystals, which is expected based on the EDS spectra shown in **Figure 20** (a) and (b). Oxygen could not be detected anywhere on the specimen, besides the FeCO₃ prisms. As in previous element mappings, carbon is distributed between the steel surface and FeCO₃ crystals. Iron is mostly present on the bare metal surface. Since oxygen represents the FeCO₃ prisms, it is an indicator of

coverage of the sample surface by corrosion product crystals. Based on this analogy, only *ca.* 3% of the specimen surface is covered by FeCO_3 .

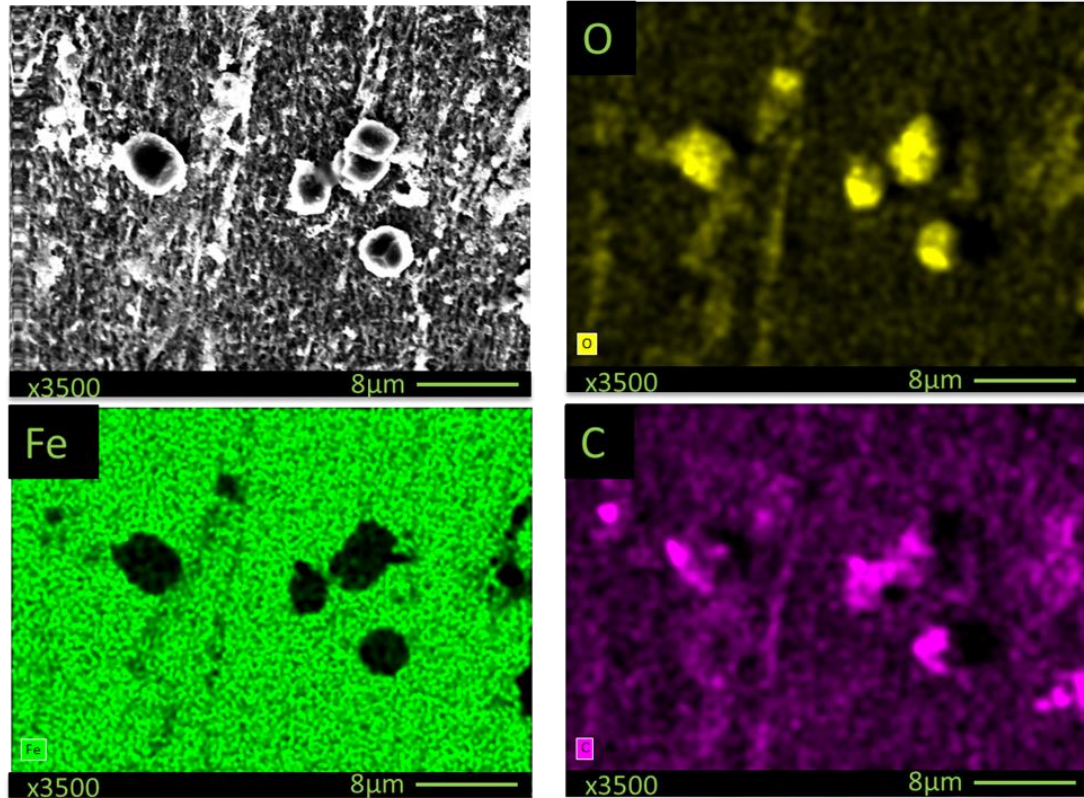


Figure 21. x3500 SEM image showing EDS elemental mapping for 1000 rpm ($V_{eq} = 1.2 \text{ m/s}$, 2 Pa) experiment with pure Fe under the conditions: $T=80^\circ\text{C}$, $p\text{CO}_2 = 0.53 \text{ bar}$, initial pH 6.6, initial $S_{\text{FeCO}_3} \approx 150$

Figure 22 shows the Raman spectra acquired for the 1000 rpm ($V_{eq} = 1.2 \text{ m/s}$, 2 Pa) sample surface. The characteristic peaks shown are that of siderite⁶⁷⁻⁶⁹. However, there is a broad peak at *ca.* 670 cm^{-1} , absent in **Figure 10** and **Figure 16**, for the stagnant and 500 rpm ($V_{eq} = 0.6 \text{ m/s}$, 0.8 Pa) specimens, respectively. It has been reported in the literature that the high excitation laser used for Raman analysis can cause oxidation of

samples; the peak at 670 cm^{-1} has been previously reported as magnetite, $\text{Fe}_3\text{O}_4^{69,72}$, as shown in **Figure 22**.

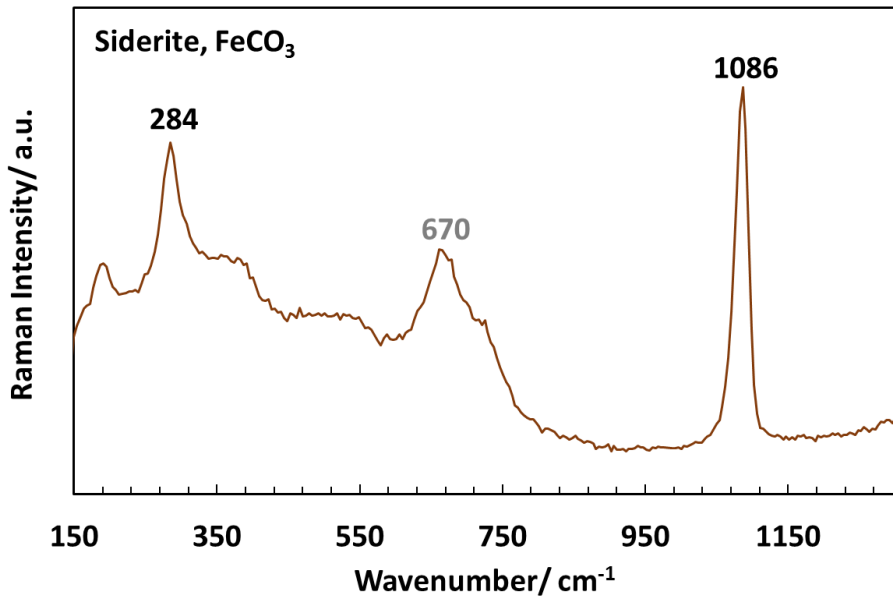


Figure 22. Raman spectra of 1000 rpm ($V_{eq} = 1.2\text{ m/s}, 2\text{ Pa}$) pure Fe surface confirming presence of FeCO_3 under the conditions: $T=80^\circ\text{C}$, $p\text{CO}_2 = 0.53\text{ bar}$, initial pH 6.6, initial $S_{\text{FeCO}_3} \approx 150$

4.1.2.4 2000 rpm, $V_{eq} = 2.0\text{ m/s} (7\text{ Pa})$

Figure 23 displays a plot of measured LPR corrosion rates taken every hour for the duration of the experiment at a constant rotational speed of 2000 rpm ($V_{eq} = 2.0\text{ m/s}, 7\text{ Pa}$). Corrosion rate values are plotted on the left axis and saturation values on the right axis. Similarly, the initial corrosion rate is compared to what FREECORP 2.0 predicts under the same environmental conditions. Compared to previous rotational speeds, the 2000 rpm ($V_{eq} = 2.0\text{ m/s}, 7\text{ Pa}$) condition shows the most difference between what FREECORP 2.0

predicts versus the LPR obtained corrosion rate measurement, *ca.* 2.0 mm/yr, a cause of the high purity iron⁷⁰ and higher flow velocities⁷¹.

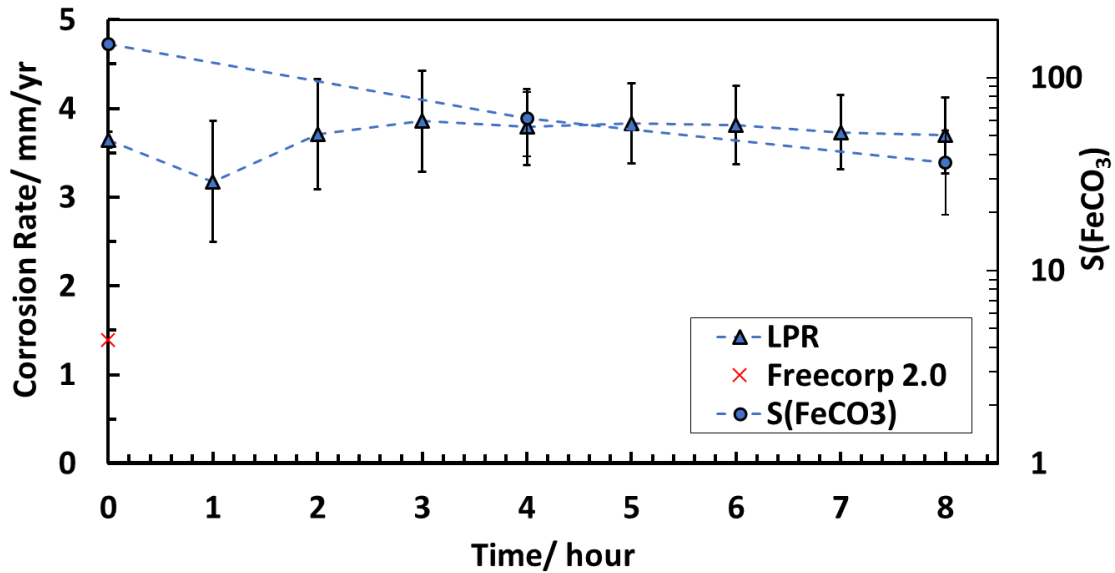


Figure 23. Comparison of LPR corrosion rates, predicted initial FREECORP 2.0 and saturation of FeCO₃ over time for 2000 rpm ($V_{eq} = 2.0$ m/s, 7 Pa) experiment with pure Fe under the conditions: T=80°C, pCO₂ = 0.53 bar, initial pH 6.6, initial S_{FeCO₃} ≈ 150

Figure 23 shows the highest initial corrosion rate compared to those at lower speeds and stagnant conditions, as shown in **Figure 5**, **Figure 11**, and **Figure 17**, in order of increasing rotational speed. The corrosion rate of the 2000 rpm ($V_{eq} = 2.0$ m/s, 7 Pa) trials is about 2 mm/yr higher than the stagnant condition. Correspondingly, it can be reported that the LPR corrosion rate measurements are stable for the entire experiment, which is true for all non-stagnant conditions. **Figure 23** also plots saturation values and it is noted that these drop significantly from the value at the beginning of the experiment, which is also the case for experiments at 1000 rpm conditions, as shown in **Figure 17**.

Figure 24 shows SEM images of the 2000 rpm ($V_{eq} = 2.0$ m/s, 7 Pa) sample surface at two different magnifications. It can be observed that there are no FeCO_3 crystals precipitated on the sample surface. This is true for the entire sample surface. The fact that FeCO_3 did not form on the surface of the sample, agrees with the stable LPR corrosion rate measurements shown in **Figure 23**.

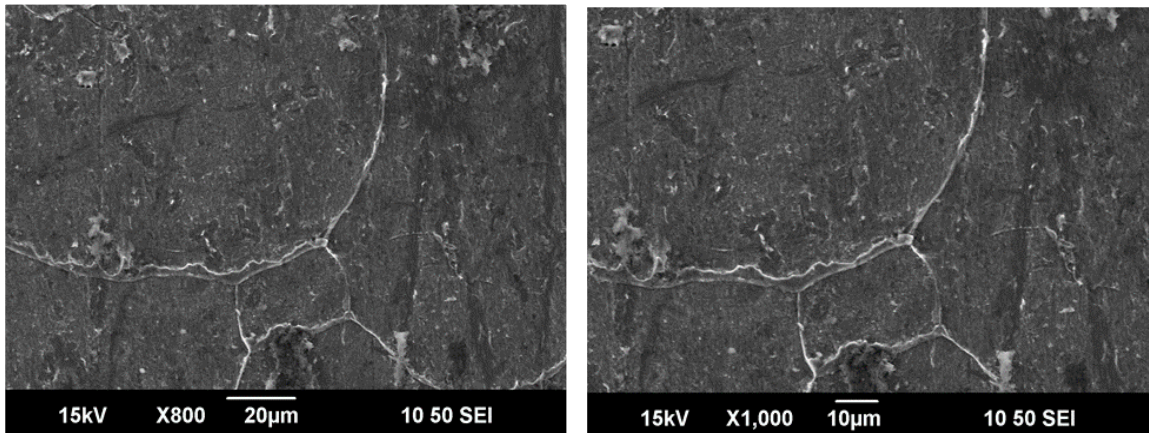


Figure 24. x800 and x1000 SEM images showing surface morphology for 2000 rpm ($V_{eq} = 2.0$ m/s, 7 Pa) experiment with pure Fe under the conditions: $T=80^{\circ}\text{C}$, $p\text{CO}_2 = 0.53$ bar, initial pH 6.6, initial $S_{\text{FeCO}_3} \approx 150$

Figure 25 shows the SEM image of the specimen surface that was used for EDS analysis, and highlights the red area labelled 1 to indicate the area selected for elemental analysis.

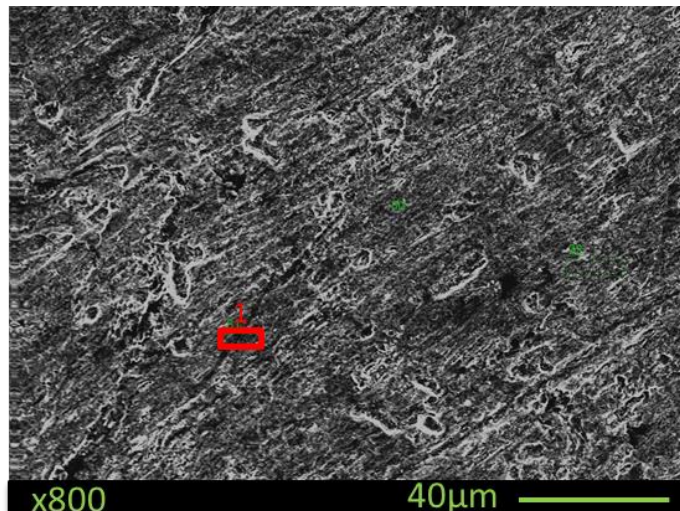


Figure 25. x800 SEM image showing areas used for EDS analysis showing surface morphology for 2000 rpm ($V_{eq} = 2.0$ m/s, 7 Pa) experiment with pure Fe surface under the conditions: T=80°C, pCO₂ = 0.53 bar, initial pH 6.6, initial S_{FeCO₃} ≈ 150

Figure 26 is indicative of the absence of FeCO₃ prisms since there is no spectral peak for oxygen. The EDS spectra shows that there are some impurities present in the pure iron (99.8%) indicated by the presence of a low concentration of nickel.

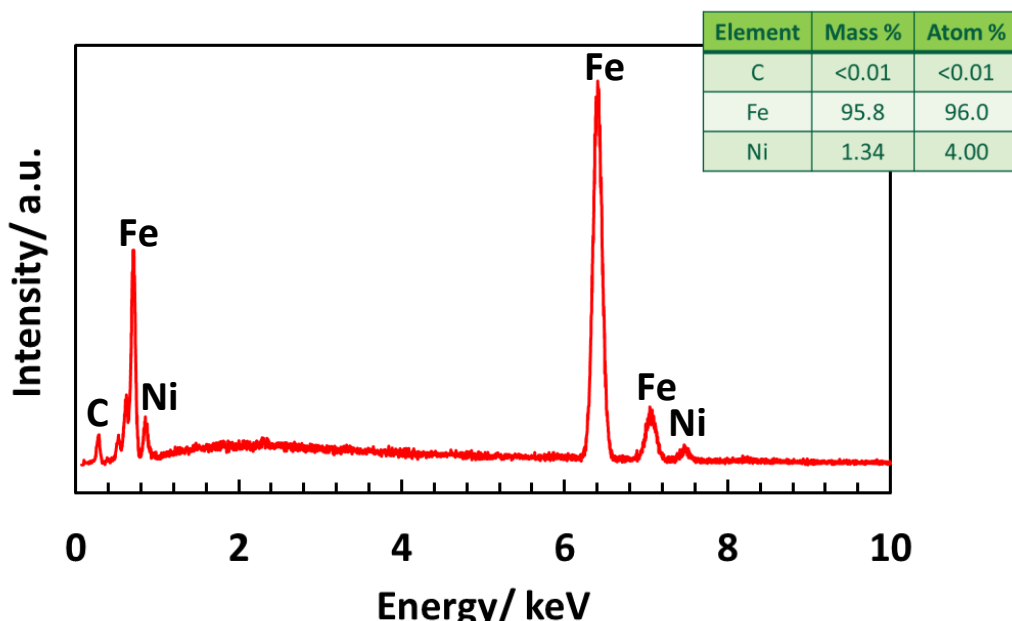


Figure 26. EDS spectrum taken on 2000 rpm ($V_{eq} = 2.0$ m/s, 0.8 Pa) pure Fe surface at area 1 shown in **Figure 25**

Figure 27 shows elemental mapping performed on the SEM image shown in **Figure 25**. **Figure 27** shows that all elements shown in the EDS spectra in **Figure 26** are evenly distributed on the sample surface. However, the nature of the presence of nickel and carbon may be misleading. By just looking at this elemental mapping based on color intensity, it seems as if there were the same amount of nickel, carbon and iron on the material surface, which is false. The mass content of the surface is given by the mass percentage content as shown in **Figure 26**. As stated previously, an intense oxygen peak and high mass % content is indicative of FeCO_3 formation. Since there was no presence of oxygen in this EDS analysis, it can be deduced that no FeCO_3 crystals formed on the specimen surface.

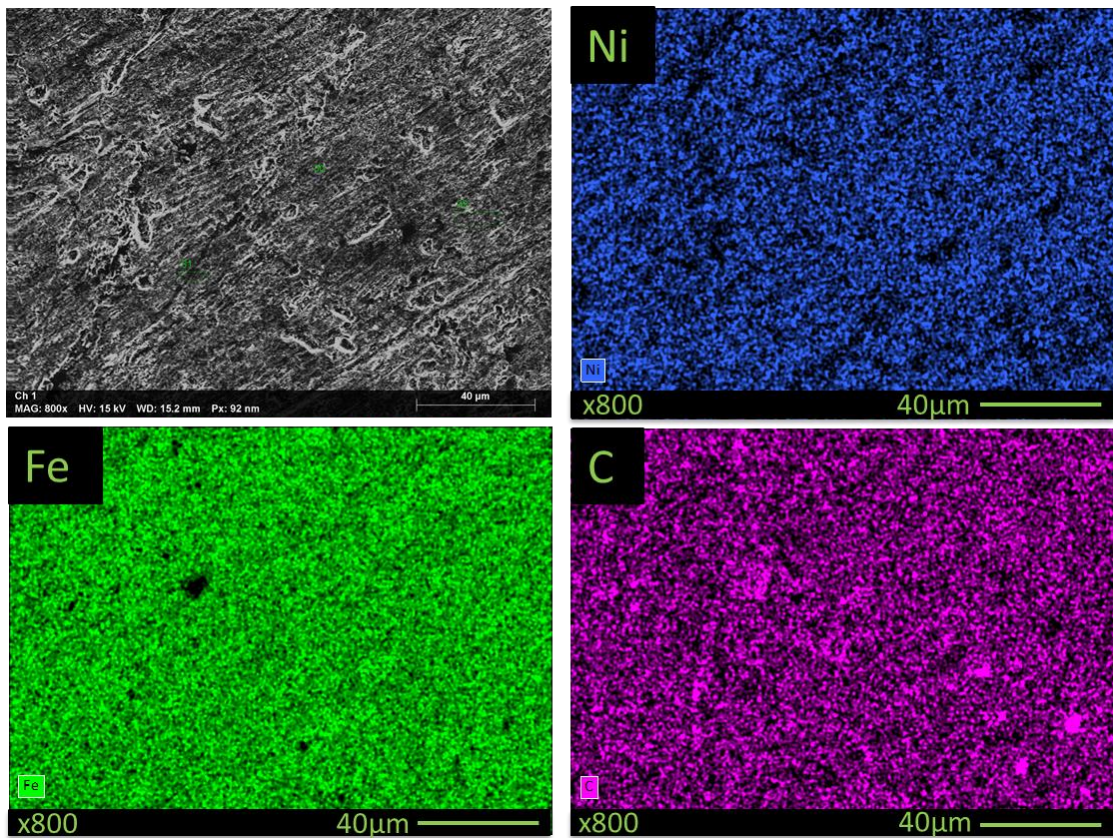


Figure 27. x800 SEM image showing EDS elemental mapping for 2000 rpm ($V_{eq} = 2.0$ m/s, 7 Pa) experiment with pure Fe under the conditions: $T=80^{\circ}\text{C}$, $\text{pCO}_2 = 0.53$ bar, initial pH 6.6, initial $S_{\text{FeCO}_3} \approx 150$

Raman analysis performed on the specimen surface, as shown in **Figure 28**, was done in order to further confirm the presence of corrosion products on the specimen surface. There is a broad band shown in the Raman spectra with a peak at *ca.* 670 cm^{-1} . This peak corresponds to magnetite, Fe_3O_4 , and may be an artefact of oxidation of specimens during local heating (caused by the laser used in the Raman spectroscopy technique)^{69,72}. There is an additional peak at 486 cm^{-1} , which has been associated with maghemite ($\gamma\text{-Fe}_2\text{O}_3$)⁶⁹, also a result of heating/oxidizing the sample.

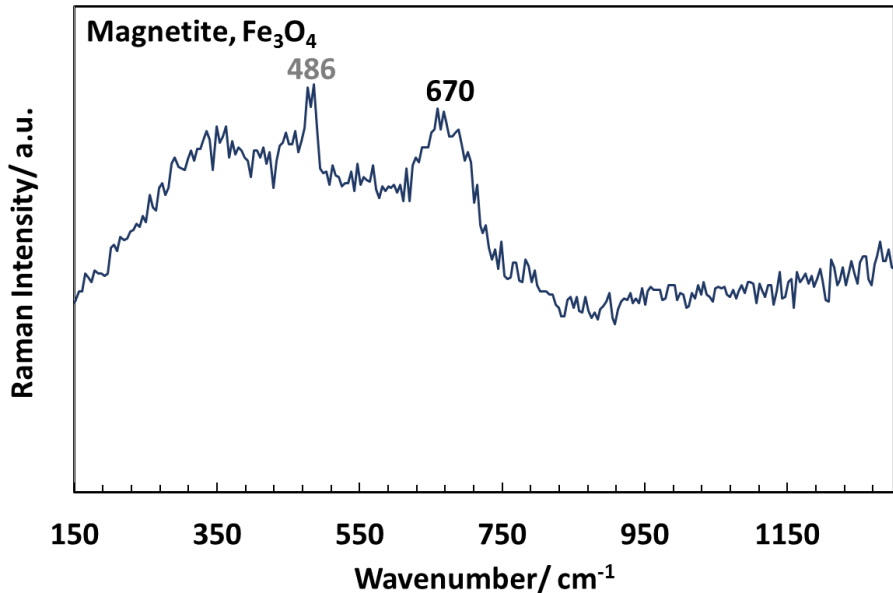


Figure 28. Raman spectra of 2000 rpm ($V_{eq} = 2.0 \text{ m/s}$, 7 Pa) pure Fe surface under the conditions: $T=80^{\circ}\text{C}$, $p\text{CO}_2 = 0.53 \text{ bar}$, initial pH 6.6, initial $S_{\text{FeCO}_3} \approx 150$

4.1.3 Summary

By plotting average LPR corrosion rate measurements for all velocities, it was noted that the initial corrosion rate increased as the rotational speed increased. This is shown in **Figure 29**. However, in these conditions (pH of 6.6, temperature of 80°C and $p\text{CO}_2$ of 0.53 bar), the corrosion mechanism should be under charge transfer control and consequently the initial corrosion rate should be relatively insensitive to flow. This discrepancy between the experimental results and the expected behavior is postulated to be related to shear stress, which in some cases could be high enough to detach the corrosion products from the steel surface³⁰. It can also be seen that the only specimen that reached a low stable corrosion rate was the stagnant specimen since, as the rotational speed increased, fewer FeCO_3 prisms were detected. In addition, the CO_2 corrosion mechanisms have been

determined using mostly steel samples and it is also possible that pure iron displays some unique characteristics due to its specific microstructure.

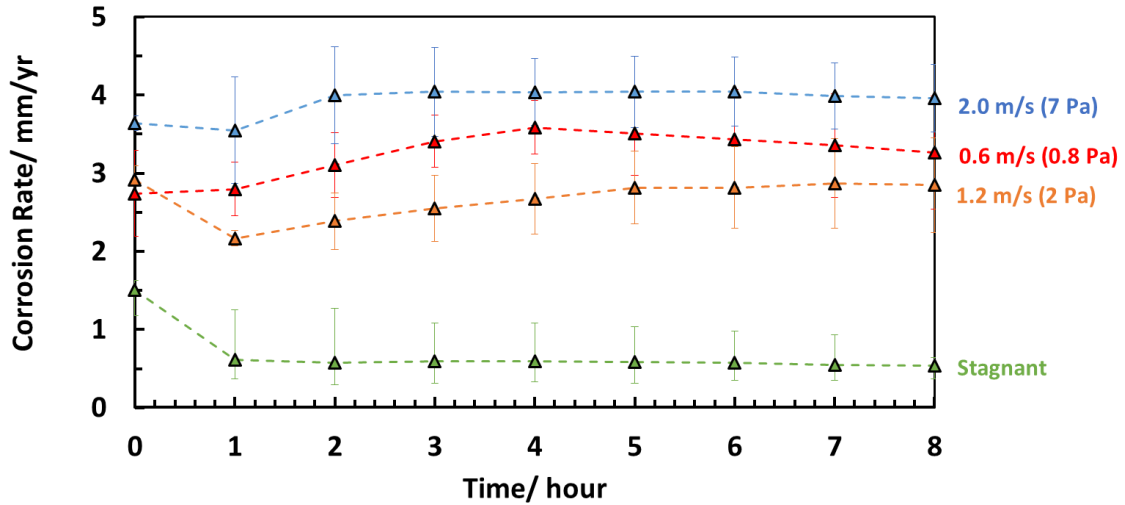


Figure 29. Comparison of LPR corrosion rates over time for stagnant, 500 rpm ($V_{eq} = 0.6 \text{ m/s}, 0.8 \text{ Pa}$), 1000 rpm ($V_{eq} = 1.2 \text{ m/s}, 2 \text{ Pa}$), and 2000 rpm ($V_{eq} = 2.0 \text{ m/s}, 7 \text{ Pa}$) experiments with pure Fe under the conditions: $T=80^{\circ}\text{C}$, $p\text{CO}_2 = 0.53 \text{ bar}$, initial pH 6.6, initial $S_{\text{FeCO}_3} \approx 150$

Additionally, as the rotational speed increased, the saturation value at the end of the experiment decreased, as shown in **Figure 30**. FeCO_3 could have precipitated somewhere else in the glass cell and not on the surface of the sample, since no other form of mixing occurred in the electrolyte, besides the RCE. The higher rotational speed promotes transport of ionic species (concentration gradient is not as pronounced as in stagnant or lower rotational speeds) and thus FeCO_3 precipitation.

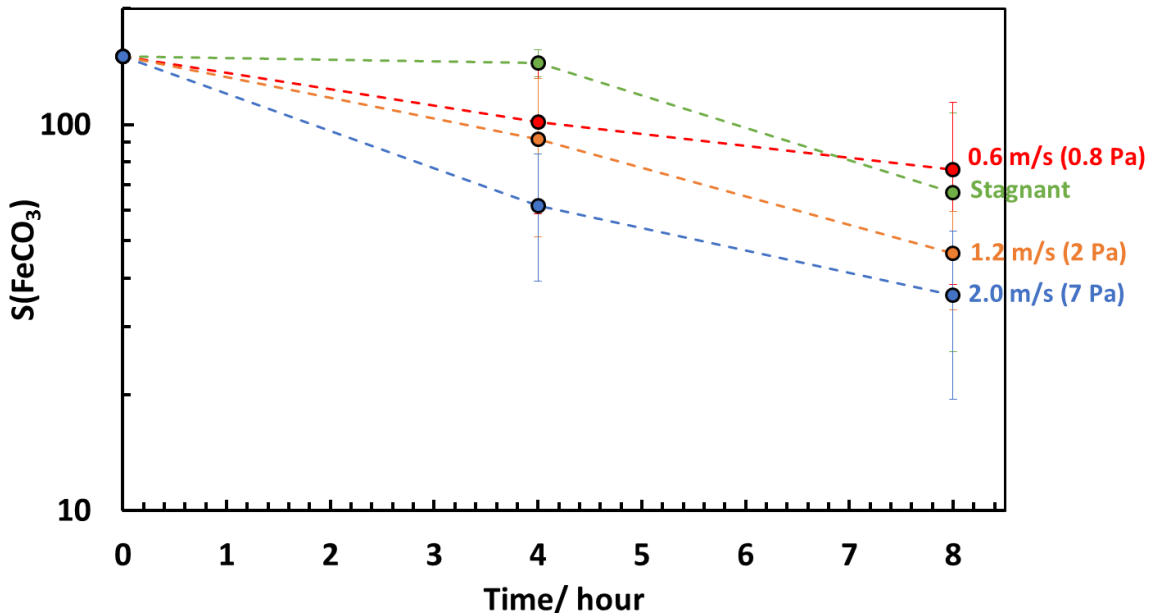


Figure 30. Comparison of average saturation of $FeCO_3$ values over time for stagnant, 500 rpm ($V_{eq} = 0.6$ m/s, 0.8 Pa), 1000 rpm ($V_{eq} = 1.2$ m/s, 2 Pa), and 2000 rpm ($V_{eq} = 2.0$ m/s, 7 Pa) experiments with pure Fe under the conditions: $T=80^{\circ}C$, $pCO_2 = 0.53$ bar, initial pH 6.6, initial $S_{FeCO_3} \approx 150$

The scaling tendency was also calculated for all velocities based on the final corrosion rate immediately before the sample was taken out of solution, using measured masses of the corrosion product layer. **Figure 31** shows a plot of scaling tendency (calculated from equation (17)), final corrosion rates of all experiments in mm per year and FREECORP 2.0 corrosion rate predictions. **Figure 31** also shows that the scaling tendency decreased as the rotational speed increased, which indicated that precipitation of $FeCO_3$ was unlikely at higher rotational speeds. This coincides with the experimental results, where there was no $FeCO_3$ precipitation at the highest velocity tested.

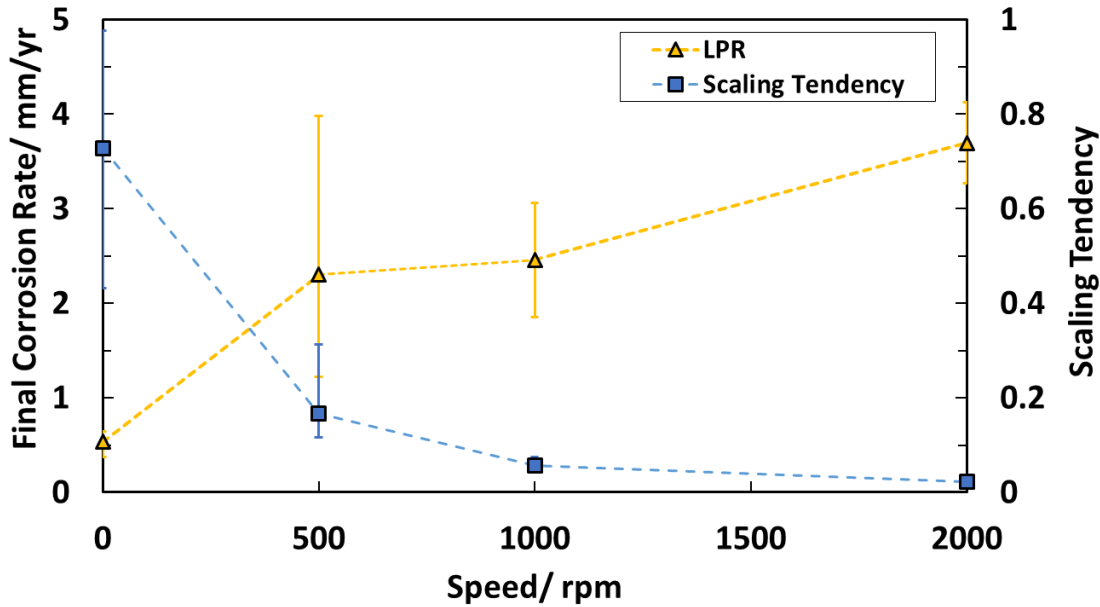


Figure 31. Comparison of scaling tendency, final LPR corrosion rate, and FREECORP 2.0 after 8 hours for stagnant, 500 rpm ($V_{eq} = 0.6$ m/s, 0.8 Pa), 1000 rpm ($V_{eq} = 1.2$ m/s, 2 Pa), and 2000 rpm ($V_{eq} = 2.0$ m/s, 7 Pa) experiments with pure Fe under the conditions: $T=80^{\circ}\text{C}$, $\text{pCO}_2 = 0.53$ bar, initial pH 6.6, initial $S_{\text{FeCO}_3} \approx 150$

It was found that a critical velocity exists above which there no formation of FeCO_3 on the specimen surface and corrosion rates remained high. These findings were obtained using a conventional three electrode glass cell setup with an RCE. The next section focuses on the combined effect of flow and steel microstructure and utilizes a different experimental setup. When different laboratory systems, it is important to make sure that the results are not “setup dependent” and that similar findings are obtained when similar experimental conditions are run. Consequently, the first experiment of the next test series only aimed at ensuring proper reproducibility of conditions and results. This was done by considering an equivalent pipeline velocity of 0.6 m/s (0.8 Pa) in the new setup discussed in section 4.2.

4.2 Task #2: Study of the Effect of Microstructure on FeCO₃ Nucleation and Retention

The aim of this set of experiments is to identify how Fe₃C and material microstructure aid in the precipitation of FeCO₃ when the source of ferrous ions comes from the metal.

4.2.1 Methodology

This set of experiments was performed using the experimental setup shown in **Figure 32**. The advantages of this setup, shown in **Figure 32**, over the setup described in Task #1 (**Figure 3**) are presented in the next section. Tests were conducted at two impeller velocities, expressed as rotations per minute (rpm), with a low initial saturation value of *ca.* 10 with respect to FeCO₃. In this set of experiments, the source of the ferrous ions is from the metal, *i.e.*, associated with the corrosion rate. Four different materials and/or microstructures were tested, namely pure iron, API 5L X65, a ferritic-pearlitic UNS G10180, and a tempered martensite UNS G10180. This facilitated testing the effect of microstructure and carbon content in flowing conditions. **Table 5** summarizes all of the experimentation parameters in the form of a test matrix and will be further described in the following sections. The environmental conditions selected ensure optimal corrosion product layer forming conditions, based on the literature review and analyses performed. Additionally, the water chemistry is controlled in these experimentation in order to better mimic field conditions. In small volume setups, such as a 2 L glass cell, large fluctuations in water chemistry can occur, and do not necessarily reflect field conditions.

Appendix 3: Water Chemistry with No Ferrous Iron Control shows fluctuations in ferrous iron concentration when the water chemistry is not controlled. Four materials were tested at two different flow velocities. In order to ensure accuracy of results, some experiments were repeated to ensure reproducibility.

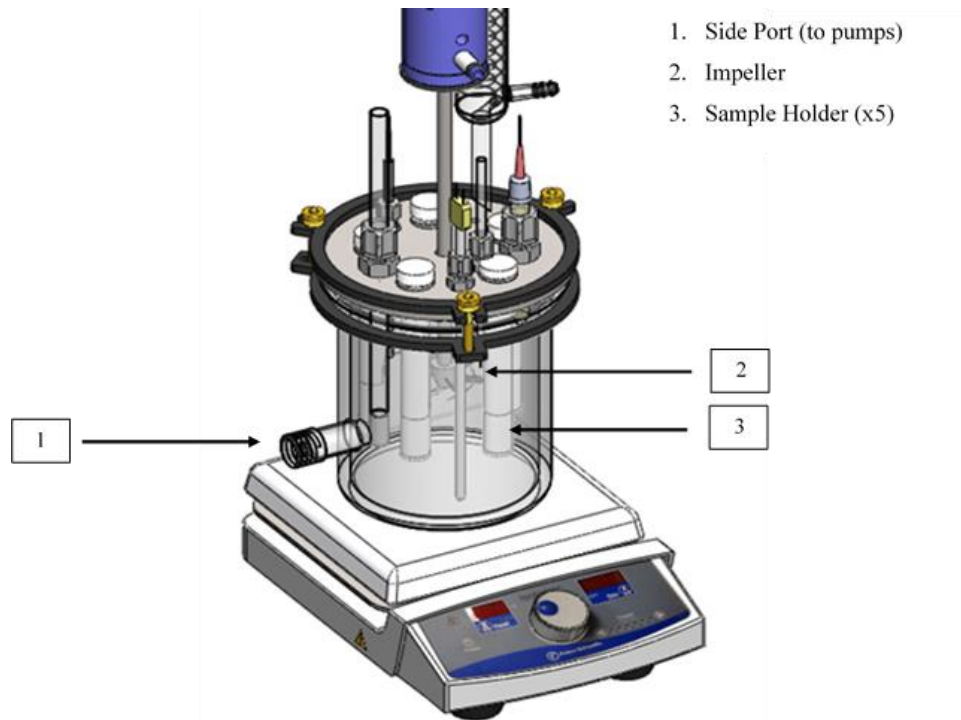


Figure 32. Experimental setup of 2 L glass cell using impeller (image courtesy of Cody Shafer, ICMT)

Table 5. Test matrix for task # 2: study of the effect of microstructure on FeCO₃ nucleation and retention

Materials	Pure Fe (99.8%)	
	UNS G10180 ferritic-pearlitic	
	UNS G10180 tempered martensite	
	API 5L X65 ferritic with Fe ₃ C precipitates	
Flow Velocities	Impeller velocity (rpm)	Equivalent velocity in 25.5 cm ID pipe (m/s)
	150	0.4
	250	0.6
Shear Stress (Pa)	0.3 (150 rpm) and 0.5 (250 rpm)	
Experimental Setup	2 L Glass cell	
Electrolyte	1 wt.% NaCl	
pH	6.6 ± 0.03	
Temperature (°C)	80	
Total Pressure (bar)	1.0	
CO ₂ Partial Pressure (bar)	0.53	
[Fe ²⁺] (ppm)	1-6	
Saturation w.r.t. FeCO ₃	10 – 30	
Electrochemical Measurements	LPR ±5 mV vs. EOC, 0.125 mV/s B = 26 mV/decade EIS 0 mV vs. EOC, Frequency range: 5000- 0.1 Hz.	
Surface Analysis	SEM EDS XRD Cross-section	

4.2.1.1 Experimental Setup

The experimental system used for these experiments was also a three-electrode electrochemical 2 L glass cell, as described in relation to the methodology for objective 1. However, the system was improved by eliminating centrifugal and centripetal forces found in an RCE by employing a controlled mass transfer setup, as well as the advantage of having multiple specimens in one experiment allowing for further analysis. This new system was designed to hold five flat metal samples (labeled 3 in **Figure 32**) at a fixed height and distance from the impeller, located in the center of the glass cell (labeled 2 in **Figure 32**), ensuring turbulent conditions with controlled mass transfer. Additional views of how the impeller and sample holders are located in the glass cell are shown in **Figure 33**. Moreover, stable solution chemistry was implemented using a setup that consisted of two pumps used to run electrolyte through an H-ion exchange resin and a Na-ion exchange resin, controlling the pH and ferrous ion concentration, respectively. The electrolyte flowed out of the solution through a side port located at the bottom of the glass cell (labeled 1 in **Figure 32**). The stable solution chemistry setup is shown in **Figure 34**.

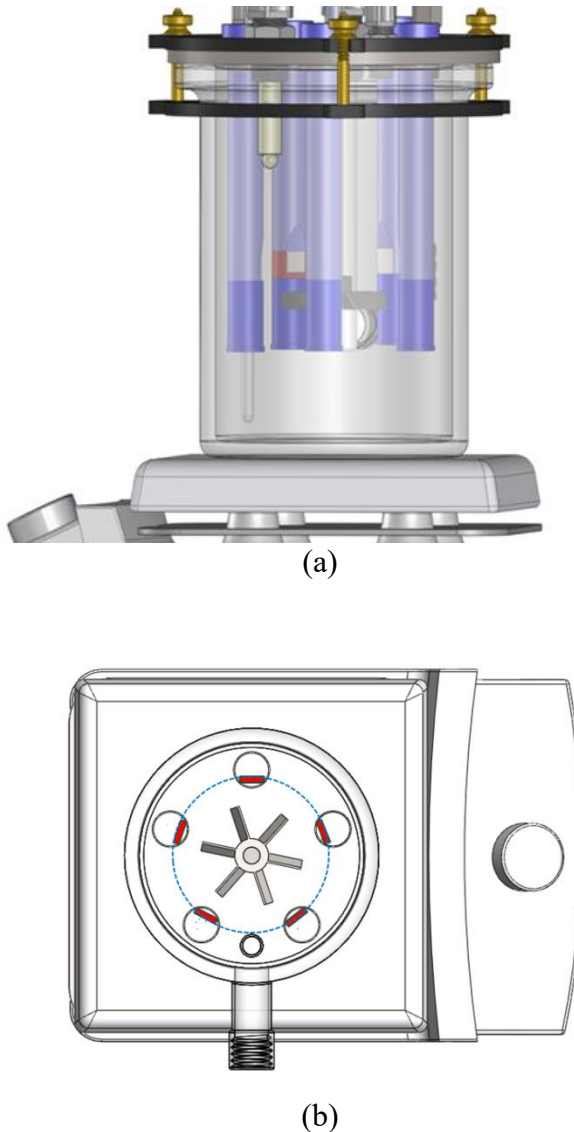


Figure 33. Experimental setup of 2 L glass cell with controlled mass-transfer system (a) side view and (b) top view (images courtesy of Cody Shafer, ICMT)

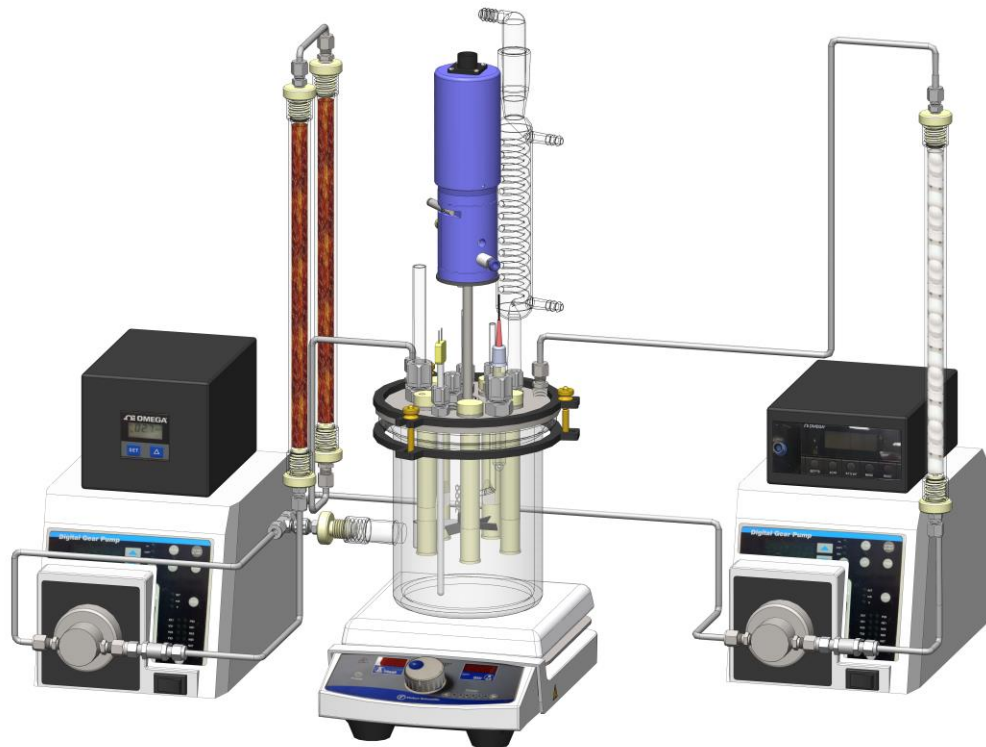


Figure 34. Stable solution chemistry setup (image courtesy of Cody Shafer, ICMT)

Figure 34 depicts how two pumps are used to run electrolyte through the H-ion exchange resin and the Na-ion exchange resin. The electrolyte runs through the H-ion exchange resin column when the bulk pH of the solution is above 6.62. Also, the electrolyte can run simultaneously through the Na-ion exchange resin columns to control the ferrous ion concentration in solution. Since there is no *in situ* technique to measure ferrous ion concentration in solution, a timer was used instead to turn the pump on and off. Based on preliminary results⁷³, it was found that the ferrous ion concentration was best controlled when the pump is on for 20 minutes and off for 10 minutes. The flow rate of the electrolyte running through the Na-ion exchange resin columns was approximately 4 mL per minute. The electrolyte used in this set of experiments was a 1 wt.% NaCl aqueous solution, such

as the one described for fulfillment of objective 1. It was prepared following the same procedure and sparged with CO₂ gas for at least two hours. The ion exchange resin columns were also sparged during this time to avoid any oxygen contamination. After all of this was done, temperature was raised slowly (15°C every 20 minutes) to 80°C using the hotplate. The total pressure of the system was 1 bar since it was an open system and the partial pressure of CO₂ was 0.53 bar once temperature reached 80°C. A temperature compensated pH meter was used to monitor the bulk pH of the solution at all times. The pH was initially set to pH and adjusted accordingly by injecting deoxygenated hydrochloric acid (HCl) or sodium bicarbonate (NaHCO₃) to decrease or increase the solution pH, respectively. The temperature was continuously monitored during the course of the experiments. The pH was also measured throughout the experiment, but it did not require adjustment as the pump running solution through the H-ion exchange resin turned on when the pH reached a value above 6.62.

Five samples were used, four for weight loss/surface/cross-sectional analyses, and one for electrochemical measurements. **Figure 35** shows how both electrochemical and weight loss samples are mounted on the specimen holders.

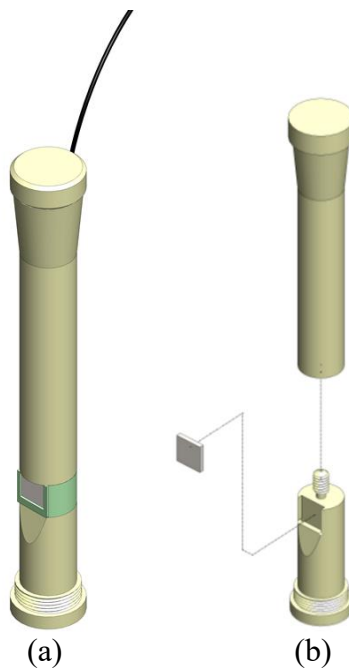


Figure 35. Specimen holders (a) electrochemical sample (b) removable weight loss sample (images courtesy of Cody Shafer, ICMT)

Prior to immersing specimen holders with weight loss samples mounted, the back and the sides of the samples were coated with Xylan® coating to avoid any corrosion at the sides of the specimens. Dimensions were taken in order to calculate surface areas of test specimens, necessary for appropriate corrosion rate measurements; surface areas ranged from $1.3 - 1.4 \text{ cm}^2$. Gravimetric measurements facilitated calculation of specimen weight loss at the conclusion of experiments. Specimens were wet-polished with silicon carbide abrasive paper up to 600 grit in order to ensure uniform preparation, *i.e.*, surface characteristics, prior to the start of experiments; this included rinsing with isopropyl alcohol and use of ultrasonication to remove any residue from the specimen surfaces. Samples were dried with cold air before being mounted into their respective specimen holders, as shown in **Figure 35** (a). For the specimen used for electrochemical measurements, a cable was soldered to its back prior to placement in an epoxy mold; this

permitted connection to a potentiostat. The mold is filled with an epoxy mixture to avoid any liquid entrainment therein that could damage the cable soldered to the sample; this assembly is depicted in **Figure 35** (b).

4.2.1.2 Water Chemistry

Aqueous FeCl₂ was injected into the solution after the first LPR measurements were conducted, which gave a repeatable initial corrosion rate, in order to reach the desired starting ferrous ion concentration of 2 ppm. The deoxygenated aqueous FeCl₂ was prepared by dissolving 1.8 grams of ferrous chloride tetrahydrate (FeCl₂·4H₂O) in 50 mL solution of deionized water sparged with nitrogen gas (N₂) for 30 minutes (oxygen free solution). After this solution was prepared, 0.4 mL was added into the glass cell using a syringe. By following this procedure, the saturation of the solution was 10; according to equation (15). Aqueous ferrous ion concentrations were measured spectrophotometrically, at appropriate time intervals, during the course of the experiments.

4.2.1.3 Electrochemical Measurements

Electrochemical measurements for this set of experiments were taken following the same procedure used to fulfill task #1 in section 4.

4.2.1.4 Flow Velocities

Since the geometry of this experimental setup is different from the typical RCE used in objective 1, a mass transfer characterization must be done in order to understand flow geometry and hydrodynamics when using an impeller. The impeller geometry is shown in **Figure 36**, the type depicted is commonly known as a pitched blade turbine

impeller. The mass transfer coefficients were successfully determined by Iteamsupapong⁷⁴ using ferro/ferrocyanide experiments for this exact impeller geometry.

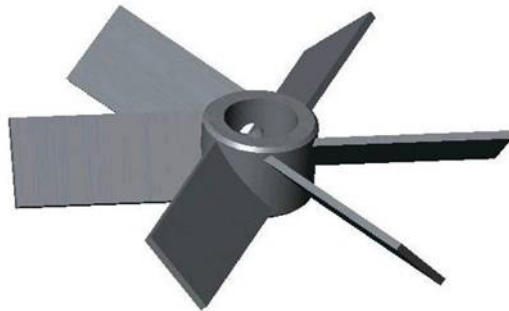
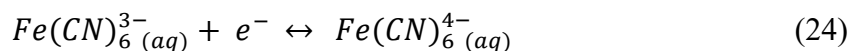


Figure 36. Pitched blade turbine impeller geometry (image courtesy of Cody Shafer, ICMT)

Iteamsupapong⁷⁴ used the ferri/ferrocyanide coupled electrochemical reaction to quantify the mass transfer coefficients. This method is commonly used to determine mass transfer coefficients in flowing environments with varying flow geometries⁶³. The following electrochemical reaction was utilized, equation (24):



Potentiodynamic sweeps were conducted in an electrolyte consisting of an equimolar mixture of ferrocyanide trihydrate ($K_4Fe(CN)_6 \cdot 3H_2O$) and potassium hydroxide (KOH) at 22°C⁷⁴. Limiting current densities were recorded at various impeller rotation speeds, facilitating determination of mass transfer coefficients. The cathodic potentiodynamic sweeps at various velocities are shown in **Figure 37**, as tested by Iteamsupapong⁷⁴. **Figure 38** shows a comparison of the limiting current densities of RCE current densities and impeller current densities⁶³. It can be seen from **Figure 38** that it takes twice the speed for

a RCE than an impeller to obtain the same current density. The empirical mass transfer correlation, equation (25), describes the flow hydrodynamics for this impeller-based glass cell setup⁷⁴:

$$Sh = 0.22Re^{0.6}Sc^{0.3} \quad (25)$$

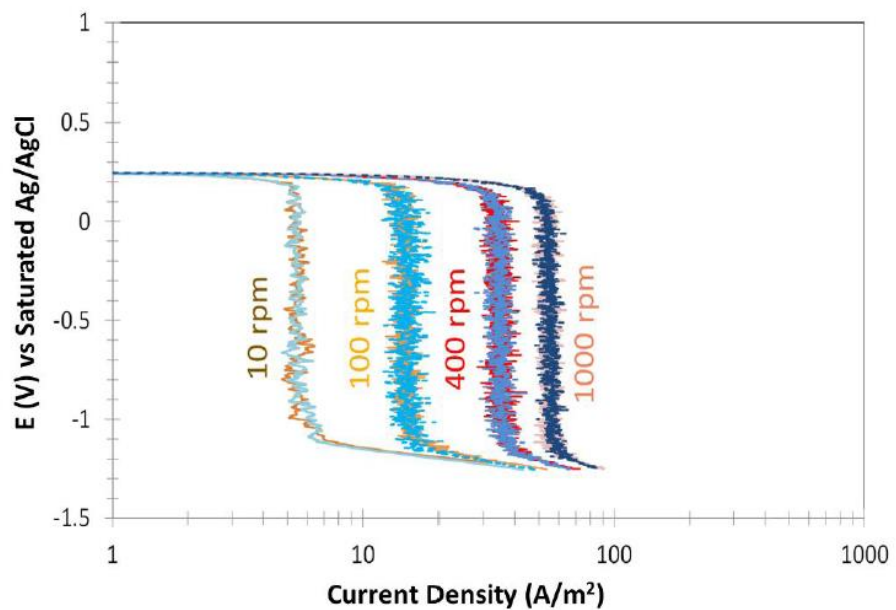


Figure 37. Cathodic potentiodynamic sweeps showing limiting currents for various impeller rotational velocities⁷⁴

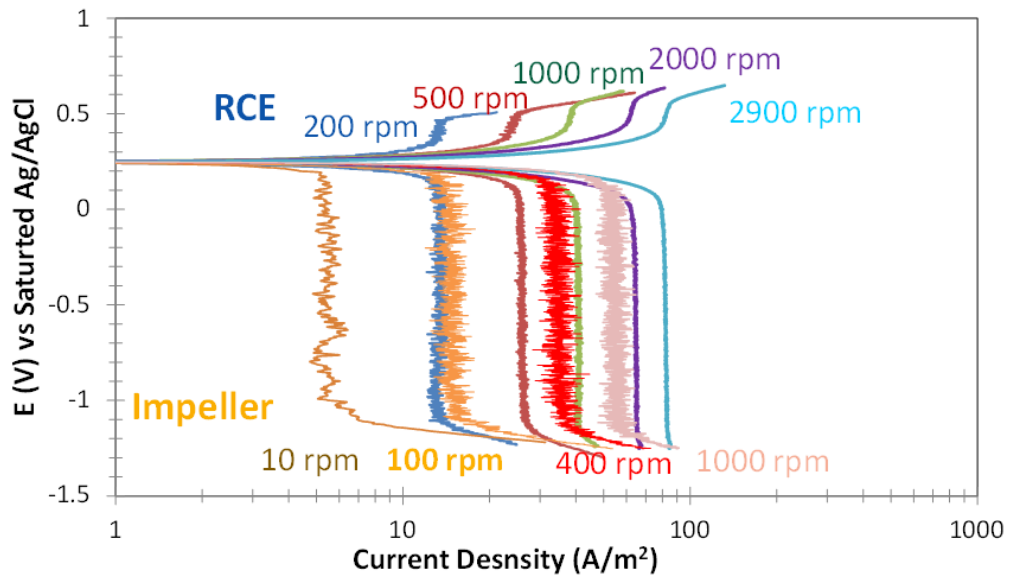


Figure 38. Current density comparison between rotating cylinder shaft and impeller⁷⁴

Table 6 summarizes the impeller rotation speeds chosen for this set of experiments, as well as the equivalent velocity in a 25.5 cm ID pipe calculated by using the empirical mass transfer correlation, shown in equation (25) and the wall shear stresses calculated via ANSYS simulations (simulations shown in Appendix 4: Flow Simulations of Impeller Setup

Table 6. Summary of impeller rotational speeds and corresponding pipe fluid velocities and wall shear stresses

Impeller Rotational Speed (rpm)	V_{eq} , Equivalent Velocity in 25.5 cm ID pipe (m/s)	Wall Shear Stress (Pa)
150	0.4	0.3
250	0.6	0.5

4.2.1.5 Material Composition

The materials used in this set of experiments include pure Fe (Surepure Chemetals, 99.8%), API 5L X65 and UNS G10180. Additionally, the same base material with different microstructures, derived associated with particular heat treatments of UNS G10180 was utilized. The as-received UNS G10180 has a ferritic-pearlitic microstructure that, by appropriate thermal treatment underwent the required phase transformations to yield a tempered martensite. Likewise, since the as-received API 5L X65 has a much smaller grain size than the as-received UNS G10180, the API 5L X65 samples had to undergo an annealing process to increase the grain size of the material; and obtain a similar grain size between UNS G10180 and API 5L X65 for more direct comparison. If grain size is varied across the materials tested in this procedure, it can pose an effect on the corrosion behavior as previous studies have shown that a decrease in grain size can affect corrosion behavior⁷⁵.

Table 7 and **Table 8** show the chemical compositions of the materials used in these experiments for API 5L X65 and UNS G10180, respectively, determined by Direct Reading Atomic Emission Spectroscopy (AES).

Table 7. Chemical composition of API 5L X65 (wt.%)

API 5L X65 mild steel (balance Fe)						
C	Mn	Nb	P	S	Ti	V
0.05	1.51	0.03	0.004	<0.001	0.01	0.04

Table 8. Chemical composition of UNS G10180 steel (wt.%)

UNS G10180 (balance Fe)										
Al	As	C	Co	Cr	Cu	Mn	Mo	Nb	Ni	
0.008	0.006	0.18	0.003	0.12	0.18	0.75	0.020	0.002	0.065	
P	S	Sb	Si	Sn	Ti	V	W	Zn	Zr	
0.011	0.021	0.009	0.16	0.009	0.002	0.003	0.014	0.004	0.003	

4.2.1.6 Heat Treatment of Steels

The as-received UNS G10180 has a ferritic-pearlitic microstructure, verified by microscopic characterization after specimen grinding, polishing and etching (with 2% Nital [ethanolic HNO₃]). The microstructure of the as-received sample is shown in **Figure 39**, as an optical micrograph, and in **Figure 40**, as a SEM image. **Figure 40** clearly shows the pearlite colonies, where the cementite, Fe₃C, is shown as thin lamellae. By using the grain size intercept method⁷⁶, it was found that the grain size of the as-received UNS G10180 is *ca.* 20 µm.

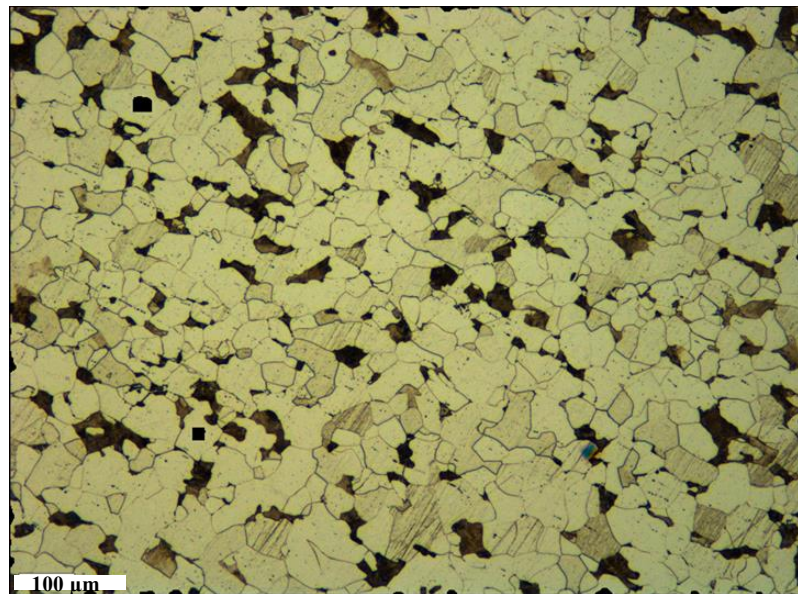


Figure 39. Optical micrograph of as-received UNS G10180 with a ferritic-pearlitic microstructure

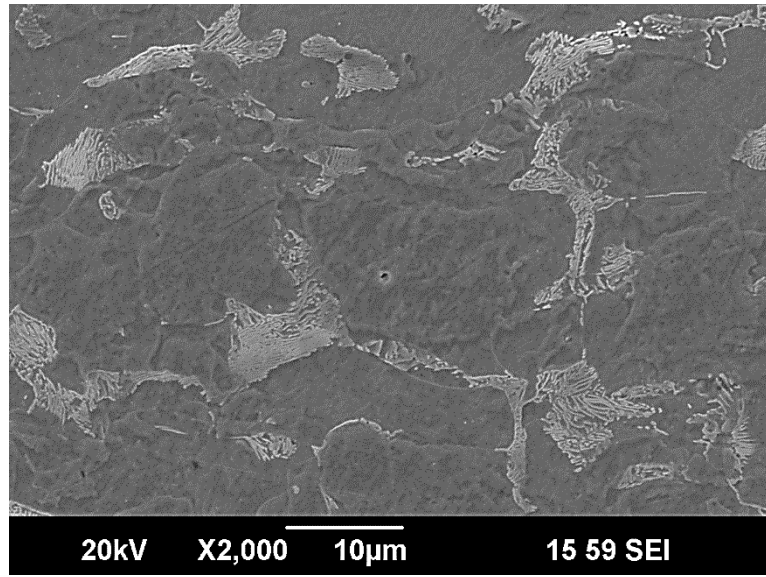


Figure 40. x2000 SEM image of as-received UNS G10180 with a ferritic-pearlitic microstructure

In order to test the effect of microstructure, a heat treatment was done to the UNS G10180 in order to obtain specimens with a tempered martensite microstructure. The specimens were rinsed using isopropyl alcohol, dried with cold air, and placed in a muffle furnace. The furnace was switched on and programmed to reach 950°C; it typically takes one hour to reach this temperature. The specimens were left in the furnace for about 1 hour and 45 minutes, as long as the furnace reached the desired temperature of 950°C within an hour. The specimens were then removed from the furnace, quenched in water for five minutes, and dried with cold air. Subsequently, the samples were placed in another muffle furnace at 500°C for two hours in the tempering process. The specimens were removed from this second furnace, being placed on its top, heat resistant, surface overnight. The microstructure of one of the heat treated specimens was then verified by grinding, polishing, etching (with 2% Nital) and microscopic characterization. **Figure 41** shows the microstructure of the sample after heat treatment. Similarly, **Figure 42** shows the SEM

image of the microstructure. It can be verified that the microstructure obtained was consistent with a tempered martensite^{48,77}. Hardness values were also obtained to further confirm the tempered martensite microstructure. By using a Brale indenter and applying a 100 kg load, Rockwell B hardness (HRB) values were obtained. The hardness value for the tempered martensite UNS G10180 was 97 ± 2.2 (HRB). This is consistent with has been found in the literature for a UNS G10180 following the same thermal treatment as the one performed in these experimentation, with a hardness value of 93 HRB⁷⁸.

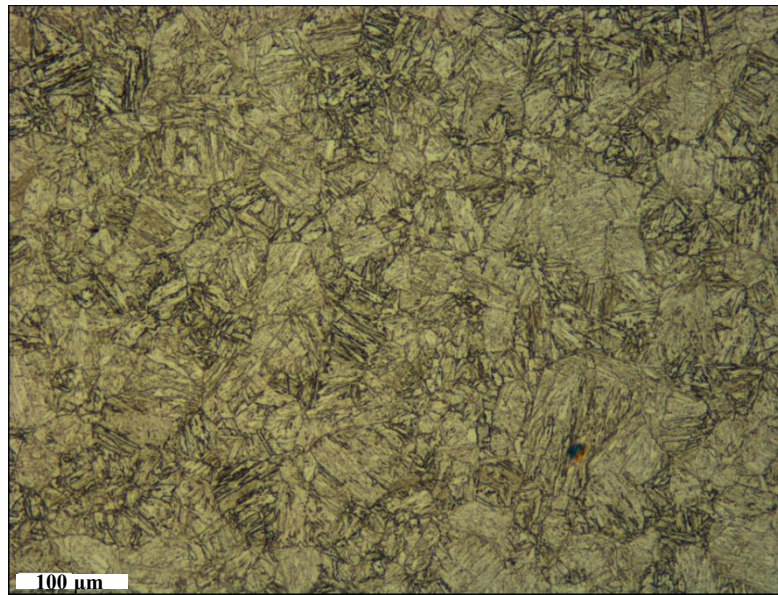


Figure 41. Optical micrograph showing tempered martensite microstructure of heat treated UNS G10180

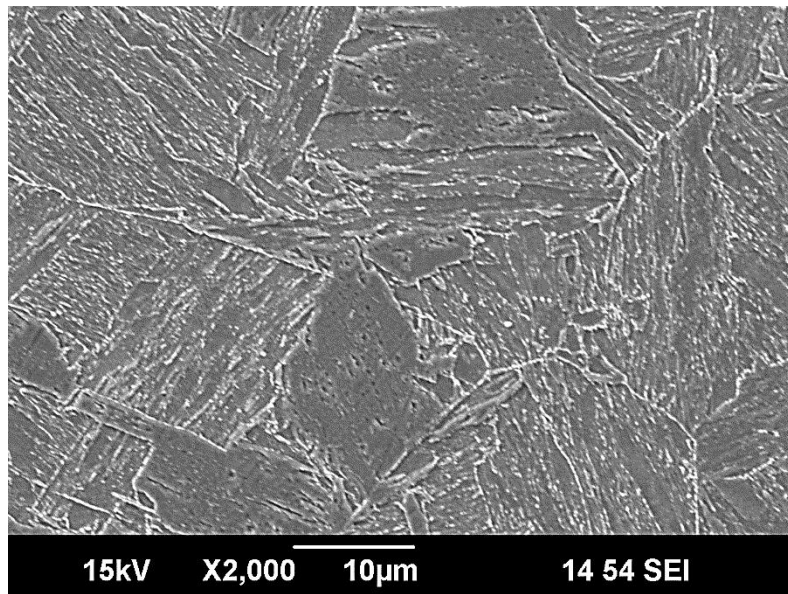


Figure 42. x2000 SEM image of UNS G10180 with a tempered martensitic microstructure

A heat treatment/annealing process was performed on API 5L X65 specimens in order to obtain a similar grain size to that of the as-received UNS G10180. The specimens were placed in a muffle furnace for *ca.* three hours at 930°C (temperature required for an annealing process given the carbon content of the material); including one hour to bring the furnace up to temperature. After three hours, the furnace was switched off and the specimens left therein to cool overnight. The microstructure was then verified by grinding, polishing and etching (with 2% Nital) one of the specimens as previously described. The microstructure of the specimen, shown in **Figure 43** and **Figure 44**, was characterized by optical microscopy and SEM. By using the grain size intercept method⁷⁶, it was found that the grain size of the heat treated API 5L X65 is *ca.* 18 µm. This grain size is comparable to that of the ferritic-pearlitic UNS G10180. This microstructure has dispersed cementite particles that are difficult to see because of the low carbon content of the material (0.05

wt.% C). However, EDS was used to identify the locations of the cementite particles were located on the sample, see **Figure 45**.

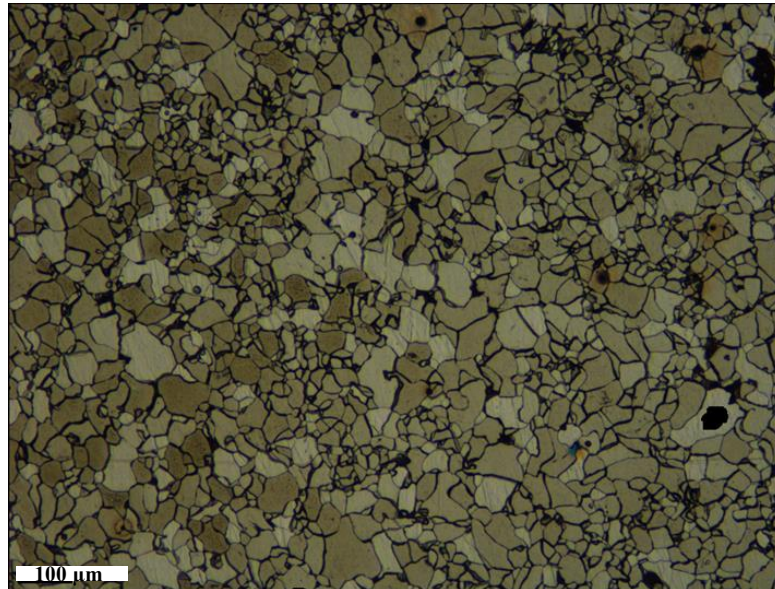


Figure 43. Optical micrograph showing microstructure of heat treated API 5L X65

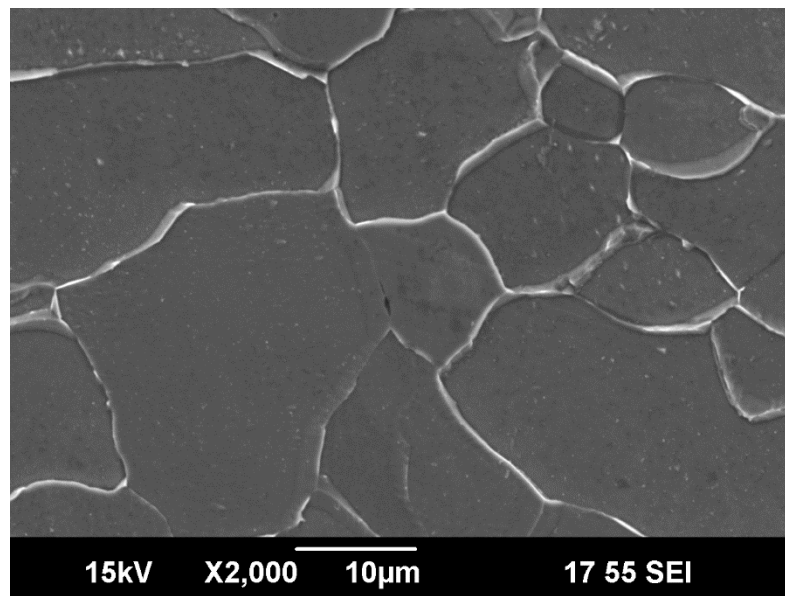


Figure 44. x2000 SEM image of heat treated API 5L X65 with a ferritic with Fe₃C precipitates microstructure

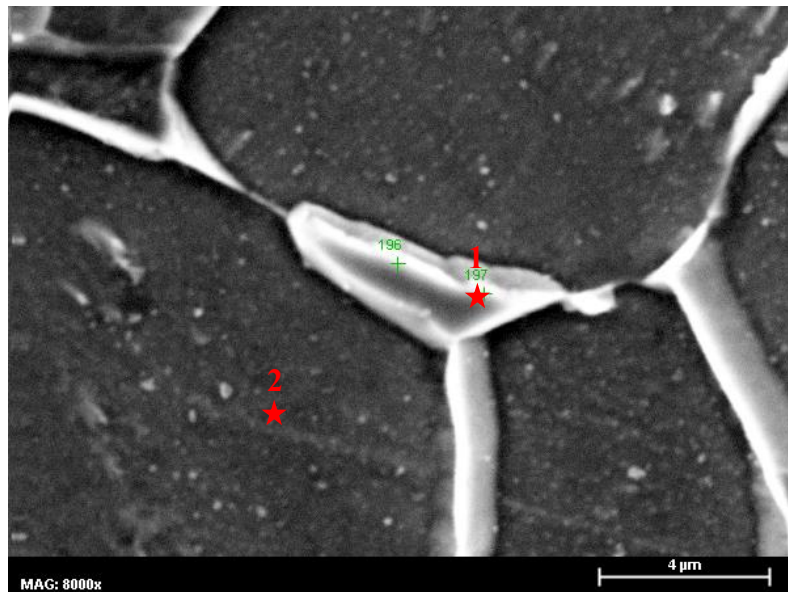


Figure 45. x8000 SEM image of heat treated API 5L X65 showing Fe₃C precipitate

Figure 45 shows small precipitates (white constituents) at the grain boundaries and a gray surface. The indicated points 1 and 2 were analyzed by EDS to determine the presence of cementite; point 1 corresponds to an intergranular precipitate, while point 2 is more representative of the gross specimen surface. The EDS spectrum for point 1 is shown in **Figure 46 (a)**. This displays a carbon peak, at relatively high atom %, and a low alloying element content; this is indicative that the white particles are cementite. The EDS spectrum for point 2, shown in **Figure 46 (b)**, does not show a carbon peak but shows significant manganese at a concentration broadly consistent with that reported (**Table 7**) for the initial untreated steel. Therefore, the SEM/EDS data is indicative of the material possessing a ferritic microstructure with cementite precipitated at the grain boundaries. This compositional analysis confirms the microstructure of the API 5L X65 specimens. Rockwell B hardness values were also obtained for this material and are found to be 62 ± 1.2 HRB. This is consistent with what has been found in the literature for carbon steels with

similar microstructures and carbon content^{47,79}. The yield strength can be estimated using a correlation between yield strength and hardness⁸⁰. It was found that by using the linear correlation between yield strength and hardness, the yield strength is *ca.* 45 ksi⁸⁰. It is understood that this yield strength no longer matches the definition of an API 5L X65; however it will be referred to as API 5L X65 in this document for ease of comprehension.

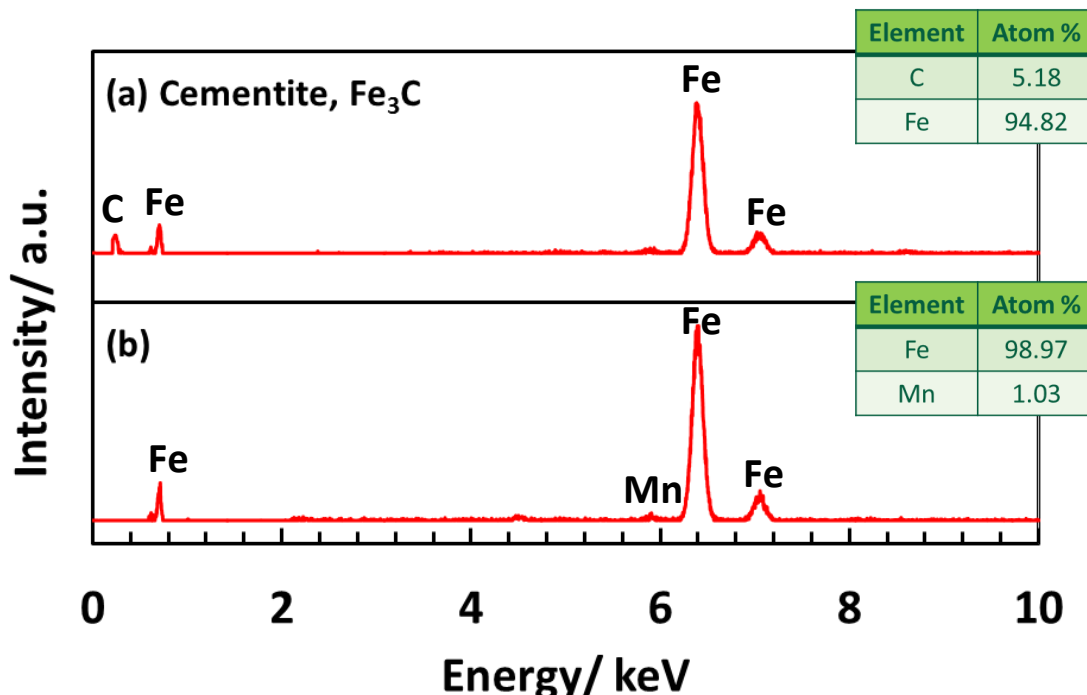


Figure 46. EDS spectra taken on API 5L X65 sample on (a) point 1 and (b) point 2

4.2.1.7 Sample characterization

Experimental duration was five days, with the test setup designed to accommodate four specimens for characterization and corrosion rate measurements. One specimen was removed after the first day of exposure, another on the third day, and the last two on the fifth day. Retrieved specimens were rinsed with N₂ sparged deionized water then isopropyl

alcohol and dried with cold air. Specimens were stored in a dessicator cabinet flushed with nitrogen to avoid any oxygen contamination. SEM was used to characterize the surface morphology for specimen after day one, three, and five. After completion of surface characterization, specimens were mounted in epoxy and prepared for cross-sectional analysis using SEM; this permitted characterization of layer morphology, thickness, and surface topography, as well as any formation of FeCO₃ within the Fe₃C network. The EDS coupled to the SEM was also used for elemental analysis. The other remaining specimen removed on the fifth day was analyzed by XRD, to characterize compounds formed on the steel surface, followed by weight loss measurement of corrosion rate.

4.2.1.8 Weight Loss Measurements per ASTM G1-03⁸¹

After completion of surface analyses, specimens were weighed in order to determine the degree of corrosion product layer growth. Specimens were then immersed in Clarke solution, which was prepared following the procedure outlined in ASTM G1-03⁸¹, to remove corrosion products; an as-made batch of Clarke solution consists of 1000 mL of hydrochloric acid (Assay 38.0%) with 20 grams of Sb₂O₃ and 50 g of SnCl₂ dissolved therein. Once the Clarke solution was prepared, specimens are dipped into a small volume of solution, typically of the order of tens of milliliters, for about 30 seconds. After removal of the specimen from Clarke solution, it was rinsed with deionized water, followed by isopropyl alcohol and air dried. Once the sample was completely dried, it was immediately weighed. This procedure of immersing a specimen in Clarke solution was repeated until the weight of the sample reached a steady value. Once an average of various stable values

is obtained, the corrosion rate in millimeters per year (mm/yr) is calculated based on the following equation (26):

$$CR = 87,600 * \frac{\Delta m}{A*t*\rho} \quad (26)$$

Where Δm is the change in mass over the time of the experiment in grams (g), A is the area of the sample (cm^2), t is experiment time in hours, and ρ is the density of iron (g/cm^3). The number 87,600 is a conversion factor to determine corrosion rate in millimeters per year (mm/yr).

4.2.2 Results and Discussion

4.2.2.1 Pure Fe (99.8%)

4.2.2.1.1 Water Chemistry

Figure 47 shows the change of pH throughout the course of experiments using the H-ion exchange resin. It can be seen that the pH was well controlled within a ± 0.03 range from the desired value of pH 6.60 and that, for both velocities, the pH was successfully controlled. **Figure 48** shows the comparison of ferrous ion concentration change throughout the course of the experiments. The ferrous ion concentration was well controlled using the Na-ion exchange resin within a ± 4 ppm from the desired value of 2 ppm ($S_{FeCO_3} \approx 10$). However, a pump failure between the 50th and 70th hour caused the ferrous ion concentration to spike slightly above the desired 6 ppm for the 250 rpm ($V_{eq} = 0.6 \text{ m/s}, 0.5 \text{ Pa}$) experiment. However, even after taking this failure into consideration, the average ferrous ion concentration in solution only reached 4.7 ppm compared to an average of 4.0 ppm for the 150 rpm ($V_{eq} = 0.4 \text{ m/s}, 0.3 \text{ Pa}$) experiment. Thus, it can be concluded

that changes in pH and ferrous iron concentration were similar and maintained fairly constant values.

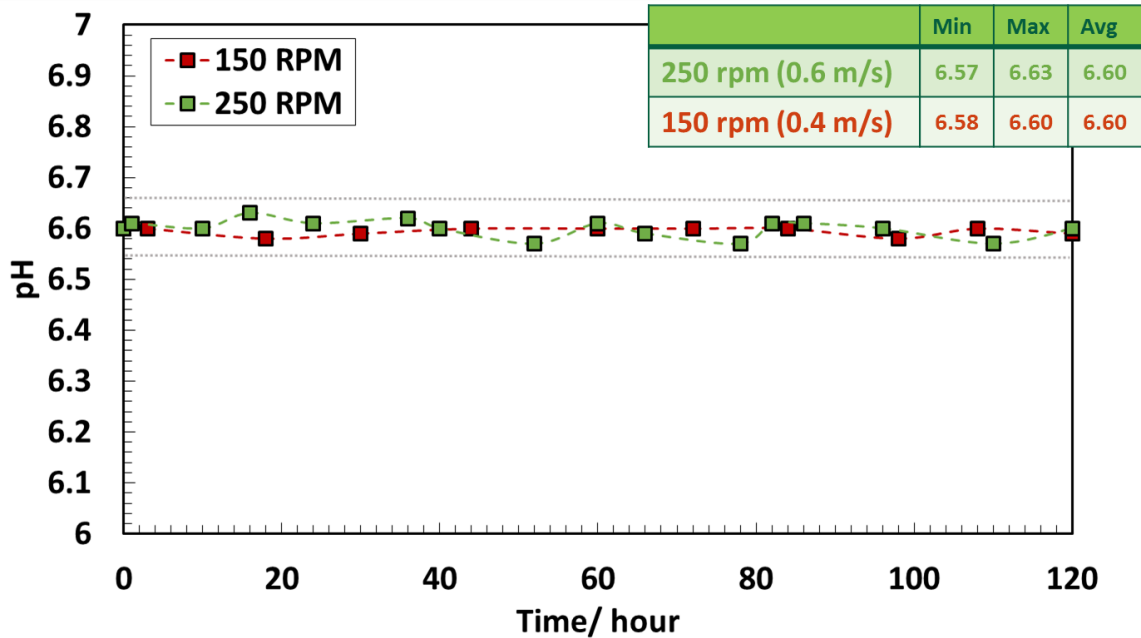


Figure 47. Comparison of pH change over time for 150 rpm ($V_{eq} = 0.4 \text{ m/s}, 0.3 \text{ Pa}$) and 250 rpm ($V_{eq} = 0.6 \text{ m/s}, 0.5 \text{ Pa}$) experiments with pure Fe under the conditions: $T=80^\circ\text{C}$, $p\text{CO}_2 = 0.53 \text{ bar}$, pH 6.6, $S_{\text{FeCO}_3} \approx 10$

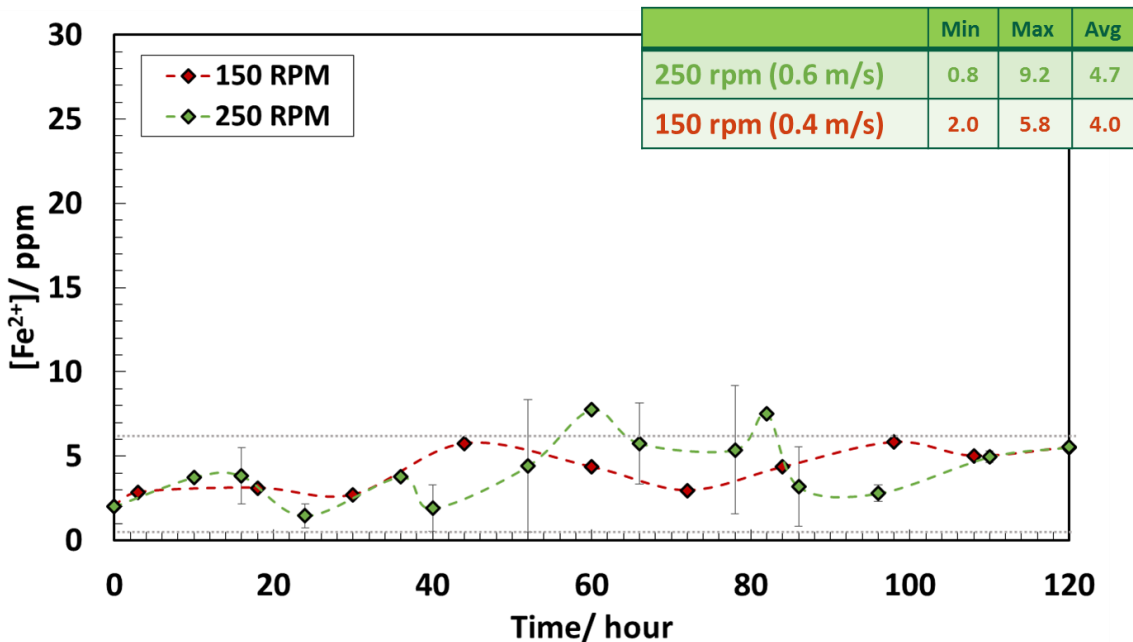


Figure 48. Comparison of $[Fe^{2+}]$ change over time for 150 rpm ($V_{eq} = 0.4$ m/s, 0.3 Pa) and 250 rpm ($V_{eq} = 0.6$ m/s, 0.5 Pa) experiments with pure Fe under the conditions:

$T=80^{\circ}\text{C}$, $\text{pCO}_2 = 0.53$ bar, pH 6.6, $S_{\text{FeCO}_3} \approx 10$

4.2.2.1.2 Corrosion Rate and Open Circuit Potential

Figure 49 shows the comparison of LPR corrosion rates over time. The corrosion rate at both velocities starts at *ca.* 4 mm/yr and maintains a steady value for the entire experimental duration. However, at the 80th hour, the corrosion behavior for both experiments differs. At the lower velocity of 150 rpm ($V_{eq} = 0.4$ m/s, 0.3 Pa), the corrosion rate starts to decrease from about 4.5 mm/yr to a final corrosion rate of 3 mm/yr; postulated to be due to the nucleation and growth of FeCO_3 . However, for the higher velocity experiment, the corrosion rate is stable⁴⁹. The weight loss corrosion rate closely matches to that obtained from LPR measurements, as expected, for the 250 rpm ($V_{eq} = 0.6$ m/s, 0.5 Pa) experiment.

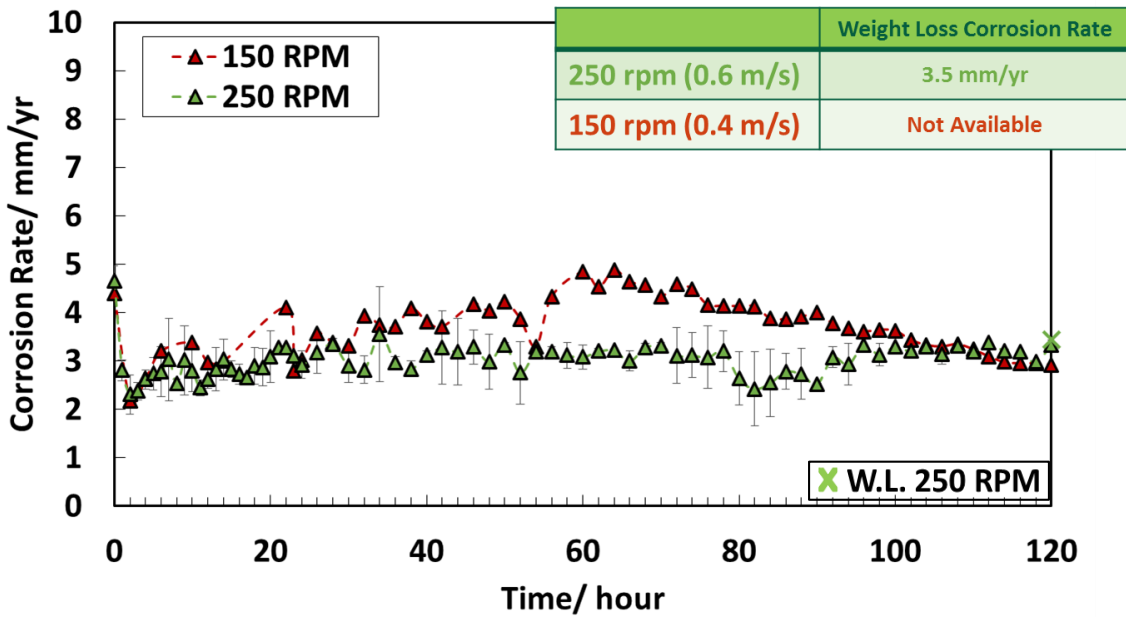


Figure 49. Comparison of LPR corrosion rate over time for 150 rpm ($V_{eq} = 0.4 \text{ m/s}, 0.3 \text{ Pa}$) and 250 rpm ($V_{eq} = 0.6 \text{ m/s}, 0.5 \text{ Pa}$) experiments with pure Fe under the conditions:
 $T=80^{\circ}\text{C}$, $\text{pCO}_2 = 0.53 \text{ bar}$, $\text{pH } 6.6$, $S_{\text{FeCO}_3} \approx 10$

Figure 50 shows the open circuit potential (OCP) over the course of the experiment for both 150 rpm ($V_{eq} = 0.4 \text{ m/s}, 0.3 \text{ Pa}$) and 250 rpm ($V_{eq} = 0.6 \text{ m/s}, 0.5 \text{ Pa}$) experiment. It can be observed that the OCP does not vary significantly throughout the duration of the experiments.

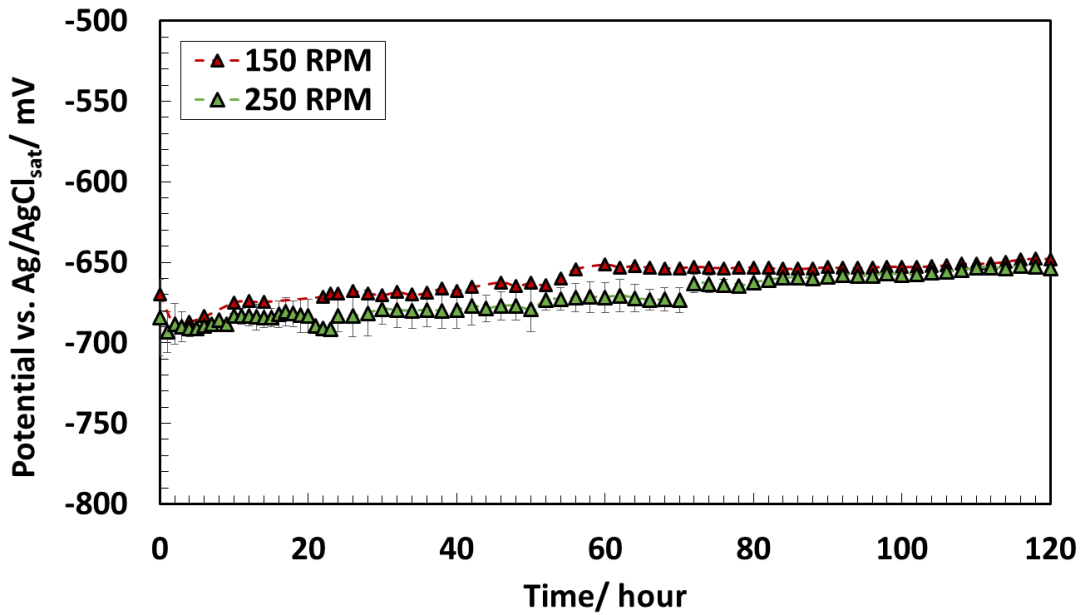


Figure 50. Comparison of OCP over time for 150 rpm ($V_{eq} = 0.4$ m/s, 0.3 Pa) and 250 rpm ($V_{eq} = 0.6$ m/s, 0.5 Pa) experiments with pure Fe under the conditions: $T=80^{\circ}\text{C}$, $\text{pCO}_2 = 0.53$ bar, pH 6.6, $S_{\text{FeCO}_3} \approx 10$

4.2.2.1.3 Surface Morphologies and Characterization

Figure 51 shows a comparison of surface morphologies of specimens from the 250 rpm ($V_{eq} = 0.6$ m/s, 0.5 Pa) and 150 rpm ($V_{eq} = 0.4$ m/s, 0.3 Pa) experiments when samples were taken out after days 1, 3, and 5. The surface morphologies of specimens recovered after the first day are similar for each flow condition, each shows a rough surface with no major surface indentations. Specimens recovered after day 3, for both experiments, show development of porosity as well as surface grooves. For day 5 specimens, there are some noteworthy differences. For the 250 rpm ($V_{eq} = 0.6$ m/s, 0.5 Pa) experiment, the sample shows major cracks on the surface of the sample. The 150 rpm ($V_{eq} = 0.4$ m/s, 0.3 Pa) experiment also shows some cracks but they are broader and, in addition, there is potential evidence of FeCO_3 crystal growth. **Figure 52**, a higher magnification image of the 150 rpm

($V_{eq} = 0.4$ m/s, 0.3 Pa) day 5 sample, shown in **Figure 51**, further confirms this was indeed FeCO₃ due to its characteristic prismatic morphology and supported by the EDS spectrum, shown in **Figure 53**, due to the high energy peak of oxygen.

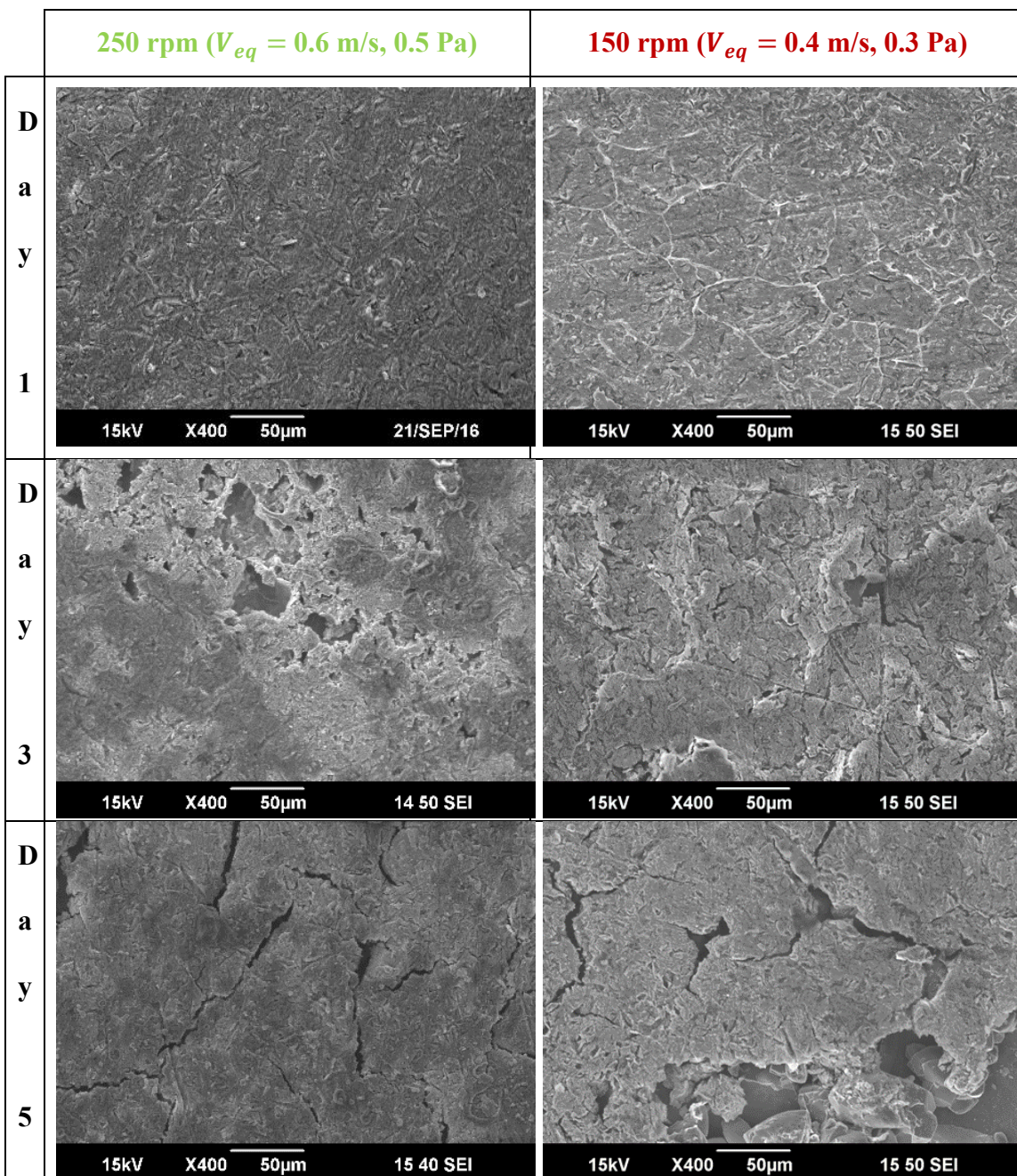


Figure 51. x400 SEM images showing comparison of surface morphologies over time for 150 rpm ($V_{eq} = 0.4 \text{ m/s}, 0.3 \text{ Pa}$) and 250 rpm ($V_{eq} = 0.6 \text{ m/s}, 0.5 \text{ Pa}$) experiments with pure Fe under the conditions: $T=80^\circ\text{C}$, $p\text{CO}_2 = 0.53 \text{ bar}$, pH 6.6, $S_{\text{FeCO}_3} \approx 10$

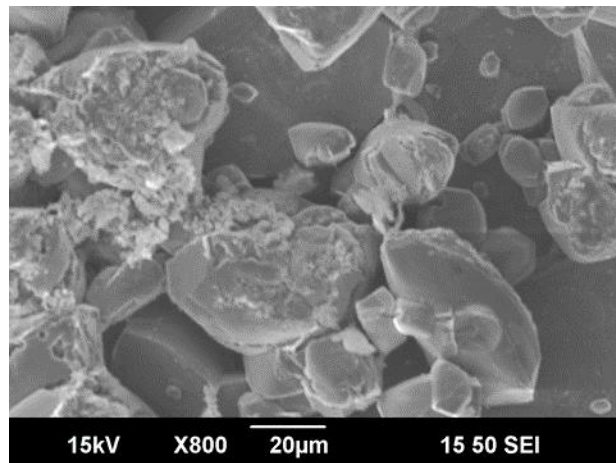


Figure 52. x800 SEM image showing the surface morphology of pure Fe for 150 rpm ($V_{eq} = 0.4$ m/s, 0.3 Pa) experiment on day 5 showing FeCO_3 crystals under the conditions: $T=80^{\circ}\text{C}$, $p\text{CO}_2 = 0.53$ bar, pH 6.6, $S_{\text{FeCO}_3} \approx 10$

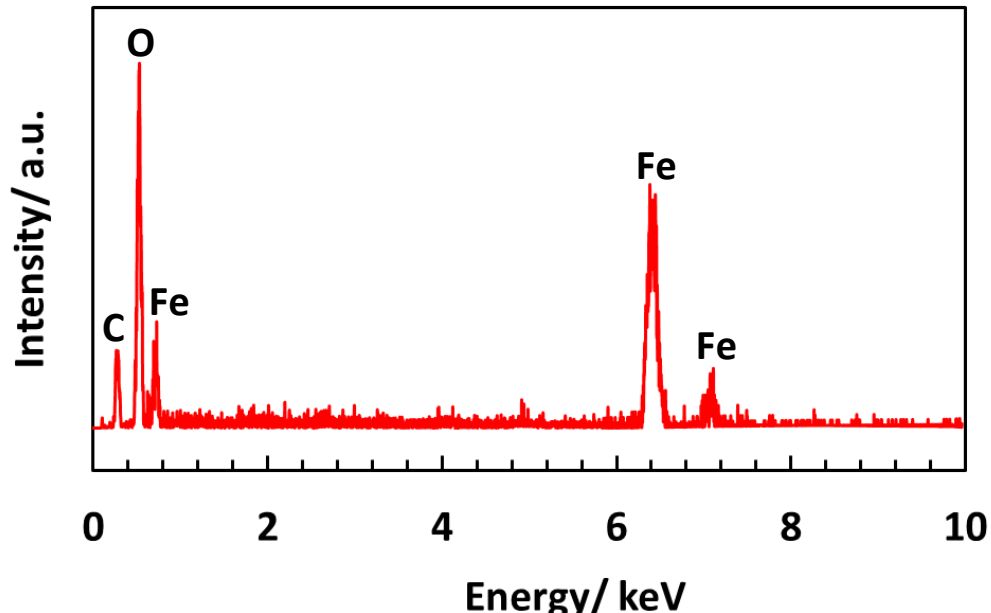


Figure 53. EDS spectrum of FeCO_3 crystals shown in **Figure 52**

Figure 54 shows the XRD pattern for the 250 rpm ($V_{eq} = 0.6$ m/s, 0.5 Pa) pure Fe sample taken out on day 5; XRD data is unavailable for the 150 rpm ($V_{eq} = 0.4$ m/s, 0.3 Pa) experiment as a weight loss/XRD sample was not used for this experiment. It is

noteworthy that FeCO_3 is absent, the shown XRD data shown in **Figure 54** being consistent with the surface morphologies shown in **Figure 51**.

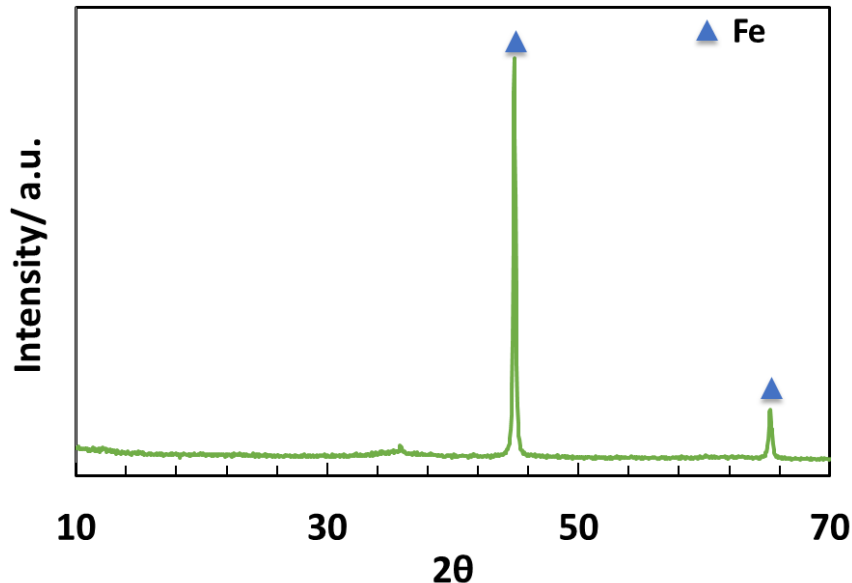


Figure 54. XRD analysis on pure Fe day 5 specimen for 250 rpm ($V_{eq} = 0.6 \text{ m/s}, 0.5 \text{ Pa}$) experiment under the conditions: $T=80^\circ\text{C}$, $p\text{CO}_2 = 0.53 \text{ bar}$, $\text{pH} 6.6$, $S_{\text{FeCO}_3} \approx 10$

4.2.2.1.4 Cross-Sectional Morphologies

Figure 55 shows a comparison of cross-sectional morphologies associated with the 250 rpm ($V_{eq} = 0.6 \text{ m/s}, 0.5 \text{ Pa}$) and 150 rpm ($V_{eq} = 0.4 \text{ m/s}, 0.3 \text{ Pa}$) experiments when specimens were taken out on days 1, 3 and 5. The cross-sectional morphologies for both experiments are similar after the first day, showing no major metal loss. After day 3 of both experiments the specimens each began to show grooves on their surfaces as the metal loss increases. For the day 5 samples, there are some significant differences. At 250 rpm ($V_{eq} = 0.6 \text{ m/s}, 0.5 \text{ Pa}$), the sample shows some grooves with no evidence of formation of FeCO_3 . However, the 150 rpm ($V_{eq} = 0.6 \text{ m/s}, 0.5 \text{ Pa}$) experiment also shows some grooves, but

under these grooves there are some crystals that grew on the specimen surface. Elemental mapping, through a line scan, was done for this cross-sectional image, shown in **Figure 56**, which displays the presence of oxygen, iron and carbon in these crystals. This finding confirms that these crystals were most likely FeCO_3 since the presence of these elements are consistent with its formation. Additionally, the thin line of corrosion product above the FeCO_3 crystals appears to be a small trace of nickel, as shown in **Figure 56**.

The metal loss values shown in **Figure 55** were calculated from weight loss measurements for the 250 rpm ($V_{eq} = 0.6 \text{ m/s}, 0.5 \text{ Pa}$) experiment and from LPR corrosion rates for 150 rpm ($V_{eq} = 0.4 \text{ m/s}, 0.3 \text{ Pa}$) experiment (since a weight loss specimen was not available). These values are consistent with the metal loss calculated from thickness of metal exposed, as shown on the SEM images and by weight loss measurements.

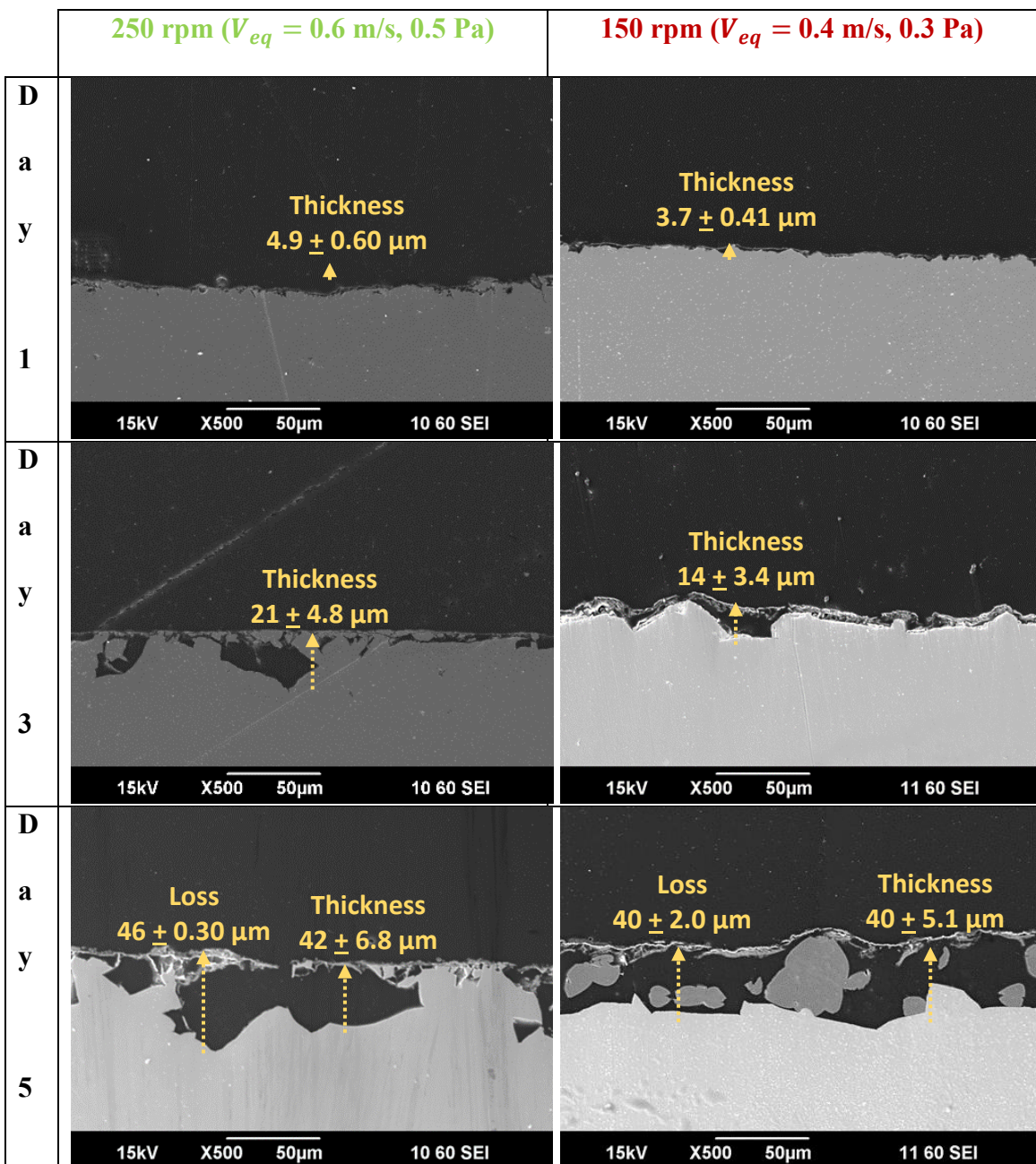


Figure 55. x500 SEM images showing cross-sectional morphologies over time for 150 rpm ($V_{eq} = 0.4 \text{ m/s}, 0.3 \text{ Pa}$) and 250 rpm ($V_{eq} = 0.6 \text{ m/s}, 0.5 \text{ Pa}$) experiments with pure Fe under the conditions: $T=80^\circ\text{C}$, $\text{pCO}_2 = 0.53 \text{ bar}$, $\text{pH} 6.6$, $S_{\text{FeCO}_3} \approx 10$

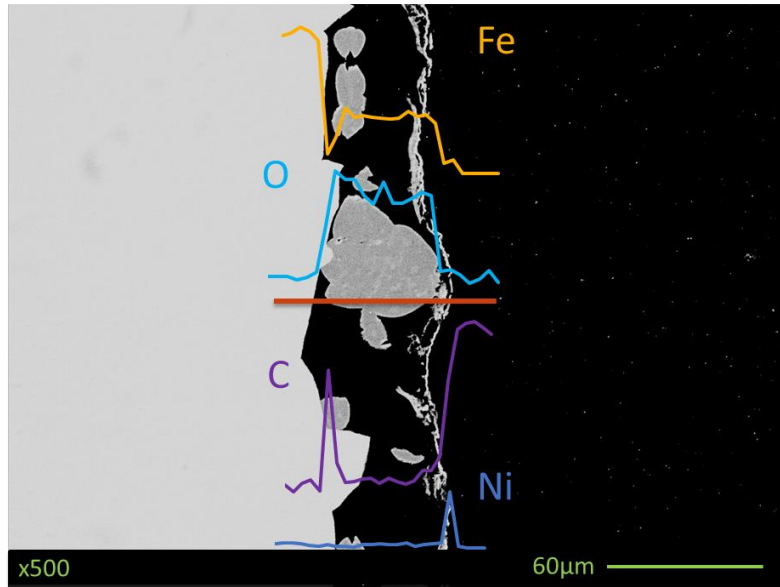


Figure 56. x500 SEM image showing cross-sectional elemental mapping of pure Fe on day 5 at 150 rpm ($V_{eq} = 0.4$ m/s, 0.3 Pa) confirming evidence of FeCO_3 due to oxygen peak under the conditions: $T=80^\circ\text{C}$, $p\text{CO}_2 = 0.53$ bar, pH 6.6, $S_{\text{FeCO}_3} \approx 10$

4.2.2.2 UNS G10180 ferritic pearlitic

4.2.2.2.1 Water Chemistry

Figure 57 shows the change of pH through the course of the experiments at each velocity using the H-ion exchange resin. Similarly to the case of pure Fe, pH was well controlled within a ± 0.03 range from the desired value of pH 6.60 for both velocities. The average pH values for both velocities was 6.60. **Figure 58** shows the comparison of ferrous concentration changes throughout the course of the experiments. The ferrous ion concentration was well controlled using the Na-ion exchange resin within 1 to 6 ppm, with the desired starting value being 2 ppm ($S_{\text{FeCO}_3} \approx 10$). There was a slight increase of ferrous ion concentration for the 250 rpm ($V_{eq} = 0.6$ m/s, 0.5 Pa) experiment, but the average was maintained at a value of 3.5 ppm, which is still within the desired range. Minor changes in

pH, and ferrous iron concentration (steady values) occurred throughout the experiments which allowed for a realistic simulation of field conditions.

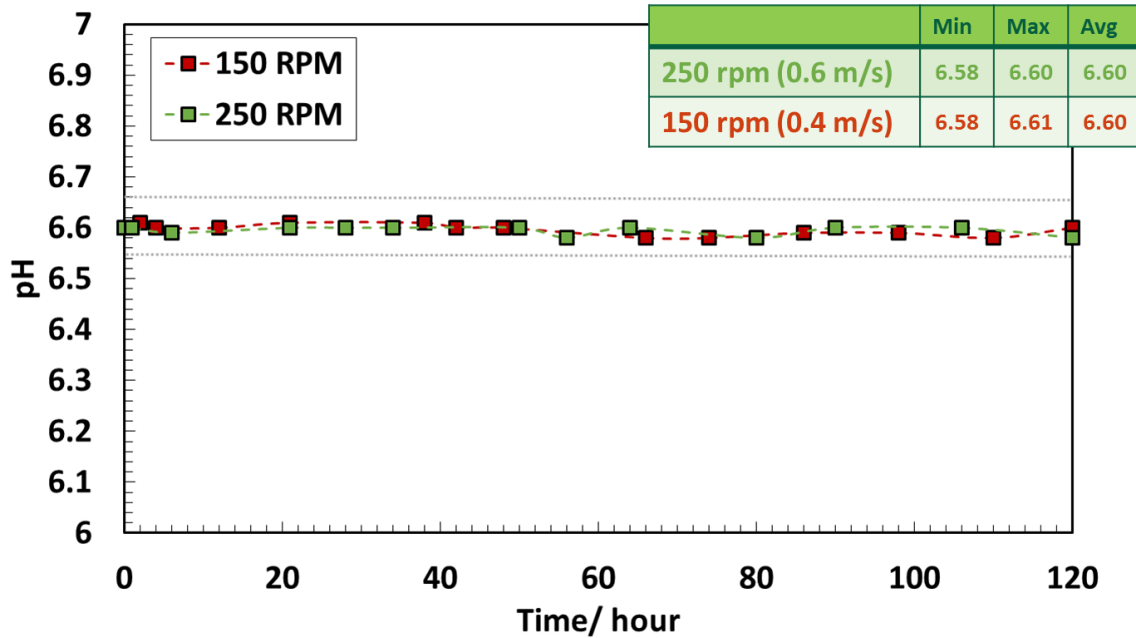


Figure 57. Comparison of pH change over time for 150 rpm ($V_{eq} = 0.4$ m/s, 0.3 Pa) and 250 rpm ($V_{eq} = 0.6$ m/s, 0.5 Pa) experiments with UNS G10180 ferritic-pearlitic under the conditions: T=80°C, pCO₂ = 0.53 bar, pH 6.6, S_{FeCO₃} ≈ 10

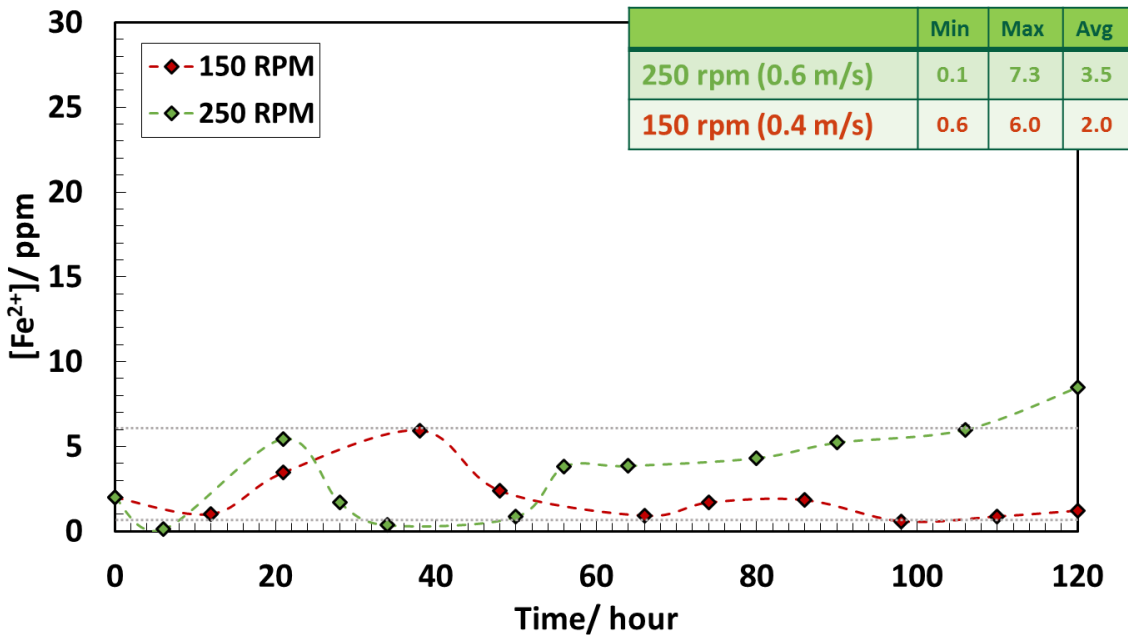


Figure 58. Comparison of $[Fe^{2+}]$ change over time for 150 rpm ($V_{eq} = 0.4$ m/s, 0.3 Pa) and 250 rpm ($V_{eq} = 0.6$ m/s, 0.5 Pa) experiments with UNS G10180 ferritic-pearlitic under the conditions: $T=80^{\circ}\text{C}$, $p\text{CO}_2 = 0.53$ bar, pH 6.6, $S_{\text{FeCO}_3} \approx 10$

4.2.2.2.2 Corrosion Rate and Open Circuit Potential

Figure 59 shows the comparison of LPR corrosion rate over time for each velocity.

It can be observed that initial corrosion rates start at about 2 mm/yr and increase over time, mainly because of the presence of Fe_3C . These findings are unlike what was observed in the case for pure iron, shown in **Figure 49**, since pure iron corrodes at a stable rate over time, whereas steels that contain the Fe_3C phase corrode at much faster rates since Fe_3C acts as an active cathodic site^{8,46,47,49-54}. In other words, the presence of Fe_3C increases the overall cathodic area which in turn promotes the dissolution of the anodic^{8,46,47,49-54}. This increase in corrosion rate over time has been termed as the active corrosion stage^{7,32}. For the 150 rpm ($V_{eq} = 0.4$ m/s, 0.3 Pa) experiment, the corrosion rate stops increasing over time after the first day, and is maintained from the on at a stable value until the 65th hour

after which the corrosion rate starts decreasing to a low and steady value; this is indicative of FeCO_3 formation. The stage where the corrosion rate is at a low and steady value has been commonly referred to as the ‘pseudo-passivation’ stage^{7,32}. For the 250 rpm ($V_{eq} = 0.6 \text{ m/s}, 0.5 \text{ Pa}$) experiment, the corrosion rate increases until the 80th hour. After the 80th hour, the corrosion rate starts to rapidly decrease, which is also indicative of FeCO_3 formation. The stage where the corrosion rate starts to decrease but has not yet reached a stable value is known as the ‘nucleation and growth of FeCO_3 ’ stage^{7,32}.

Figure 60 shows the open circuit potential for the entire experiment at both velocities tested. It can be seen that the open circuit potential starts to increase after the 80th hour for both experiments. This is because of pseudo-passivation due to the formation of FeCO_3 ^{7,32,34,82}.

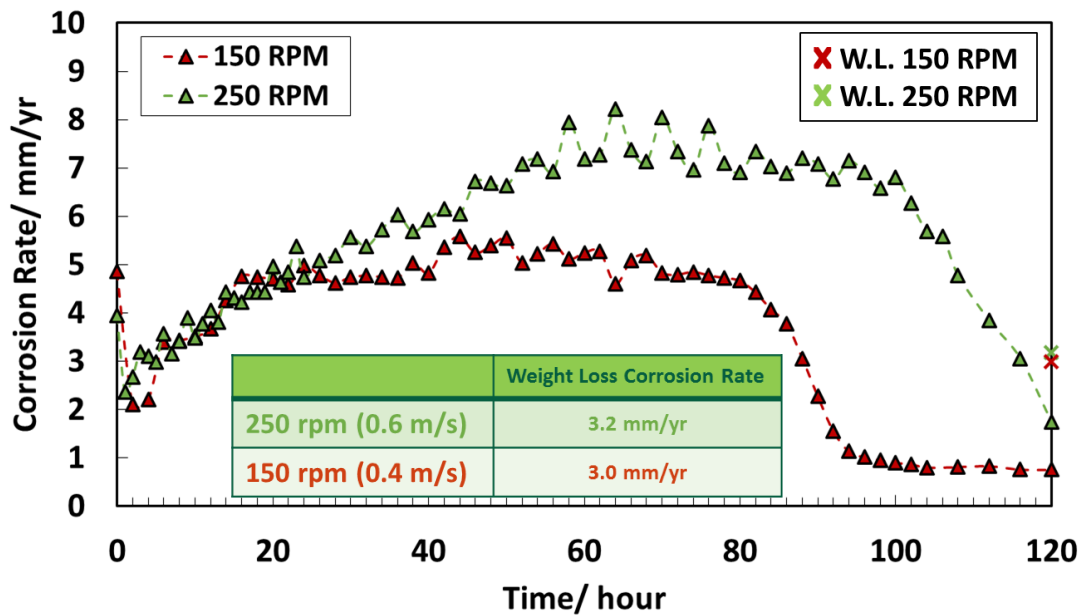


Figure 59. Comparison of LPR corrosion rate over time for 150 rpm ($V_{eq} = 0.4$ m/s, 0.3 Pa) and 250 rpm ($V_{eq} = 0.6$ m/s, 0.5 Pa) experiments with UNS G10180 ferritic-pearlitic under the conditions: $T=80^{\circ}\text{C}$, $\text{pCO}_2 = 0.53$ bar, pH 6.6, $S_{\text{FeCO}_3} \approx 10$

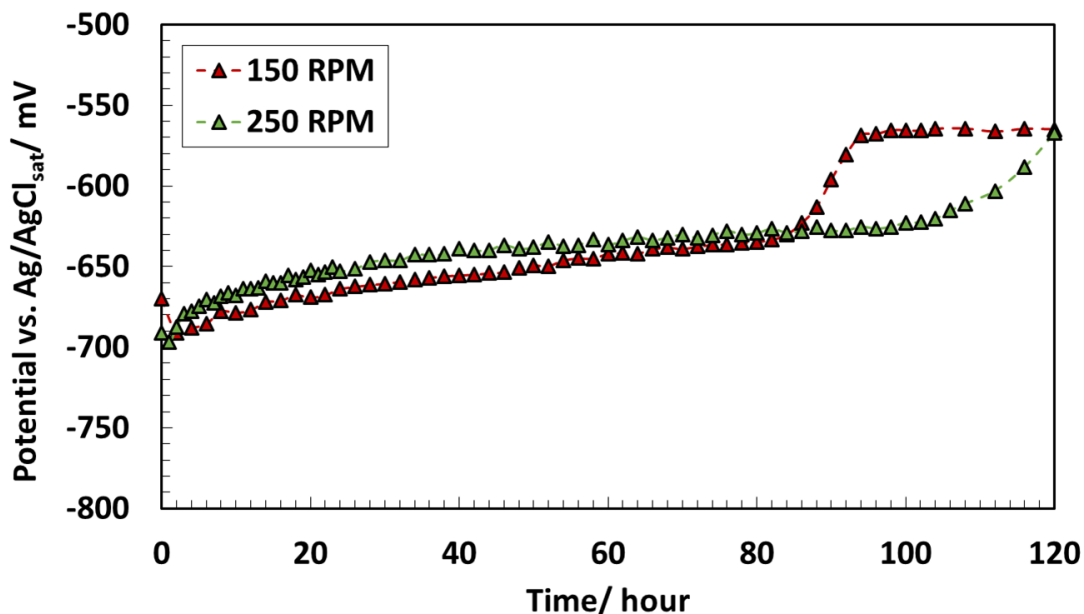


Figure 60. Comparison of OCP over time for 150 rpm ($V_{eq} = 0.4$ m/s, 0.3 Pa) and 250 rpm ($V_{eq} = 0.6$ m/s, 0.5 Pa) experiments with UNS G10180 ferritic-pearlitic under the conditions: $T=80^{\circ}\text{C}$, $\text{pCO}_2 = 0.53$ bar, pH 6.6, $S_{\text{FeCO}_3} \approx 10$

4.2.2.2.3 Surface Morphologies and Characterization

Figure 61 shows various SEM images of the surface of the specimens for the 250 rpm ($V_{eq} = 0.6$ m/s, 0.5 Pa) and 150 rpm ($V_{eq} = 0.4$ m/s, 0.3 Pa) experiments removed on the first, third and last day of the experiments. The surface morphology of the first sample for both rotational velocities show similar findings: a rough surface with no visible precipitation of FeCO_3 . However, different findings are found on the samples taken out on the third day as there is visible precipitation of FeCO_3 , in the form of prismatic crystals, for the 150 rpm ($V_{eq} = 0.4$ m/s, 0.3 Pa) experiment, whereas the 250 rpm ($V_{eq} = 0.6$ m/s, 0.5 Pa) experiment still shows a bare rough surface with no precipitation. Lastly, for the fifth and last day of the experiment, the surface of the sample for the 250 rpm ($V_{eq} = 0.6$ m/s, 0.5 Pa) experiment shows some grooves on the surface and no precipitation of FeCO_3 . However, grooves have been associated with a thick and porous layer of Fe_3C , since the ferrite phase preferentially corrodes over cementite^{7,34}. The sample for the 150 rpm ($V_{eq} = 0.4$ m/s, 0.3 Pa) experiment taken out on the fifth day shows a surface covered in FeCO_3 prismatic crystals, which indicates that these prisms are protective as indicated by the decrease of corrosion rate to a low and steady value as shown in **Figure 59** and the increase of OCP due to passivation shown in **Figure 60**.

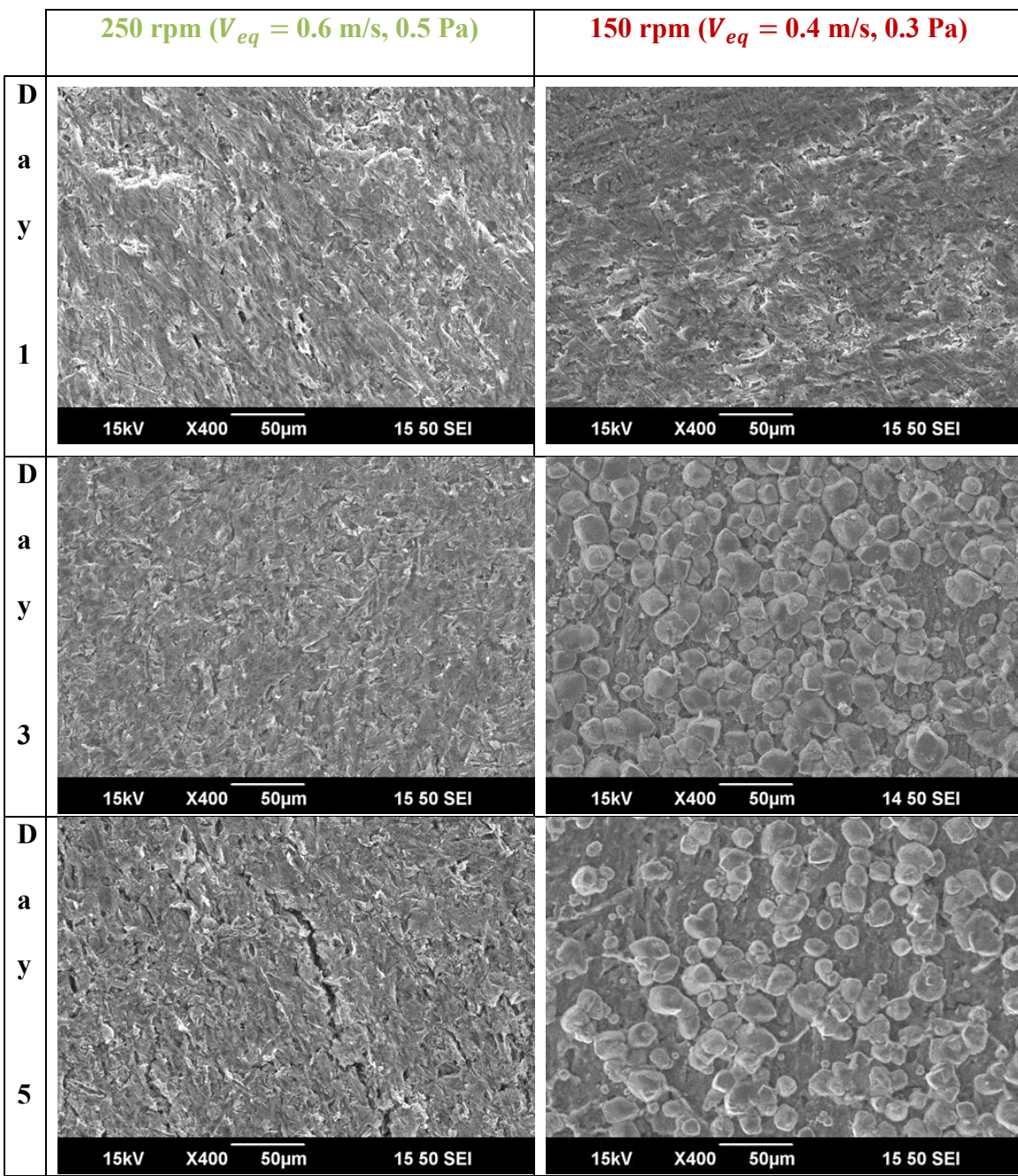


Figure 61. x400 SEM images showing comparison of surface morphologies over time for 150 rpm ($V_{eq} = 0.4 \text{ m/s}, 0.3 \text{ Pa}$) and 250 rpm ($V_{eq} = 0.6 \text{ m/s}, 0.5 \text{ Pa}$) experiments with UNS G10180 ferritic-pearlitic under the conditions: $T=80^\circ\text{C}$, $p\text{CO}_2 = 0.53 \text{ bar}$, pH 6.6,
 $S_{\text{FeCO}_3} \approx 10$

Figure 62 shows the XRD patterns for the specimens retrieved from the 150 rpm ($V_{eq} = 0.4$ m/s, 0.3 Pa) and 250 rpm ($V_{eq} = 0.6$ m/s, 0.5 Pa) experiments after day 5. The dominant corrosion product for the 150 rpm ($V_{eq} = 0.4$ m/s, 0.3 Pa) experiment is FeCO_3 . For the 250 rpm ($V_{eq} = 0.6$ m/s, 0.5 Pa) experiments, the corrosion products are Fe_3C and FeCO_3 . The XRD analysis confirms the formation of FeCO_3 on both specimens. However, as shown by the surface morphologies and the XRD patterns, **Figure 61** and **Figure 62**, respectively, FeCO_3 is more dominant on the 150 rpm ($V_{eq} = 0.4$ m/s, 0.3 Pa) sample, which confirms that there is an effect of flow on the formation of FeCO_3 . It is also noteworthy that the corrosion product layers are sufficiently thick that no diffraction from ferrite (α -Fe) is observed.

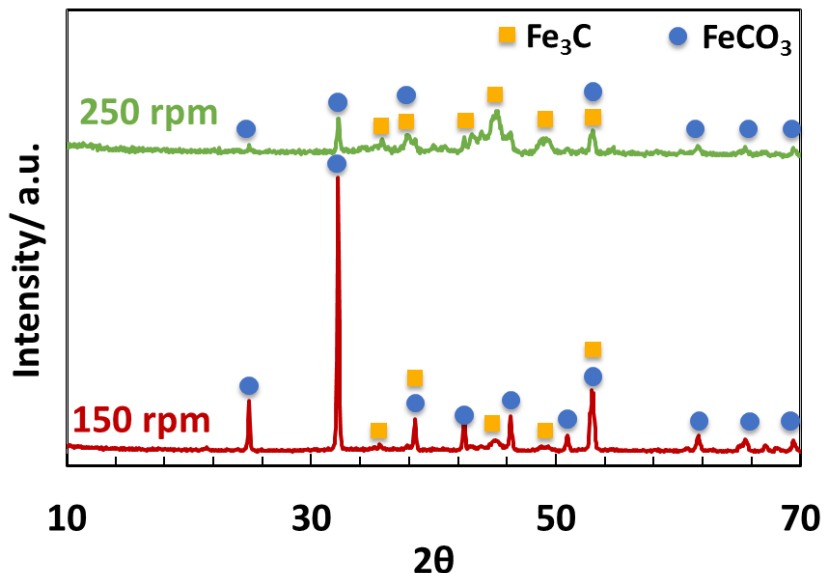


Figure 62. XRD analysis on UNS G10180 ferritic-pearlitic day 5 specimens for 150 rpm ($V_{eq} = 0.4$ m/s, 0.3 Pa) and 250 rpm ($V_{eq} = 0.6$ m/s, 0.5 Pa) experiments under the conditions: $T=80^\circ\text{C}$, $p\text{CO}_2 = 0.53$ bar, $\text{pH} 6.6$, $S_{\text{FeCO}_3} \approx 10$

4.2.2.2.4 Cross-Sectional Morphologies

Figure 63 shows cross-section morphologies for both rotational velocities for the extracted specimens after days 1, 3, and 5. For the first day, it can be seen that no significant corrosion has occurred and that Fe₃C is only about 5 µm thick for both experiments. For the third day, a more significant Fe₃C network developed on both experiments. For the 150 rpm ($V_{eq} = 0.4$ m/s, 0.3 Pa) experiment after day 3, it can be observed that some FeCO₃ has precipitated within the porous layer of Fe₃C, but it does not cover the surface entirely, which is why the corrosion rate has not significantly decreased at this time, as shown in **Figure 59**. Finally, on day 5, the 150 rpm ($V_{eq} = 0.4$ m/s, 0.3 Pa) samples shows that FeCO₃ has precipitated fully within the porous layer of Fe₃C. The 250 rpm ($V_{eq} = 0.6$ m/s, 0.5 Pa) sample also shows that some precipitation occurred within the pores of Fe₃C but only close to the surface of the steel, which is why no FeCO₃ prismatic crystals were visible on the surface of the specimen, as shown in **Figure 61**.

Figure 63 also shows the metal loss calculated from LPR corrosion rate measurements in the respective SEM images. It is important to note that the thickness of the porous Fe₃C layer matches the metal loss calculated from the maximum LPR corrosion rate measurement for both experiments. At this point, the steel stops corroding as FeCO₃ starts precipitating within the Fe₃C. As mentioned in the literature review section, Fe₃C acts as a diffusion barrier for Fe²⁺ and H⁺ from the corrosion process, allowing for local increase of pH and saturation values that favor FeCO₃ precipitation within the Fe₃C network immediately adjacent to the steel surface^{7,32,34}. **Figure 64** further confirms through

an elemental line scan of the 250 rpm ($V_{eq} = 0.6$ m/s, 0.5 Pa) day 5 sample, shown in **Figure 63** that dark gray areas are FeCO₃ as evidenced by the oxygen peak.

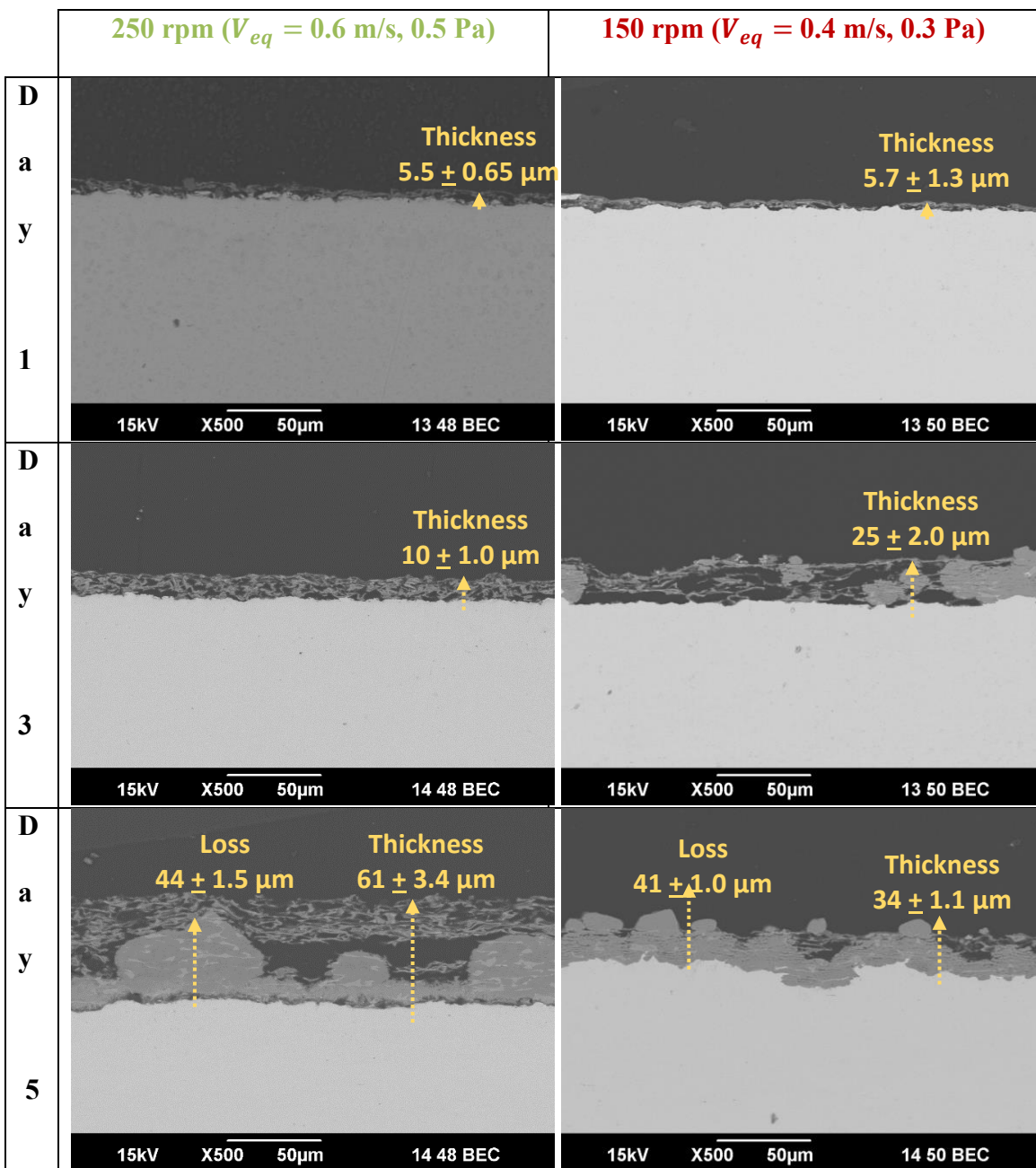


Figure 63. x500 SEM images showing cross-sectional morphologies over time for 150 rpm ($V_{eq} = 0.4 \text{ m/s}, 0.3 \text{ Pa}$) and 250 rpm ($V_{eq} = 0.6 \text{ m/s}, 0.5 \text{ Pa}$) experiments with UNS G10180 ferritic-pearlitic and metal loss from LPR corrosion rate under the conditions:

$$T=80^\circ\text{C}, p\text{CO}_2 = 0.53 \text{ bar}, \text{pH } 6.6, S_{\text{FeCO}_3} \approx 10$$

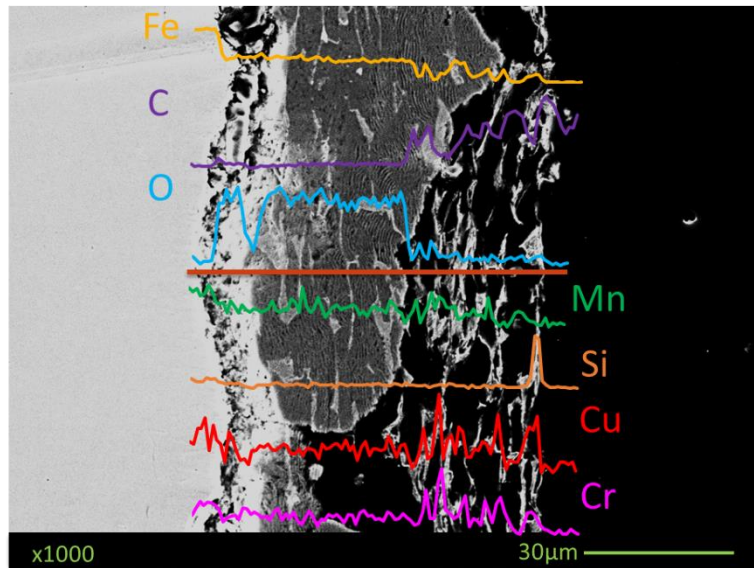


Figure 64. x1000 SEM image showing cross-sectional elemental mapping of UNS G10180 ferritic-pearlitic on day 5 at 250 rpm ($V_{eq} = 0.6$ m/s, 0.5 Pa) confirming evidence of FeCO_3 due to oxygen peak under the conditions: $T=80^{\circ}\text{C}$, $p\text{CO}_2 = 0.53$ bar, pH 6.6,
 $S_{\text{FeCO}_3} \approx 10$

4.2.2.3 UNS G10180 tempered martensite

4.2.2.3.1 Water Chemistry

Figure 65 and **Figure 66** show data related to the water chemistry acquired during the course of the experiments conducted at different velocities. This indicates that reasonable constant water chemistry conditions, associated with desired pH and ferrous ion concentration ranges/values, are maintained by the ion exchange resins. The pH was controlled within a ± 0.03 range from the initial pH value of 6.60, as for the same previous materials shown. The average pH value for both experiments was 6.59. **Figure 66** shows ferrous ion concentration at different time intervals during the course of the experiment. Even though a maximum of 7.7 ppm was obtained for the 250 rpm ($V_{eq} = 0.6$ m/s, 0.5 Pa) experiment, the average value of all data obtained was 4.0 ppm ($S_{\text{FeCO}_3} \approx 25$) , only 2.0

ppm ($S_{FeCO_3} \approx 10$) away from the starting value. Since there were no significant changes in pH and ferrous ion concentration, it can be concluded that these environmental conditions were well controlled during all trials with no supersaturation values and/or drastic changes in pH values that can alter the formation of FeCO₃ and skew results.

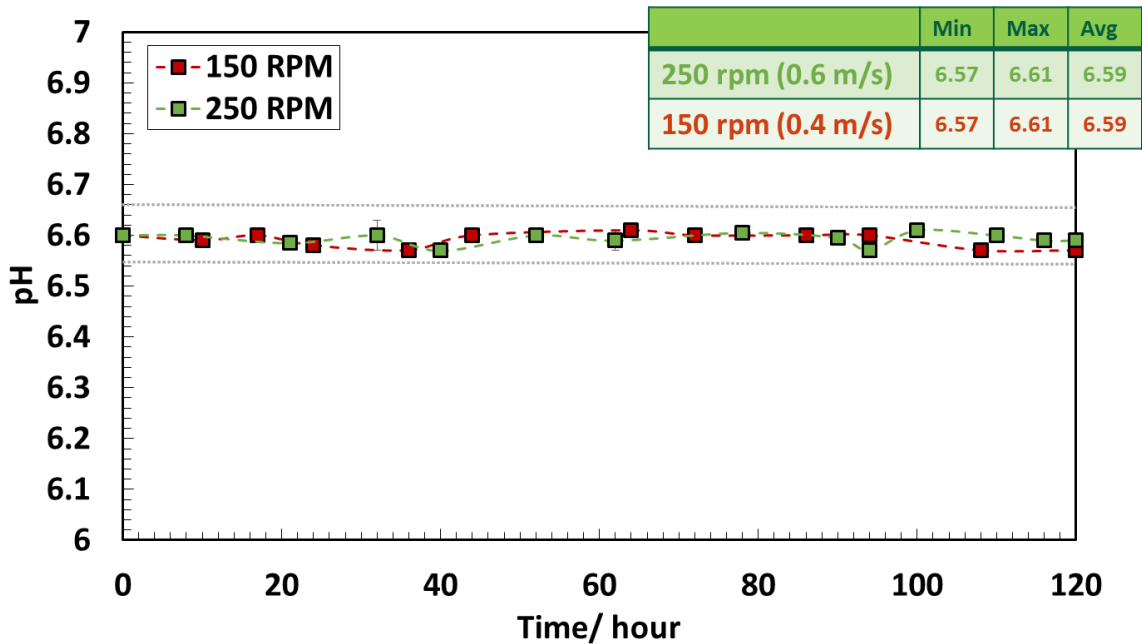


Figure 65. Comparison of pH change over time for 150 rpm ($V_{eq} = 0.4$ m/s, 0.3 Pa) and 250 rpm ($V_{eq} = 0.6$ m/s, 0.5 Pa) experiments with UNS G10180 tempered martensitic under the conditions: T=80°C, pCO₂ = 0.53 bar, pH 6.6, $S_{FeCO_3} \approx 10$

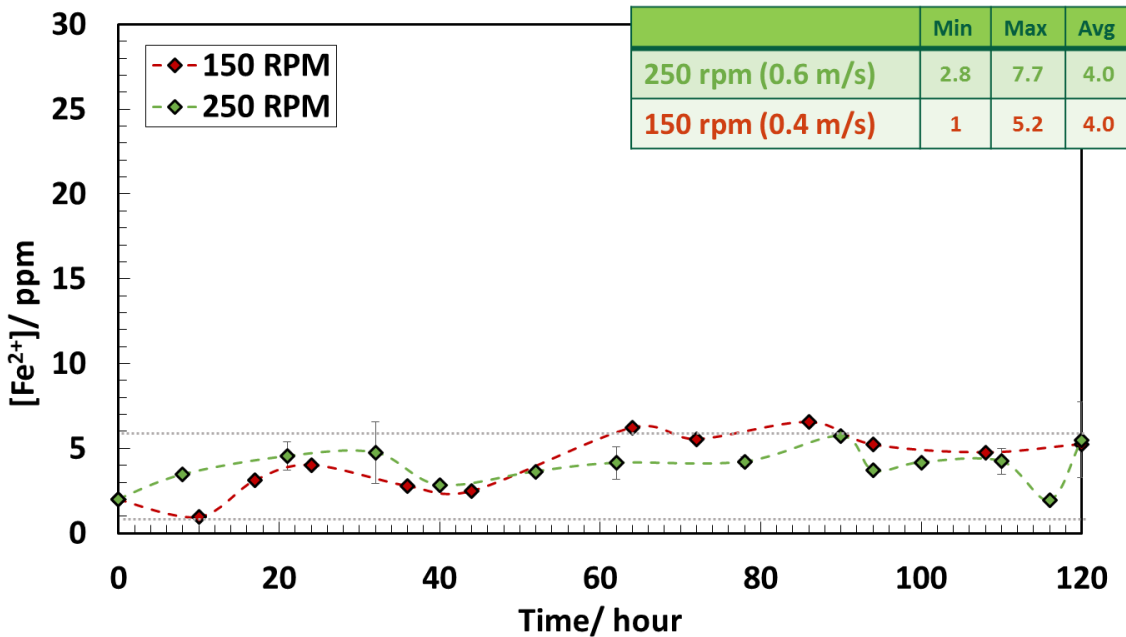


Figure 66. Comparison of $[Fe^{2+}]$ change over time for 150 rpm ($V_{eq} = 0.4$ m/s, 0.3 Pa) and 250 rpm ($V_{eq} = 0.6$ m/s, 0.5 Pa) experiments with UNS G10180 tempered martensitic under the conditions: $T=80^{\circ}C$, $pCO_2 = 0.53$ bar, pH 6.6, $S_{FeCO_3} \approx 10$

4.2.2.3.2 Corrosion Rate and Open Circuit Potential

Figure 67 shows the corrosion rate measurements obtained electrochemically over time. It can be seen, similar to the case of UNS G10180 ferritic-pearlitic, that corrosion rate increases over time. Once again, this is due to the preferential corrosion of the ferrite phase, leaving the Fe_3C behind which acts as a cathode^{8,46,47,49-54}. However, unlike UNS G10180 ferritic-pearlitic where various stages of corrosion were identified in the plot of LPR corrosion rate measurements, as shown in **Figure 59**, based on previous studies^{7,32}, UNS G10180 tempered martensite only showed an active corrosion stage. This trend may be an indication that no formation of $FeCO_3$ occurred since a low and steady corrosion rate was never achieved. Lastly, the corrosion rate obtained through weight loss measurements does not match the corrosion rate obtained through electrochemical measurements, which is

similar to the findings in UNS G10180 ferritic-pearlitic since the presence of Fe₃C accelerates electrochemical corrosion rates.

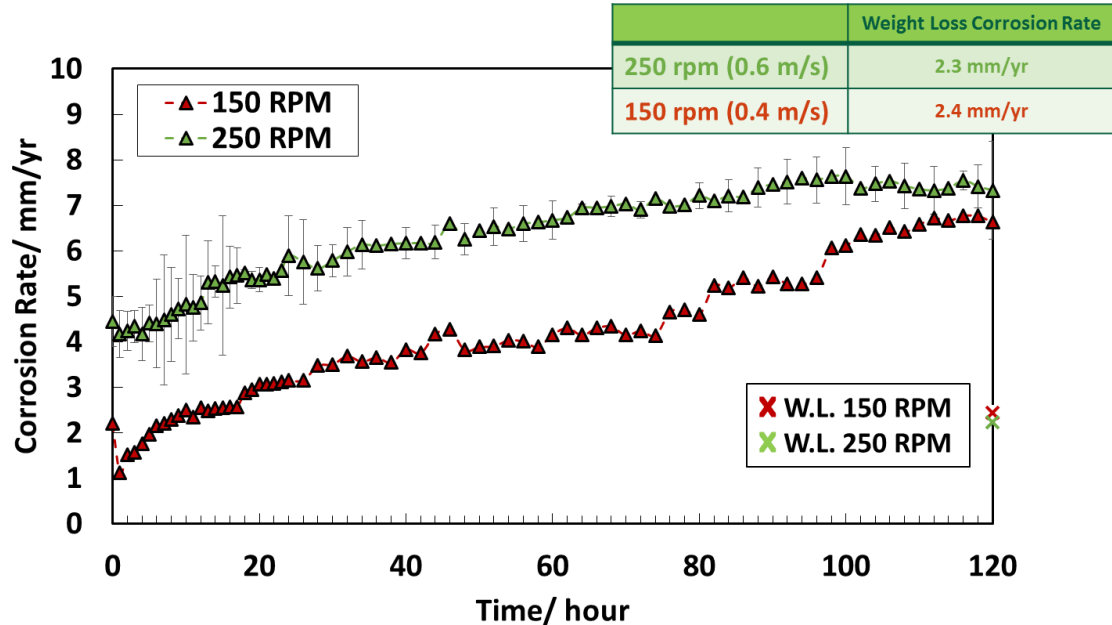


Figure 67. Comparison of LPR corrosion rate over time for 150 rpm ($V_{eq} = 0.4 \text{ m/s}, 0.3 \text{ Pa}$) and 250 rpm ($V_{eq} = 0.6 \text{ m/s}, 0.5 \text{ Pa}$) experiments with UNS G10180 tempered martensitic under the conditions: $T=80^{\circ}\text{C}$, $p\text{CO}_2 = 0.53 \text{ bar}$, $\text{pH} 6.6$, $S_{\text{FeCO}_3} \approx 10$

Figure 68 shows that the OCP was maintained at a steady value during the course of the experiment, and no evidence of pseudo-passivation occurred, as no sharp increase of OCP is observed^{34,82}.

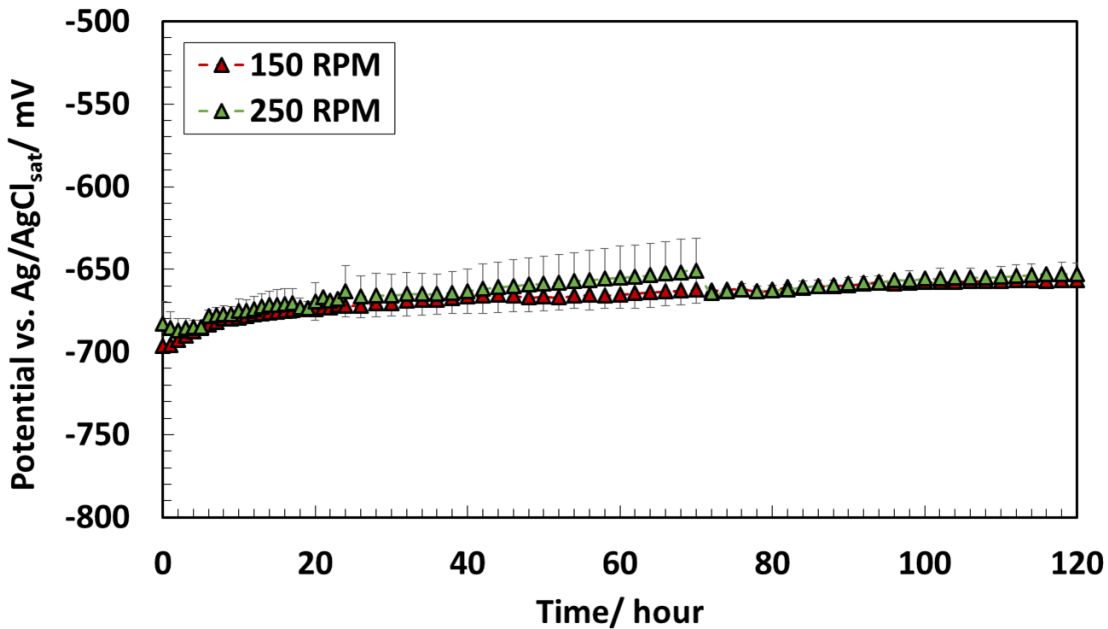


Figure 68. Comparison of OCP corrosion rate over time for 150 rpm ($V_{eq} = 0.4$ m/s, 0.3 Pa) and 250 rpm ($V_{eq} = 0.6$ m/s, 0.5 Pa) experiments with UNS G10180 tempered martensitic under the conditions: $T=80^{\circ}\text{C}$, $\text{pCO}_2 = 0.53$ bar, pH 6.6, $S_{\text{FeCO}_3} \approx 10$

4.2.2.3.3 Surface Morphologies and Characterization

Figure 69 shows SEM images of the surface of the sample for the 250 rpm ($V_{eq} = 0.6$ m/s, 0.5 Pa) and 150 rpm ($V_{eq} = 0.4$ m/s, 0.3 Pa) experiments taken out after the first, third, and fifth days of the experiment. The surface morphology of the samples taken out on the first day for both rotational velocities show a crinkly surface with more defined grooves on the 250 rpm ($V_{eq} = 0.6$ m/s, 0.5 Pa) sample than that for the 150 rpm ($V_{eq} = 0.4$ m/s, 0.3 Pa) experiment. Grooves became more defined and obvious, changing their appearance to that of a crack through the course of the experiments for both rotational speeds. Other researchers have found that these cracks can appear during the drying process, and were visible with the naked eye⁸³⁻⁸⁵. However, upon removal of specimens from test solution and drying, the surfaces remained smooth with no appearance of cracks.

Although the same trend is followed for both experiments, it can be observed that the 250 rpm ($V_{eq} = 0.6$ m/s, 0.5 Pa) condition shows wider cracks than those from the 150 rpm ($V_{eq} = 0.4$ m/s, 0.3 Pa) experiment. As for the case of UNS G10180 ferritic-pearlitic, cracks are related to exposure of a Fe₃C network^{7,34}. There is no evidence of FeCO₃ formation, as there is no presence of prismatic-shaped crystals on the steel surface, as was shown in **Figure 61** for the UNS G10180 ferritic-pearlitic material.

Figure 70 shows XRD analysis done on samples taken out on the last day for both rotational velocities. It can be seen that both 250 rpm ($V_{eq} = 0.6$ m/s, 0.5 Pa) and 150 rpm ($V_{eq} = 0.4$ m/s, 0.3 Pa) specimens show the presence of Fe₃C and iron, and an absence of FeCO₃. Nonetheless, the Fe₃C peaks for the 250 rpm ($V_{eq} = 0.6$ m/s, 0.5 Pa) sample are less pronounced than those from the 150 rpm ($V_{eq} = 0.4$ m/s, 0.3 Pa) XRD pattern. On the contrary, the pure iron peaks are more pronounced for the 250 rpm ($V_{eq} = 0.6$ m/s, 0.5 Pa) specimen than the 150 rpm ($V_{eq} = 0.4$ m/s, 0.3 Pa) specimen. This may be due to the thickness and compactness of the Fe₃C. Consequently, it is postulated that flow plays a role in the removal of some of the exposed Fe₃C on the steel surface.

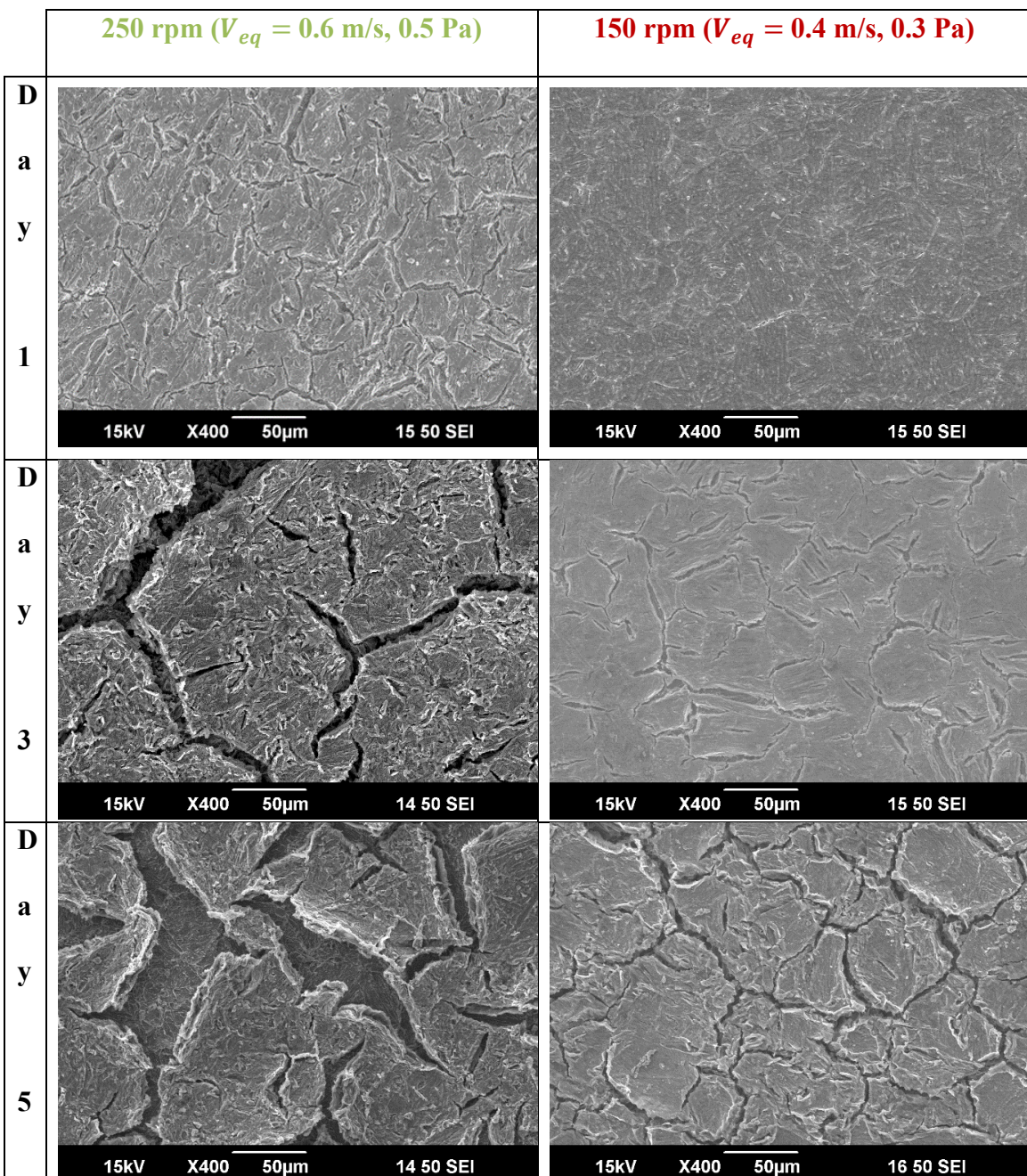


Figure 69. x400 SEM images showing comparison of surface morphologies over time for 150 rpm ($V_{eq} = 0.4 \text{ m/s}, 0.3 \text{ Pa}$) and 250 rpm ($V_{eq} = 0.6 \text{ m/s}, 0.5 \text{ Pa}$) experiments with UNS G10180 tempered martensitic under the conditions: $T=80^{\circ}\text{C}$, $p\text{CO}_2 = 0.53 \text{ bar}$, $\text{pH} = 6.6$, $S_{\text{FeCO}_3} \approx 10$

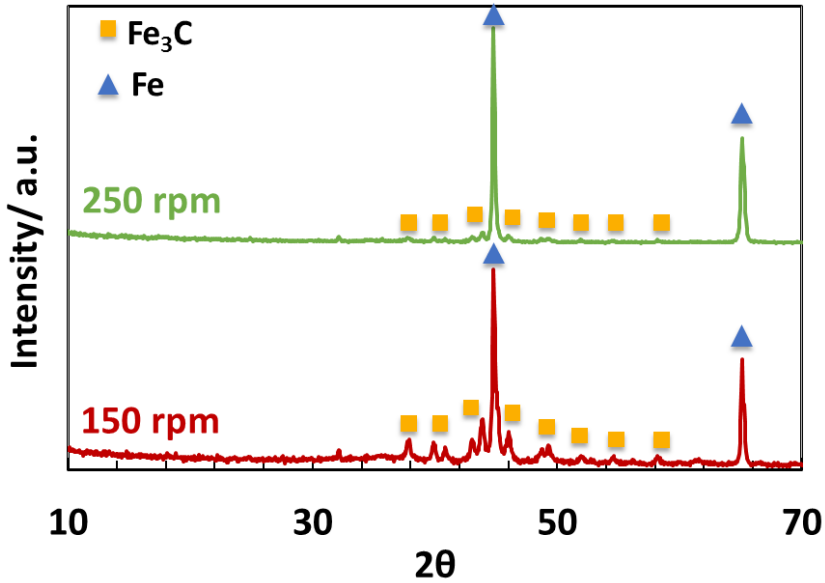


Figure 70. XRD analysis on UNS G10180 tempered martensitic day 5 specimens for 150 rpm ($V_{eq} = 0.4$ m/s, 0.3 Pa) and 250 rpm ($V_{eq} = 0.6$ m/s, 0.5 Pa) experiments under the conditions: T=80°C, pCO₂ = 0.53 bar, pH 6.6, S_{FeCO₃} ≈ 10

4.2.2.3.4 Cross-Sectional Morphologies

Figure 71 shows the cross sectional morphologies for the samples shown in **Figure 69**. After the first day there is no presence of corrosion product on the surface of steel, no significant corrosion has occurred at this time. On the third day, however, there is some development of Fe₃C on the surface of the specimens, as confirmed by an EDS line scan, shown in **Figure 72**. However, the thickness of the Fe₃C shown in the cross-sectional morphology does not match with the metal loss calculated from LPR corrosion rate measurements. This indicates that most of the Fe₃C has been removed by flow at this time. For both rotational velocities, the thickness of the Fe₃C is less than 10 μm, while the metal loss is more than doubled (~57 μm and 35 μm for the 250 rpm [$V_{eq} = 0.6$ m/s, 0.5 Pa]) and 150 rpm [$V_{eq} = 0.4$ m/s, 0.3 Pa] velocities, respectively). More Fe₃C has been removed in

the UNS G10180 material with a tempered martensite microstructure than the UNS G10180 with a ferritic-pearlitic microstructure. This can be attributed to the distribution of the cementite in the material microstructure as the ferrite phase dissolves at higher rates in a ferritic-pearlitic microstructure^{49,52}. The sample showing a cross-section from the last day shows some exposed Fe₃C on the surface of the sample but no presence of FeCO₃ within the pores of the Fe₃C. This may be associated with the fact that most of the Fe₃C has been sheared away by flow and no thick porous layer is allowed to be exposed which will eventually create a diffusion barrier for ferrous ion and favor precipitation of FeCO₃. This shows that although UNS G10180 tempered martensitic and UNS G10180 ferritic-pearlitic have the same carbon content, the microstructure plays a vital role for the formation of FeCO₃ within the Fe₃C matrix.

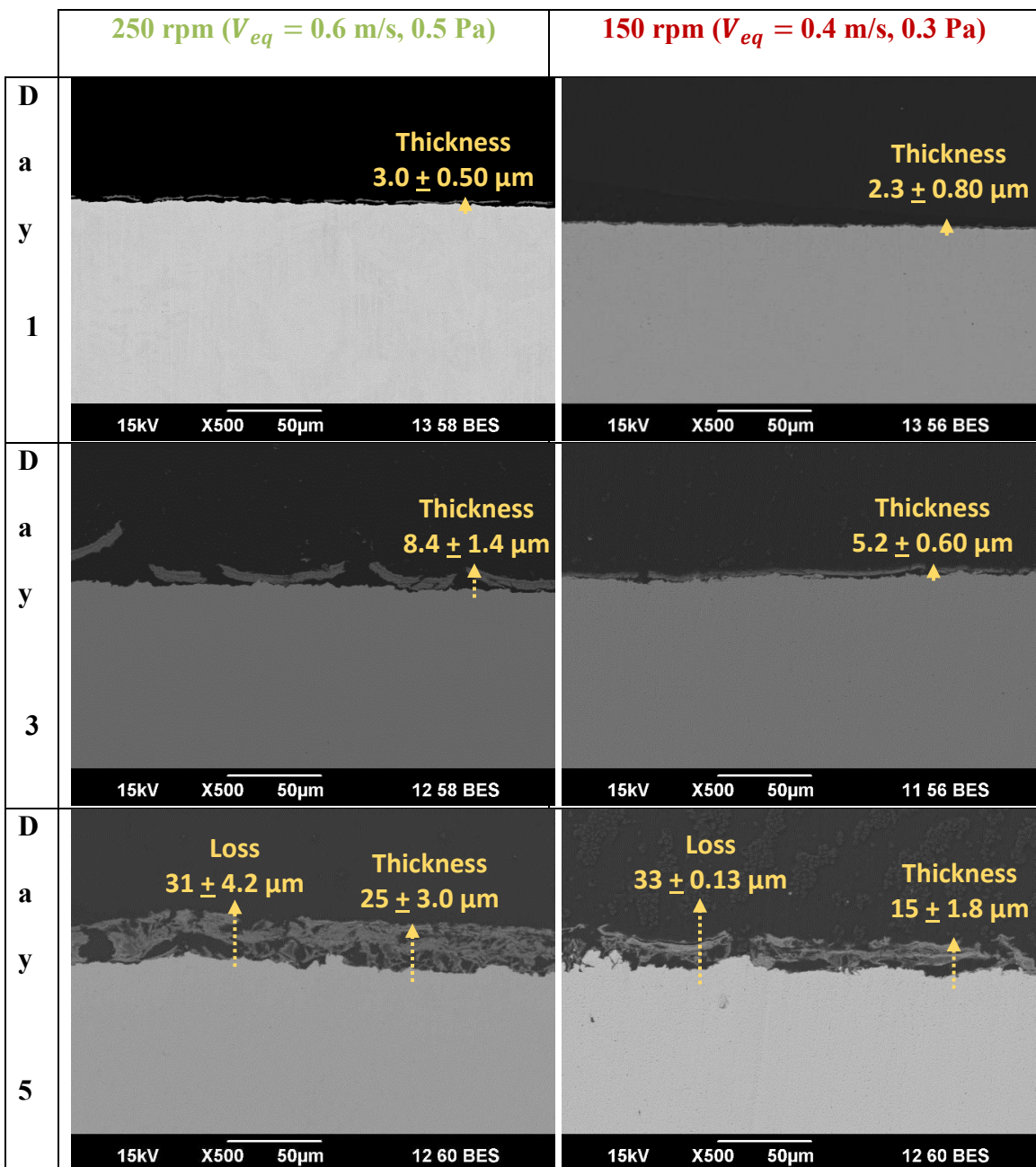


Figure 71. x500 SEM images showing cross-sectional morphologies over time for 150 rpm ($V_{eq} = 0.4 \text{ m/s}, 0.3 \text{ Pa}$) and 250 rpm ($V_{eq} = 0.6 \text{ m/s}, 0.5 \text{ Pa}$) experiments with UNS G10180 tempered martensitic and metal loss from LPR corrosion rate under the conditions: $T=80^\circ\text{C}$, $\text{pCO}_2 = 0.53 \text{ bar}$, $\text{pH } 6.6$, $S_{\text{FeCO}_3} \approx 10$

Figure 72 shows an EDS elemental line scan. From this figure, it can be observed that there is no obvious formation of FeCO_3 because there is no apparent oxygen peak.

However, the carbon peak in areas where it shows a Fe₃C matrix shows a higher intensity than the steel, which may give further confirmation of the presence of Fe₃C. It is noteworthy that the alloying elements copper and chromium show enrichment in the outermost region of the corrosion product layer.

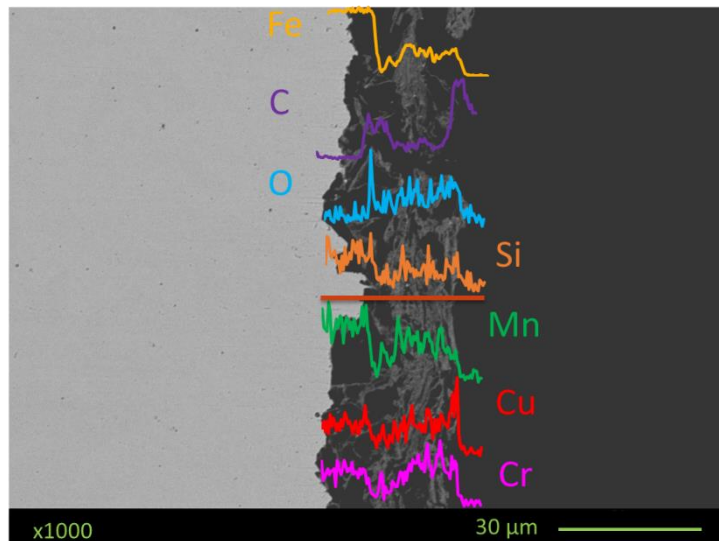


Figure 72. x1000 SEM image showing cross-sectional elemental mapping of UNS G10180 tempered martensitic on day 5 at 150 rpm ($V_{eq} = 0.4$ m/s, 0.3 Pa) under the conditions: T=80°C, pCO₂ = 0.53 bar, pH 6.6, S_{FeCO₃} ≈ 10

4.2.2.4 API 5L X65

4.2.2.4.1 Water Chemistry

Figure 73 and **Figure 74** show changes in pH and ferrous ion concentration, respectively, for both rotational velocities for the entire duration of experiments. As has been the case for all materials and velocities tested so far, pH values and ferrous ion concentration were well controlled and stable for all experiments over their entire duration. This proves that all ion exchange resins for controlling both pH and ferrous ion

concentration work regardless of material, microstructure, and carbon content. Minor deviations from starting values ensure that environmental conditions do not become a controlling factor in observed results. Peaks in ferrous ion concentration, such as the one shown on the 24th hour for the 250 rpm ($V_{eq} = 0.6 \text{ m/s}$, 0.5 Pa) experiment, were controlled by either adjusting flow rate of electrolyte going through the ion exchange resin or adjusting the timer which controls how long electrolyte will run through the ion exchange resin.

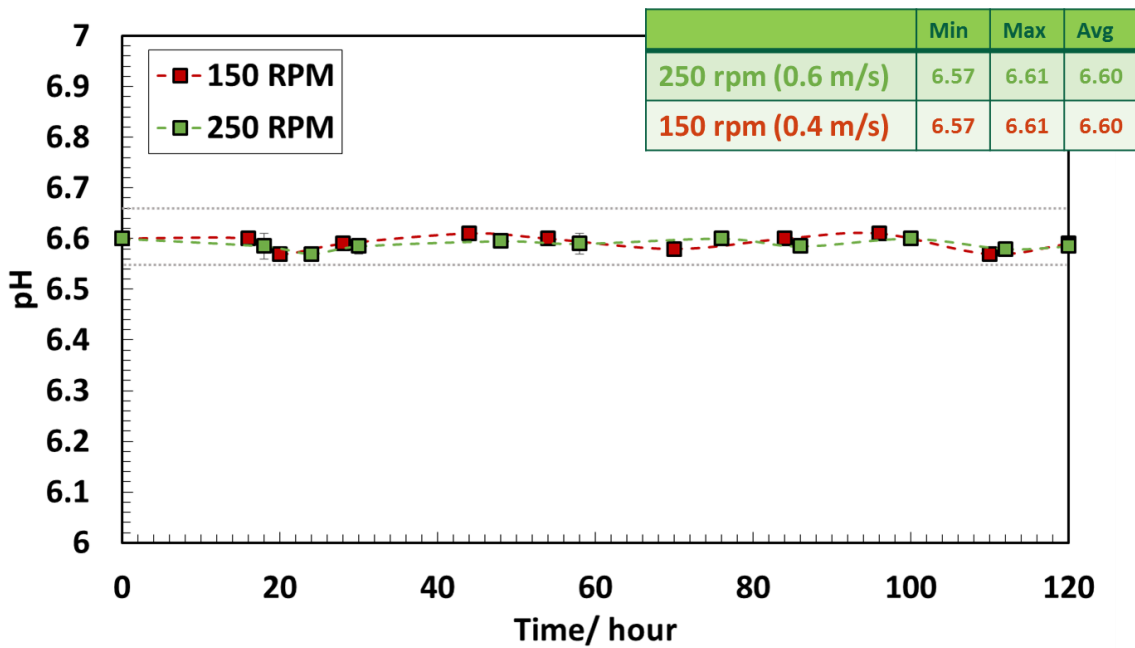


Figure 73. Comparison of pH change over time for 150 rpm ($V_{eq} = 0.4 \text{ m/s}$, 0.3 Pa) and 250 rpm ($V_{eq} = 0.6 \text{ m/s}$, 0.5 Pa) experiments with API 5L X65 under the conditions:
 $T=80^{\circ}\text{C}$, $p\text{CO}_2 = 0.53 \text{ bar}$, $\text{pH } 6.6$, $S_{\text{FeCO}_3} \approx 10$

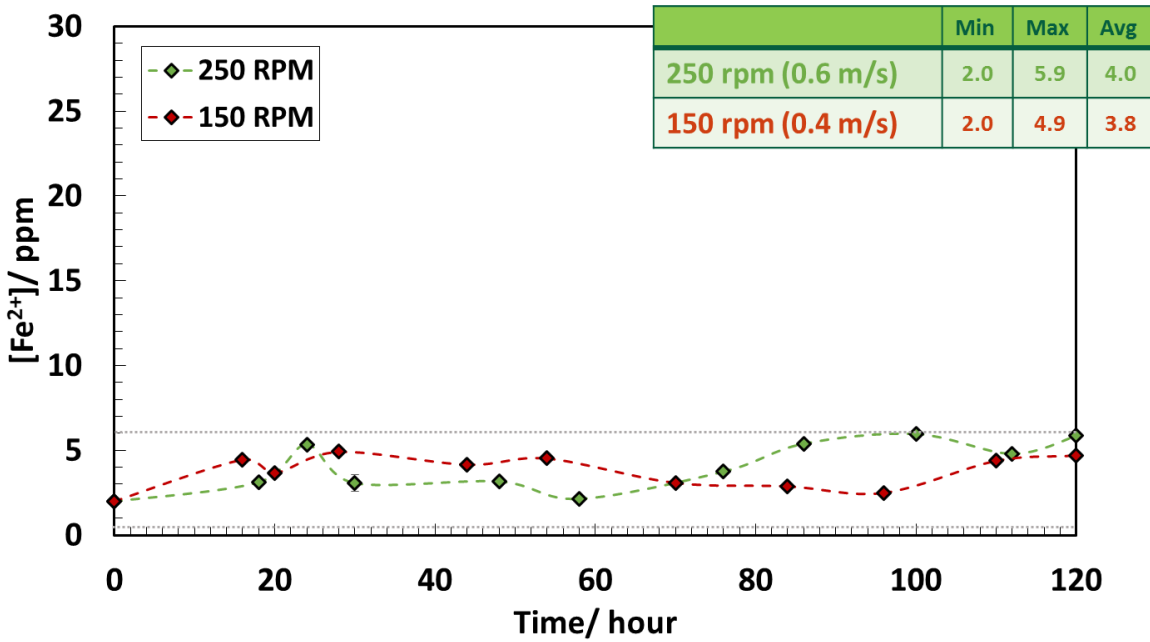


Figure 74. Comparison of $[Fe^{2+}]$ change over time for 150 rpm ($V_{eq} = 0.4$ m/s, 0.3 Pa) and 250 rpm ($V_{eq} = 0.6$ m/s, 0.5 Pa) experiments with API 5L X65 under the conditions:

$$T=80^{\circ}\text{C}, \text{pCO}_2 = 0.53 \text{ bar}, \text{pH } 6.6, S_{\text{FeCO}_3} \approx 10$$

4.2.2.4.2 Corrosion Rate and Open Circuit Potential

Figure 75 shows the corrosion rate over time for both the 150 rpm ($V_{eq} = 0.4$ m/s, 0.3 Pa) and 250 rpm ($V_{eq} = 0.6$ m/s, 0.5 Pa) experiments. It can be seen that corrosion rates stay stable over time and do not increase, which has been previously referred to as the active corrosion stage and associated with formation of Fe_3C ^{7,32}. In fact, the LPR corrosion rate measurements follow a similar trend to that of pure Fe, as shown in **Figure 49**. This may be associated with the fact that the carbon content of this material is low (0.05 wt.%) and the Fe_3C exposed was weak enough to be sheared away by flow and thus not affect the corrosion rate. Previously, it has been found that the carbon content does affect corrosion rate of steels, as reported in these findings^{41,45,46}. Additionally, the distribution of Fe_3C also affects corrosion rate behavior^{51,52}; however a study performed by Al-Hassan,

et al., concluded that there is no true effect of microstructure at temperatures above 60°C on corrosion rates⁵², which contradicts these findings, as shown in **Figure 49**, **Figure 59**, **Figure 67**, **Figure 75**. Clearly, the findings show different corrosion rate behavior depending on the microstructure and carbon content, which correlate with previous studies^{7,32,52}.

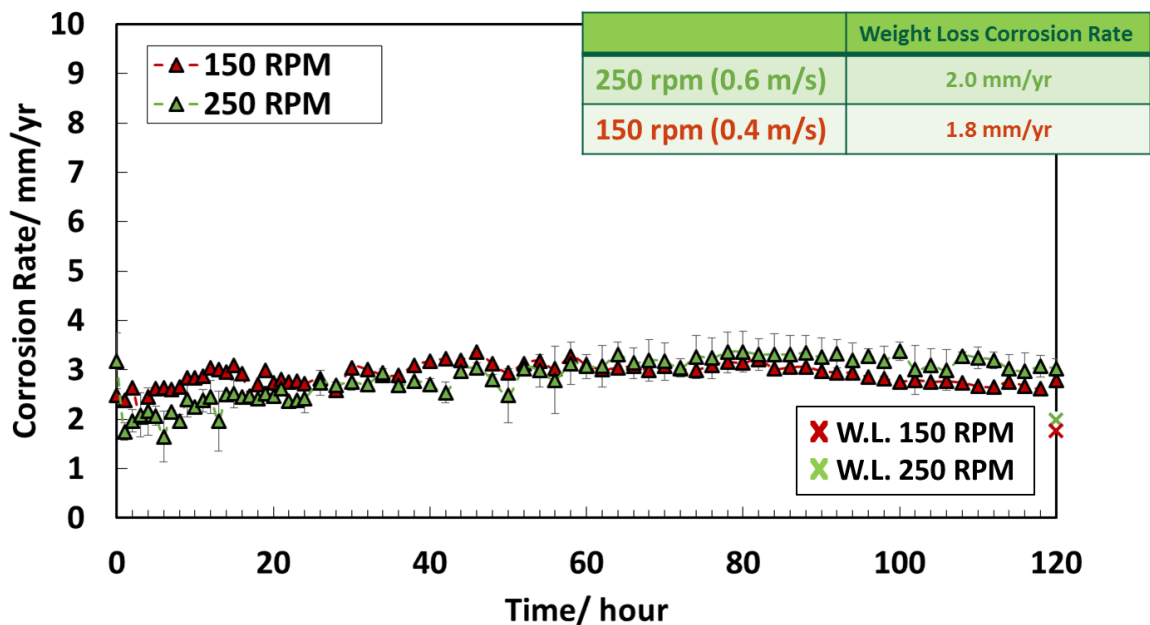


Figure 75. Comparison of LPR corrosion rate over time for 150 rpm ($V_{eq} = 0.4 \text{ m/s}, 0.3 \text{ Pa}$) and 250 rpm ($V_{eq} = 0.6 \text{ m/s}, 0.5 \text{ Pa}$) experiments with API 5L X65 under the conditions: $T=80^{\circ}\text{C}$, $\text{pCO}_2 = 0.53 \text{ bar}$, $\text{pH } 6.6$, $S_{\text{FeCO}_3} \approx 10$

Figure 76 shows OCP throughout the course of experiments, which is similar to what has been found before for pure Fe, and UNS G10180 tempered martensitic (**Figure 50** and **Figure 68** respectively).

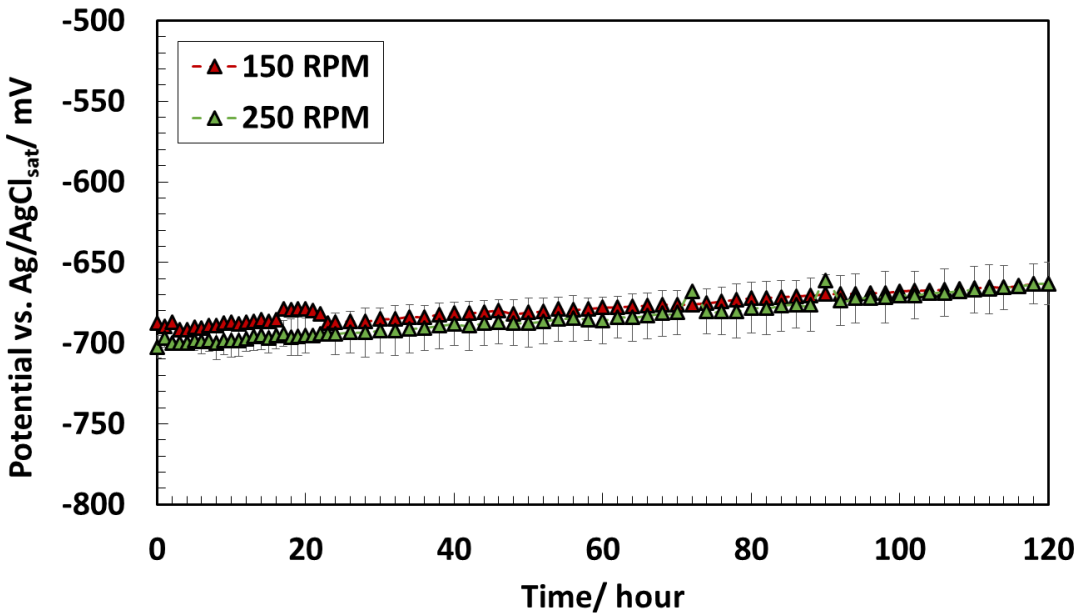


Figure 76. Comparison of OCP over time for 150 rpm ($V_{eq} = 0.4$ m/s, 0.3 Pa) and 250 rpm ($V_{eq} = 0.6$ m/s, 0.5 Pa) with API 5L X65 under conditions: $T=80^{\circ}\text{C}$, $\text{pCO}_2 = 0.53$ bar, pH 6.6, $S_{\text{FeCO}_3} \approx 10$

4.2.2.4.3 Surface Morphologies and Characterization

Figure 77 shows the changes on surface morphology during the course of the experiment. No major differences are observed on the surface of the samples taken out after the first day, both specimens show a rough surface. Nevertheless, some differences are noted on the surface of the samples as grooves are witnessed on the 150 rpm ($V_{eq} = 0.4$ m/s, 0.3 Pa) sample and not on the 250 rpm ($V_{eq} = 0.6$ m/s, 0.5 Pa) sample. On the last day, grooves are more noticeable on the specimen retried from the 250 rpm ($V_{eq} = 0.6$ m/s, 0.5 Pa) experiment than from the 150 rpm ($V_{eq} = 0.4$ m/s, 0.3 Pa) test. These grooves are different from those shown in **Figure 71** for UNS G10180 tempered martensitic, since the grooves on those samples appear to be continuous and form a crack. These cracks have the same morphology as seen in previous studies, where these cracks have been associated

with Fe₃C presence^{7,34}. FeCO₃ is absent as there are no precipitated crystals on the surface of the samples.

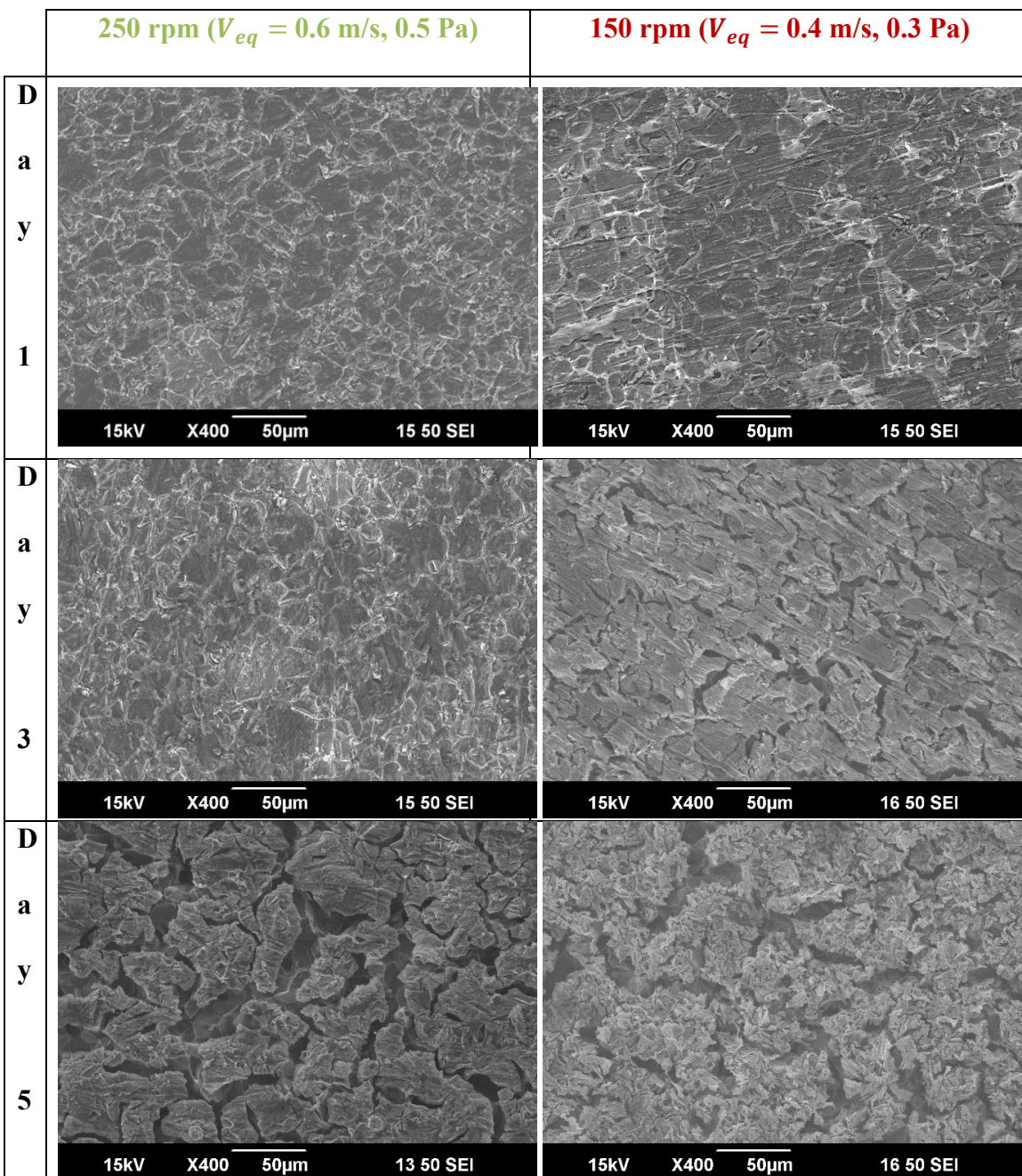


Figure 77. x400 SEM images showing comparison of surface morphologies over time for 150 rpm ($V_{eq} = 0.4 \text{ m/s}, 0.3 \text{ Pa}$) and 250 rpm ($V_{eq} = 0.6 \text{ m/s}, 0.5 \text{ Pa}$) experiments with API 5L X65 under the conditions: $T=80^\circ\text{C}$, $p\text{CO}_2 = 0.53 \text{ bar}$, pH 6.6, $S_{\text{FeCO}_3} \approx 10$

Figure 78 shows the XRD patterns for the surface of the sample taken out on the last day of the experiment. It can be seen that only pure iron (α -Fe) peaks are present, and

no corrosion products are identified, such as FeCO_3 and Fe_3C , indicating that Fe_3C was either never present or removed by flow, which may be due either to the low carbon content^{41,45,46} or the distribution of the Fe_3C ⁵².

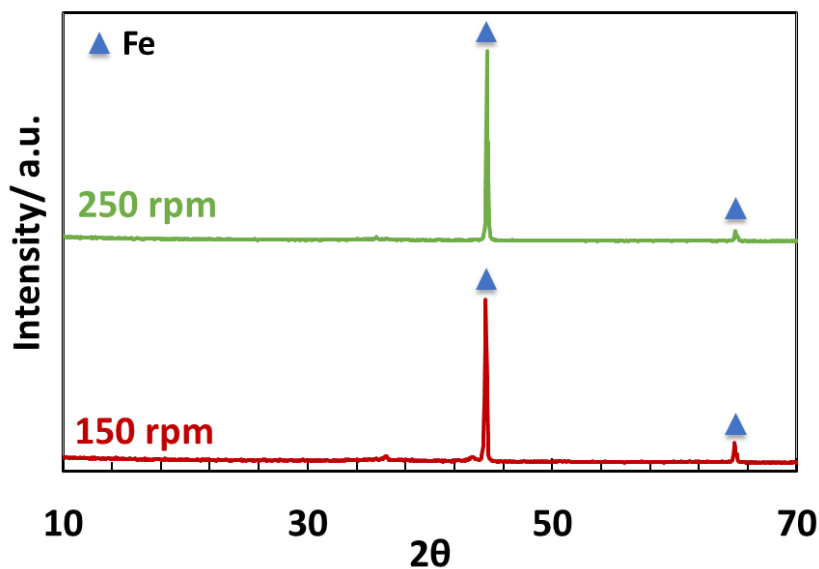


Figure 78. XRD analysis on API 5L X65 day 5 surface specimens for 150 rpm ($V_{eq} = 0.4$ m/s, 0.3 Pa) and 250 rpm ($V_{eq} = 0.6$ m/s, 0.5 Pa) experiments under the conditions:
 $T=80^{\circ}\text{C}$, $p\text{CO}_2 = 0.53$ bar, pH 6.6, $S_{\text{FeCO}_3} \approx 10$

4.2.2.4.4 Cross-Sectional Morphologies

Figure 79 shows cross-sectional morphologies of the samples shown in **Figure 77**. There is no significant evidence of Fe_3C up to the first three days of corrosion. On the fifth day, however, a thin layer appears on the steel surface. This was confirmed by EDS to be a thin layer of Fe_3C and alloying elements, as shown in **Figure 80**. This correlates with the surface morphologies obtained by SEM, but not XRD analysis, as shown in **Figure 78**. This can be attributed to the fact that the Fe_3C is very thin and could not be detected by

XRD; due to the penetration depth by incident X-rays governing magnitude of detected diffraction peaks.

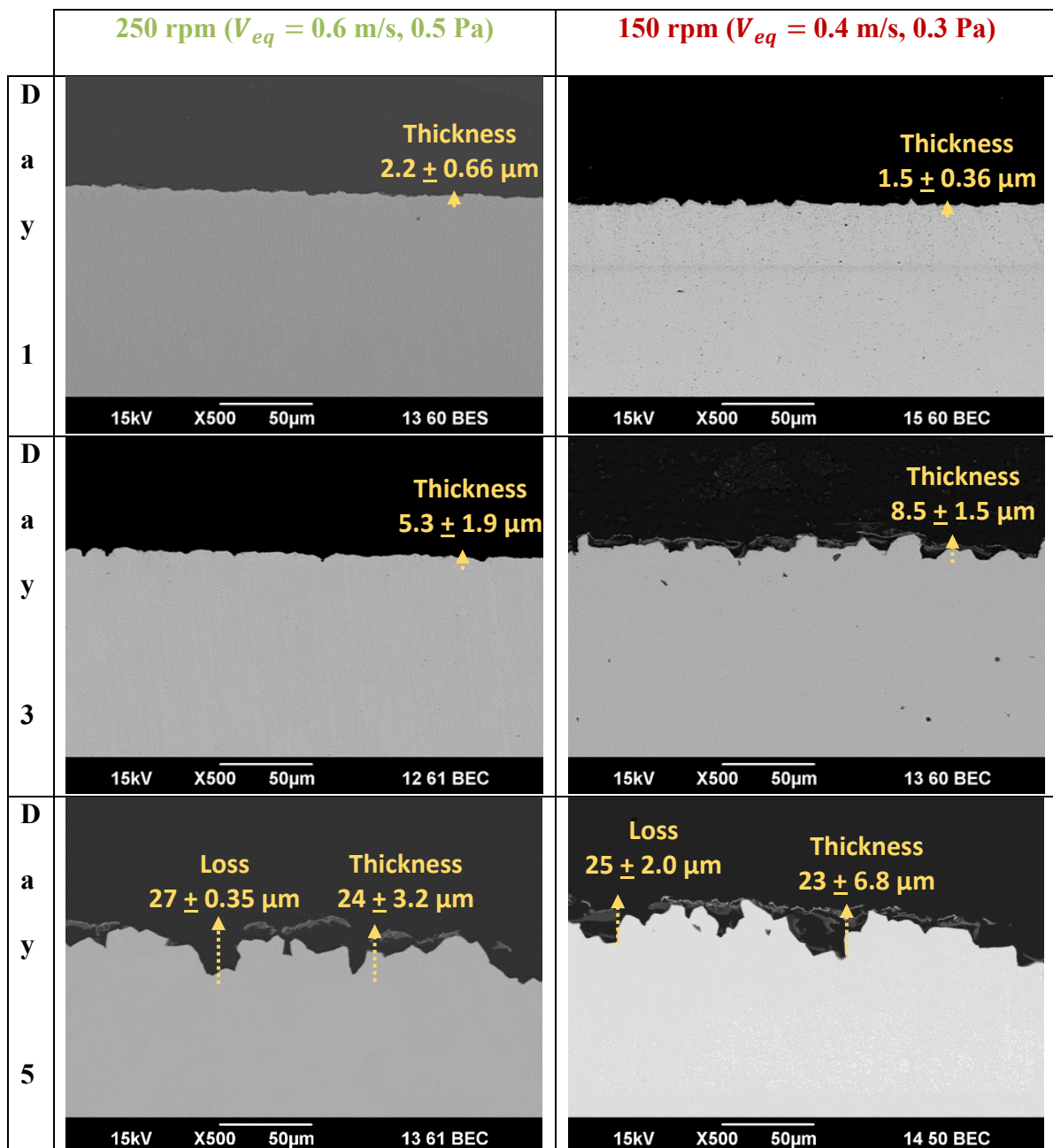


Figure 79. x500 SEM images showing cross-sectional morphologies over time for 150 rpm ($V_{eq} = 0.4 \text{ m/s}, 0.3 \text{ Pa}$) and 250 rpm ($V_{eq} = 0.6 \text{ m/s}, 0.5 \text{ Pa}$) experiments with API 5L X65 and metal loss from LPR corrosion rate under the conditions: $T=80^\circ\text{C}$, $\text{pCO}_2 = 0.53 \text{ bar}$, $\text{pH } 6.6$, $S_{\text{FeCO}_3} \approx 10$

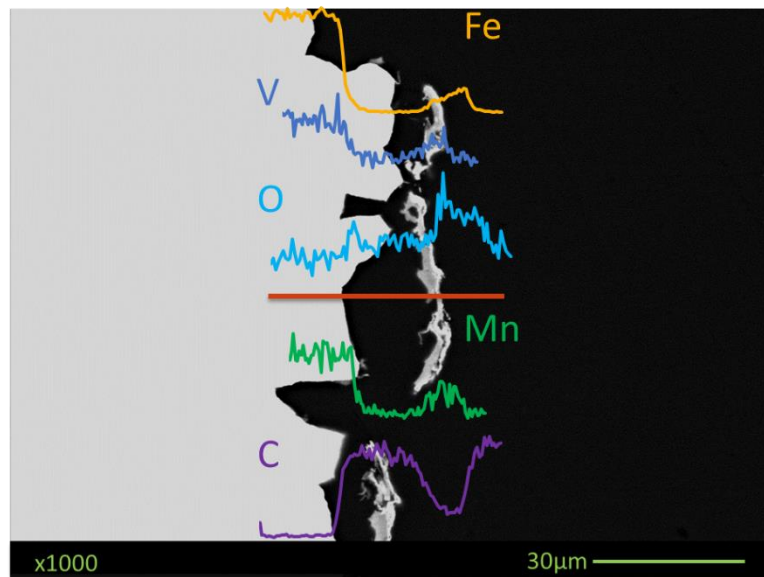


Figure 80. x1000 SEM image showing cross-sectional elemental mapping of API 5L X65 on day 5 at 150 rpm ($V_{eq} = 0.4$ m/s, 0.3 Pa) under the conditions: $T=80^{\circ}\text{C}$, $p\text{CO}_2 = 0.53$ bar, pH 6.6, $S_{\text{FeCO}_3} \approx 10$

4.2.3 Summary

An impeller setup was used and improved upon from the RCE setup discussed in section 4.1 in order to provide a controlled mass transfer and water chemistry environment. the main finding is that, under turbulent conditions, only a ferritic-pearlitic specific microstructure with a high carbon content aided in FeCO_3 formation.

The next section focuses on the effect of shear stress on iron carbide characteristics and utilizes a different experimental setup: the thin channel flow cell or TCFC. For reproducibility purposes, the first test is run in conditions similar to one of the “impeller” experiment. The results obtained in the impeller setup at the equivalent pipeline velocity of 0.6 m/s are compared with the results obtained in the TCFC at $V_{eq} = 0.75$ m/s, 0.8 Pa.

4.3 Task # 3: Removal of Fe₃C

The objective of this set of experiments is to identify the velocity required to remove the Fe₃C matrix from the steel surface, which will prohibit further formation of FeCO₃.

4.3.1 *Methodology*

This set of experiment were carried out in an equipment built in-house called the Thin Channel Flow Cell (TCFC), shown in **Figure 81**. Experiments were conducted at three different velocities, higher than those tested in tasks # 1 and # 2. **Table 9** summarizes all of the experimental parameters used in this set of experiments.



Figure 81. Thin channel flow cell (TCFC) (image courtesy of Cody Shafer, ICMT)

Table 9. Test matrix for task # 3: removal of Fe₃C

Material	UNS G10180 ferritic-pearlitic
Flow Velocities (m/s)	0.6, 2 and 6
Shear Stress (Pa)	0.8, 20 and 100
Experimental Setup	TCFC
Electrolyte	1 wt.% NaCl
Initial pH	6.6 ± 0.01
Temperature (°C)	80
Total Pressure (bar)	1.0
CO ₂ Partial Pressure (bar)	0.53
Initial [Fe ²⁺] (ppm)	2
Initial Saturation w.r.t FeCO ₃	10
Electrochemical Measurements	LPR ±5 mV vs. EOC, 0.125 mV/s B = 26 mV/decade EIS 0 mV vs. EOC, Frequency range: 5000- 0.1 Hz.
Surface Analysis	SEM EDS Raman Cross-section

4.3.1.1 Experimental Setup

Figure 81 shows the experimental setup used for this set of experiments, which require higher velocity experiments beyond the capability of the RCE and impeller setups described in task 1 and task 2, respectively. The Thin Channel Flow Cell, shown in **Figure**

81, is a well-defined 316 L stainless steel single phase flow system that can reach a velocity of up to 17 m/s⁸⁶⁻⁸⁸. The tank of the TCFC, which has a maximum capacity of 40 gallons, was filled with 35 gallons of 1 wt.% NaCl. NaHCO₃ was also added to the salt solution to adjust the pH to 6.60. The solution in the TCFC was sparged with CO₂ for 4 hours for deoxygenation of the solution. The experiments were conducted at ambient pressure and, as discussed in previous methodologies, the partial pressure of CO₂ was 0.53 bar at the temperature of 80°C. Two valves are located upstream and downstream of the cell shown in **Figure 82**, where samples are mounted. These valves can isolate the test section from the rest of the system, enabling mounting of the samples only once the experimental conditions have been reached and avoiding any oxygen contamination. A centrifugal pump, shown in **Figure 82**, circulated the fluid in the TCFC. A flow meter was located downstream of the test section shown in **Figure 83**, which gave a mean volumetric flow rate. This rate was adjusted according to the desired surface velocities by adjusting the pump. The flow test section is approximately 89 mm wide and 3 mm tall, shown in **Figure 83**; the fluid velocity on the specimen surface was calculated based on the flow rate obtained from the meter on the TCFC and the flow test section dimensions.

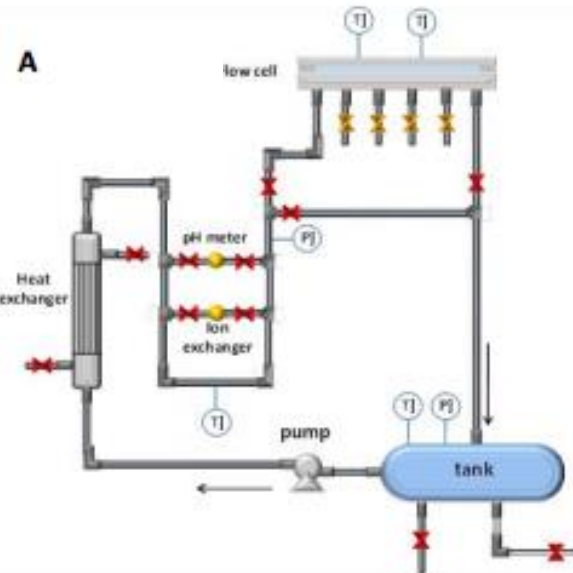


Figure 82. Piping & instrumentation diagram of the TCFC⁸⁶⁻⁸⁸

Figure 83 shows where samples used for characterization and the probe for electrochemical measurements are mounted.

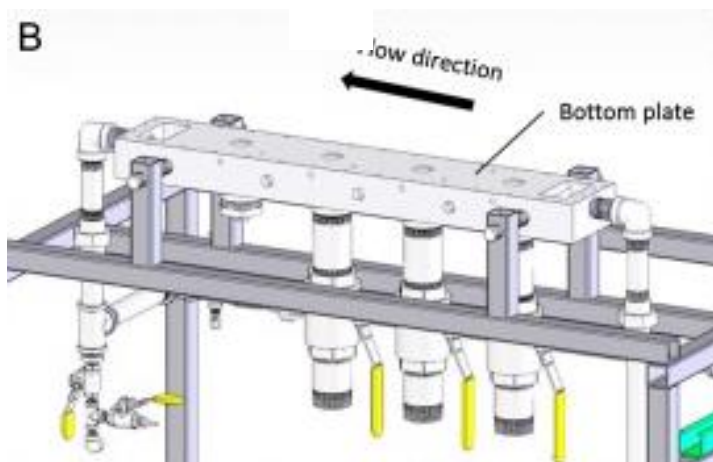


Figure 83. Specimen mount and flow test section of TCFC⁸⁷

Figure 84 shows the specimens configuration. **Figure 84 (a)** presents the electrochemical sample used for LPR measurements; the working electrode has a surface

area of *ca.* 0.88 cm². **Figure 84** (b) shows the mild steel probe assembly used for surface and cross-sectional analysis; these samples have a surface area *ca.* 7 cm². Prior to mounting samples on the TCFC ports, the back and the sides of the specimens were coated with Xylan® coating to avoid any corrosion at the sides of the specimens.

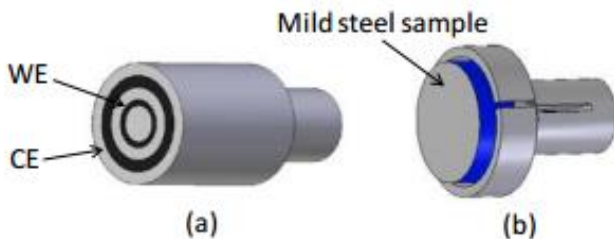


Figure 84. Specimens used for TCFC experiments (a) electrochemical specimen (b) characterization specimens⁷

4.3.1.2 Water Chemistry

Once an initial, repeatable LPR measurement was taken, aqueous FeCl₂ was injected into the solution to reach the desired starting ferrous ion concentration of 2 ppm. The aqueous FeCl₂ was prepared by dissolving 3.1 grams of ferrous chloride tetrahydrate (FeCl₂·4H₂O) in 50 mL of deionized water sparged with nitrogen gas, N₂, for 30 minutes (oxygen free solution); 15 mL of this solution was then added into the TCFC with the use of a syringe. By following this procedure the saturation of the solution is 10, according to equation (15). Ferrous ion concentration in solution was measured at appropriate time intervals during the course of the experiment using a spectrophotometer.

4.3.1.3 Electrochemical Measurements

Electrochemical measurements for this set of experiments were taken following the same procedure from task # 1, found in section 4.

4.3.1.4 Flow Velocities

As described in the experimental setup section, the mean volumetric flow rate is obtained by a flow meter installed downstream of the thin channel test section. Using the cross-sectional dimensions of the test section, shown in **Figure 83**, a mean velocity can be obtained. Li obtained wall shear stress measurements using a floating element sensor and compared his results with Patel's correlations⁸⁶⁻⁸⁹. **Figure 85** shows that Li's results have a good agreement with Patel's correlations. The wall shear stress corresponding to the experimental velocities tested were gathered from **Figure 85** and shown in **Table 9**. **Table 10** summarizes the TCFC fluid velocities chosen for experimental runs, wall shear stresses as well as the equivalent pipeline velocity calculated using the Sherwood correlation for a smooth pipe.

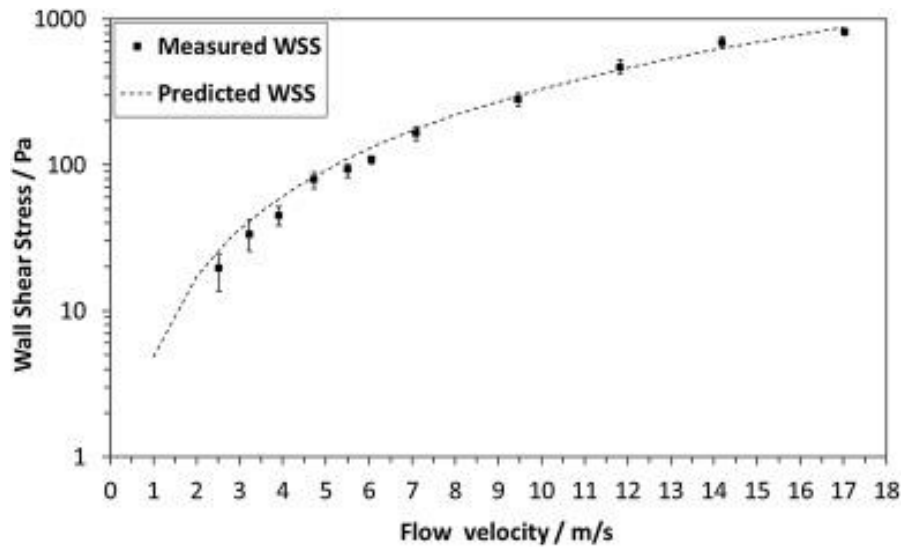


Figure 85. Comparison of Patel's correlations⁸⁹ with Li's experimental results using a floating element sensor⁸⁶⁻⁸⁸

Table 10. Summary of TCFC flow velocities, wall shear stresses and corresponding pipe fluid velocities

TCFC Mean Velocity (m/s)	V_{eq} , Equivalent Velocity in 25.5 cm ID pipe (m/s)	Wall Shear Stress (Pa)
0.4	0.75	0.8
2	4.7	20
6	12.0	100

4.3.1.5 Materials Composition and Choice

UNS G10180 was chosen as the material to be tested in this set of experiments since this material showed Fe₃C residues as demonstrated by XRD and cross-sectional analysis, as shown in **Figure 62**, **Figure 63**, **Figure 70**, and **Figure 71**. The composition of UNS G10180 is shown in **Table 8**. The microstructure of the UNS G10180 material chosen for experiments conducted in the TCFC setup was ferritic-pearlitic as this microstructure showed clear tendency to facilitate FeCO₃ formation.

4.3.1.6 Sample Characterization

The duration of the experiment was set to five days. The experimental set up allows three specimens for characterization and analysis. One specimen was removed on the third day, and the last two on the fifth/last day. Specimens were not taken out on the first day as no significant Fe₃C has formed at this time, based on results from task # 2, as shown in **Figure 63** and **Figure 71**. By retrieving two specimens on the last day of the experiment, this can assure the accuracy of the results without repeating experiments at the same conditions. Specimens were removed from the mount section, shown in **Figure 83**, and cleaned with N₂ sparged deionized water, rinsed with isopropyl alcohol, and dried with

cold air. Specimens were stored in a dessicator cabinet to avoid any oxygen contamination and subsequent surface oxidation. SEM was used to characterize the surface morphology for one sample on day one, and two on the last day of the experiment. Once the surface characterization was finished, the sample was mounted in epoxy for cross-sectional analysis using SEM; as before that was used to characterize layer morphology, thickness, surface topography, as well as any formation of FeCO_3 within the Fe_3C network, if any. The EDS coupled to the SEM was also used for elemental analysis. Raman analysis was performed using Witec Alpha 300 Confocal Raman through x20 objective lenses to properly characterize corrosion products. The laser detector was used at a 532 nm wavelength at a laser intensity of $\sim 1000 \text{ kW/cm}^2$.

4.3.1.7 *Weight Loss Measurements per ASTM G1-03⁸¹*

Weight loss measurements for this set of experiments were taken following the same procedure from task # 2, found in section 4.2.1.8.

4.3.2 *Results and Discussion*

4.3.2.1 *Water Chemistry*

Figure 86 and **Figure 87** show changes in water chemistry, pH and ferrous ion concentration, respectively, in the TCFC set up for the UNS G10180 ferritic-pearlitic tested at three different velocities. It can be seen that some deviations from the initial pH and ferrous ion concentration are noticed, due to the fact that water chemistry was not controlled as opposed to experimentations described in section 4.2. Changes in water chemistry, especially in pH, can result in saturation value, S_{FeCO_3} , deviations. However, changes in water chemistry are not drastic and do not affect the results of this set of

experimentations, Thus, the removal of Fe_3C can be properly analyzed without any environmental factors affecting validity of the results.

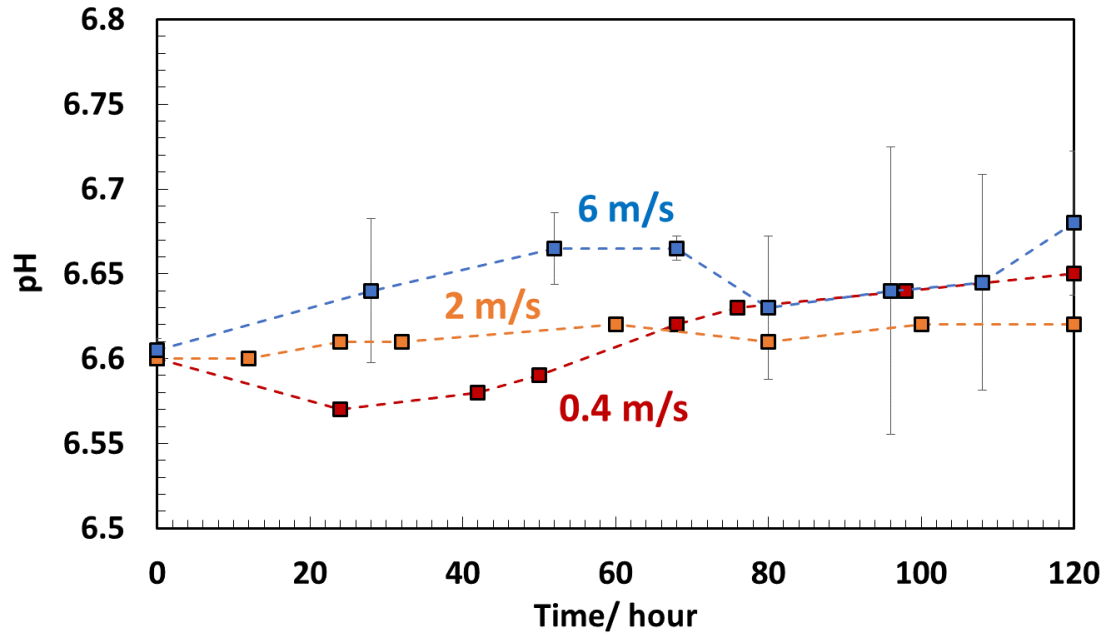


Figure 86. Comparison of pH change over time for 0.4 m/s ($V_{eq} = 0.75 \text{ m/s}, 0.8 \text{ Pa}$), 2 m/s ($V_{eq} = 4.7 \text{ m/s}, 20 \text{ Pa}$) and 6 m/s ($V_{eq} = 12 \text{ m/s}, 100 \text{ Pa}$) experiments with UNS G10180 ferritic-pearlitic under the conditions: $T=80^{\circ}\text{C}$, $\text{pCO}_2 = 0.53 \text{ bar}$, initial pH 6.6, initial $S_{\text{FeCO}_3} \approx 10$

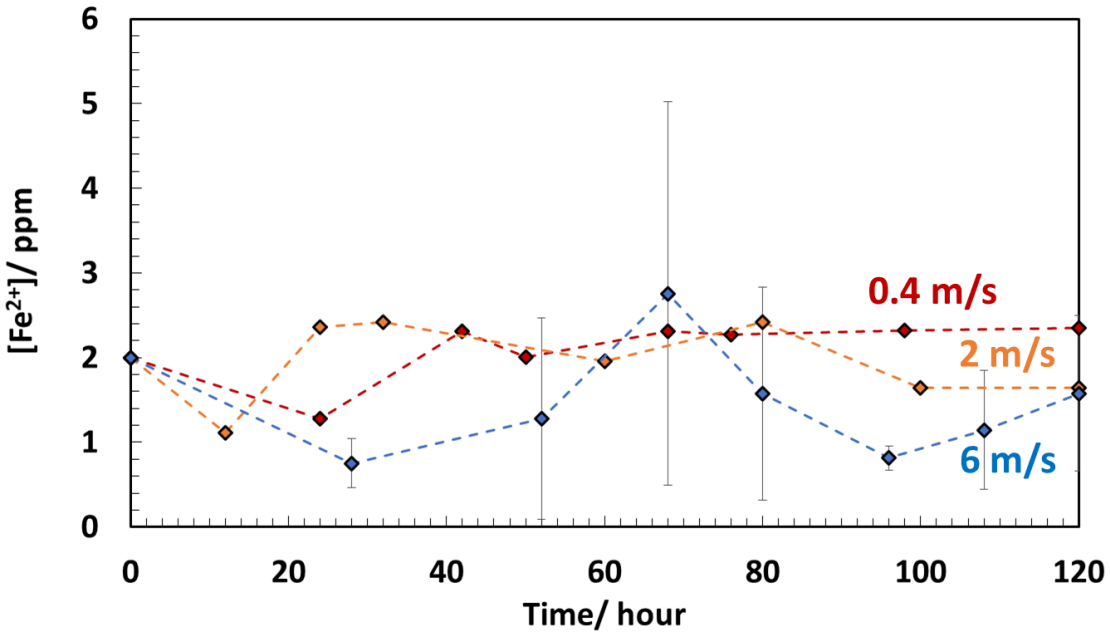


Figure 87. Comparison of $[Fe^{2+}]$ change over time for 0.4 m/s ($V_{eq} = 0.75$ m/s, 0.8 Pa), 2 m/s ($V_{eq} = 4.7$ m/s, 20 Pa) and 6 m/s ($V_{eq} = 12$ m/s, 100 Pa) experiments with UNS G10180 ferritic-pearlitic under the conditions: $T=80^{\circ}C$, $pCO_2 = 0.53$ bar, initial pH 6.6, initial $S_{FeCO_3} \approx 10$

4.3.2.2 Corrosion Rate

Figure 88 shows LPR corrosion rate measurements during the course of the experiments with UNS G10180 ferritic-pearlitic tested at three different velocities. It can be seen that for the 0.4 m/s ($V_{eq} = 0.75$ m/s, 0.8 Pa) and 2 m/s ($V_{eq} = 4.7$ m/s, 20 Pa), the corrosion rate increases over time until reaching a value of about 7 mm/yr after about 40 hours. As discussed previously, this is because of the exposure of Fe_3C due to the corrosion process, and described as the active corrosion stage^{7,32}. For the 0.4 m/s ($V_{eq} = 0.75$ m/s, 0.8 Pa), it can be seen that the corrosion rate starts decreasing at about the 45th hour down to a low and stable value of about 0.2 mm/yr. This can be attributed to the nucleating and growth of $FeCO_3$ ^{7,32}. When comparing the results obtained from previous experiments, as

shown in **Figure 59** for the same conditions and velocity, it can be witnessed that there is a good reproducibility of the results, even though experimental set ups are different.

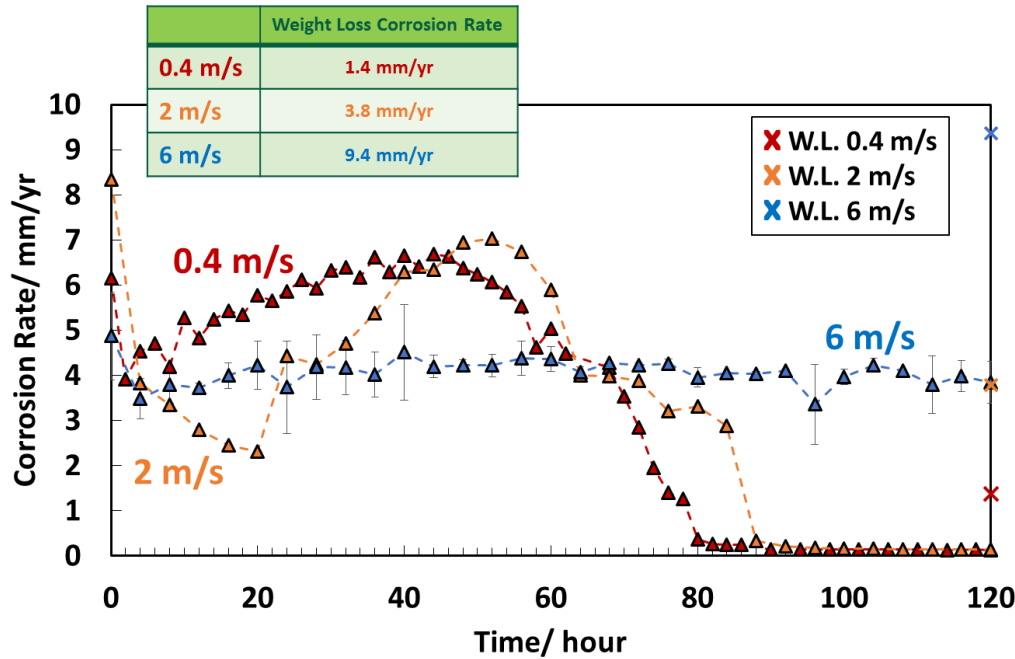


Figure 88. Comparison of LPR corrosion rate over time for 0.4 m/s ($V_{eq} = 0.75$ m/s, 0.8 Pa), 2 m/s ($V_{eq} = 4.7$ m/s, 20 Pa) and 6 m/s ($V_{eq} = 12$ m/s, 100 Pa) experiments with UNS G10180 ferritic-pearlitic under the conditions: $T=80^{\circ}\text{C}$, $\text{pCO}_2 = 0.53$ bar, initial pH 6.6, initial $S_{\text{FeCO}_3} \approx 10$

For the 2 m/s ($V_{eq} = 4.7$ m/s, 20 Pa), corrosion rate starts decreasing at about the 60th hour to a low and stable corrosion rate value of about 2 mm/yr, similar to 0.4 m/s. For the 6 m/s ($V_{eq} = 12$ m/s, 100 Pa) experiment, however, the corrosion rate is stable at a value of about 4 mm/yr, indicating no presence of the active corrosion stage seen in the lower velocities tested. This stable corrosion rate value may be due to the removal of Fe_3C , which cause the corrosion rate behavior to perform similarly to that of pure iron, as shown in **Figure 49**. The corrosion rate trend correlates to Akeer's previous finding that the

corrosion rate was maintained at a high and stable corrosion rate value⁴⁰. Additionally, the weight loss corrosion rate for the 6 m/s ($V_{eq} = 12$ m/s, 100 Pa) specimen was 9.4 mm/yr, which was significantly higher than the two other measurements at lower velocities. This may be due to the fact that some of the Xylan® coating was removed when the specimen was dipped in Clarke Solution, which did not happen for the other specimens. LPR corrosion rate results shown in **Figure 88** obtained from the TCFC setups were compared with those obtained with the controlled mass transfer and water chemistry setup described in section 4.2 and shown in **Figure 59**. It can be observed that FeCO_3 formed after *ca.* 100 hours for 250 rpm ($V_{eq} = 0.6$ m/s, 0.5 Pa) experimental trial. Whereas, FeCO_3 tested in the TCFC at 2 m/s ($V_{eq} = 4.7$ m/s, 20 Pa) formed after *ca.* 60 hours. Although the higher shear stress had earlier FeCO_3 formation, this can be a result of fluctuations in the water chemistry, especially pH values. For the impeller setup, pH does not rise above 6.61, as shown in **Figure 57**; however, for the TCFC, pH can rise up to 6.7. This change can quickly alter the saturation value, S_{FeCO_3} , from 10 to 30, according to equation (15).

4.3.2.3 Surface Morphologies and Characterization

Figure 89 shows the surface morphologies of the samples taken out on days 3 and 5. It can be seen that 0.4 m/s ($V_{eq} = 0.75$ m/s, 0.8 Pa) and 2 m/s ($V_{eq} = 4.7$ m/s, 20 Pa) samples for days 3 and 5 show similar surface morphologies with a non-uniform surface. This uneven surface confirms that the preferential dissolution of ferrite has occurred, while the Fe_3C acted as a cathode and remained on the steel surface^{8,46,47,49-54}. The 0.4 m/s surface morphology is similar to the findings from the glass cell setup under the same environmental conditions, as shown in **Figure 61**, as there is some precipitation of FeCO_3 .

prisms on the surface of the specimens. The 2 m/s ($V_{eq} = 4.7$ m/s, 20 Pa) specimens also show some FeCO_3 precipitation on the steel surface. Raman spectra shown in **Figure 90** and **Figure 91** for 0.4 m/s ($V_{eq} = 0.75$ m/s, 0.8 Pa) and 2 m/s ($V_{eq} = 4.7$ m/s, 20 Pa) specimens, respectively, retrieved after the fifth day confirm that the corrosion product is FeCO_3 based on spectra obtained from the literature⁶⁷⁻⁶⁹.

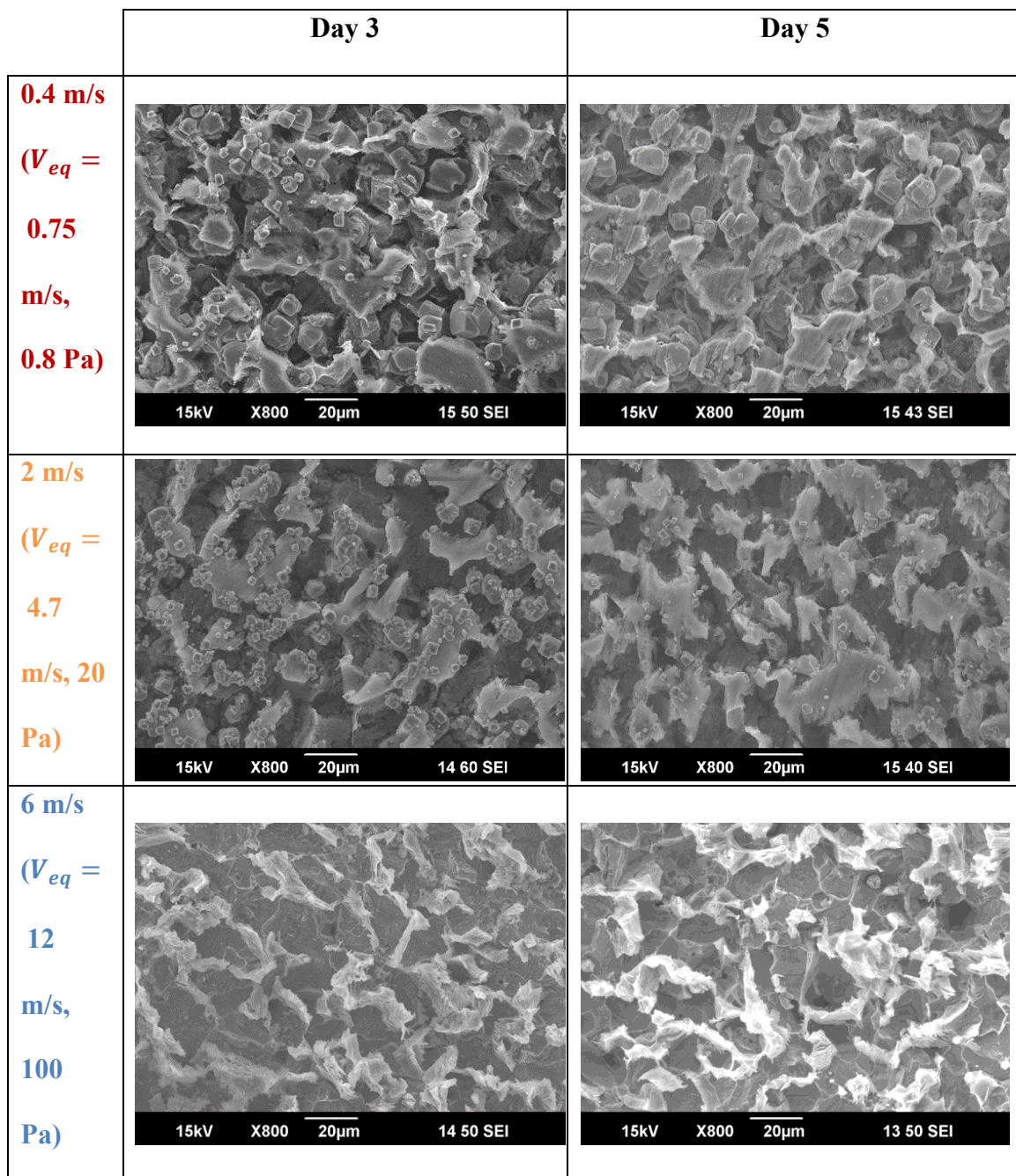


Figure 89. x800 SEM images showing comparison of surface morphologies over time for 0.4 m/s ($V_{eq} = 0.75$ m/s, 0.8 Pa), 2 m/s ($V_{eq} = 4.7$ m/s, 20 Pa) and 6 m/s ($V_{eq} = 12$ m/s, 100 Pa) experiments with UNS G10180 ferritic-pearlitic under the conditions: T=80°C, pCO₂ = 0.53 bar, initial pH 6.6, initial S_{FeCO₃} ≈ 10

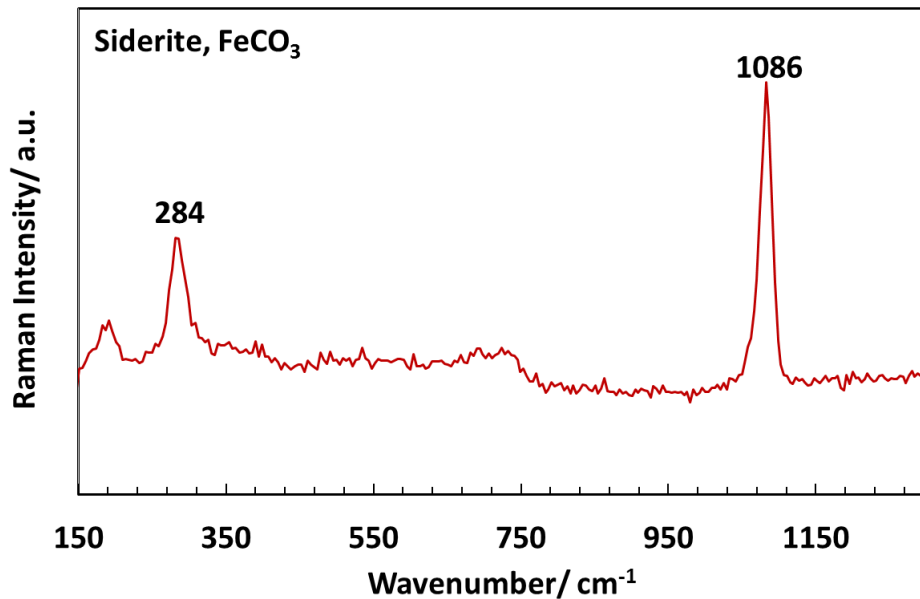


Figure 90. Raman spectra of surface confirming FeCO_3 as a corrosion product for 0.4 m/s ($V_{eq} = 0.75$ m/s, 0.8 Pa) experiment with UNS G10180 ferritic-pearlitic under the conditions: $T=80^{\circ}\text{C}$, $\text{pCO}_2 = 0.53$ bar, initial pH 6.6, initial $S_{\text{FeCO}_3} \approx 10$

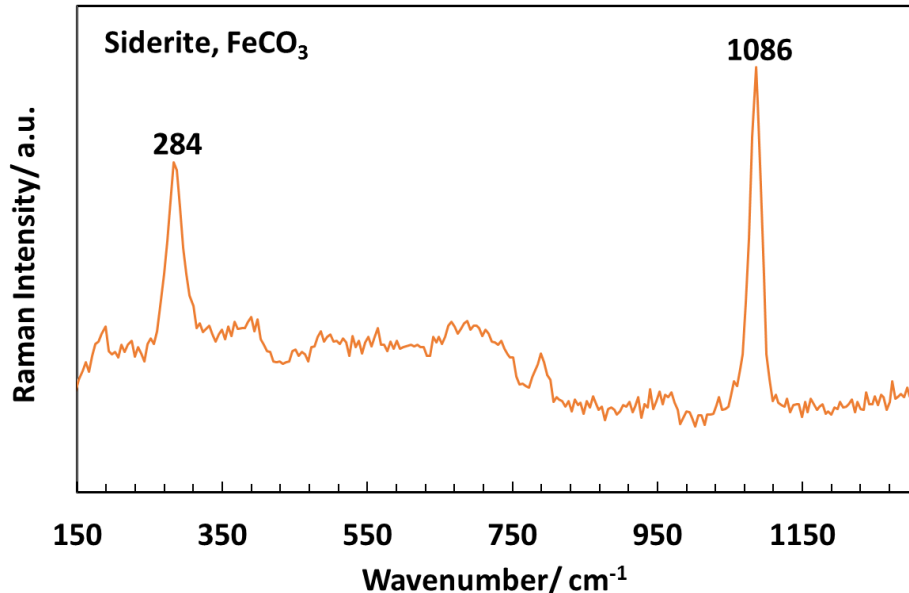


Figure 91. Raman spectra of surface confirming FeCO_3 as a corrosion product for 2 m/s ($V_{eq} = 4.7$ m/s, 20 Pa) experiment with UNS G10180 ferritic-pearlitic under the conditions: $T=80^{\circ}\text{C}$, $\text{pCO}_2 = 0.53$ bar, initial pH 6.6, initial $S_{\text{FeCO}_3} \approx 10$

For the 6 m/s ($V_{eq} = 12$ m/s, 100 Pa) specimen, however, a bare steel surface with white residues is observed, which may be due to the removal of Fe₃C due to turbulent conditions. There is no evidence of grooves, which are indicative of carbide remaining on the steel surface^{7,34}. This surface morphology shows similar results to Akeer's previous study⁴⁰. **Figure 92** shows the SEM image used for EDS analysis in order to determine the nature of the white residues, the points labelled 1 and 2 were analyzed. **Figure 93** shows the EDS spectrum for the point labelled 1 which analyzes the white residue. It is noteworthy that there is enrichment of alloying elements and, as indicated by the mass% and atom% values, there is no significant presence of carbon. It is safe to determine that this is not a Fe₃C network, but rather surface enrichment with respect to the alloying elements of the UNS G10180. **Figure 94** shows EDS analysis performed on the point labelled 2 on **Figure 92**, which shows that this is indeed a bare steel surface as only the presence of iron is detected. This finding correlates with Akeer's previous study, where no carbide was witnessed on the surface of such a steel specimen⁴⁰.

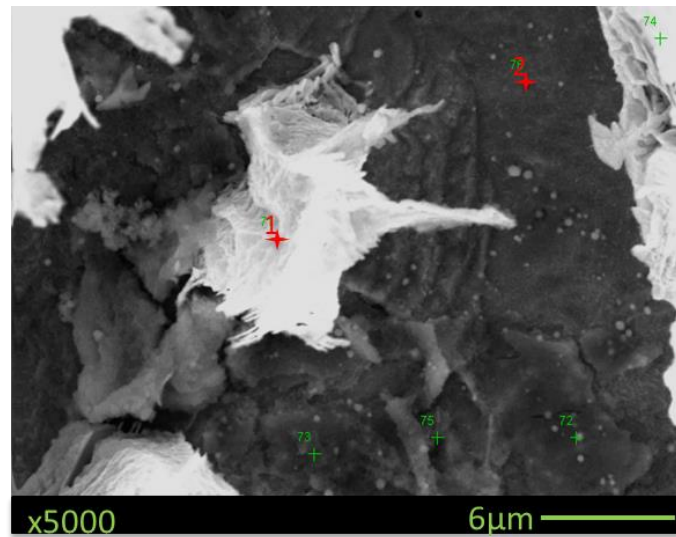


Figure 92. x5000 SEM image used for EDS analysis showing surface morphology after day 5 for 6 m/s ($V_{eq} = 12$ m/s, 100 Pa) experiment with UNS G10180 ferritic-pearlitic under the conditions: T=80°C, pCO₂ = 0.53 bar, initial pH 6.6, initial S_{FeCO₃} ≈ 10

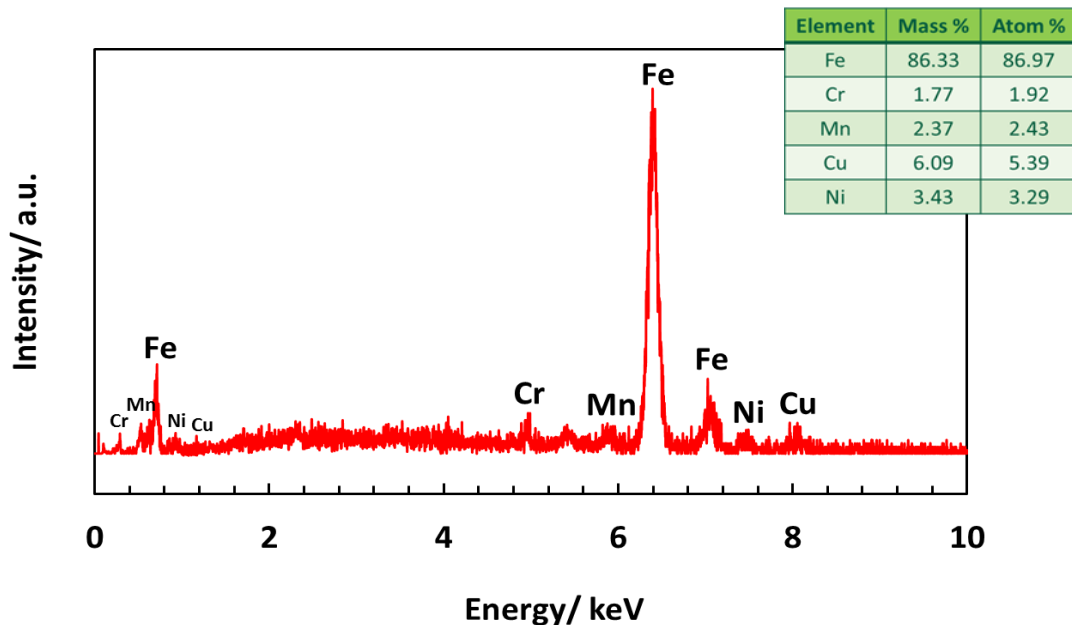


Figure 93. EDS spectrum taken at point labelled 1 shown in **Figure 92** confirming presence of alloying elements

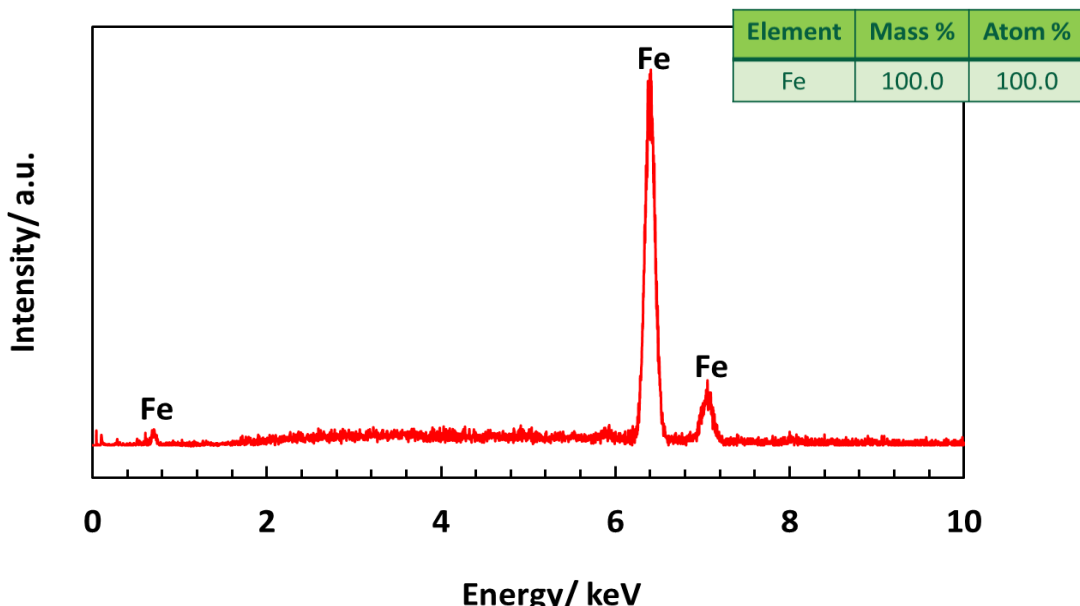


Figure 94. EDS spectrum taken at point labelled 2 shown in **Figure 92**

Raman analysis was also performed to determine if there is evidence of any corrosion product on the surface of the specimen, shown in **Figure 95**. It can be seen that there is no peak which corresponds to siderite (1084 cm^{-1}). However, a peak was found at 693 cm^{-1} . Upon searching of the literature on Raman spectroscopy and given the content of alloying elements in the UNS G10180, shown in **Table 8**, it was found that this peak corresponds to FeCr_2O_4 (chromite)⁹⁰. Raman spectra, surface morphologies, EDS analysis and corrosion rate trend obtained from LPR measurements confirm that no FeCO_3 formed on the sample surface and no Fe_3C was retained. Fe_3C was removed by high flow velocities, similar to what Akeer established⁴⁰.

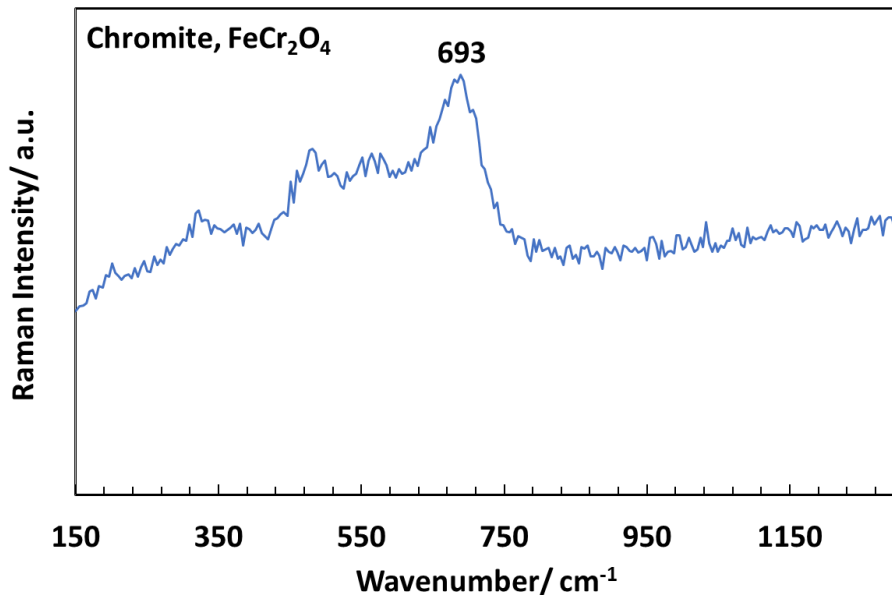


Figure 95. Raman spectra of surface for 6 m/s ($V_{eq} = 12 \text{ m/s}$, 100 Pa) experiment with UNS G10180 ferritic-pearlitic under the conditions: T=80°C, $p\text{CO}_2 = 0.53 \text{ bar}$, initial pH 6.6, initial $S_{\text{FeCO}_3} \approx 10$

4.3.2.4 Cross-Sectional Morphologies

Figure 96 shows cross-sectional morphologies of specimens shown in **Figure 89**.

The 0.4 m/s specimens show a Fe_3C network with FeCO_3 precipitation, which correlates to the corrosion rate shown in **Figure 88**. These results are similar to what was found in the same test conditions but using a glass cell set up, as shown in **Figure 59**. The 2 m/s ($V_{eq} = 4.7 \text{ m/s}$, 20 Pa) also shows a Fe_3C network with FeCO_3 precipitation therein. However, there is more visibility of the Fe_3C network in areas where precipitation of FeCO_3 has not occurred. On the other hand, the 6 m/s ($V_{eq} = 12 \text{ m/s}$, 100 Pa) specimen shows no significant Fe_3C network nor FeCO_3 precipitation, which can further confirm that the removal of Fe_3C occurred and hence prevented the precipitation of FeCO_3 . This is supported by the corrosion rate trend shown in **Figure 88**, for the 6 m/s ($V_{eq} = 12 \text{ m/s}$, 100

Pa), where the corrosion rate does not show an active corrosion rate stage as well as the metal lost value obtained from weight loss measurements^{7,32,40}.

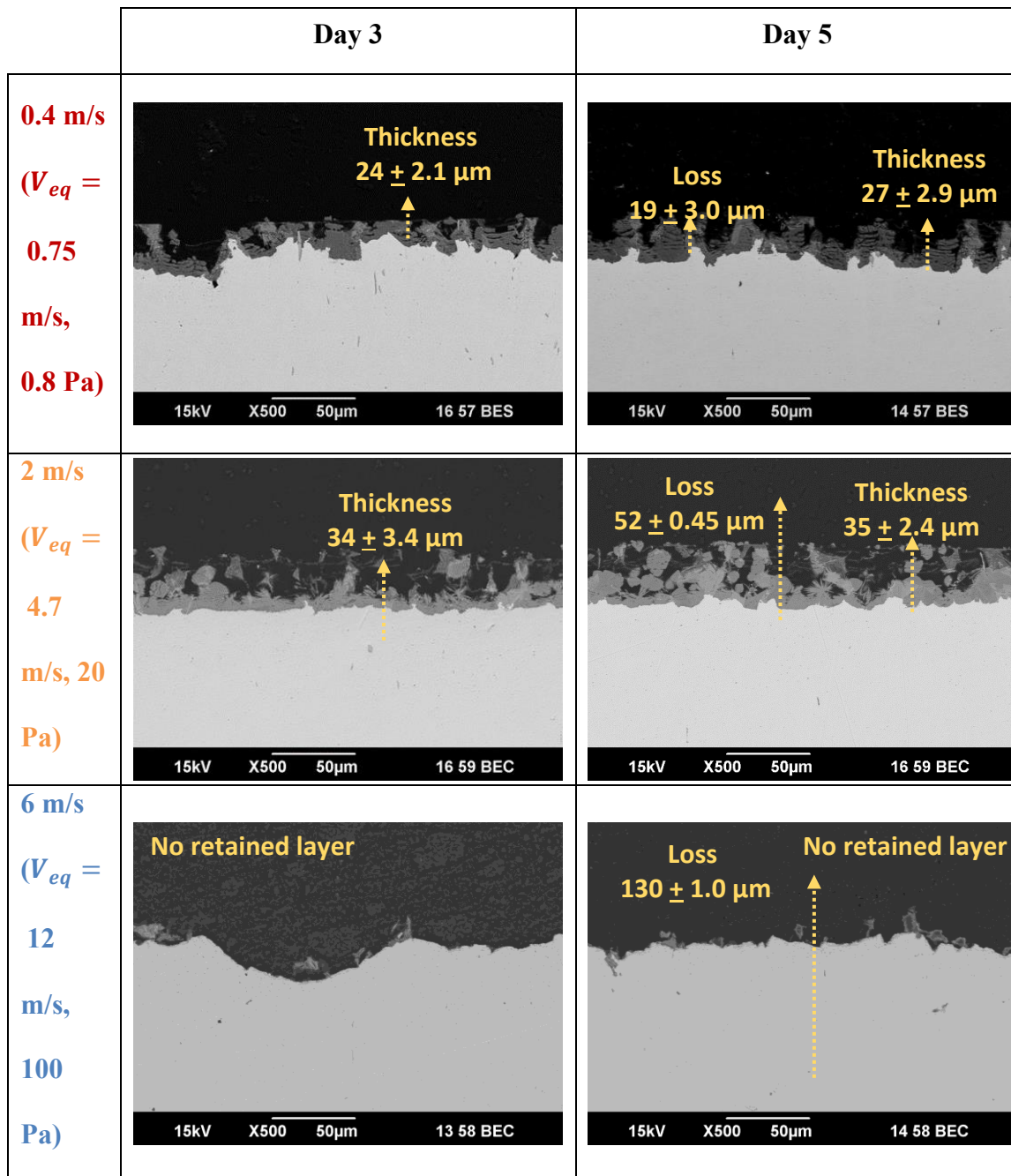


Figure 96. x500 SEM images showing cross-sectional morphologies over time for 0.4 m/s ($V_{eq} = 0.75 \text{ m/s, } 0.8 \text{ Pa}$), 2 m/s ($V_{eq} = 4.7 \text{ m/s, } 20 \text{ Pa}$) and 6 m/s ($V_{eq} = 12 \text{ m/s, } 100 \text{ Pa}$) experiments with UNS G10180 ferritic-pearlitic under the conditions: $T=80^\circ\text{C}$, $p\text{CO}_2 = 0.53 \text{ bar}$, initial pH 6.6, initial $S_{\text{FeCO}_3} \approx 10$

4.3.3 *Summary*

The TCFC was used to identify the velocity required for removal of a Fe₃C layer, considering a steel with ferritic-pearlitic microstructure. At the lowest velocity tested ($V_{eq} = 0.75$ m/s, 0.8 Pa), similar results were obtained from section 4.2 where FeCO₃ precipitation within Fe₃C network occurred and hence a decrease in corrosion rate. At the highest velocity tested ($V_{eq} = 12$ m/s, 100 Pa), however, neither precipitation of FeCO₃ occurred nor was a Fe₃C layer retained.

CHAPTER 5: SUMMARY AND DISCUSSION

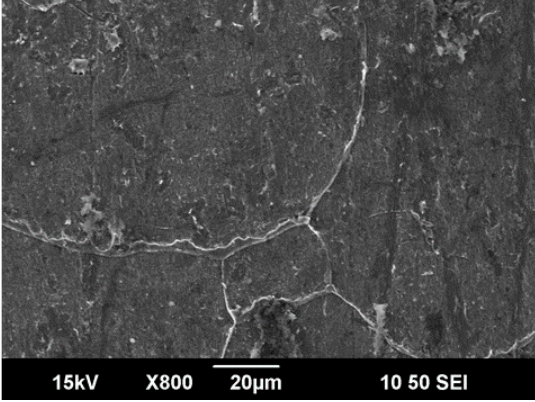
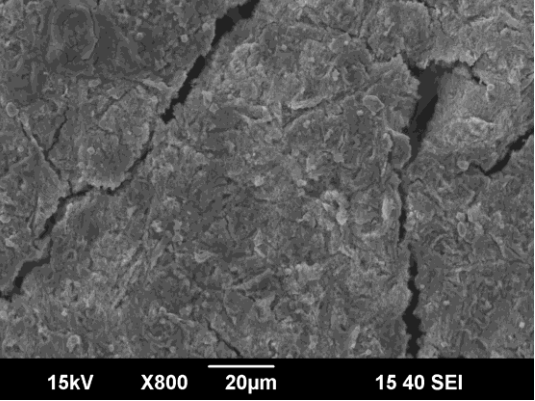
Within this context, three different experimental test setups were used to identify if the formation of FeCO₃ can be prevented at high turbulent flow (high velocities/shear stresses) even if the conditions favor precipitation of FeCO₃. The choice of equivalent pipeline velocities and shear stresses underwent careful consideration in order to ensure reproducibility of results across all setups. This chapter aims at revisiting the initial research hypotheses by taking into account the main findings of this work.

In the first set of experiments, it was hypothesized a critical velocity can be identified above which precipitation of FeCO₃ onto a metal surface would not be possible. The purpose was then to investigate how flow impedes formation of FeCO₃ in highly saturated solutions (replete with ferrous ions) in the absence of Fe₃C. Precipitation of FeCO₃ occurred in stagnant conditions, leading to a sharp decrease in corrosion rate. This was fully expected as the saturation value with respect to FeCO₃ was favorable and sufficiently high (an order of magnitude above unity) during specimen exposure. However, as flow velocity increased (≥ 0.6 m/s, 0.8 Pa) and reached a critical value (2.0 m/s, 7 Pa), the corrosion rate over time did not decrease over time. In addition, a gradual decrease in terms of FeCO₃ coverage as confirmed by SEM images, EDS analysis, and Raman spectroscopy. The reason why the extent of FeCO₃ precipitation on the metal surface (in the absence of Fe₃C) decreased as the fluid velocity increased, is attributed to local shear stresses (≥ 0.8 Pa) on the surface of the specimen which impeded the precipitation of FeCO₃. Carbonate and ferrous (in supersaturated solutions) ions must reach the specimen for precipitation of FeCO₃. Ferrous ions generated from the corrosion process must remain

on the specimen surface for precipitation of FeCO_3 . However, at high flow velocities and wall shear stresses, these ionic species are being continuously removed from the surface of the specimen unable to form a protective corrosion product layer of FeCO_3 even in supersaturated conditions. These local shear stresses on the specimen surface can also easily detach most of the already precipitated $\text{Fe}_2(\text{OH})_2\text{CO}_3$ (precursor of FeCO_3) since the plate morphology of $\text{Fe}_2(\text{OH})_2\text{CO}_3$ is very frail. These results present a different perspective to previous studies where the formation of FeCO_3 always occurred at stagnant conditions and the effect of flow was not further investigated^{6,37,38}. It was proven that the hypothesis was correct, FeCO_3 precipitation did not occur on the pure iron surface at an equivalent pipe velocity of 2.0 m/s and a wall shear stress of 7 Pa, even though previous studies and FREECORP 2.0 predictions suggested environmental conditions favored precipitation.

In the second task of experiments, the effect of microstructure and carbon content were investigated to determine the precipitation of FeCO_3 within a Fe_3C network. Findings for pure iron specimens from this set of experiments were similar to those of the first task, as no precipitation of FeCO_3 on the specimen surface due to the high flow velocities. These findings are summarized in **Table 11**.

Table 11. Comparison of equivalent pipe velocities, wall shear stresses, final corrosion rates and surface morphologies showing no FeCO₃ precipitation on pure Fe for RCE and impeller setups

Setup	V_{eq} , Equivalent Pipeline Velocity in a 25.5 cm ID pipe (m/s)	Wall Shear Stress (Pa)	Final Corrosion Rate (mm/yr)	Surface Morphology
RCE	2.0	7	4.0	 <p>15kV X800 20μm 10 50 SEI</p>
Impeller	0.6	0.5	3.4	 <p>15kV X800 20μm 15 40 SEI</p>

However, microstructure combined with carbon content played a key role in precipitation of FeCO₃. It was found that a ferritic pearlitic microstructure with a 0.18 wt.% C favored precipitation of FeCO₃ within the Fe₃C network. Accordingly, the results indicate that the order and distribution of Fe₃C are crucial in regards to FeCO₃ precipitation.

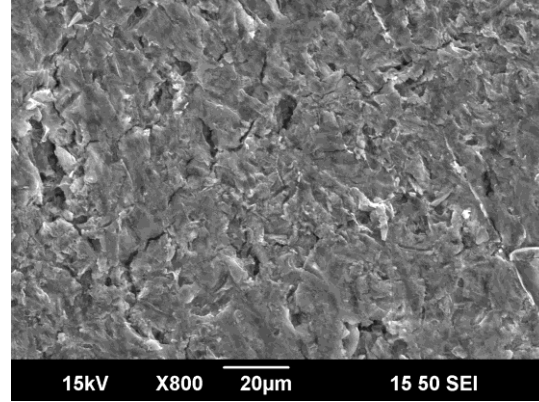
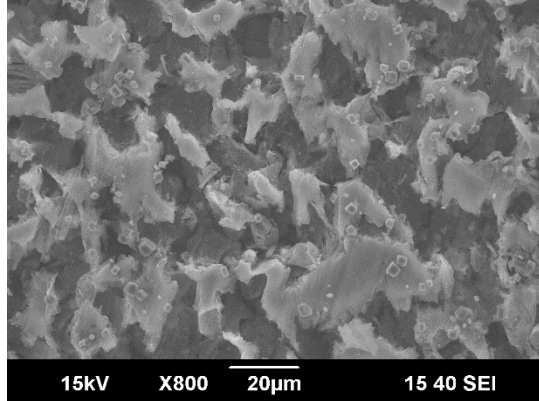
The lamellar structure of Fe₃C in tight microconstituents (pearlite) allow for favorable local conditions for FeCO₃ precipitation (trap ferrous and carbonate ions), which are less susceptible to removal by flow due to the compactness and distribution of Fe₃C in a lamellar structure. In a tempered martensitic microstructure, since the distribution of Fe₃C is unordered and random in the material microstructure, the Fe₃C is more subjected to removal by flow (flimsy Fe₃C layer), which allows for release of ferrous ions into the electrolyte without trapping them in the Fe₃C network, as opposed to what was found in a ferritic-pearlitic microstructure. It was hypothesized that the material microstructure (Fe₃C) aids in the precipitation of FeCO₃ at high flow velocities. This hypothesis is partially true as only a very specific microstructure, ferritic-pearlitic combined with a high carbon content of 0.18 wt.% C, was able to precipitate FeCO₃ within a Fe₃C network. These findings seem to coincide with what many researchers suggest is a superior microstructure for FeCO₃ formation^{51,56}, as opposed to others⁵⁵. **Table 12** compares findings for this set of experiments for all steels tested.

Table 12. Comparison of equivalent pipe velocities, wall shear stresses, final corrosion rate and precipitation of FeCO_3

Material	V_{eq} , Equivalent Pipeline Velocity in a 25.5 cm ID pipe (m/s)	Wall Shear Stress (Pa)	Final Corrosion Rate (mm/yr)	Precipitation of FeCO_3 occurred?
UNS G10180 ferritic-pearlitic	0.4 and 0.6	0.3 and 0.5	0.7 and 1.7	Yes
UNS G10180 tempered martensite			6.6 and 7.3	No
API 5L X65 ferritic with Fe_3C precipitates			2.8 and 3.0	No

In the last set of experimental results, high flow velocities and wall shear stresses were the main focus as a velocity for the removal of Fe_3C was sought after based on the hypothesis and previous results⁴⁰. The findings at the lowest velocities tested of 0.4 m/s ($V_{eq} = 0.75$ m/s, 0.8 Pa) and 2 m/s ($V_{eq} = 4.7$ m/s, 20 Pa) were similar to those from the second task where minor to no precipitation of FeCO_3 occurred on the steel surface. The results from TCFC and impeller setup are compared in **Table 13**.

Table 13. Comparison of equivalent pipe velocities, wall shear stresses, final corrosion rates and surface morphologies showing FeCO_3 precipitation for impeller and TCFC setups under the conditions: $T=80^{\circ}\text{C}$, $p\text{CO}_2 = 0.53$ bar, pH 6.6, $S_{\text{FeCO}_3} \approx 10$

Setup	V_{eq} , Equivalent Pipeline Velocity in a 25.5 cm ID pipe (m/s)	Wall Shear Stress (Pa)	Final Corrosion Rate (mm/yr)	Surface Morphology
Impeller	0.6	0.5	1.7	 15kV X800 20μm 15 50 SEI
TCFC	0.75	0.8	0.2	 15kV X800 20μm 15 40 SEI

However, at the highest velocity tested of 6 m/s ($V_{eq} = 12$ m/s, 100 Pa), no Fe_3C was found, which inhibited further precipitation of FeCO_3 as suggested by corrosion rate trends, SEM and cross-sectional images, as well as Raman analysis. These results suggest two major findings: (1) removal of Fe_3C does occur as it is very weak and fragile as

suggested by the literature^{8,40}; (2) Fe₃C aids in the precipitation of FeCO₃. A clear pattern is shown in **Figure 97**, where 0.4 m/s ($V_{eq} = 0.75$ m/s, 0.8 Pa) specimens show a complete coverage of FeCO₃ within the Fe₃C network, 2 m/s ($V_{eq} = 4.7$ m/s, 20 Pa) specimen shows partial FeCO₃ formation within the Fe₃C network closest to the steel surface, and the 6 m/s ($V_{eq} = 12$ m/s, 100 Pa) specimen showing no significant retained Fe₃C network and no precipitation of FeCO₃.

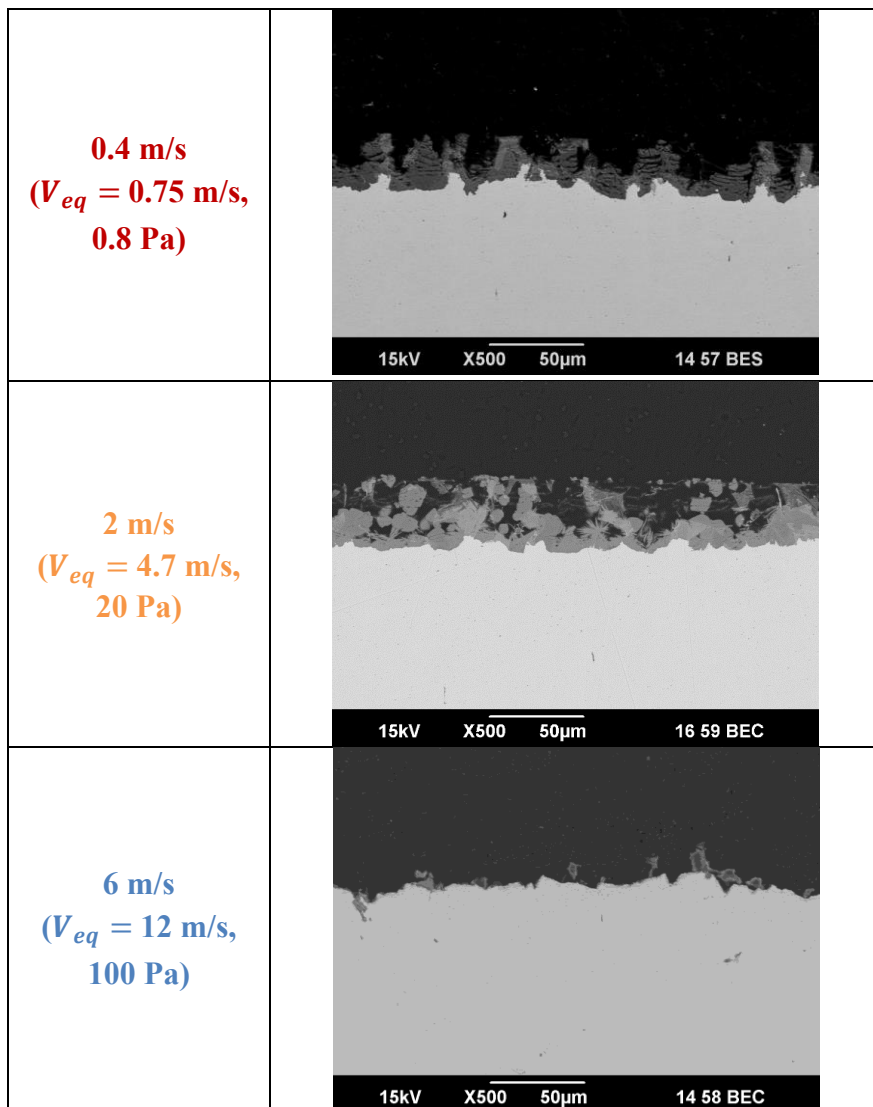


Figure 97. x500 SEM images showing pattern of FeCO_3 formation and Fe_3C exposure for 0.4 m/s ($V_{eq} = 0.75 \text{ m/s}$, 0.8 Pa), 2 m/s ($V_{eq} = 4.7 \text{ m/s}$, 20 Pa) and 6 m/s ($V_{eq} = 12 \text{ m/s}$, 100 Pa) experiments with UNS G10180 ferritic-pearlitic under the conditions: day 5, $T=80^\circ\text{C}$, $p\text{CO}_2 = 0.53 \text{ bar}$, initial pH 6.6, initial $S_{\text{FeCO}_3} \approx 10$

These findings support the hypothesis that Fe_3C can be removed by flow and hinder nucleation of FeCO_3 as well as previous results⁴⁰. However, it is important to note that this velocity found for removal of Fe_3C is not a universal velocity and strongly depends on experimental conditions.

CHAPTER 6: CONCLUSIONS AND FUTURE WORK

6.1 Conclusions

An experimental study was performed with the aim of identifying the mechanisms of FeCO_3 formation in turbulent conditions. Experiments were run in different setups to determine the effect of flow and microstructure in regards to FeCO_3 formation. After analyzing the data obtained from all experimental procedures, the following conclusions could be made:

- In the environments evaluated, the corrosion products when solution is saturated with ferrous ions mostly consist of FeCO_3 prismatic crystals and $\text{Fe}_2(\text{OH})_2\text{CO}_3$ plates.
- Nucleation of FeCO_3 on the steel surface is significantly reduced as turbulence/flow increases even when the water chemistry is favorable and the formation of iron carbide is minimized.
- Higher carbon content, 0.18 wt.% vs. 0.05 wt.% C, favors precipitation of FeCO_3 .
- Ferritic-pearlitic microstructure facilitates FeCO_3 precipitation due to the distribution/order of the Fe_3C precipitates, which enable local water chemistry conditions favorable to precipitation of FeCO_3 .
- Flow can also impact precipitation of FeCO_3 due to the removal of Fe_3C from the steel surface.
- Fe_3C is removed at higher flow velocities ($V_{eq} \geq 12$ m/s, 100 Pa) which further impedes formation of FeCO_3 .

6.2 Future Work

Based on the results and conclusions drawn from these results, the following topics can be further investigated:

- Formation of an iron sulfide (FeS) layer (given the polymorphs of FeS [mackinawite, pyrite, troilite, etc.]) in turbulent conditions and the effect of microstructure or Fe₃C network. A comparison can be drawn between CO₂ corrosion and H₂S corrosion.
- Formation of a FeCO₃ and/or FeS corrosion product layer in a Fe₃C network under H₂S/CO₂ conditions to determine if the presence of a Fe₃C network is advantageous. Additionally, it can be determined if both corrosion products can be formed simultaneously or if one preferentially forms over the other.
- In-situ monitoring of Fe₂(OH)₂CO₃ plates and FeCO₃ growth via Raman spectroscopy to identify how plates grow into prisms. This can be further studied with the effect of flow to determine if plates can be easily detached from the steel surface due to shear stresses on the specimen surface.
- Inhibitor performance in the presence of FeCO₃ and/or Fe₃C. The performance of an inhibitor can be affected if the interaction between the inhibitor and steel surface is altered by the presence of corrosion products. As proven in these studies, corrosion product can form without necessarily assuring protection, which may require inhibition.
- FREECORP does not accurately predict corrosion rates for pure iron specimens when compared to corrosion rate values obtained by electrochemical measurements

in the various setups tested. This may be attributed to the purity of the iron specimen. Incorporating the effect of materials into FREECORP may predict corrosion rates more accurately and draw better comparison with experimental results.

REFERENCES

1. Koch, G. H., Brongers, M. P., Thompson, N. G., Virmani, Y. P., & Payer, J. H. (2002). *Corrosion cost and preventive strategies in the United States* (No. FHWA-RD-01-156)
2. Sun, Y. (2003). *Localized CO₂ Corrosion in Horizontal Wet Gas Flow* (Doctoral dissertation) Ohio University, Athens, OH.
3. Ruzic, V., Veidt, M., & Nešić, S. (2006). Protective Iron Carbonate Films-Part 1: Mechanical Removal in Single-Phase Aqueous Flow. *Corrosion*, 62(5), 419-432.
4. Ruzic, V., Veidt, M., & Nešić, S. (2006). Protective Iron Carbonate Films-Part 2: Chemical Removal by Dissolution in Single-Phase Aqueous Flow. *Corrosion*, 62(7), 598-611.
5. Ruzic, V., Veidt, M., & Nešić, S. (2007). Protective Iron Carbonate Films-Part 3: Simultaneous Chemo-Mechanical Removal in Single-Phase Aqueous Flow. *Corrosion*, 63(8), 758-769.
6. Yang, Y. (2012). *Removal Mechanisms of Protective Iron Carbonate Layer in Flowing Solutions* (Doctoral dissertation) Ohio University, Athens, OH.
7. Farelas, F., Brown, B., & Nešić, S. (2013). Iron Carbide and its Influence on the Formation of Protective Iron Carbonate in CO₂ Corrosion of Mild Steel. CORROSION/2013, paper 2291.
8. Groysman, A. (2009). *Corrosion for Everybody*. Springer Science & Business Media.

9. Nordsveen, M., Nešić, S., Nyborg, R., & Stangeland, A. (2003). A Mechanistic Model for Carbon Dioxide Corrosion of Mild Steel in the Presence of Protective Iron Carbonate Films-Part 1: Theory and Verification. *Corrosion*, 59(5), 443-456.
10. De Waard, C., & Milliams, D. E. (1975). Carbonic Acid Corrosion of Steel. *Corrosion*, 31(5), 177-181.
11. Nešić, S. (2007). Key Issues Related to Modelling of Internal Corrosion of Oil and Gas Pipelines—A Review. *Corrosion Science*, 49(12), 4308-4338.
12. Tran, T. (2014). *Corrosion Mechanisms of Mild Steel in Weak Acids* (Doctoral dissertation) Ohio University, Athens, OH.
13. Gray, L. G., Anderson, B. G., Danysh, M. J., & Tremaine, P. R. (1990). Effect of pH and Temperature on the Mechanism of Carbon Steel Corrosion by Aqueous Carbon Dioxide. CORROSION/1990, paper 40.
14. Wang, S., George, K., & Nešić, S. (2004). High Pressure CO₂ Corrosion Electrochemistry and the Effect of Acetic Acid. CORROSION/2004, paper 4375.
15. George, K., & Nešić, S., (2004). Electrochemical Investigation and Modeling of Carbon Dioxide Corrosion of Carbon Steel in the Presence of Acetic Acid. CORROSION/2004, paper 4379.
16. Nešić, S., Wang, S., Cai, J., & Xiao, Y. (2004). Integrated CO₂ Corrosion-Multiphase Flow Model. CORROSION/2004, paper 4626
17. Sun, Y., & Nešić, S. (2004). A Parametric Study and Modeling on Localized CO₂ Corrosion in Horizontal Wet Gas Flow. CORROSION/2004, paper 4380.

18. Revie, R. W., & Uhlig, H. H. (2011). *Uhlig's corrosion handbook* (Vol. 51). John Wiley & Sons
19. Nešić, S., Solvi, G. T., & Enerhaug, J. (1995). Comparison of the Rotating Cylinder and Pipe Flow Tests for Flow-Sensitive Carbon Dioxide Corrosion. *Corrosion*, 51(10), 773-787.
20. De Waard, C., & Williams, D. E. (1976). Prediction of carbonic acid corrosion in natural gas pipelines. *Ind. Finish. Surf. Coatings*, 28(340), 24-26.
21. De Waard, C. & Lotz, U. (1993). Prediction of CO₂ Corrosion of Carbon Steel. CORROSION/1993, paper 69.
22. De Waard, C., Lotz, U., & Dugstad, A. (1995). Influence of Liquid Flow Velocity on CO₂ Corrosion: A Semi-Empirical Model. CORROSION/1995, paper 128.
23. Nešić, S., Li, H., Huang, J., & Sormaz, D. (2009). An Open Source Mechanistic Model for CO₂/H₂S Corrosion of Carbon Steel. CORROSION/2009, paper 09572.
24. Sun, W., Nešić, S., & Woollam, R. C. (2009). The Effect of Temperature and Ionic Strength on Iron Carbonate (FeCO₃) Solubility Limit. *Corrosion Science*, 51(6), 1273-1276.
25. Sun, W., & Nešić, S. (2008). Kinetics of Corrosion Layer Formation: Part 1 – Iron Carbonate Layers in Carbon Dioxide Corrosion. *Corrosion*, 64(4), 334-346.
26. Van Hunnik, E.W., Pots, B., & Hendriksen, E.L. (1996). The Formation of Protective FeCO₃ Corrosion Product Layers in CO₂ Corrosion. CORROSION/1996, paper 6.

27. Nazari, M. H., Allahkaram, S. R., & Kermani, M. B. (2010). The Effects of Temperature and pH on the Characteristics of Corrosion Product in CO₂ Corrosion of Grade X70 Steel. *Materials & Design*, 31(7), 3559-3563
28. Yin, Z. F., Feng, Y. R., Zhao, W. Z., Bai, Z. Q., & Lin, G. F. (2009). Effect of Temperature on CO₂ Corrosion of Carbon Steel. *Surface and Interface Analysis*, 41(6), 517-523.
29. Tanupabungsun, T. (2013). *Thermodynamics and kinetics of carbon dioxide corrosion of mild steel at elevated temperatures* (Doctoral dissertation) Ohio University, Athens, OH.
30. Paolinelli, L. (2013). *Effect of High Wall Shear Stress on FeCO₃ Nuclei*. Retrieved from March 2013 ICMT Board Meeting Reports
31. Pandarinathan, V., Lepková, K., & Van Bronswijk, W. (2014). Chukanovite (Fe₂(OH)₂CO₃) Identified as a Corrosion Product at Sand-Deposited Carbon Steel in CO₂-Saturated Brine. *Corrosion Science*, 85, 26-32.
32. Gao, K., Yu, F., Pang, X., Zhang, G., Qiao, L., Chu, W., & Lu, M. (2008). Mechanical properties of CO₂ corrosion product scales and their relationship to corrosion rates. *Corrosion Science*, 50(10), 2796-2803.
33. Iteamsupapong, S., Brown, B., Singer, M., & Nešić, S. (2017). Effect of Solution pH on Corrosion Product Layer Formation in a Controlled Water Chemistry System. CORROSION/2017, paper 9160.

34. Pessu, F., Barker, R., & Neville, A. (2015). The Influence of pH on Localized Corrosion Behavior of X65 Carbon Steel in CO₂-Saturated Brines. *Corrosion*, 71(12), 1452-1466.
35. Han, J., Brown, B. N., & Nešic, S. (2010). Investigation of the Galvanic Mechanism for Localized Carbon Dioxide Corrosion Propagation using the Artificial Pit Technique. *Corrosion*, 66(9), 095003-1-095003-12.
36. Xia, Z., Chou, K. C., & Szklarska-Smialowska, Z. (1989). Pitting Corrosion of Carbon Steel in CO₂-Containing NaCl Brine. *Corrosion*, 45(8), 636-642.
37. Xiong, Y. (2011) *AFM Studies of the Metallicity of Single-walled Carbon Nanotubes and Corrosion Inhibitor Adsorption* (Doctoral Dissertation) Ohio University, Athens, OH.
38. Yang, Y., Brown, B. N., & Nešic, S. (2010). Mechanical Strength and Removal of a Protective Iron Carbonate Layer Formed on Mild Steel in CO₂ Corrosion. CORROSION/2010, paper 10383.
39. Akeer, E., Brown, B. N., & Nešic, S. (2013). The Influence of Mild Steel Metallurgy on the Initiation of Localized CO₂ Corrosion in Flowing Conditions. CORROSION/2013, paper 2383.
40. Akeer, E. S. (2014). *Effect of Carbon Steel Composition and Microstructure on CO₂ Corrosion* (Doctoral Dissertation) Ohio University, Athens, OH.
41. J. R. Vera, A. Viloria. M. Castillo, A. Ikeda, & M. Ueda. (1994). Flow Velocity Effect on CO₂ Corrosion Of Carbon Steel Using a Dynamic Field Tester. In Predicting CO₂

- Corrosion in the Oil and Gas Industry. *European Federation of Corrosion Publications*, 13, 59-93.
42. J. Vera, A. Viloria, J. Morales, A. Ikeda, & M. Ueda. (1993). Effect of Flow Velocity on Carbon Steel CO₂ Corrosion and Surface Films using a Dynamic Field Tester. 12th International Corrosion Congress, paper 307.
43. J. Vera, A. Viloria, M. Castillo, A. Ikeda, & M. Ueda. (1992). Flow Velocity Effect on Carbon Steel CO₂ Corrosion Using a Dynamic Field Tester. 1st Pan-American Corrosion Conference, Vol. I. p.115-139
44. A. Ikeda, M. Ueda, J. Vera, M. Castillo, & A. Viloria. Introduction of a New Dynamic Field Tester and Preliminary Results on Flow Effects on CO₂ Corrosion. CORROSION/1992, paper 48.
45. A. Ikeda, M. Ueda, & S. Mukai. CO₂ Corrosion Behavior of Carbon Steel and Alloy Steel. CORROSION/1983, paper 45.
46. Berntsen, T., Seiersten, M., & Hemmingsen, T. (2013). Effect of FeCO₃ Supersaturation and Carbide Exposure on the CO₂ Corrosion Rate of Carbon Steel. *Corrosion*, 69(6), 601-613.
47. Callister, W. D., & Rethwisch, D. G. (2007). *Materials Science and Engineering: an Introduction* (Vol. 7, pp. 665-715). New York: Wiley.
48. Bramfitt, B. L., & Benscoter, A. O. (2001). *Metallographer's Guide: Practice and Procedures for Irons and Steels*. ASM International.

49. Clover, D., Kinsella, B., Pejcic, B., & De Marco, R. (2005). The Influence of Microstructure on the Corrosion Rate of Various Carbon Steels. *Journal of Applied Electrochemistry*, 35(2), 139-149.
50. Staicopolus, D. N. (1963). The role of cementite in the acidic corrosion of steel. *Journal of the Electrochemical Society*, 110(11), 1121-1124.
51. Eliyan, F. F., & Alfantazi, A. (2014). On the Theory of CO₂ Corrosion Reactions—Investigating their Interrelation with the Corrosion Products and API-X100 Steel Microstructure. *Corrosion Science*, 85, 380-393.
52. Al-Hassan, S., Mishra, B., Olson, D. L., & Salama, M. M. (1998). Effect of Microstructure on Corrosion of Steels in Aqueous Solutions Containing Carbon Dioxide. *Corrosion*, 54(6), 480-491.
53. Crolet, J. L., Thevenot, N., & Nešić, S. (1998). Role of Conductive Corrosion Products in the Protectiveness of Corrosion Layers. *Corrosion*, 54(3), 194-203.
54. Farida, W., Hemmingsen, T., Berntsen, T., & Rabindran, P. (2012). Effect of Precorrosion and Temperature on the Formation Rate of Iron Carbonate Film. *7th Pipeline Technology Conference*, pp. 1-16.
55. Dugstad, A., Hemmer, H., & Seiersten, M. (2001). Effect of Steel Microstructure on Corrosion Rate and Protective Iron Carbonate Film Formation. *Corrosion*, 57(4), 369-378.
56. Ochoa, N., Vega, C., Pébère, N., Lacaze, J., & Brito, J. L. (2015). CO₂ Corrosion Resistance of Carbon Steel in Relation with Microstructure Changes. *Materials Chemistry and Physics*, 156, 198-205.

57. Stern, M., & Geary, A. L. (1957). Electrochemical Polarization I. A Theoretical Analysis of the Shape of Polarization Curves. *Journal of the Electrochemical Society, 104*(1), 56-63.
58. *Getting Started with Electrochemical Corrosion Measurement: Review of the Electrochemical Basis of Corrosion*. Retrieved from
<https://www.gamry.com/application-notes/corrosion-coatings/basics-of-electrochemical-corrosion-measurements/>
59. Silverman, D. C. (2004). The Rotating Cylinder Electrode for Examining Velocity-Sensitive Corrosion-A Review. *Corrosion, 60*(11), 1003-1023.
60. Silverman, D. C. (1984). Rotating Cylinder Electrode for Velocity Sensitivity Testing. *Corrosion, 40*(5), 220-226.
61. Silverman, D. C. (1988). Rotating Cylinder Electrode-Geometry Relationships for Prediction of Velocity-Sensitive Corrosion. *Corrosion, 44*(1), 42-49.
62. Silverman, D. C. (2005). Technical Note: Conditions for Similarity of Mass-Transfer Coefficients and Fluid Shear Stresses between the Rotating Cylinder Electrode and Pipe. *Corrosion, 61*(6), 515-518.
63. Eisenberg, M., Tobias, C. W., & Wilke, C. R. (1954). Ionic Mass Transfer and Concentration Polarization at Rotating Electrodes. *Journal of the Electrochemical Society, 101*(6), 306-320.
64. Lide, D. R., & Haynes, W. M. (2009). *CRC handbook of chemistry and physics: a ready-reference book of chemical and physical data-/editor-in-chief, David R. Lide; ass. ed. WM" Mickey" Haunes*. Boca Raton, Fla: CRC.

65. Eisenberg, M., Tobias, C. W., & Wilke, C. R. (1955). Mass Transfer at Rotating Cylinders. *Chem. Engng Prog. Symp. Ser.*, 51(16), 1-16.
66. ASTM G185-06(2016), Standard Practice for Evaluating and Qualifying Oil Field and Refinery Corrosion Inhibitors Using the Rotating Cylinder Electrode, ASTM International, West Conshohocken, PA, 2016, www.astm.org
67. Azoulay, I., Conforto, E., Refait, P., & Rémazeilles, C. (2013). Study of Ferrous Corrosion Products on Iron Archaeological Objects by Electron Backscattered Diffraction (EBSD). *Applied Physics A*, 110(2), 379-388.
68. Remazeilles, C., Dheilly, A., Sable, S., Lanneluc, I., Neff, D., & Refait, P. (2010). Microbiologically Influenced Corrosion Process of Archaeological Iron Nails from the Sixteenth Century. *Corrosion Engineering, Science and Technology*, 45(5), 388-394.
69. Oh, S. J., Cook, D. C., & Townsend, H. E. (1998). Characterization of iron oxides commonly formed as corrosion products on steel. *Hyperfine interactions*, 112(1-4), 59-66.
70. Akiyama, A., Patterson, R. E., & Nobe, K. (1970). Electrochemical Characteristics of Iron During Corrosion: Effect of Heat Treatment and Purity. *Corrosion*, 26(2), 51-57.
71. Greco, E. C., & Wright, W. B. (1962). Corrosion of Iron in an H₂S-CO₂-H₂O System. *Corrosion*, 18(3), 119t-124t.
72. Ohtsuka, T., Kubo, K., & Sato, N. (1986). Raman Spectroscopy of Thin Corrosion Films on Iron at 100 to 150 C in Air. *Corrosion*, 42(8), 476-481.

73. Zhong, X., Brown, B., Li, W., Nešić, S., & Singer, M. (2016). How to Maintain a Stable Solution Chemistry When Simulating CO₂ Corrosion in a Small Volume Laboratory System. CORROSION/2016, paper 7780.
74. Ieamsupapong, S. (2016). *Mechanisms of Iron Carbonate Formation on Mild Steel in Controlled Water Chemistry Conditions* (Doctoral Dissertation) Ohio University, Athens, OH.
75. Ralston, K. D., & Birbilis, N. (2010). Effect of Grain Size on Corrosion: A Review. *Corrosion*, 66(7), 075005-075005.
76. ASTM E112-13, Standard Test Methods for Determining Average Grain Size, ASTM International, West Conshohocken, PA, 2013, www.astm.org
77. Bramfitt, B. L. (1998). Structure/Property relationships in irons and steels. *Materials Park, OH: ASM International*, 1998, 153-173.
78. Griffin, R. D., & Griffin, J. (1998, October). The effect of quench rate and tempering temperature on the microstructure and hardness of commercial steels. 18th ASM Heat Treating Society Conference and Exposition including the Liu Dai Memorial Symposium, pp. 320-328.
79. Masseria, V. (Ed.). (1981). *Metals Handbook: Heat Treating*. American Society for Metals.
80. Pavlina, E. J., & Van Tyne, C. J. (2008). Correlation of Yield Strength and Tensile Strength with Hardness for Steels. *Journal of Materials Engineering and Performance*, 17(6), 888-893.

81. ASTM G1-03(2011), Standard Practice for Preparing, Cleaning, and Evaluating Corrosion Test Specimens, ASTM International, West Conshohocken, PA, 2011, www.astm.org
82. Han, J., Yang, Y., Nešić, S., & Brown, B. N. (2008). Roles of Passivation and Galvanic Effects in Localized CO₂ Corrosion of Mild Steel. CORROSION/2008, paper 8332.
83. Singer, M., Brown, B., Camacho, A., & Nešić, S. (2011). Combined effect of carbon dioxide, hydrogen sulfide, and acetic acid on bottom-of-the-line corrosion. *Corrosion*, 67(1), 015004-1.
84. Singer, M., Camacho, A., Brown, B., & Nešić, S. (2011). Sour top-of-the-line corrosion in the presence of acetic acid. *Corrosion*, 67(8), 085003-1.
85. Singer, M., Hinkson, D., Zhang, Z., Wang, H., & Nešić, S. (2013). CO₂ top-of-the-line corrosion in presence of acetic acid: a parametric study. *Corrosion*, 69(7), 719-735.
86. Li, W., Xiong, Y., Brown, B., Kee, K. E., & Nešić, S. (2015). Measurement of Wall Shear Stress in Multiphase Flow and Its Effect on Protective FeCO₃ Corrosion Product Layer Removal, CORROSION/2015, paper 5922.
87. Li, W., Pots, B. F. M., Brown, B., Kee, K. E., & Nešić, S. (2016). A Direct Measurement of Wall Shear Stress in Multiphase Flow – Is it an Important Parameter in CO₂ Corrosion Of Carbon Steel Pipelines?, *Corrosion Science*, 110, 35-45
88. Li, W. (2016). *Mechanical Effects of Flow on CO₂ Corrosion Inhibition of Carbon Steel Pipelines* (Doctoral Dissertation) Ohio University, Athens, OH.

89. Patel, V. C., & Head, M. R. (1969). Some Observations on Skin Friction and Velocity Profiles in Fully Developed Pipe and Channel Flows. *Journal of Fluid Mechanics*, 38(01) 181-201.
90. Wang, A., Kuebler, K. E., Jolliff, B. L., & Haskin, L. A. (2004). Raman spectroscopy of Fe-Ti-Cr-oxides, case study: Martian meteorite EETA79001. *American Mineralogist*, 89(5-6), 665-680.

APPENDIX 1: PRELIMINARY EXPERIMENTATION FOR FECO₃

REPRODUCIBILITY

The purpose of this experiment was to develop a reproducible protective iron carbonate layer on the carbon steel surface in CO₂ corrosion environment based on Yang's previous tests⁶. The formation of the FeCO₃ layer was tested in a three-electrode glass cell with a rotating cylinder setup as shown on **Figure 3**. The test matrix for these experiments is shown in **Table 14** and procedures followed those described in objective 1 for short-term high S_{FeCO_3} . The change of corrosion rate and saturation level of the solution during the test are shown in **Figure 98** for Yang's results. The results of this study are shown in **Figure 99**. The solution was kept at a higher saturation value of 300 with respect to FeCO₃ in order to shorten the time to build a corrosion product layer. As shown in **Figure 99**, the corrosion rate gradually decreased over time to a low value (~0.2 mm/yr) since a layer of protective FeCO₃ formed on the steel surface. The saturation value decreased from 300 to around 10 due to precipitation of the FeCO₃ on the steel surface and in the bulk solution, which consumed the ferrous ions that were released from the steel specimen due to corrosion and the ferrous ions that were added at the beginning of the experiment. When the corrosion rate decreased to a low value and stabilized, the RCE was taken out of the glass cell for surface analysis using SEM, as shown in **Figure 100**.

Table 14. Test matrix for replicated work

Material	API 5L X65 (0.14% C)
Flow Velocity	Stagnant
Experimental Setup	2 L Glass cell
Electrolyte	1 wt.% NaCl
Initial pH	6.6 \pm 0.01
Temperature (°C)	80
Total Pressure (bar)	1.0
CO ₂ Partial Pressure (bar)	0.53
Initial [Fe ²⁺] (ppm)	50
Initial Saturation w.r.t. FeCO ₃	300
Electrochemical Measurement	LPR ± 5 mV vs. EOC, 0.125 mV/s
Surface Analysis	SEM EDS

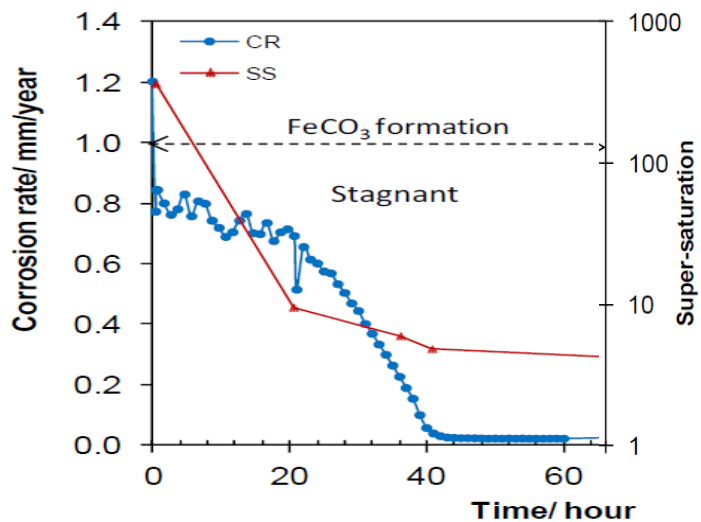


Figure 98. Comparison of LPR corrosion rates and saturation of FeCO₃ over time from Yang's study⁶ for stagnant experiment with API 5L X65 (0.14 wt.% C) under the conditions: T=80°C, pCO₂ = 0.53 bar, initial pH 6.6, initial S_{FeCO₃} ≈ 300

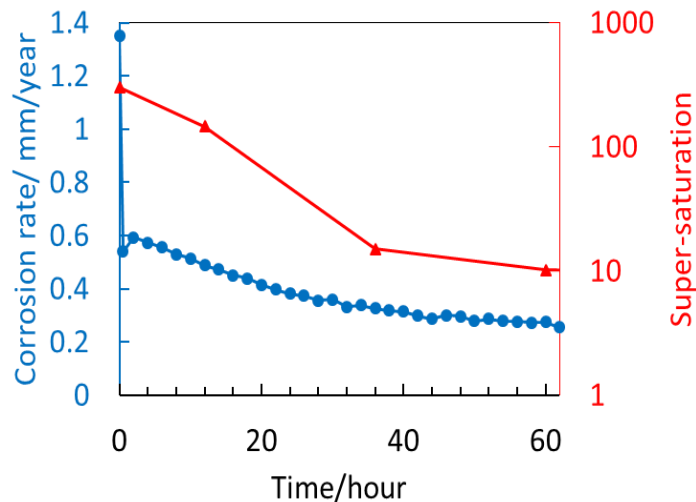


Figure 99. Comparison of LPR corrosion rates and saturation of FeCO_3 over time for stagnant experiment with API 5L X65 (0.14 wt.% C) under the conditions: $T=80^{\circ}\text{C}$, $\text{pCO}_2 = 0.53$ bar, initial pH 6.6, initial $S_{\text{FeCO}_3} \approx 300$

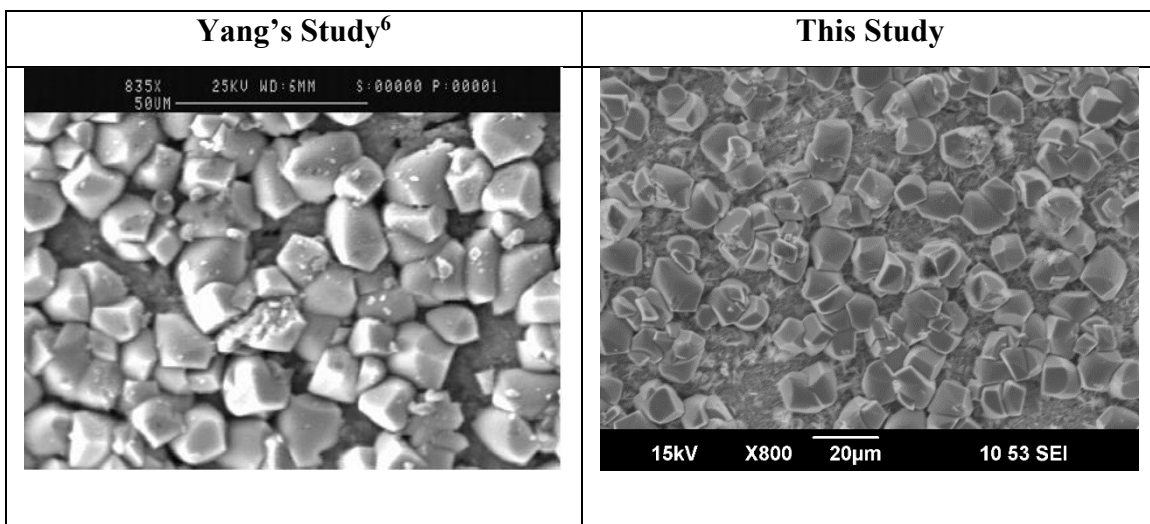


Figure 100. x800 SEM images showing comparison of surface morphologies for stagnant experiment with API 5L X65 (0.14 wt.% C) under the conditions: $T=80^{\circ}\text{C}$, $\text{pCO}_2 = 0.53$ bar, initial pH 6.6, initial $S_{\text{FeCO}_3} \approx 300$

When comparing Yang's study with the results from this study, it can be seen that the initial corrosion rates are above 1 mm/yr. The corrosion rate then suddenly drops after that and slowly decreases to a low stable corrosion rate. The low stable corrosion rate is

reached past 40 hours for both experiments, which proved a protective layer formed on the surface. Although the curves differ in behavioral trend, they indeed look similar since they start at similar initial corrosion rates and end with low corrosion rates and saturation values. Variabilities in the LPR corrosion rate plots have been reported previously by Yang⁶ and other researchers³⁻⁵ due to centripetal/centrifugal forces attributed to the geometry of the working electrode, in this case an RCE. Additionally, by comparing the surface analysis in **Figure 100**, it can be seen that the steel surface is covered with FeCO₃ prisms of the same size.

**APPENDIX 2: HIGH INITIAL S(FECO₃), SHORT-TERM EXPERIMENTS
WITH API 5L X65**

The experimental objective and procedure described for experiments in task #1, section 4.1, were also applied to experiments using API 5L X65 as-received. Since the experiment duration is short, microstructure does not play a role in this set of experiments even though API 5L X65 is used. The test matrix described in **Table 3** for task #1, apply to these set of experiments, except for the material. **Figure 101** shows the LPR corrosion rate measurements taken during the eight hour experiment. It is noted that as velocity increased, the initial corrosion rate increased. It can also be seen that the only specimen that reached a low stable corrosion rate was the stagnant specimen. Although it seems that the 0.6 m/s (0.8 Pa) drops to a low stable corrosion rate, the corrosion rate was actually increasing after the first drop.

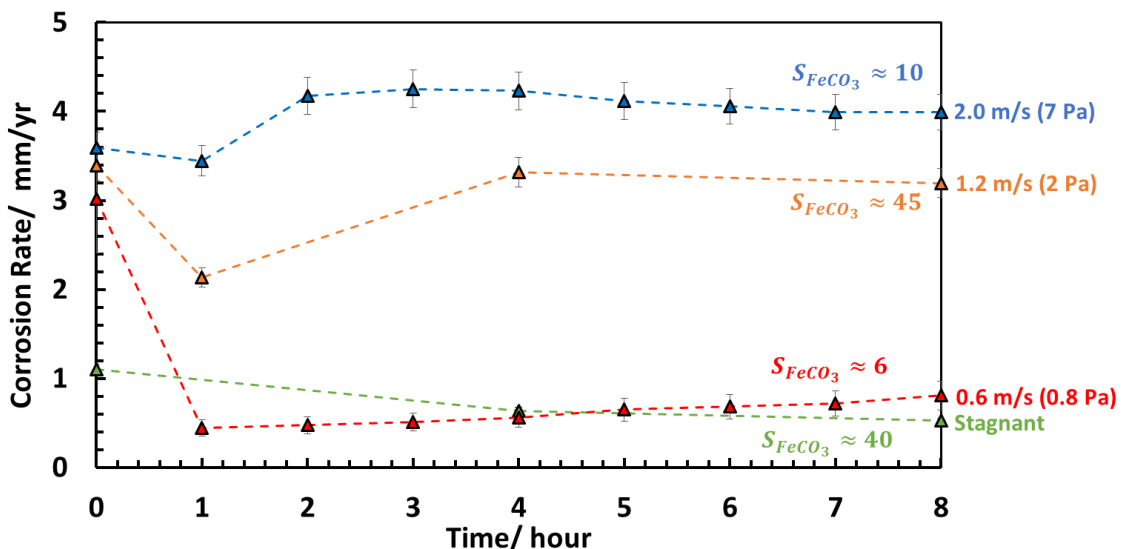


Figure 101. Comparison of LPR corrosion rates over time for stagnant, 0.6 m/s (0.8 Pa), 1.2 m/s (2 Pa), and 2.0 m/s (7 Pa) experiments with API 5L X65 under the conditions: T=80°C, pCO₂ = 0.53 bar, initial pH 6.6, initial S_{FeCO₃} ≈ 150

Figure 102 shows SEM images for the four different velocities. It is noted that as the fluid velocity increased, there was visually less presence/attachment of FeCO₃ on the steel surface. Additionally, the stagnant specimen showed a covered surface with FeCO₃. However, there was visually more Fe₂(OH)₂CO₃ plates than FeCO₃ prisms. All other specimens see sporadic attachment of FeCO₃ prisms. This correlates with the findings described in section 4.1.

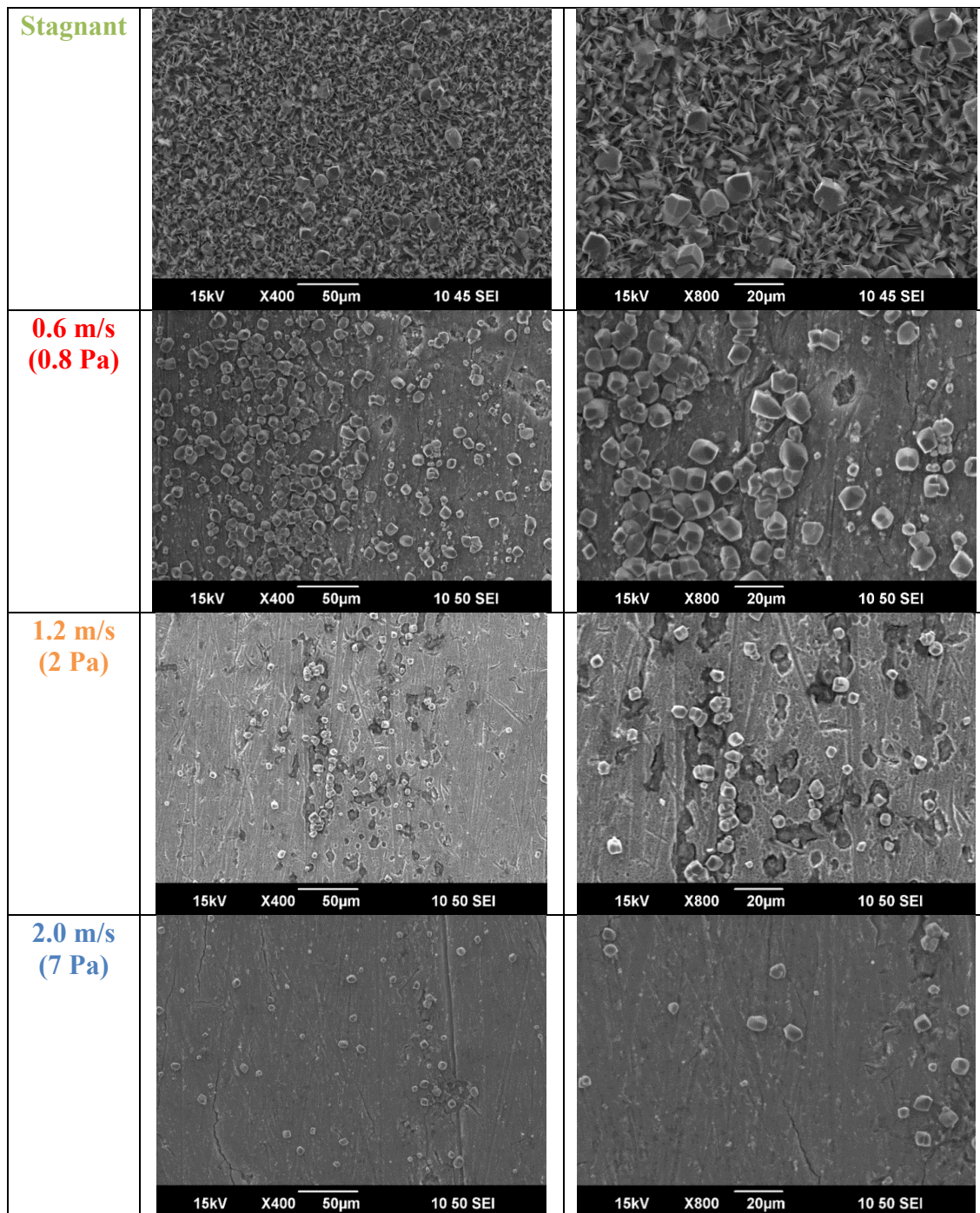


Figure 102. x400 and x800 SEM images showing comparison of surface morphologies after 8 hours for stagnant, 0.6 m/s (0.8 Pa), 1.2 m/s (2 Pa), and 2.0 m/s (7 Pa) experiments with API 5L X65 under the conditions: T=80°C, pCO₂ = 0.53 bar, initial pH 6.6, initial S_{FeCO₃} ≈ 150

APPENDIX 3: WATER CHEMISTRY WITH NO FERROUS IRON CONTROL

The purpose of this experiment was to understand the effectiveness of the Na-ion exchange resin, in relation to the behavior/role of ferrous ion concentration. This experiment was performed following the methodology and experimental matrix described in the task #2, section 4.1.1 and **Table 5**, respectively. **Figure 103** shows how the ferrous ion concentration quickly increases to high values and fall out of the range of the desired concentration during the experiment (1 ppm – 6 ppm). This fluctuation significantly affects the water chemistry of the system and the results obtained from this set of experiments.

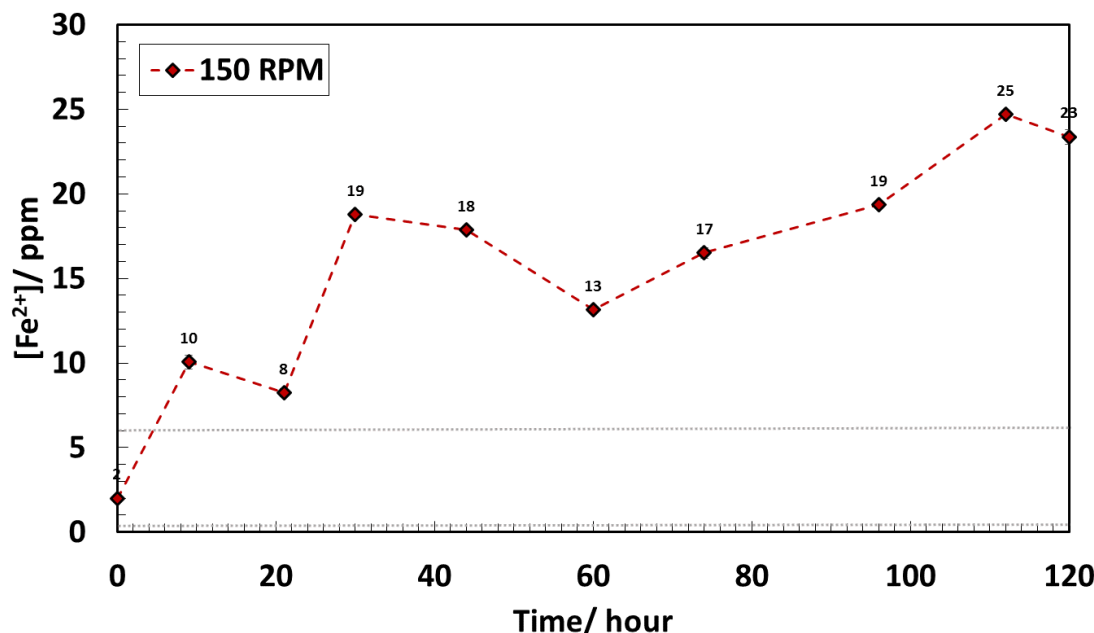


Figure 103. $[\text{Fe}^{2+}]$ change over time with no $[\text{Fe}^{2+}]$ control for 150 rpm experiment with API 5L X65 under the conditions: $T=80^{\circ}\text{C}$, $p\text{CO}_2 = 0.53$ bar, initial pH 6.6, initial $S_{\text{FeCO}_3} \approx 10$

APPENDIX 4: FLOW SIMULATIONS OF IMPELLER SETUP

The flow simulations shown in this appendix were executed on ANSYS and performed by Ezechukwu Anyanwu, a Ph.D. candidate at ICMT. In order to properly run the simulations on ANSYS, the following glass cell domains were used, shown in **Figure 104**:

- Rotor (rotating) domain: Region around the impeller assembly
- Sample (stationary) holder domain: Region around the sample holder
- Stator (stationary) domain: Region outside the rotor domain and sample holder

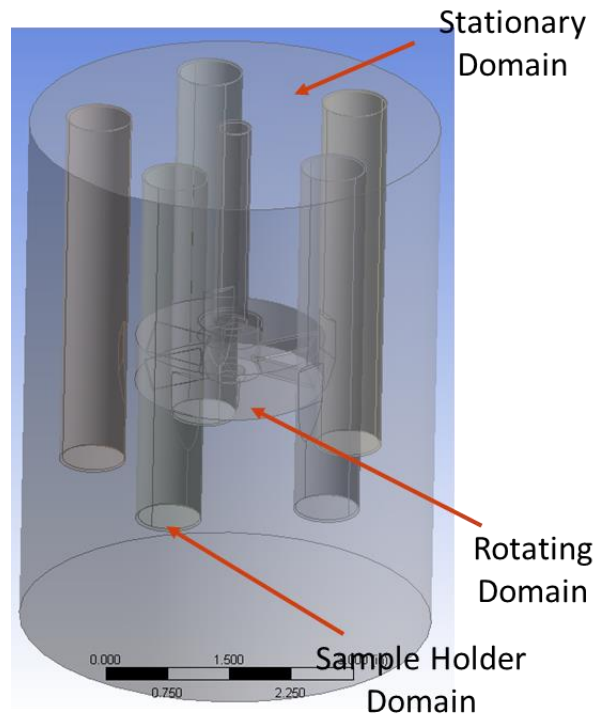


Figure 104. Glass cell geometry and domains setup

The turbulence model used was the shear stress transport was used. This model switches between models with the help of a blending function; $\kappa-\omega$ model in wall regions

and κ - ϵ model in shear free regions. This model applies automatic near wall treatment as follows:

- Large y^+ (> 20) uses standard wall function treatment
- Small y^+ (< 2) uses low Reynolds wall treatment
- Transition region uses a blend of both wall treatments above

Figure 105 and **Figure 106** show the velocity and wall shear stress contours, respectively, for the two rotational speeds used in experimentations discussed in task #2, section 4.2.

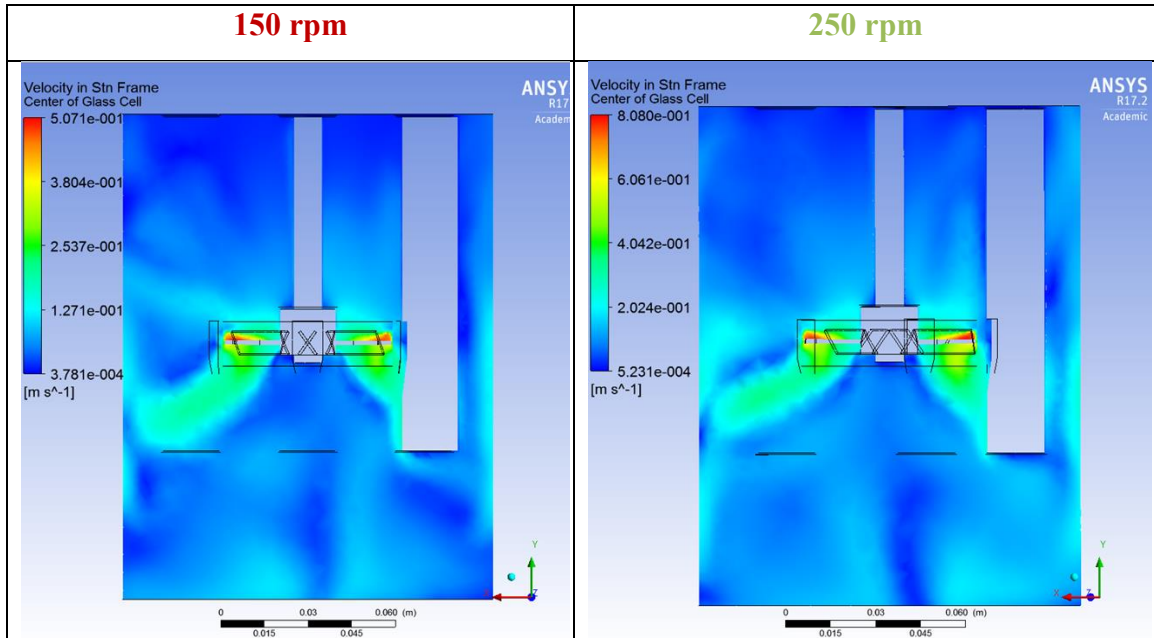


Figure 105. Velocity contour for 150 rpm and 250 rpm impeller rotational speeds in stationary frame for pitched blade impeller in 2 L glass cell in water at 80°C

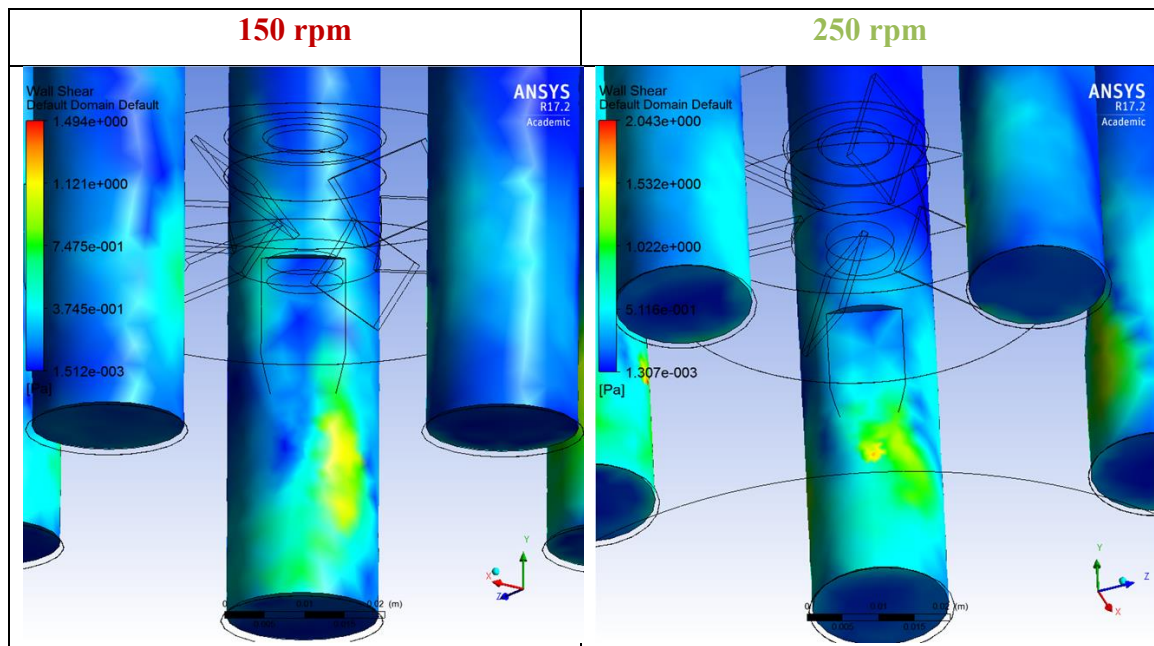


Figure 106. Wall shear contour profile in stationary frame for pitched blade impeller in 2 L glass cell in water at 80°C

The wall shear stress results obtained from this simulation and the equivalent pipeline velocity (25.5 cm ID pipe) are summarized in **Table 6**.



Thesis and Dissertation Services